EUMETSAT

European Organisation for the Exploitation of Meteorological Satellites

Programme Development Department

Technical Memorandum No. 8

ISSWG Line-by-line Intercomparison Experiment

by

S.A. Tjemkes[a], T. Patterson[a], R. Rizzi[b], M.W. Shephard[c], S.A. Clough[c], M. Matricardi[d], J. Haigh[e], M. Höpfner[f], S. Payan[g], A. Trotsenko[h], N. Scott[i], P. Rayer[j], J.P Taylor[j], C. Clerbaux[k], L.L. Strow[l], S. DeSouza-Machado[l], D. Tobin[m], R. Knuteson[m]

Prepared for the IASI Sounder Science Working Group

October, 2001

[a]European Organisation for the Exploitation of Meteorological Satellites, Germany
[b]Atmospheric Dynamics Group Bologna, Bologna, Italy
[c]Atmospheric & Environmental Research, Inc., United States of America
[d]European Centre for Medium-Range Weather Forecasts, United Kingdom
[e]Imperial College of Science, Technology and Medicine, United Kingdom
[f]Forschungszentrum Karslruhe, Germany
[g]Laboratoire de Physique Moléculaire et Applications, France
[h]Laboratory for Information Technologies and Mathematical Simulation, RRC Kurchatov Institute, Russia
[i]Laboratoire de Météorologie Dynamique du C.N.R.S., France
[j]The Met Office, United Kingdom
[k]Service d'Aéronomie, France
[l]University of Maryland, Baltimore County, United States of America
[m]University of Wisconsin-Madison, United States of America

ISSWG Line-by-line Intercomparison Experiment

S.A. Tjemkes[0] T. Patterson[0] R. Rizzi[1] M.W. Shephard[2]
S.A. Clough[2] M. Matricardi[3] J. Haigh[4] M. Höpfner[5]
S. Payan[6] A. Trotsenko[7] N. Scott[8] J.P. Rayer[9]
J. Taylor[9] C. Clerbaux[10] L.L. Strow[11]
S. DeSouza-Machado[11] D. Tobin[12] R. Knuteson[12]

October 19, 2001

[0]European Organisation For The Exploitation Of Meteorological Satellites, Germany
[1]Atmospheric Dynamics Group Bologna, Bologna, Italy
[2]Atmospheric & Environmental Research, Inc., United States of America
[3]European Centre for Medium-Range Weather Forecasts, United Kingdom
[4]Imperial College of Science, Technology and Medicine, United Kingdom
[5]Forschungszentrum Karslruhe, Germany
[6]Laboratoire de Physique Moléculaire et Applications, France
[7]Laboratory for Information Technologies and Mathematical Simulation (LITMS), RRC Kurchatov Institute, Russia
[8]Laboratoire de Météorologie Dynamique du C.N.R.S., France
[9]The Met Office, United Kingdom
[10]Service d'Aéronomie, France
[11]University of Maryland, Baltimore County, United States of America
[12]University of Wisconsin-Madison, United States of America

Contents

List of Tables

Abstract

To document the performance of current line by line radiative transfer models, a study was performed to compare the model simulations with real observations and also intercompare the simulations themselves. Two observational datasets were analysed where high spectral resolution observations were made and at the same time the atmospheric state was carefully monitored. The first dataset consisted of radiance observations using the HIS interferometer during the CAMEX-1 campaign off the east coast of the USA. The second dataset consisted of observations from the ARIES interferometer collected during the ASCENSION island campaign over the tropical Atlantic. These two cases are very different with the Ascension island case being much warmer and humid than the CAMEX case. In total 13 different research groups participated with 7 different line-by-line models. The results of this study indicated that in many spectral regions the models are capable to reproduce the observations within the observed noise. In some spectral regions relatively large differences between the simulations and observations exists. For almost all relevant differences the reason for these differences is known, and are subject of active research. The results documented in this report are important for the interpretation of atmospheric state observations by new generation of atmospheric sounder instruments like AIRS, IASI and TES for which fast radiative transfer codes capable of simulating the observed spectra are being generated.

Chapter 1

Introduction

Measurements from the IASI instrument, which is due to fly on the METOP polar orbiters, comprise top of atmosphere radiances from 8461 channels in the infrared wavelength range from 645 $cm^{-1}$to 2940 cm^{-1}[Cayla, 1993]. The objective of making these radiance observations is to infer temperature and water vapour profiles and total column concentrations of some minor gases. In order to assimilate these data in NWP models or perform stand-alone retrievals a pre-requisite is to be able to accurately model the radiances with a radiative transfer (RT) model. For operational use these RT models must be fast and several models have been developed for IASI [e.g. Hannon et al., 1996, Matricardi and Saunders, 1999]. These fast RT models rely upon using a dataset of transmittances or radiances computed from an accurate line-by-line (LbL) model which simulates all the known spectroscopic processes occurring in an atmosphere free of cloud and aerosol. These LbL models are of necessity expensive to run and store the datasets. To determine how much the fast RT models are limited in their accuracy by the LbL models on which they are based an assessment of the LbL models themselves has been undertaken with the following objectives:

- To document the current line by line infrared models and spectral databases
- To quantify their errors in terms of IASI simulations
- To quantify differences between the models
- To assess which models and spectral databases are suitable for IASI simulations
- To identify where more work is needed either in LbL model development or in spectroscopic measurements (laboratory and/or atmospheric)

Our current knowledge of atmospheric absorption mechanisms is not complete, for instance the particular formulations for line mixing in the carbon dioxide P/R branches or for the water vapour continuum are still open to some debate. Typically the line parameters themselves are only accurate to 5% in line intensity and 10% in line width and there may be missing lines in the standard spectroscopic databases. The discretisation of the LbL models (i.e. atmospheric layering, initial spectral grid for computations) is another potential source of errors. One step in determining the magnitude of these uncertainties is to compare the differences between LbL model-computed radiances for all the IASI channels given the same input atmospheric profile. Several intercomparisons of LbL and fast models have already been carried out [e.g. Chédin et al., 1988, Ellingson and Fouquart, 1991, Garand et al., 2001] but these have all been for much broader spectral channels than IASI and so are not detailed enough spectrally for IASI simulations.

It is important to be able to quantify the errors of the fast RT computations, of which LbL model errors is one component, for several reasons. Firstly if there are regions of the spectrum which current LbL models cannot accurately simulate then these should be identified and rejected for use in assimilation or retrievals. Secondly the magnitude of the (observation + RT model) error covariance is required for variational data assimilation. The component of RT model error due to the fast models approximations can be determined [e.g. Matricardi and Saunders, 1999, Sherlock, 2000], but it is harder to estimate the absolute accuracy of the LbL model on which the fast model is based.

The IASI Science Sounder Working Group (ISSWG) approved the commencement of this LbL model intercomparison project at their second meeting in Cordes, France in 1996 and subsequently there were submissions from 12 participants. The intercomparison was designed to compare model calculations with observations, in this case from aircraft, in order to assess not only the relative differences between models but also the absolute differences from measurements. The observations were necessarily of a similar spectral resolution to IASI and were as close as possible to top of atmosphere measurements. The aircraft data used were from the HIS instrument flying on the ER-2 over the sea off the Virginia coast in the CAMEX experiment and from the ARIES instrument on the C-130 over the tropical Atlantic close to Ascension Island. The two atmosphere types were quite different, one representative of mid-latitudes, and the other of the tropics.

This report summarizes the results obtained from this ISSWG LbL comparison. The participants and models are documented in section 2, the observational datasets in section 3 and the results in section 4. The results from this report are not only applicable to IASI but also other satellite infrared spectrometers and radiometers (e.g. AIRS, TES, HIRS and MODIS).

Chapter 2

Participants

This intercomparison presents results of line-by-line calculations by a large group of scientists. The key features of the models participated in the comparison study are listed in Table 2.1. This information is provided by the individual participant.

The table indicates that there were seven different line-by-line models, namely LBLRTM (at AER, EUMETSAT, SA and UW), GENLN2 (at ECMWF, IMCOL, the Met Office and UMBC), HARTCODE, KOPRA, LARA, LITMS, and 4A. Most of the participants adopted HITRAN 96 line database in combination with CKD 2.1, 2.2 or 2.4 model for water vapor continuum. Furthermore, four participants used the HITRAN 96 database revised with the Toth H_2O spectroscopic parameters in the 10 micron region[1]. Two models adopted the GEISA 97 spectroscopical database, which included the Toth revision as well. For the intercomparison most models provided monochromatic radiances at a dispersion of roughly 0.001 cm^{-1}, HARTCODE provided the integrated result at roughly the same resolution.

[1]In the remainder part of the document this revision of the H_2O spectroscopy in the 10 micorn region will be refered to as the Toth revision

Table 2.1: Summary of the submitted results

Acronym	Model	DataB[a]	Res.[b]	Type[c]	Cont.[d]	Mix[e]
ADGB	HARTCODE[1]	G97	5	A	CKD 2.4	ROD99
AER	LBLRTM V5.4[2]	H96+T	1	B	CKD 2.4	HOK89
ECMWF	GENLN2[3]	H96	1	B	CKD 2.1	STH94
EUMETSAT	LBLRTM V5.4	H96	0.8	B	CKD 2.4	HOK89
IMCOL	RFM V4.03_OXF[4]	H96	1	B	CKD 2.1	STH94
KOPRA[5]	KOPRA	H96	1	B	CKD 2.2	FUN98
LPMA	LARA	H96	1	B	CKD 2.4	ROD99
LITMS	LITMS[6]	H96	1	B	CKD 2.2	STH94
LMD	4A00[7]	G97	1	B	CKD 2.1	ROD99
METOF	GENLN2 V4	H96	1	B	CKD 2.1	STH94
SA	LBLRTM V5.4	H96+T	1	B	CKD 2.4	HOK89
UMBC	kCarta V1.04[8]	H96	2.5	B	CKD 2.3	STH94
UW	LBLRTM V5.4	H96+T	0.8	B	CKD 2.4	HOK89

[a] Line parameter databases: Geisa 97 (G97, Jacquinet-Husson et al. [1999], http://ara01.polytechnique.fr), HITRAN 96 (H96, Rothman et al. [1998], http://www.hitran.com), HITRAN 96 + Toth Revision (H96+T),

[b] Dispersion resolution of results in 0.001 cm^{-1}.

[c] Results represent monochromatic (B) or integrated (A) radiances at the given dispersion.

[d] Water vapor continuum model used.

[e] Carbon dioxide line mixing model: ROD99: Rodrigues et al. [1999], Kochel et al. [1997]; STH94: Strow et al. [1994]; HOK89: Hoke et al. [1989]; FUN98: Funke et al. [1998].

Selected References:

[1] Rizzi et al. [2001]

[2] Clough et al. [1992], Clough and Iacono [1995], Clough et al. [1995]

[3] Edwards [1992], Strow et al. [1994], Clough et al. [1989, 1980]

[4] http://www.atm.ox.ac.uk/RFM

[5] Stiller et al. [1998], Höpfner et al. [1998], Kuntz et al. [1998], von Clarmann et al. [2000] http://www-imk.fzk.de:8080/imk2/ame/publications/kopra_docu/kopra_docu.html

[6] Trotsenko and Fomin [1989], Trotsenko et al. [1993, 1995]

[7] W.J. et al. [1996], Thibault et al. [1997], Perrin and Hartman [1989], Gamache et al. [2000], Scott and Chédin [1981], Clough et al. [1980]

[8] http://asl.umbc.edu/pub/kcarta/kcarta.html

Table 2.2: Point of contact.

Participant	Acronym
Dr. R. Rizzi (R.Rizzi@adgb.df.unibo.it)	ADGB
Dr. M.W. Shepard (mshep@aer.com)	AER
Dr. M. Matricardi (stm@ecmwf.int)	ECMWF
Dr. S. Tjemkes (tjemkes@eumetsat.de)	EUMETSAT
Dr. J. Haigh (j.haigh@ic.ac.uk)	IMCOL
Dr. M. Höpfner (Michael.Hoepfner@imk.fzk.de)	KOPRA
Dr. S. Payan (payan@ccr.jussieu.fr)	LPMA
Dr. A. Trotsenko (ant@imp.kiae.ru)	LITMS
Dr. N. Scott (scott@ara01.polytechnique.fr)	LMD
P. Rayer (peter.rayer@metoffice.com)	METOF
Dr. C. Clerbaux (catherine.clerbaux@aero.jussieu.fr)	SA
Dr. S.DeSouza-Machado (sergio@umbc.edu)	UMBC
Dr. D. Tobin (davet@ssec.wisc.edu)	UW

Chapter 3

Observations

Two different datasets were used in the intercomparison. The first dataset consisted of HIS observed spectra and associated atmospheric state data for the night of 09/29/93 during the CAMEX I observing campaign. The second dataset consisted of ARIES observed spectra and associated atmospheric state data for 06/05/1999 during the 1999 ASCENSION Island campaign.

3.1 CAMEX

This dataset was prepared by D. Tobin, B. Knuteson and R. Rizzi. The up-welling radiance spectrum measured by the HIS during the "third northbound pass" of the HIS over the ocean offshore of Wallops Island, Virginia on 29 Sept 1993 UTC. The observations adopted for the intercomparison were averaged over 24 independent scans. The mean observation and its associated error (defined by the rms error) are shown in Figures 7.1 - 7.5 in radiance and equivalent brightness temperature units respectively. The observations are taken at approximately 20 km above the surface. The scale of the error in the mean observed radiance is shown on the right y-axis and is a factor 10 smaller than the scale of the mean observations. The figures show that, except for the spectral region between roughly 2250 - 2380 cm^{-1}, the uncertainty in the observations is so low that the signal to noise ratio is very large.(Note that in the radiance scales on the y-axes are chosen such that if the two lines of the mean observation and its associated error crosses, the signal to noise ratio is 10.)

The atmospheric state file used in the calculations was a composite from different sources and of selected state variables is shown in Fig. 7.7. The figure shows the presence of a dry layer around 800 hPa. The sea surface skin temperature is not observed using an independent device. The skin temperature was set to 293.0 which gives the best fit for a surface emissivity of 1 and FASCODE calculations. Climatological values for the vertical distribution of heavy molecules were adopted. A summary is given in Table 3.1.

Table 3.1: Summary of the atmospheric state for the CAMEX case.

Observational Height	19.97 km
Included in Calculations	H_2O, CO_2, O_3, N_2O, CO, CH_4, O_2, NO, SO_2, NO_2, N_2, CCL_3F(F11), CCL_2F_2(F12), CCL_4
Observed	Temperature, Pressure, H_2O, O_3
Assumed	CO_2,N_2O, CO, CH_4, O_2, NO, SO_2, NO_2, N_2, CCL_3F(F11), CCL_2F_2(F12), CCL_4
CO_2 Mixing Ratio	358 ppmv (Assumed)
Surface Temperature	293.000 K (Assumed)
Surface Emissivity	1.000 (Assumed)
Surface Pressure	1018.000 (Observed)

3.2 ASCENSION

This dataset was prepared by J. Taylor of the Met Office. The up-welling radiance field was measured by the instrument at 7.9 km altitude and are shown in Figures 7.8 - 7.10. The observations were averaged over 500 scans, and as a result the associated noise in the observations is relatively low. In a few specific narrow spectral intervals, the large value of the absorption coefficient prevents a proper calibration of the observations. This results in spikes in the observational dataset.

The atmospheric state profile used in the calculations was a combination of observed values for temperature, water vapour and carbon monoxide mixing ratio and climatological values for the other gases. The surface temperature was observed as 301.8 K and a surface emissivity of 0.980 was adopted. Figure 7.12 shows the atmospheric state of selected state variables. A summary is given in Table 3.2

From Figs. 7.7 and 7.12 one can see that the two cases are very different from each other. The Ascension Island case is much more humid and warm than the CAMEX case. Because of the much lower observational level in the Ascension Island case, the ozone amount below the observational level is distinctly different for the two cases. It is also worth noting that the CO volume mixing ratio profile in the Ascension Island case shows much more structure than the CAMEX case and also increases in concentration with height.

Table 3.2: Summary of the atmospheric state for the ASCENSION case.

Observational Height	7.924 km
Included in Calculations	H_2O, CO_2, O_3, N_2O, CO, CH_4, O_2, NO, SO_2, NO_2, N_2, CCL_3F(F11), CCL_2F_2(F12), CCL_4
Observed	Temperature, Pressure, H_2O, CO
Assumed	CO_2, O_3, N_2O, CH_4, O_2, NO, SO_2, NO_2, N_2, CCL_3F(F11), CCL_2F_2(F12), CCL_4
CO2 Mixing Ratio	365 ppmv (Assumed)
Surface Temperature	301.8 K (Assumed)
Surface Emissivity	0.98 (Assumed)
Surface Pressure	1008.920 (Observed)

Chapter 4

Results

4.1 Preamble

In this section the results of the intercomparison are presented for each of the observing campaigns. It is split in two parts, namely one part describing the comparison between the observations and the model calculations. The second part describes the intercomparison between the models.

The discussion on the comparison between model simulations and observations consists of two parts. In the first part common features among the various models are highlighted for each of the three HIS bands and the two ARIES bands are discussed. This is done through the presentation of a series of figures[1]. The first two figures show the simulated results in radiance space ($Wm^{-2}sr^{-1}\left(cm^{-1}\right)^{-1}$ units) and in equivalent brightness temperature space (K units) respectively. The difference between the simulations ($\mathcal{R}^s$) and the observations ($\mathcal{R}^o$) are presented in three different ways. First the straight difference ($\Delta\mathcal{R} = \mathcal{R}^s - \mathcal{R}^o$) in radiance space as a function of wavenumber is presented, followed by two more figures representing the normalised radiance difference and the noise equivalent brightness temperature difference respectively. The normalised radiance difference is calculated as the ratio of the radiance difference with the uncertainty in the mean observation ($\Delta\mathcal{R}_n = \Delta\mathcal{R}/\sigma^o$). The noise equivalent brightness temperature (NeΔT), is calculated from the radiance difference and the Planck-function at the actual scene temperature. These two figures facilitate an easier interpretation of the results.

Then in the second part, the performance of the different models are compared in spectral bands of interest to IASI applications. These bands are listed in Table 4.1 together with an estimation of the error in the HIS and ARIES observations and the potential application of the IASI observations in these bands. The listed error is the average uncertainty in the observations in the particular spectral interval. The results here are presented as a series of figures of the normalised radiance difference as a function of wavenumber for the spectral region of interest. No attempt is made to condense the presented results in an average difference for each interval.

[1]The header of the figures list the name of the instrument (HIS/ARIES), the band and an additional identifier (STD) to refer to the results for the standard or baseline setup. This identifier was needed because in addition to calculations for the baseline scenario, several participants provided results from additional scenarios, e.g. with a different sea surface emissivity. The results of these calculations are presented at the end of the report.

Table 4.1: Selected spectral intervals of interest to IASI applications. Also listed in the Table is a noise estimation of the different instruments. For the HIS and ARIES instrument the listed numbers are average of the uncertainty in the observation.

Channels	HIS	ARIES	IASI	Comments
650.0 – 770.0	≈ 0.09K	≈ 0.02	< 0.2K	Temperature
770.0 – 980.0	≈ 0.08K	≈ 0.03K	< 0.2K	Surface properties + Clouds
1000.0 – 1070.0	≈ 0.16K	≈ 0.02K	≈ 0.15K	Ozone
1080.0 – 1150.0	≈ 0.28K	≈ 0.03K	≈ 0.2K	Surface Properties
1250.0 – 1350.0	≈ 0.08K	≈ 0.1K	≈ 0.1K	Water Vapour + Trace gases
2100.0 – 2150.0	≈ 0.09K	≈ 0.08K	≈ 0.15K	Carbon monoxide
2150.0 – 2250.0	≈ 0.22K	≈ 0.07K	< 0.2K	Temperature
2350.0 – 2420.0	≈ 3.41K	≈ 0.16K	< 0.4K	Temperature
2420.0 – 2600.0	≈ 0.46K	≈ 0.37K	≈ 1.0K	Surface Properties

4.2 HIS band1

4.2.1 Experiments

To illustrate the relative position of the absorption features of the individual atmospheric constituents, some experimental runs with a particular line-by-line model (namely LBLRTM) were performed. As input to the LBLRTM model, the atmospheric state for the particular case study was modified such that the model calculated the effect of one atmospheric constituent on the surface radiance field transmitted to the observational. This means that the mixing ratio of one absorber was left unchanged, while the mixing ratio of the other absorbers were set to zero. The effects of the continuum absorption on the radiance field at the observational level was not calculated in any of these experiments.

Figure 7.13 shows the results of these radiance calculations after a convolution with the ISRF for HIS band 1. This band extends from approximately 600 - 1100 cm^{-1}. Many weak absorption lines of water vapour are present throughout the band. Strong absorption by carbon dioxide occurs between 600 - 700 cm^{-1}, and some weaker carbon dioxide absorption features at 791 cm^{-1}, and around 950 and 1060 cm^{-1}. The 791 cm^{-1} Q-branch absorption lines are only very slightly offset with respect to some water vapour lines around 800 cm^{-1}, while the absorption around 1060 cm^{-1} coincides with the strong 9.6 μm ozone band.

Ozone also presents some absorption in the 15 μm region. The same is true for nitrous oxide. Finally there is some weak absorption by CFC11 and CFC12. Although the absorption by these chlorofluorocarbons are weak, in the absence of strong absorption by other gases, the interaction with radiation by these molecules is noticeable.

4.2.2 Simulations

Entire Band

As can be seen from Figures 7.14 - 7.17, in general all models perform reasonable well in the window region (800 - 1000 cm^{-1}), provided that the effects of the chlorofluorocarbons (CFC-11 and CFC-12) are included in the simulations. There is also good agreement between the observations and calculation in the 15 μm CO_2 band. Larger differences between the observations and calculations are found in the wings of the 15 μm CO_2 band. This difference tends to be positive with a high frequency variation superimposed on this. The radiation in 791 cm^{-1} Q-branch of CO_2 is underestimated by most of the models, while the radiation in the water vapour band at 800 cm^{-1} is mostly overestimated. Analysis by the LITMS group (not presented here) suggests that the feature around 800 cm^{-1} is a residual of incomplete water vapour spectroscopy. The SA and UW calculations included the Toth revision, which resulted in a better performance in selected regions in the window region, in line with the findings of the LITMS group. Possibly the two groups used a different version of the Toth revision, or the settings of some of the parameters of the adopted line-by-line model was different, which could explain the different performance in this region. Although the ADGB, and 4A simulations were also done using the Toth revision, this did not remove the underestimation in these spectral regions.

Almost all models overestimate the radiance in the 9.6 μm O_3 band. Differences can be as large as 3 - 4 K. This general overestimation in the 9.6 μm O_3 band might be the result of incorrect specification of the atmospheric state. At the other hand, good agreement is found by the UMBC, UW and LITMS simulations. The good agreement of the LITMS model might be related to the internal vertical discretisation of the atmospheric state. The LITMS model did not perform the calculations on on the specified levels, but on a much finer grid. This suggests that for this model, the results in this part of the spectrum are sensitive to the actual vertical discretisation. Calculations by the AER group discovered that UW results were obtained for a slightly different atmospheric profile (see section 5.3.1). In their simulations they used a value of 20.691 km for the aircraft altitude, in stead of the 19.97 km. This resulted in a larger ozone amount below the aircraft and consequently a better fit to the observations in this part of the spectral domain. This could also explain the overestimation of the radiation in the 15 μm CO_2 region, where the simulations are sensitive to the temperature profile near the aircraft.

As a result of these findings, the AER group performed additional calculations. The results of these calculations are presented in section 5.3. For instance, they analyzed the effect of vertical discretisation, the inclusion of latest compilation of the Toth revision, and the effect of incorrect specification of the O_3 profile. Although the results presented in the section 5.3 are obtained with a particular model, it is believed that their findings are general applicable.

Detail

Figures 7.20 - 7.22 show the residuals for the first three bands of Table 4.1. It confirms that most of the models have a very similar performance in this spectral domain. The good performance by UMBC, UW and LITMS in the ozone band is clearly visible in Figure 7.22. It is worth to notice that only in the window region the absolute value of the normalised radiance difference is below 10.

Looking at Figure 7.20, we see that between 700-740 cm^{-1}, the residence residuals of kCARTA, and to a lesser extend LARA, are consistently in one direction, as compared to the other models where the residuals are in the negative direction from 700-720 cm^{-1}, and then in the positive direction from 720-740 cm^{-1} (this can best be seen by looking at the broader "black envelopes" in these regions). kCARTA uses a new formulation for the P/R-Branch line-mixing in this region (as well as in the 4.3 μm band of CO_2), which could explain the differences between this and the other codes. Figure 7.19 shows that the differences occur mainly between the lines.

4.3 HIS band2

4.3.1 Experiments

Fig. 7.23 illustrates the results of the single gas experiments performed for this band. Here the strong ν_2 band of water vapour resides, resulting in a large number of strong absorption lines throughout this spectral interval. Methane has a strong absorption band around 1300 cm^{-1}, and there is also noticeable interaction by nitrous oxide. Some weak absorption in the wings of the 9.6 μm ozone band around 1100 cm^{-1} are present, and finally CFC12 interacts weakly around 1150 cm^{-1}.

4.3.2 Simulations

Because of the large number of strong lines, the residual plots show much more structure in this band than in Band1. Performance of the different line-by-line models are very similar. That is, the normalised radiance differences are all relatively small and fluctuates around zero in the edges of the domain, while in the region between 1250 - 1500 cm^{-1} it is predominately negative (cf. Figure 7.28). All models agree with the observations within 2 K (cf. Figure 7.27). The models deviate more in certain details. For instance, the center of the water vapour ν_2 band at 1600 wavenumbers appears to be better represented by the LITMS, LMD, the Met Office and ECWMF simulations than by the others. The combined absorption of methane and water vapour around 1480 cm^{-1} appears to be better captured by the ADGB, and LARA simulation.

4.4 HIS band3

4.4.1 Experiments

Fig. 7.31 illustrates the results of the single gas experiments performed for this band. In this spectral domain, the 4.3 μm carbon dioxide band resides. Up to about 2400 cm^{-1} a large number of strong absorption lines by water vapour, carbon monoxide, carbon dioxide and nitrous oxide are present. Beyond this wavenumber only a few weak lines of methane and nitrous oxide and water vapour are visible in these simulations. Ozone has some weak lines around 2100 cm^{-1}.

4.4.2 Simulations

General

In the third HIS band, the prominent feature is the N_2 pressure-induced continuum around 2400 cm^{-1}. In this spectral domain the modelling of the CO_2 lineshape poses some difficulties as it is sub-Lorentzian. The radiance residual plots (Figure 7.34), show that the ADGB, IMCOL and the LARA simulation deviate more from the observations there than the other simulations. In general the normalised radiance residual plots indicate that the simulations are within roughly 10σ from the observations. A fundamental problem with this spectral interval is that the up-welling energy at the observational level is very small. This means that the difference between the simulations and observations when expressed as an equivalent brightness temperature difference easily exceed 5 K (Figure 7.35).

4.5 Model intercomparison

To illustrate the difference between the models, in this section an intercomparison between the models for the CAMEX case is presented. The results are presented as a series of figures. Two different set of figures are presented. One where the residual between a particular model and the LBLRTM model as implemented at EUMETSAT are shown, and one set where the reference model is changed to GENLN2 as implemented at the Met Office (The actual reference model is indicated in the Figure Title). For each band and for each reference model, the differences are shown in radiance and in equivalent brightness temperature space.

4.5.1 Band1

Figures 7.41-7.44 show the intercomparison results for the HIS band 1. The Figures show that the relative performance between the different models, depends strongly on wavenumber. Largest difference are found in the wing of the 15 μm of CO_2, but also in the ozone absorption band differences are evident. It is interesting that substantial differences are found between the same model, but implemented at different institutes, like the difference between the SA, UW and the EUMETSAT generated results. These difference could in part be explained by the different spectroscopy adopted (cf. Table 2.1). While SA and UW included the Toth revision of the H_2O spectroscopic parameters in the 10 micron region to the HITRAN 96 database EUMETSAT adopted the Hitran 96 dataset without modifications. This resulted in the spikes in the SA and UW figures. The difference in the O_3 band between the UW and EUMETSAT submission is caused by a small difference in the adopted value for the observational level of the air borne observations. The aircraft observation represents an average over about 10 minutes of flight during which time the aircraft altitude varied between 19.8 and 20.1. the adopted value of 19.97 for the simulations represents an average flight altitude. The simulations by UW were done using a aircraft altitude value of 20.691. This resulted in a somewhat larger ozone amount below the aircraft, and consequently smaller radiance values at the observational level than the EUMETSAT simulations.

Similar difference between the same model but implemented at different institutes are also found for the GENLN2 class of models (ECMWF, METOF, IMCOL and UMBC). The high frequency residual for the pair ECMWF-METOF as shown in Figure 7.43 could be related to the different implementation of the HIS convolution routine, which also could explain the high frequency residuals in the ADGB plots.

There appears a small residual feature in the 791 cm^{-1} Q-branch of CO_2. In Figure 7.44 this is visible in the panels for the ADGB, EUMETSAT, KOPRA, LARA, LITMS and UW submission, and to a lesser extend in the panel of the SA submission. Since the GENLN2 family of models, adopt the line coupling model by Strow et al. [1994] this feature could be related to different formulation of the line-coupling in this region. However, since the LITMS submission also includes this line-coupling model, this observation is not unambiguous. The differences between UMBC and LBLRTM are related to the different description of the the P/R branch mixing.

4.5.2 Band2

Figures 7.45-7.48 show the intercomparison results for the HIS band 2. The residual plots show much more structure in band 2 than in band 1. Outside of the region between roughly 1500 - 1700 cm^{-1}, the models agree reasonably well. A high frequency variation around the zero difference line is found. In e.g. 7.45 the high frequency variation appears for the ECMWF, IMCOL, KPRA, LMD and METOF results similar in structure, but of different magnitude. For the submission by the KOPRA group the amplitude is less than e.g. METOF. Results by these groups were generated with a different version of the CKD water vapour continuum model than adopted by the EUMETSAT simulations. This could partly explain the differences (cf. discussion for ARIES band2 results).

4.5.3 Band3

Finally, Figures 7.49-7.52 show the intercomparison results for the HIS band 3. Excluding the 4.2 μm CO_2 band region and the start of the window region around 2400 cm^{-1}, the models have a very similar performance. For the 2080 cm^{-1} region, there was originally no line coupling in the LBLRTM model, which explains the large spike in this region when compared to models which included a line coupling model. The introduction of the line coupling model as formulated by Strow et al, in the LBLRTM removed this difference (cf. section 5.3.4).

4.6 ARIES Band1

Figures 7.53-7.57 show the general results for the ARIES-band 1 simulation, followed by the figures for the various sub intervals in Figures 7.58-7.59. The observations taken during the ASCENSION-island campaign by the ARIES instrument are quite different from the observations taken by the HIS istrument during the CAMEX campaign. The ARIES instrument took the observations at a much lower altitude, the ambient temperature was higher and also the amount of moisture was significantly different. Furthermore the radiance observations were complemented with atmospheric state observations by instruments on the aircraft, while during the CAMEX case it was taken from rawindsondes. This has led to different results for the comparison of the simulations with the observations.

Because of the lower altitude, the calibration of the instrument in those regions where the absorption coefficient is very high is extremely difficult. This resulted in the spikes in the residual plots. At first sight, the performance of the models in the 9.6 μm region is much better than in the CAMEX case. Figure 7.56 indicates that in this region the NeΔT is smaller than 1K, whereas in the CAMEX case values up to 4K were found (Figure 7.17). However, when the radiance difference is normalised by the uncertainty in the observations, values in excess of 20 are found for the ASCENSION island simulations, unlike CAMEX (cf. Figure, 7.57 and 7.18). The overestimation of the radiance at 800 cm^{-1} is evident in all simulations. This is also different from the CAMEX simulations, where in general an underestimation was found. The performance in the window region (800 - 1000 cm^{-1}) appears to be a function of wavenumber in the ASCENSION-island simulations. This could be an artifact of the assumption that the surface emissivity is independent of wavenumber, whereas in reality it is [e.g, Watts et al., 1996, Masuda et al., 1988].

The detailed plots presented in Figures 7.58-7.59 illustrate the difference in the two experiments even better. For instance, results presented in Figure 7.59 indicate that the use of the CKD 2.2 as used for the KOPRA and LITMS simulations gives slightly better results in the spectral region between 1000 and 1070 cm^{-1} than the later versions of the CKD continuum (see also section 4.8). Although for the ECMWF, and METOF simulations the same model was used, their performance is not the same in some of the spectral regions, and the same is true for the simulations performed by EUMETSAT and SA. For the latter the increased performance of the SA submission, is most likely due to the Toth revision to the HITRAN 96 database adopted by SA (cf section 4.2.2).

4.7 ARIES Band2

The results for the second ARIES band are shown in Figures 7.60 - 7.70. It is unfortunate that up to 2000 cm^{-1} the residual plots have a noisy appearance, for the reason discussed in section 3.2. Because the observations took place under tropical conditions, i.e. warm and relatively high water vapour abundances, there is some interest in the performance of the line-by-line models in the water vapor absorption band. It apears that all models are capable to simulate the observations within approximately 10σ in the 1400 - 1800 cm^{-1} region. It is worth to notice that for this case the actual CO profile was observed, while for the CAMEX case this was not the case. Detailed plots of the region between 2100 - 2250 cm^{-1} indicates that the simulation by LITMS and LMD deviate from the simulation by the others (cf. Figures 7.67, 7.68). Experiments showed that the presented performance by LITMS and LMD is the result of the adopted CO profile. At the initial stages of the experiments, a climatological CO profile was distributed, which was later replaced by the observed one. Experiments showed further that once the modified profiles are adopted the performance of these models are comparable to the performance of the other models. The detailed plots for the region between 2100 - 2250 cm^{-1} are not updated with the new results, as they illustrate the impact on the simulated radiances from inaccuracies in the atmospheric state of trace gases.

As was true for the 800 - 1000 cm^{-1} region there is a slight tendency for the simulations to overestimate the radiance in the window region between 2400 - 2600 cm^{-1}. Additional work is needed to see if this overestimation is the result of incomplete specification of the lower boundary condition.

4.8 Model intercomparison

To complete the section on the comparison with ARIES observations, the relative difference between the models, for the ASCENSION case are presented. The results are presented as a series of figures. Like for the HIS case, two different sets of figures are presented, one where the residual between a particular model and the LBLRTM model as implemented at EUMETSAT are shown, and one set where the reference model is changed to GENLN2 as implemented at the Met Office. For each band and for each reference model, the differences are shown in radiance and in equivalent brightness temperature space.

4.8.1 Band1

Figures 7.71-7.74 show the intercomparison results for the ARIES band 1. The Figures show that the relative performance between the different models, depend strongly on wavenumber. Largest differences are found in the wing of the 15 μm CO_2 band and in the strong H_2O band. There are some local differences around 850, 925 and 1100 cm^{-1}. Again differences are found between results generated by the same model, but implemented at different institutes.

There appears to be a wavenumber dependent bias between the IMCOL and EUMETSAT submission in the window region between $800 - 1000$ cm^{-1}. Figure 7.72 indicates that near 800 cm^{-1} the difference between these two models is about 0.3 K, which reduces to 0 K around 1000 cm^{-1}. This bias is also observed in the METOF - EUMETSAT pair but not in the ECMWF - EUMETSAT pair. In the latter case there is a constant bias of approximately -0.1 K in this region. This wavenumber dependent bias is not visible in the comparison for the CAMEX case. Figure 7.42 indicates that for the CAMEX simulation, the differences between ECMWF - EUMETSAT, IMCOL - EUMETSAT and METOF - EUMETSAT are very similar and independent of wavenumber.

Towards the high wavenumber end of Figure 7.74 there is another interesting feature found in the ASCENSION island simulations and not so visible in the CAMEX simulations. That is in the $1400 - 1600$ cm^{-1} domain of ARIES band 1, the residual between the pairs EUMETSAT - METOF, LITMS - METOF and SA - METOF tends to be negative, while the residuals between the pair LARA - METOF and to a lesser degree KOPRA - METOF and LMD - METOF tends to be positive. A simple explanation for this cannot be given. Figure 7.79 shows the high resolution results of the METOF, EUMETSAT, LITMS and LARA submission for four different parts of the ARIES band 1 domain. For instance, in the 1425 – 1430 cm^{-1} domain the LITMS results underestimates the METOF results, in the line center the LARA results overestimates the METOF results, and the EUMETSAT results are very similar to the METOF results, except near 1430 cm^{-1} where it is closer to the LITMS results. But similar behaviour is found in the other three panels. All models are using the HITRAN 96 line database. Unlike the residuals in the short wave wing of the 6.2 μm H_2O absorption band around 2000 cm^{-1} (as discussed in the next section), a simple relation to the adopted water vapour continuum model is not obvious as the LARA and EUMETSAT submissions use the CKD 2.4 model, METOF uses CKD 2.1 and LITMS CKD 2.2.

4.8.2 Band2

Figures 7.75-7.78 show the intercomparison results for the ARIES band 2. The residual plots show significant differences in the short wave wing of the 6.2 μm H_2O absorption band around 2000 cm^{-1} and in the CO absorption band around 2100 cm^{-1}. This residual is (in part) the result of the different water vapour continuum models used. For instance, the LARA submission and the LBLRTM models (submitted by EUMETSAT and SA) employs the CKD 2.4 model for water vapour continuum, while the other models employ a previous version. The residual between the LARA and LBLRTM in the region between 1800 - 2100 cm^{-1} appears to be relatively small, except for some localised differences. The difference between the other submissions in this region and the LBLRTM is substantially larger. Unfortunately, this spectral domain was not included in the CAMEX simulations, so it is not possible to compare performance for this simulation with the performance for the CAMEX case. (Again, the differences between the SA and the EUMETSAT results are due to the inclusion of the Toth revisions to the H_2O spectroscopy by SA, when these revisions are excluded from the SA submission, the EUMETSAT and SA results do not deviate from each other.)

This Figure 7.80 the spectral region shows the high resolution variation of the unconvoluted radiance with wavenumber as calculated by the GENLN2 and LBLRTM model. This figure shows that the two models simulate the same value of the radiance in the centre of the water vapor line, but they diverge in the wings. Finally, Figure 7.81 shows the so-called foreign contribution to the water vapour continuum, and in the region of interest the CKD 2.1 and CKD 2.4 models diverge, the latter model generates smaller values than the former, in line with the results shown in Figure 7.80.

An intercomparison of a numerical implementation of a physical concept can only provide relative difference information. An absolute accuracy can only be inferred from a careful comparison between calculations and detailed observations. Such a comparison presented for two models in Figures 7.62, suggests that, for this particular situation, the GENLN2 simulations deviate less from the observations than the LBLRTM simulations. This does not imply that the CKD 2.1 model performs better than the CKD 2.4, because the uncertainties in the surface conditions and in the atmospheric state specifications are too large to make such a conclusion. Detailed investigations beyond the scope of the paper are required to analyse this further.

Chapter 5

Sensitivity Experiments

In this section the results of a few additional experiments, performed by different groups are presented. The following experiments were performed,

- Inclusion of more realistic sea surface emissivity
- Sensitivity of upwelling radiance to perturbation of humidity profile
- Other sensitivity studies

5.1 Sea Surface Emissivity

For both the CAMEX and the ASCENSION test cases, the surface emissivity was fixed to a specific static value. In reality the surface emissivity depends on wavenumber. An example is given in Figure 7.82.

In Figures 7.83 - 7.88 the results of simulations by UMBC and UW, where the fixed value of the sea surface emissivity is replaced by the values in Figures in 7.82 for nadir observations are presented. The Figures consists of four panels, two for each simulation, showing the difference ($\Delta\mathcal{R} = \mathcal{R}^s - \mathcal{R}^o$) between the simulations and the observations. Differences for the standard simulation (i.e. with the wavelength independent surface emissivity) with the 'STD' extension in the title are presented as a reference for the simulations with the more realistic sea surface emissivity with the 'SEA' extension. In the $800 - 1000$ cm^{-1} domain the inclusion of the more realistic surface emissivity model resulted in an offset of approximately -0.5 K in both simulations. The inclusion of the surface emissivity model resulted in a better agreement to the observations for the UMBC simulations, while for the UW these simulations underestimated the observations by about 0.5 K. The 0.5 K bias between the two models could be the result of a small difference in surface temperature in the two simulations. Secondly it is worth to notice that the introduction of spectral varying surface emissivity reduced the slowly varying slope in the residuals. This is also seen in the simulations by AER (cf. Figs 7.101 and 7.102). In HIS band 2 the effects of the sea surface emissivity inclusion is obviously less pronounced, because of the strong atmospheric absorption. In the wing of the IR window, there is an offset of approximately -0.5 K. Finally in HIS band 3, there is a very small reduction of the radiation at the observational level from the inclusion of the sea surface emissivity. This is not surprising given the small amount of radiative energy in this spectral domain.

5.2 Water vapour profile sensitivity

Figures 7.89 – 7.99 show the effect on the upwelling radiation for the CAMEX simulation due to a change in the humidity profile. These simulations were performed with the GENLN2 model by M. Matricardi. Two types of perturbations were performed. One where the original humidity profile was modified by subtracting the uncertainty in the humidity profile (Figures 7.90 - 7.94), while for the second simulation the original humidity profile was modified by adding this observed uncertainty (Figures 7.90 - 7.94). These Figures show that a negative perturbation of the humidity profile results in a increase in the upwelling radiance at the observational level, while a positive perturbation, reduces the upwelling radiation. The changes in the radiation field are larger the closer to the center of the H_2O rotation band.

5.3 Other Sensitivity Studies

In this section the current state of spectral modeling for IASI simulations is presented, especially with respect to the influence of the spectroscopic parameters. This is illustrated through the application of a particular line-by-line model, but as can be concluded from the previous sections, to a large extent all models have a similar behaviour. It is in the details that the models diverge. This input was provided by S. A. Clough and M. W. Shephard.

In regard to the IASI study, a number interesting spectral questions applicable to all line by line models participating in the intercomparison emerged, namely:

1. What is the effect of layering?
2. What is the effect of line rejection?
3. Why do some contributors have better results than others for ozone?
4. What is the effect of using spectral emissivity appropriate to seawater?
5. What is the effect of recent updates to the line parameters, e.g. water vapor?
6. What is the situation with respect to the CO2 Q-branch at 2077 cm-1?

To address these questions, calculations were performed using the LBLRTM code with the AER_JPL_hitran_96_v2.1 spectroscopical line file, generated mostly from HITRAN 96 and the inclusion of Toth revision of the water vapor spectroscopy. In addition, the spectral surface emissivity function adapted from Wu and Smith, 1997 was used [Wu and Smith, 1997, Masuda et al., 1988]

9.6 μm O_3 band

The reason for the overestimate of radiance in the 9.6 μm O_3band for most but not all of the models was investigated. As demonstrated by the case study below, the overestimate of radiance in the models is due to an insufficient amount of O_3 in the profile and not the number of layers or line rejection.

CO_2 Q-branch Line Coupling

Summary Table 2.1, shows that EUMETSAT, SA, and UW results included the CO_2 line coupling (mixing) for Q-branches smaller then 1932 cm^{-1} using the second order line coupling approach by Hoke et al. [1989] and not by Strow et al. [1994]. Recently we have implemented, as a first order solution, Strow et al. [1994] CO_2 line coupling into LBLRTM for CO region (1932, 2076, 2093,2193 cm^{-1}) Q-branches only. In Section 5.3.4 it is shown that the line coupling reduces the residuals from approximately 9 to 4 K.

5.3.1 Atmospheric State

CAMEX Reference Case

This initial reference case was computed, in order to start with the original inputs that were provided for the intercomparision, see Table 3.1. The results are shown in Figure 7.101.

AER Reference Case

For the AER reference the following setup was used

- to mimick the SA computation in using an input 97 level profile with a maximum altitude level of 19.97 km containing accumulated total column O_3 of 1.746×10^{18} ppmv
- calculations performed on 27 layers
- with small line rejection
- increasing the input surface temperature from 293 K to 293.3 K
- using spectral varying surface emissivity values
- using an improved line file (AER_JPL_hitran_96_v2.1)

Figure 7.102 demonstrates a number of improvements to the residual. The increase in the surface temperature brings the residual values, in spectral regions that reach the surface, closer to zero. Also, the spectral varying surface emissivity eliminates the slope in the residuals (often mistakenly attributed as errors in the continuum). The new line file that includes Toth's revision to water vapour spectroscopy greatly reduces the residuals in the water vapour lines. For the 9.6 μm band Figure 7.102 shows a result similar to SA result in Figure 7.17 of the intercomparison paper, where there are large residuals with the model is overestimating the radiance (brightness temperature)

5.3.2 No Line Rejection Case

To determine the impact of the small line rejection in the AER Reference case the LBLRTM calculation was computed the same way as in the AER Reference case except with no line rejections. The results are very similar to Figure 7.102 that had the line rejection. This demonstrates that the line rejection in the AER Reference case is not responsible for the over estimate of radiance computed by the model.

5.3.3 Finer Model Layering Case

The sensitivity on the radiance field at the observational level to the number of layers was analysed, by taking the Reference case and replacing the 27 layers with 97 layers representing all the levels in the input profile. Comparing Figure 7.104 with the Reference case in Figure 7.102 shows that the finer layering does not reduce the estimated radiance in the ozone band.

UW (Tobin) Case

For additional simulations, Dave Tobin at the Univ. of Wisconsin provided the input that was used to generate better radiance estimates for the 9.6 μm for the UW model. The main differences compared with the reference case was that the last altitude level in the profile was 20.691 km instead of 19.97 km and the calculations were performed on all 97 levels in the profile.

Figure 7.105 demonstrates an improved decrease in the residuals for the ozone band. Since the number of model layers does not produce an improvement in residuals for the ozone band, raising the altitude of the top level must be somehow responsible for the improved results. Further investigation demonstrates that by increasing the altitude of the top level, and keeping everything else the same, the total column ozone amounts increased from 1.746 $\times 10^{18}$ ppmv in the reference case to 1.934 $\times 10^{18}$ ppmv in UW case. This increase in ozone provided more absorption which and decrease the estimated radiance of the model calculation reducing the residuals in the 9.6 μm region. However, raising the altitude of this top level and keeping the temperature fixed increase the residuals in the 650 – 700 cm^{-1} region by about 0.5 K in comparison to the reference case in Figure 7.102. This suggests that it is not the altitude of the top level in the input profile that needs to be changed, but that there is insufficient ozone in the top levels of the profile.

AER Scaled O_3Case

The next step is to then take the AER Reference case and increase the ozone in the top few levels, as shown in Figure 7.106. This increase the total ozone column amount from 1.746 $\times 10^{18}$ to 1.958 $\times 10^{18}$ ppmv, which is close to the 1.934 $\times 10^{18}$ ppmv amount UW has with the 20.691 km top-level input profile. Increasing the ozone in the top of the profile increased the amount of absorption in the ozone band which decreased the estimated radiance and the residuals. Also note that keeping the top altitude level at 19.97 km produces better residuals in the 650 – 700 cm^{-1} region compared with moving it to 20.691 km as was done in UW model inputs. This suggusts that the temperature profile is correct at 19.97 km.

5.3.4 CO_2 Line Coupling for Q-branches 1932, 2080, 2093, 2193 cm^{-1} in CAMEX Data

To establish a baseline, a simulation was performed without line coupling for Q-branches at 1932, 2080, 2093, 2193 cm^{-1}. For comparison the results using the input atmospheric state as defined by the IASI reference case is shown in Figure 7.108. Next the results when the atmospheric state is changed to the AER reference case, are shown in Figure 7.109. Again, one can see the improvements of Figure 7.109 over 7.108 due to increasing the surface temperature, using spectral varying surface emissivity function, and improved water vapour lines in the line file.

As shown in Figures 7.108 and 7.109, there is a large residual of 9 K for the 2076 cm^{-1} Q-branch. This is attributed to not accounting for Q-branch line coupling. Results when the calculations include the line coupling for Q-branches 1932, 2080, 2093, 2193 cm^{-1}, are shown in Figure 7.110.

Including CO_2Q-branch line coupling in the COregion reduces the residuals from about 9 to 4 K. It is presently unclear if additional improvements to the line coupling is need in order to further improve on the 4 K under estimate of the 2076 cm^{-1} Q-branch radiance. For example, including second order line coupling coefficients.

GENLN2/LBLRTM CO_2 2076 cm^{-1} Q-branch Monochromatic Comparison

The GENLN2 monochromatic calculations, which has the Strow et al. [1994] Q-banch line coupling model for the CO_2 2076 cm^{-1} Q-branch, was compared to the LBLRTM monochromatic calculation with (Figure 7.112) and without (Figure 7.111) the recently implemented Strow Q-banch line coupling for the CO region.

The residuals in the monochromatic comparision in Figure 7.112 show that the LBLRTM and GENLN2 perform equally in the 2076 cm-1 Q-branch.

Chapter 6

Summary

To document the performance of current line by line radiative transfer models capable of simulating IASI radiances a study was performed to compare the model simulations with real observations and also intercompare the simulations themselves. Two observational datasets were analysed where high spectral resolution observations were made and at the same time the atmospheric state was carefully monitored. The first dataset consisted of radiance observations using the HIS interferometer during the CAMEX-1 campaign off the east coast of the USA. The second dataset consisted of observations from the ARIES interferometer collected during the ASCENSION island campaign over the tropical Atlantic. These two cases are very different with the Ascension island case being much warmer and humid than the CAMEX case. It is also important to note the flight level in the former was much lower than in the latter case.

It is well known that the comparison of model simulations with observations critically depends on the accuracy of the specified atmospheric state. For the two cases presented it is believed the specification of the temperature, water vapour, ozone and the methane profiles were accurate enough to minimise any radiance differences due to errors in assumed atmospheric state. Some of the difference found were very subtle, and to discriminate between these the specification of the atmospheric state was not accurate enough. For some models the specification of the ozone profile for the CAMEX case was inadequate, as the high level ozone had to be enhanced to get good agreement between models and observations. For another model good agreement in the 9.6 μm Ozone band for the CAMEX similation was obtained by significantly increasing the number of levels of the original profile (from approximately 30 to more than 100). A possible other source of uncertainty may be due to uncertainties in the instrument spectral response function. And finally radiometric calibration of especially the airborne observations in those spectral regions regions where strong absorption by atmospheric constituents exists is extremely difficult. This is especially true for the observations taken at low altitudes by the ARIES instrument. Such that a detailed interpretation of the results in these spectral region is not ambigious.

In total 13 different groups participated with 7 different line-by-line models. These models used three different spectroscopic databases, namely HITRAN 96, HITRAN 96 revised with the Toth revision of the H_2O spectroscopical parameters in the 10 micron region, and GEISA 97. The large number of submissions resulted in a unique dataset to assess the uncertainties of current line-by-line models. In many regions of the spectrum it is demonstrated that all the models are capable of reproducing the observations well to within the noise. However in some regions differences from the observations are found for some or all models which require further investigations. In some cases the explanation for the observed discrepancies have been found but others require further investigations.

An additional benefit of this study was that during the process of comparing the model simulations various bugs were discovered either in the models themselves or in their implementation by the particular group. In contrast groups with models which have compared well with others and the observations have gained more confidence that their model is running correctly.

The key conclusions from the results presented in the report are:

- Current line by line models agree in large parts of the spectral interval between 800 – 2600 cm^{-1} region, provided that they use the same atmospheric and spectroscopic input.

- Residuals in the 700 - 780 cm^{-1} region between the simulations and the observations especially for the CAMEX case exists, which requires additional research. The different performance in the 2080 cm^{-1} region is attributed to the omission of the line coupling in the Q-branches of CO_2 in some model simulations. In addition to this differences in the description of the line-coupling of the P/R branch resulted in different behaviour of the radiation models in the 15 and 4.3 μm bands of CO_2.

- The inclusion of a realistic sea surface emissivity model is important for a realistic simulation of the upwelling radiation in the 800 – 1000 cm^{-1} region.

- The revision of the H_2O spectroscopical parameters by Toth removed some fine scale biases between the observations and the model simulations, in the 800 – 1000 cm^{-1} region.

- For some model can the large differences in the 9.6 μm O_3 band for the CAMEX case largely be explained by an incorrect specification of the ozone amount near the observational level, while for an other model, agreement between model simulations and observations in this spectral region was obtained after subdivision of the original atmospheric state in a large number of thin layers.

- There was a disparity between models around 2400 cm^{-1} due to their respective implementations of the nitrogen continuum absorption.

- Differences due to the water vapour continuum parametrisation employed (i.e. CKD2.1 or CKD2.4) only show up below 700 cm^{-1} and in the 1950 – 2000 cm^{-1} range and unfortunately the measurements are not able to verify which model is best in this region.

- Some residuals between the observations and simulations may be due to uncertainties in the instrument spectral response function.

An original objective of this study was to identify those models which are adequate for IASI simulations. In practice all the models submitted were found to be adequate, at least for the profiles specified, although in some parts of the spectrum some models did better and in other parts others did better and so there was no clear 'winner'. However it should be noted the initial submission of results from some models did cause concern but in the process of the comparison these models were improved to become acceptable.

There are many unresolved issues which remain. For instance the different performance in the 1400 – 1600 cm^{-1} region for the Ascension island case (cf. Figure 7.74), and in the 680 - 750 cm^{-1} region for the CAMEX case (e.g Figure 7.44) where the different models not only performed differently in the centre of the spectral lines but also in between. From this it can be seen that more work is needed especially in the formulation for the line mixing models and validation of the water vapour continuum parametrisation.

The CKD water vapour continuum model is defined as: "absorption, of slow spectral variation (compared with that for lines) which, when added to the local line contribution, provides agreement with observations". This indicates that the line absorption and the continuum are inseparable. Thus a particular version of the CKD water vapour continuum is ultimately linked to a particular version of the spectroscopical data base. The results documented in this report indicate that the best agreement between the observations and simulations is obtained with the Hitran 96 database with the Toth revision of the water vapour spectroscopy. It should be noted that the latest HITRAN (v11.0)[1] spectroscopical database, which includes the line file modifications essentially identical to the ones utilized for the sensitivity calculations performed by AER (cf. section 5.3. The changes in the strongest water vapor lines have been insignificant in for the longwave sounding region so that the effects of line parameter changes is insignificant for the continuum. So at the moment, CKD_2.4 is the most appropriate for use with this line parameter set.

As a result of this study the forward model errors for the IASI radiances can now be estimated. This should now be done, using the analysis presented here, possibly for several line by line models. Some IASI channels will have low forward model errors whereas others will have much larger errors due to uncertainties in the spectroscopy. As the NWP assimilation is unlikely to be able to make use of all of the IASI channels a channel selection will have to be made based on information content. Those channels which have high forward model errors are likely to be rejected at the first stage of channel selection.

The current study was only able to make comparisons for tropical and mid-latitude atmospheres and it is evident both sets provided different insights into the reasons for the model differences. A future comparison should include an arctic profile as it is likely further differences between models and observations will be seen for these cold dry atmospheres.

This study is an important step to quantify the errors in line by line models and hence the fast models used for assimilation and retrievals. The regions of the spectra shown to be well modelled by this study can be used with confidence for IASI radiance assimilation in NWP models and for atmospheric state retrievals. As the models and databases improve, as a result of studies such as this, the radiative transfer model errors should reduce allowing greater weight to be given to the IASI observations.

[1] presently available from http://www.hitran.com

6.1 acknowledgement

The authors would like to acknowledge the valuable input and discussion with the ISSWG co-chair drs. R. Saunders and C. Camy-Peyret during the compilation of the report.

Bibliography

F. Cayla. IASI infrared interferometer for operations and research. In M. Chahine A. Chédin and N. Scott, editors, *High Spectral Resolution Infrared Remote Sensing for Earths Weather and Climate Studies*, NATO ASI Series 1, pages 9–19, 1993.

A. Chédin, H. Fisher, K. Kunzi, D. Spankuch, and N. Scott. Report on the ITRA/IRC campaign and workshop. In Chédin et al., editor, *TBC*. University of Maryland, 1988.

S.A. Clough, M. J. Iacono, and J.-L. Moncet. Line-by-line calculation of atmospheric fluxes and cooling rates, 1, Application to water vapor. *J. Geophys. Res.*, 97: 15,761–15,78, 1992.

S.A. Clough and M.J. Iacono. Line-by-line calculation of atmospheric fluxes and cooling rates, 2, Application to carbon dioxide, ozone, methane, nitrous oxide, and the halocarbons. *J. Geophys. Res.*, 100(D8):16,519–16,535, 1995.

S.A Clough, F.X. Kneizys, R. Davies, R. Gamache, and R. Tipping. Theoretical line shape for h2o vapour; application to the continuum," in atmospheric water vapour. In A. Deepak, T.D. Wilkerson, and L.H. Ruhnke, editors, *Atmospheric water vapour*, pages 25–46. Academic, New York, 1980.

S.A. Clough, F.X. Kneizys, and R.W. Davis. Line shape and the water vapour continuum. *Atmospheric research*, 23:229–241, 1989.

S.A. Clough, C.P. Rinsland, and P. D. Brown. Retrieval of tropospheric ozone from simulations of nadir spectral radiances as observed from space. *J. Geophys. Res.*, 100:16,579–16,593, 1995.

D.P. Edwards. Genln2. a general line-by-line atmospheric transmittance and radiance model. Ncar tech. note ncar/tn-367+str, National Center for Atmospheric Research, Boulder, CO., 1992.

R.G. Ellingson and Y. Fouquart. The intercomparison of radiation codes in climate models: An overview. *J. Geophys. Res.*, 96:8925 – 8927, 1991.

B Funke, G.P. Stiller, T.v. Clarmann, G. Echle, and H. Fischer. Co_2 q-branch line mixing in MIPAS/ENVISAT limb emission spectra and its influence on retrieval of atmospheric state parameters. *J. Quant. Spetrosc. Radiat. Transfer*, 59:215–230, 1998.

R.R. Gamache, S. Kennedy, R Hawkins, and L. S. Rothman. Total internal partition sums for molecules in the terrestrial atmosphere. *J. Mol.Struct.*, 517-518:413–431, 2000.

L. Garand, D.S. Turner, M. Larocque, J. Bates, S. Boukabara, P. Brunel, F. Chevallier, G. Deblonde, R. Engelen, M. Hollingshead, D. Jackson, G. Jedlovec, J. Joiner, T. Kleespies, D.S. McKague, L.M. McMillen, J.-L. Moncet, J.R. Pardo, P.J. Rayer, E. Salathé, R. Saunders, N.A. Scott, P. Van Delst, and H. Woolf. Radiance and jacobian intercomparison of radiative transfer models applied to HIRS and AMSU channels. *J. Geophys. Res.*, In Press, 2001.

S. Hannon, L. Strow, and L.M. McMillan. Atmospheric infrared fast transmittance models: A comparison of two approaches. In *Proceedings of SPIE conference on Optical spectroscopic techniques and instrumentation for atmospheric and space research*, volume 2, 1996.

M.L. Hoke, S.A. Clough, W.J. Lafferty, and B.W. Olson. Line coupling in oxygen and carbon dioxide. In J. Lenoble and J.F. Geleyn, editors, *IRS 88: Current Problems in Atmospheric Radiation*, pages 368–371. A. Deepak Hampton, VA., 1989.

M Höpfner, G.P. Stiller, M. Kuntz, T. von Clarmann, G. Echle, H. Fischer, B. Funke, N. Glatthor, F Hase, H. Kemnitzer, and S. Zorn. The Karlsruhe Optimized and Precise Radiative transfer Algorithm. part ii: Interface to retrieval applications. In Jinxue Wang, Beiying Wu, Toshihiro Ogawa, and Zheng hua Guan, editors, *Optical Remote Sensing of the Atmosphere and Clouds*, volume 3501 of *Proceedings of SPIE*, pages 186–195, 1998.

N. Jacquinet-Husson, E. Arié, J. Ballard, A. Barbe, G. Bjoraker, B. Bonnet, L.R. Brown, C. Camy-Peyret, J.P. Champion, A. Chédin, A. Chursin, C. Clerbaux, G. Duxbury, J.M. Flaud, N. Fourrié, A. Fayt, G. Graner, R. Gamache, A. Goldman, V.L. Golovko, G. Guelachvilli, J.M. Hartmann, J.C. Hilico, J. Hillman, G. Lefèvre, E. Lellouch, S.N. Mikhaïlenko, O.V. Naumenko, V. Nemtchinov, D.A. Newnham, A. Nikitin, J. Orphal, A. Perrin, D.C. Reuter, C.P. Rinsland, L. Rosenmann, L.S. Rothman, N.A. Scott, J. Selby, L.N. Sinitsa, J.M. Sirota, A.M. Smith, K.M. Smith, Vl.G. Tyuterev, R.H. Tipping, S. Urban, P. Varanasi, and M. Weber. The 1997 spectroscopic GEISA databank. *J. Quant. Spectros. Radiat. Transfer*, 62:205–254, 1999.

J.-M. Kochel, J.-M. Hartmann, C. Camy-peyret, R. Rodrigues, and S. Payan. Influence of line-mixing on absorption by CO_2 Q-branches in atmospheric balloon-borne spectra near 13 μm. *J. Geophys. Res.*, 102:12891 − 12899, 1997.

M. Kuntz, M Höpfner, G.P. Stiller, T. von Clarmann, G. Echle, H. Fischer, B. Funke, N. Glatthor, F Hase, H. Kemnitzer, and S. Zorn. The Karlsruhe Optimized and Precise Radiative transfer Algorithm. Part iii: ADDLIN and TRANSF algorithms for modeling spectral transmittance and radiance. In Jinxue Wang, Beiying Wu, Toshihiro Ogawa, and Zheng hua Guan, editors, *Optical Remote Sensing of the Atmosphere and Clouds*, volume 3501 of *Proceedings of SPIE*, pages 247–256, 1998.

K. Masuda, T. Takashima, and Y. Takayama. Emissivity of pure and sea waters for the model sea surface in the infrared window regions. *Remote. Sens. Environ.*, 24:313–329, 1988.

M. Matricardi and R.W. Saunders. A fast radiative transfer model for simulation of IASI radiances. *Appl. Optics.*, 38:5679 − 5691, 1999.

M.Y. Perrin and J.M. Hartman. Temperature-dependent measurements and modeling of absorption by co2-n2 mixtures in the far line wings of the 4.3 microns co2 band. *J. Quant. Spec. Radiat. Trans.*, 42(4), 311-317 1989.

R. Rizzi, M. Matricardi, and F. Miskolczi. On the simulation of up-looking and down-looking high-resolution radiance spectra using two different radiative transfer models. *accepted by Applied Optics*, 2001.

R. Rodrigues, K.W. Jukus, N. Lacome, G. Blanquest, J. Valrand, W.A. Traub, B. Khalil, R. leDoucen, A. Valentin, C. Camy-Peyret, L. Bonamy, and J.M. Hartmann. Model, software and database for computation of line mixing effects in infrared Q-branches of atmospheric CO_2.I: symmetric isotopomers. *J. Quant. Spectrosc. Radiat. Transfer*, 61:153 – 184, 1999.

L.S. Rothman, C.P. Rinsland, A. Goldman, S.T. Massie, D.P. Edwards, J.-M. Flaud, A Perrin, C. Camy-Peyret, V. Dana, J.Y. Mandin, J. Schroeder, A. McCann, R.R. Gamache, R.B. Wattson, K. Yoshino, K.V. Change, K.W. Jucks, L.R. Brown, V. Nemtchinov, and P. Varanasi. The HITRAN molecular spectroscopic database and HAWKS (HITRAN Atmospheric Workstation): 1996 edition. *J. Quant. Spectros. Radiat. Transfer*, 60:665–710, 1998.

N.A. Scott and A. Chédin. A fast line-by-line method for atmospheric absorption computations. the Automized Atmospheric Absorption Atlas. *J. Appl. Meteor.*, 20:801–812, 1981.

V. Sherlock. Impact of RTIASI fast radiative transfer model error on IASI retrieval accuracy. Technical report, The Met. Office Forecasting research Technical Report 319, 2000. Available from Met. Office Library.

G.P Stiller, M. Höpfner, M. Kuntz, T. von Clarmann, G. Echle, H. Fischer, B. Funke, N. Glatthor, F Hase, H. Kemnitzer, and S. Zorn. The Karlsruhe Optimized and Precise Radiative transfer Algorithm. Part I: requirements, justification, and model error estimation. In Jinxue Wang, Beiying Wu, Toshihiro Ogawa, and Zheng hua Guan, editors, *Optical Remote Sensing of the Atmosphere and Clouds*, volume 3501 of *Proceedings of SPIE*, pages 257–268, 1998.

L.L. Strow, D.C. Tobin, and S.E. Hannon. A compilation of first-order line mixing coefficients for CO_2 Q-branches. *J.Quant. Spectrosc. Radiat. Transfer*, 52:281 – 294, 1994.

F. Thibault, V. Menoux, R Le Doucen, L. Rosenmann, J.M. Hartman, and C. Boulet. Infrared collision induced absorption by o2 near 6.4 microns for atmospheric applications : Measurements and empirical modeling. *Applied Optics*, 36:563–567, 1997.

A.N. Trotsenko and B.A. Fomin. Calculation of atmospheric radiation transfer parameters using a direct integration method. *Phys.Atmos.Ocean,*, 24(1):106–109, 1989.

A.N. Trotsenko, S.V. Romanov, and B.A. Fomin. Procedures to compute atmospheric ir radiative transfer parameters with application to remote sensing processing systems: I. line-by-line model. Technical Report Preprint, IAE-5633/1, Kurchatov Institute, 1993.

A.N. Trotsenko, A.N. Rublev, and S.V. Romanov. Line-by-line radiative parameters databases in atmospheric sensing and modelling applications. In Richard P. Santer, editor, *Atmospheric Sensing and Modeling II*, number 2582 in Proc. SPIE, pages 221–232, 1995.

T. von Clarmann, A. Dudhia, G. Echle, B. Funke, N. Glatthor, F. Hase, M. Höpfner, S. Kellmann, H. Kemnitzer, M. Kuntz, A. Linden, M. Linder, G.P. Stiller, and S. Zorn. The Karlsruhe Optimized and Precise Radiative transfer Algorithm (KOPRA). Technical Report Wissenschaftliche Berichte, Bericht Nr. 6487, Forschungszentrum Karlsruhe, 2000.

P. Watts, M. Allen, and T. Nightningale. Wind speed effects on sea surface emission and reflection for the along track scanning radiometer. *J. Atmos. and Oceanic Tech.*, 13(1):126–141, 1996.

Lafferty W.J., A.M. Solodov, A. Weber, W.B. Olson, and J.M. Hartman. Infrared collision induced absorption by n2 near 4.3 microns for applications in the atmosphere. measurements and empirical modeling. *Applied Optics*, 35:5911–5917, 1996.

X. Wu and L. Smith. Emissivity of rough sea surface for 8 – 13 μm: modeling and verification. *Appl. Opt.*, 36:2609 – 2619, 1997.

Chapter 7

Figures

7.1 List of figures

List of Figures

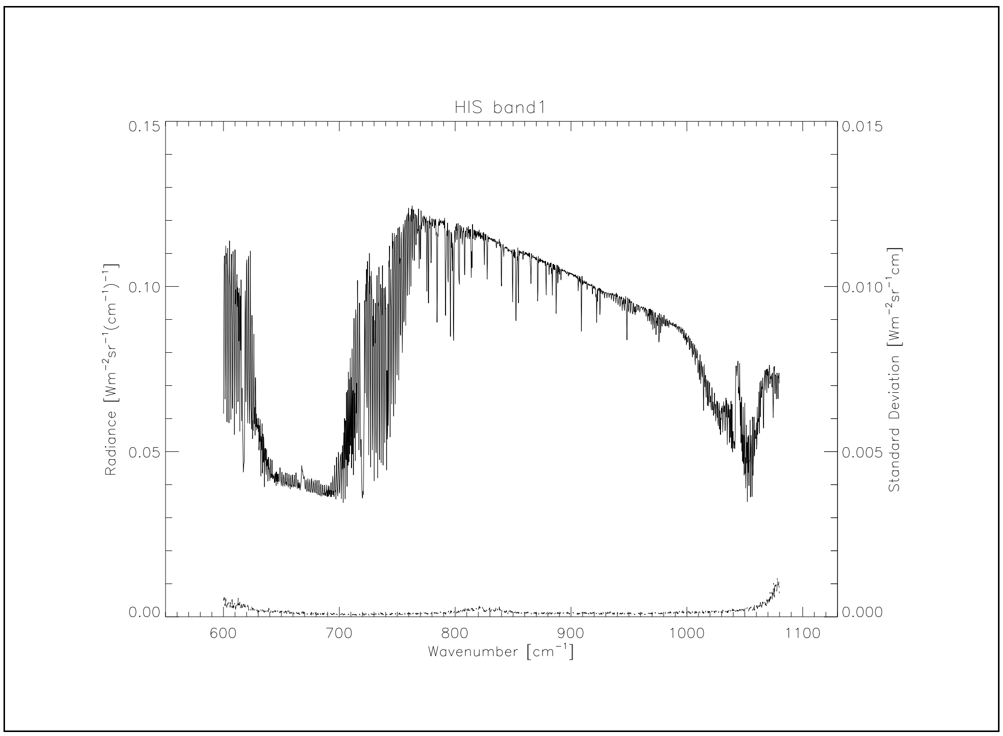

Figure 7.1: The Observed mean up-welling spectral radiance in HIS Band 1 during CAMEX-I. Solid line: mean observation, with its associated scale on the left y-axis, dashed line: the uncertainty in the mean observations, with its associated scale on the right y-axis.

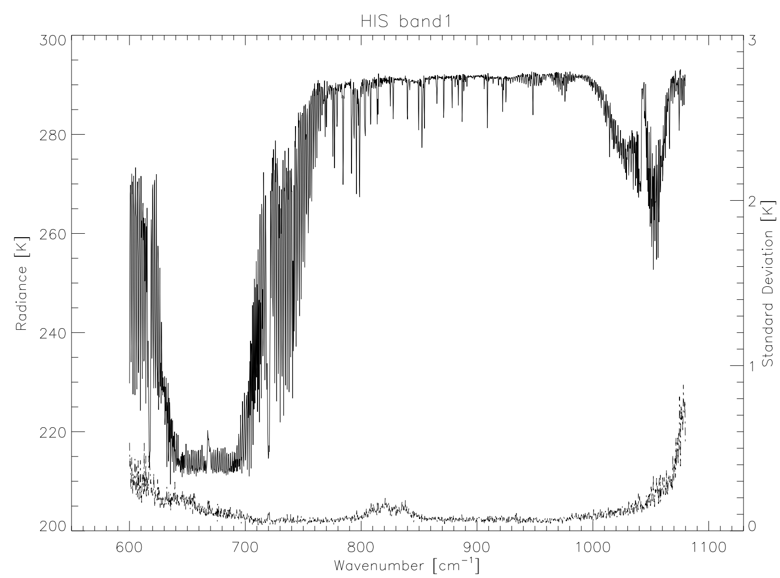

Figure 7.2: The observed mean up-welling spectral radiance converted into brightness temperature in HIS Band 1 during CAMEX-I. Solid line: mean observation, with its associated scale on the left y-axis, dashed line: the uncertainty in the mean observations, with its associated scale on the right y-axis.

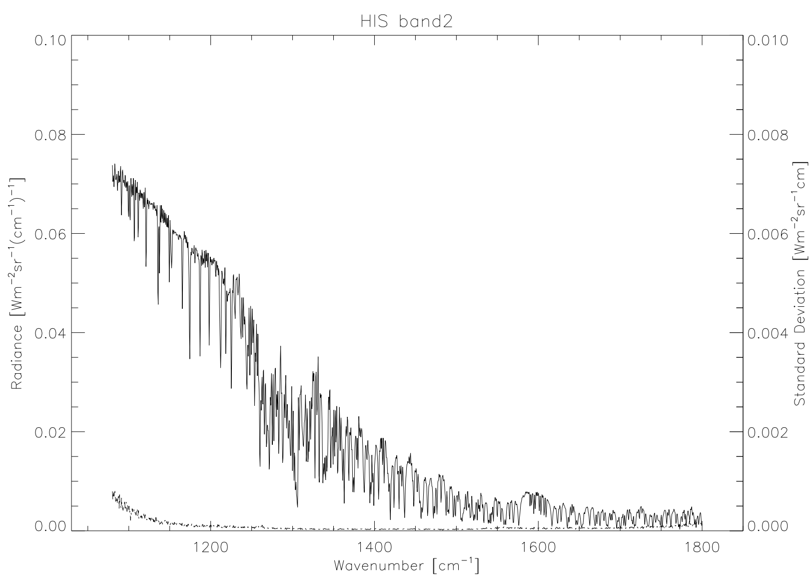

Figure 7.3: The observed mean up-welling spectral radiance in HIS Band 2 during CAMEX-I. Solid line: mean observation, with its associated scale on the left y-axis, dashed line: the uncertainty in the mean observations, with its associated scale on the right y-axis.

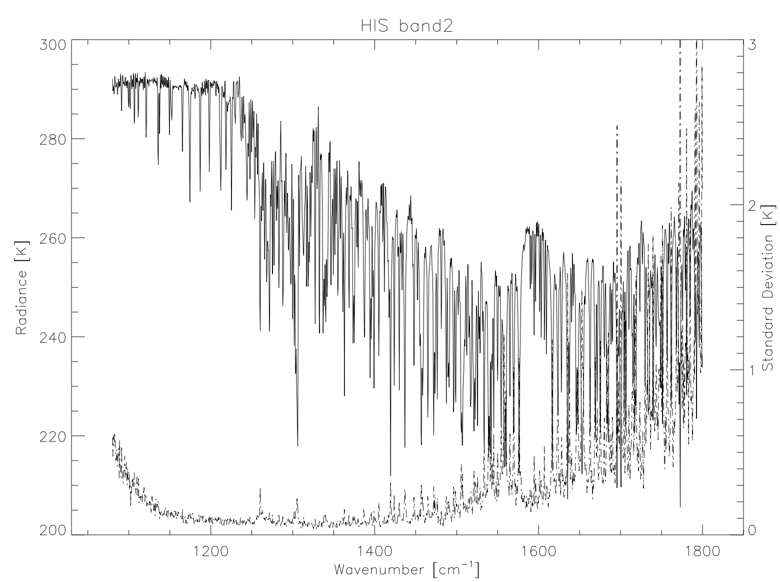

Figure 7.4: The observed mean up-welling spectral radiance converted into brightness temperature in HIS Band 2 during CAMEX-I. Solid line: mean observation, with its associated scale on the left y-axis, dashed line: the uncertainty in the mean observations, with its associated scale on the right y-axis.

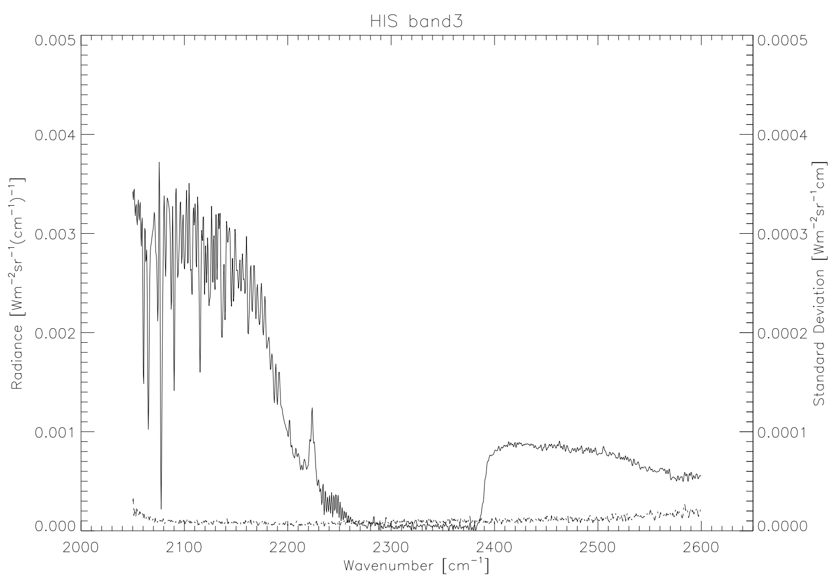

Figure 7.5: The observed mean up-welling spectral radiance in HIS Band 3 during CAMEX-I. Solid line: mean observation, with its associated scale on the left y-axis, dashed line: the uncertainty in the mean observations, with its associated scale on the right y-axis.

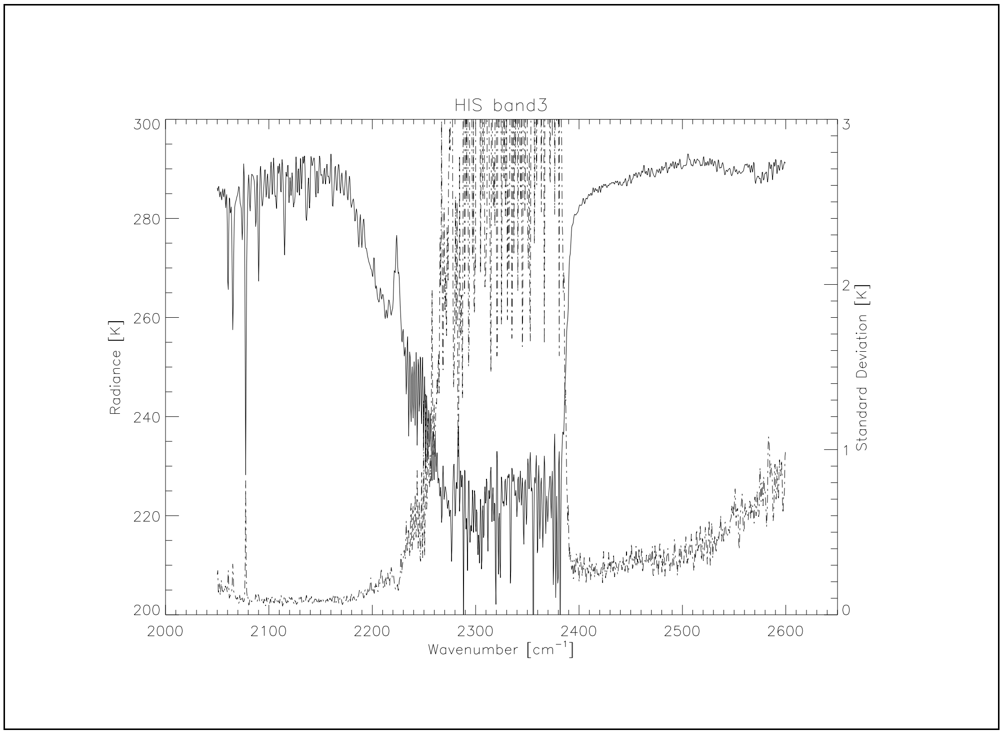

Figure 7.6: The observed mean up-welling spectral radiance converted into brightness temperature in HIS Band 3 during CAMEX-I. Solid line: mean observation, with its associated scale on the left y-axis, dashed line: the uncertainty in the mean observations, with its associated scale on the right y-axis.

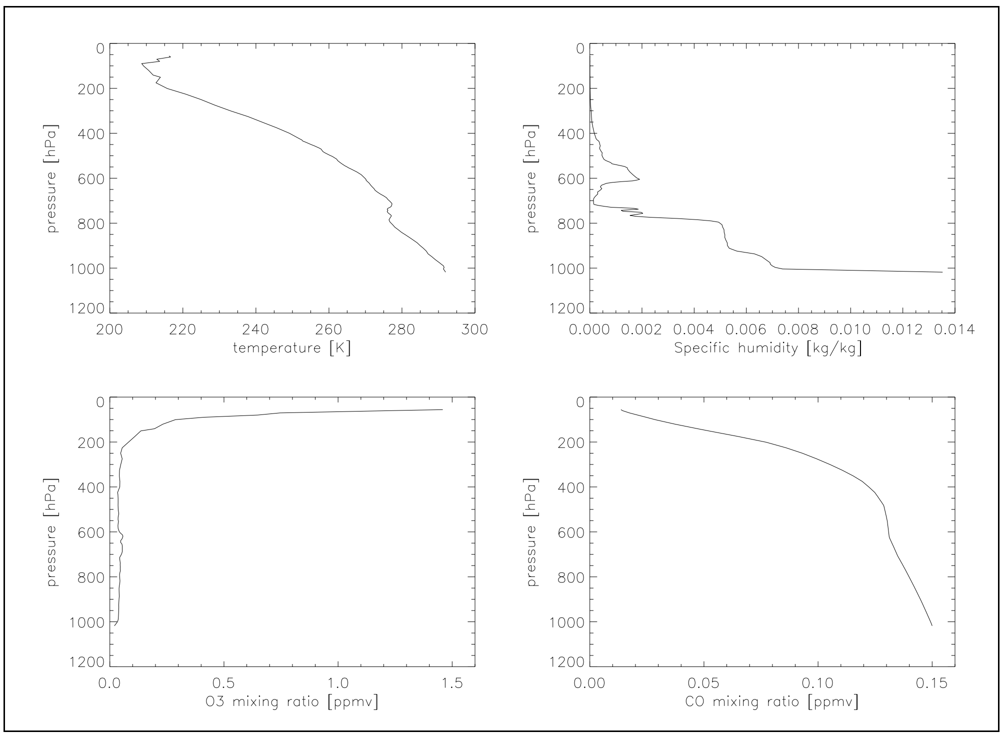

Figure 7.7: Profiles of selected atmospheric state variables for the CAMEX case, namely temperature (top left panel), specific humidity (top right panel), ozone volume mixing ratio (bottom left panel) and carbon monoxide volume mixing ratio (bottom right panel).

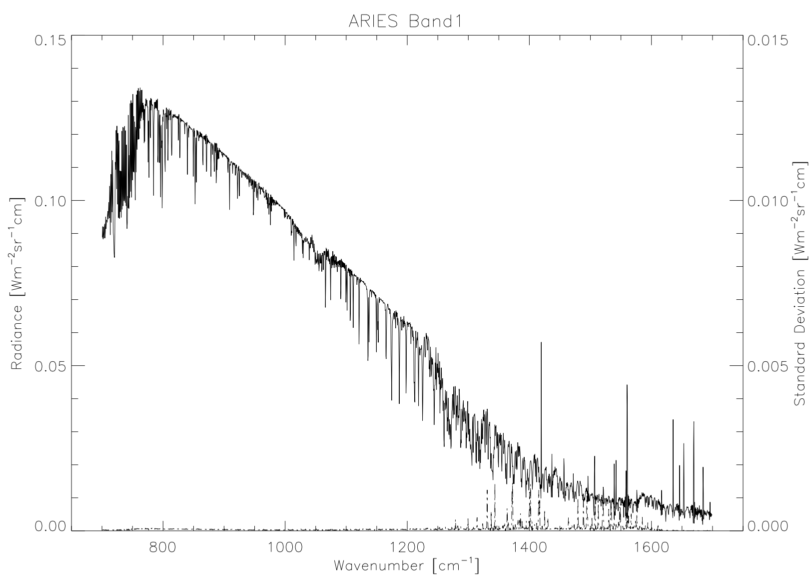

Figure 7.8: The observed mean up-welling spectral radiance in ARIES Band 1 during ASCENSION Island campaign. Solid line: mean observation, with its associated scale on the left y-axis, dashed line: the uncertainty in the mean observations, with its associated scale on the right y-axis.

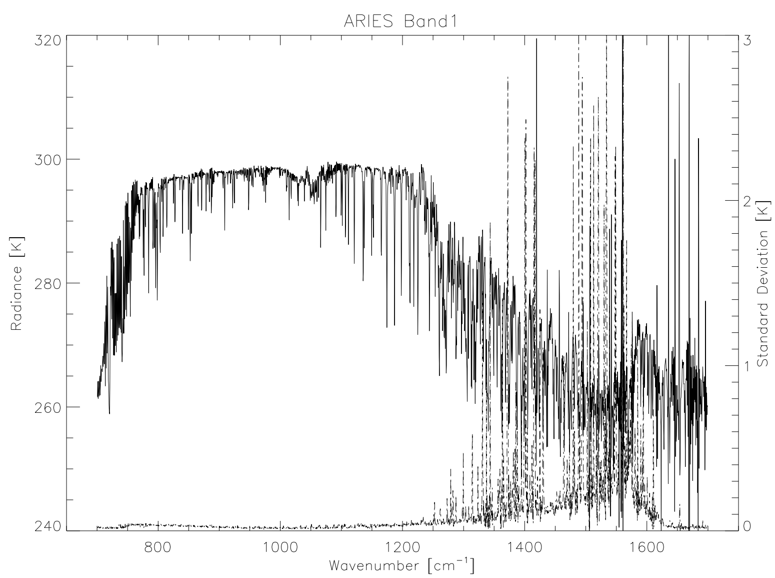

Figure 7.9: The observed mean up-welling spectral radiance converted into brightness temperature in ARIES Band 1 during ASCENSION Island campaign. Solid line: mean observation, with its associated scale on the left y-axis, dashed line: the uncertainty in the mean observations, with its associated scale on the right y-axis.

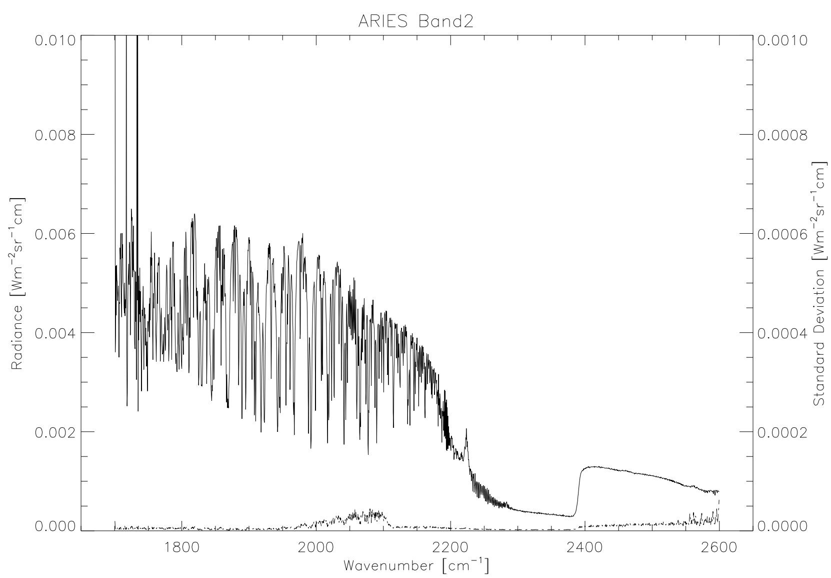

Figure 7.10: The observed mean up-welling spectral radiance in ARIES Band 2 during ASCENSION Island campaign. Solid line: mean observation, with its associated scale on the left y-axis, dashed line: the uncertainty in the mean observations, with its associated scale on the right y-axis.

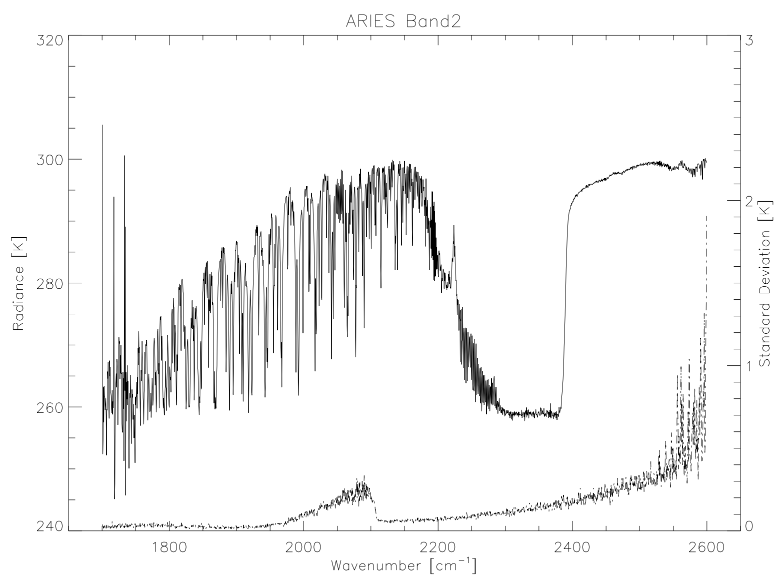

Figure 7.11: The observed mean up-welling spectral radiance converted into brightness temperature in ARIES Band 1 during ASCENSION Island campaign. Solid line: mean observation, with its associated scale on the left y-axis, dashed line: the uncertainty in the mean observations, with its associated scale on the right y-axis.

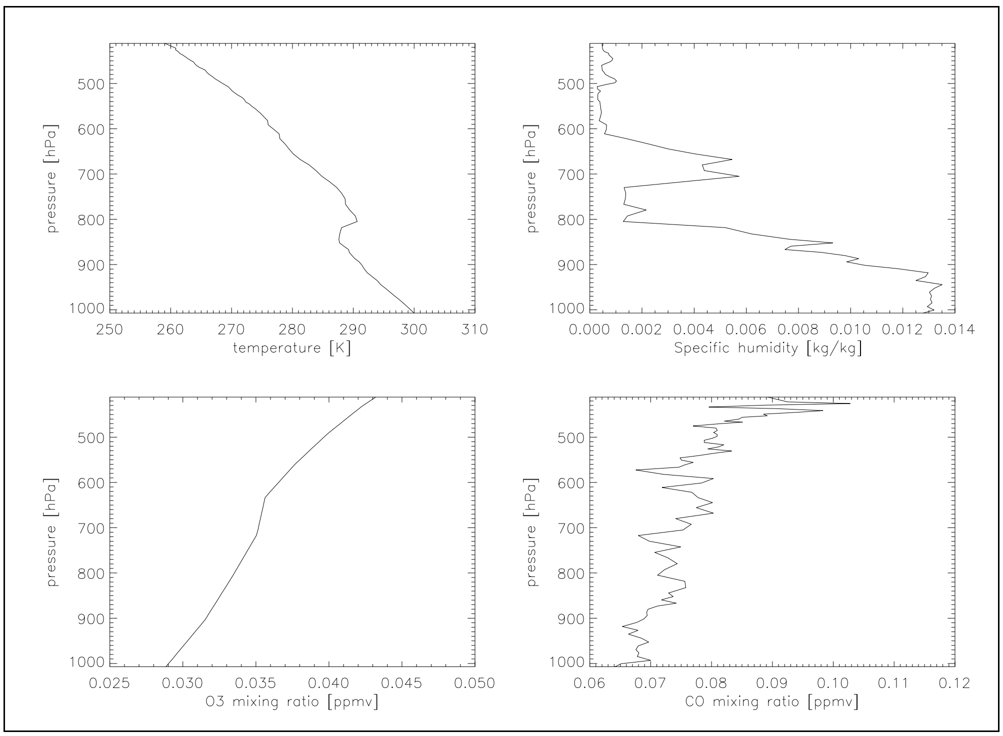

Figure 7.12: Profiles of selected atmospheric state variables for the ASCENSION Island case, namely temperature (top left panel), water vapor specific humidity (top right panel), ozone volume mixing ratio (bottom left panel) and carbon monoxide volume mixing ratio (bottom right panel).

Figure 7.13: Up-welling radiance in the HIS band 1 calculated by LBLRTM for the single gas experiments. The particular atmospheric constituent adopted for each of the runs is indicated as the title above each panel

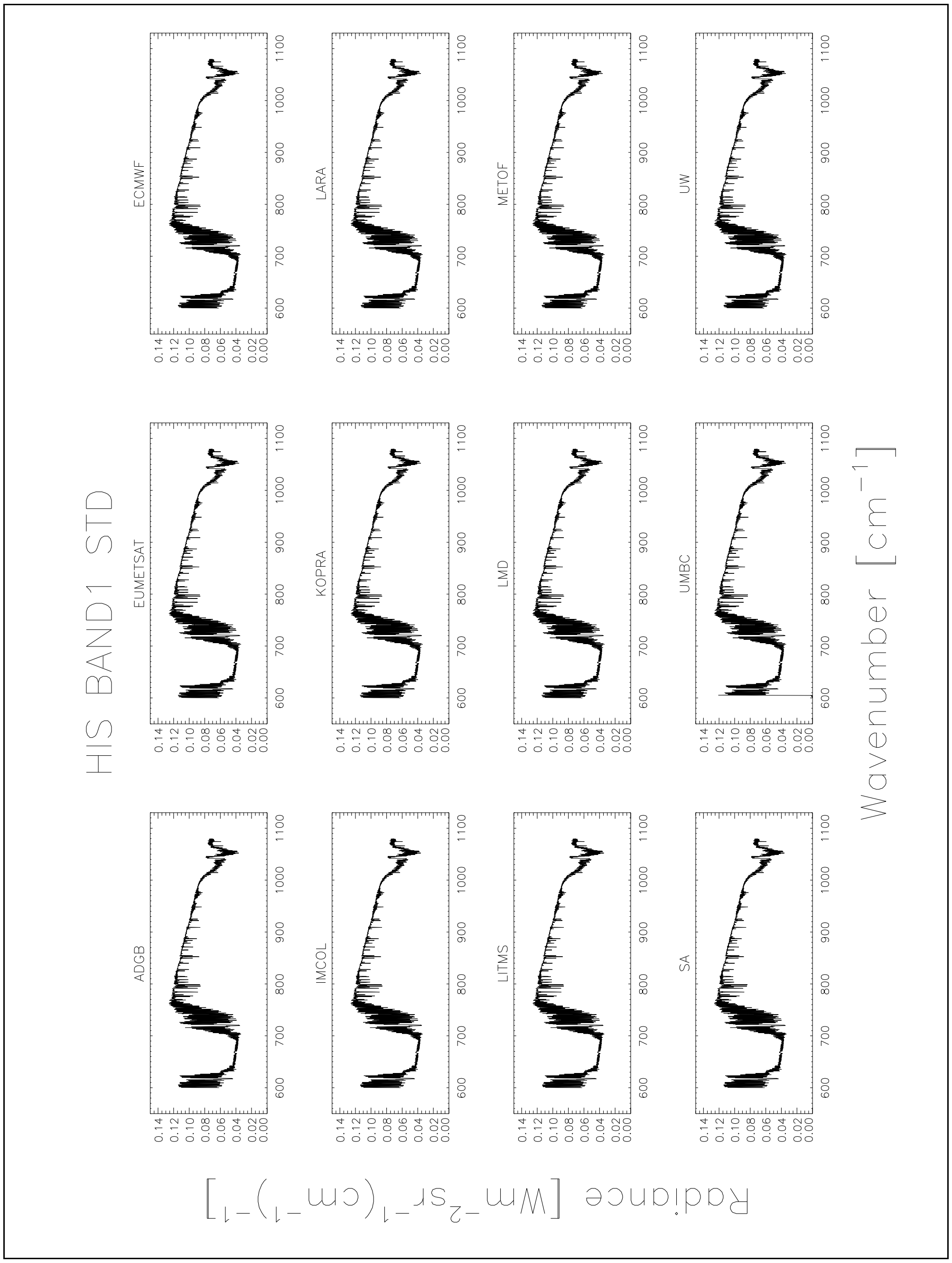

Figure 7.14: Radiance in HIS band 1 for the particular submission indicated by the title above each panel. Only the results in the optical filter range of HIS band 1 between 600 - 1080 cm^{-1} are shown.

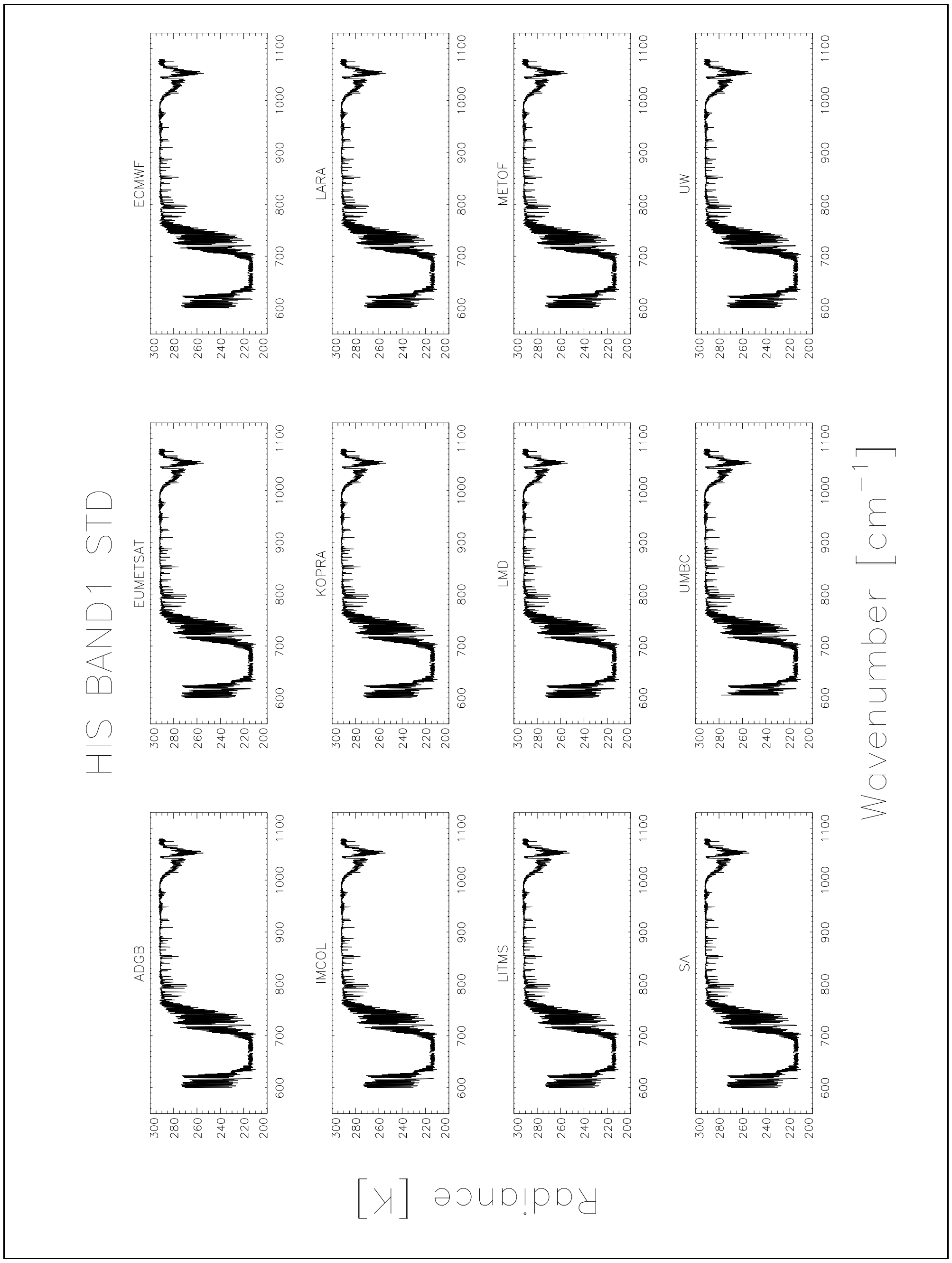

Figure 7.15: Radiance in HIS band 1 for the particular submission indicated by the title above each panel. Note that the radiances are converted into equivalent brightness temperatures using the inverse of the Planck-function. Only the results in the optical filter range of HIS band 1 between 600 - 1080 cm^{-1} are shown.

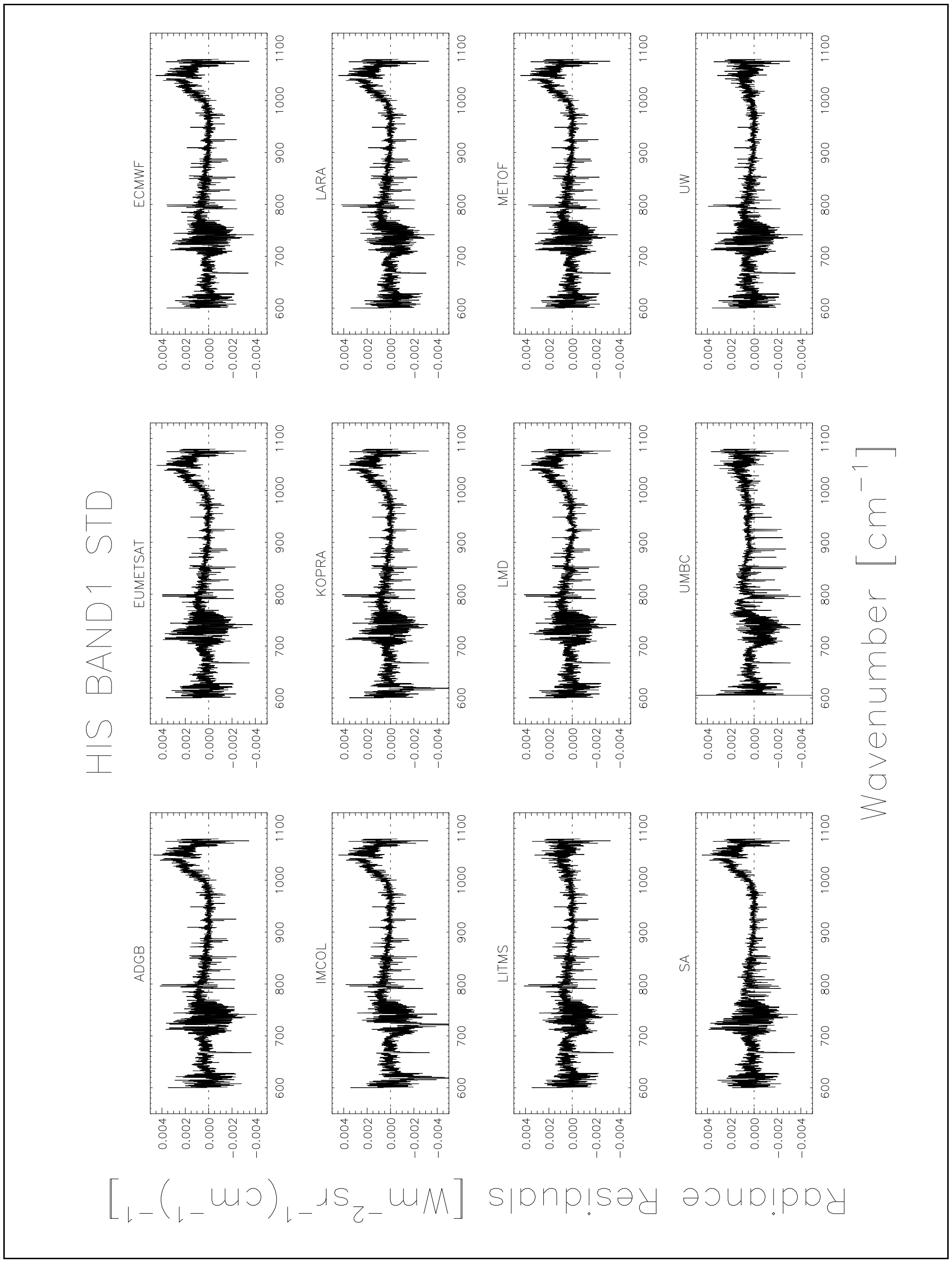

Figure 7.16: Radiance residuals between calculated and observed radiance in HIS band 1 for the particular submission indicated by the title above each panel. Only the results in the optical filter range of HIS band 1 between 600 - 1080 cm^{-1} are shown.

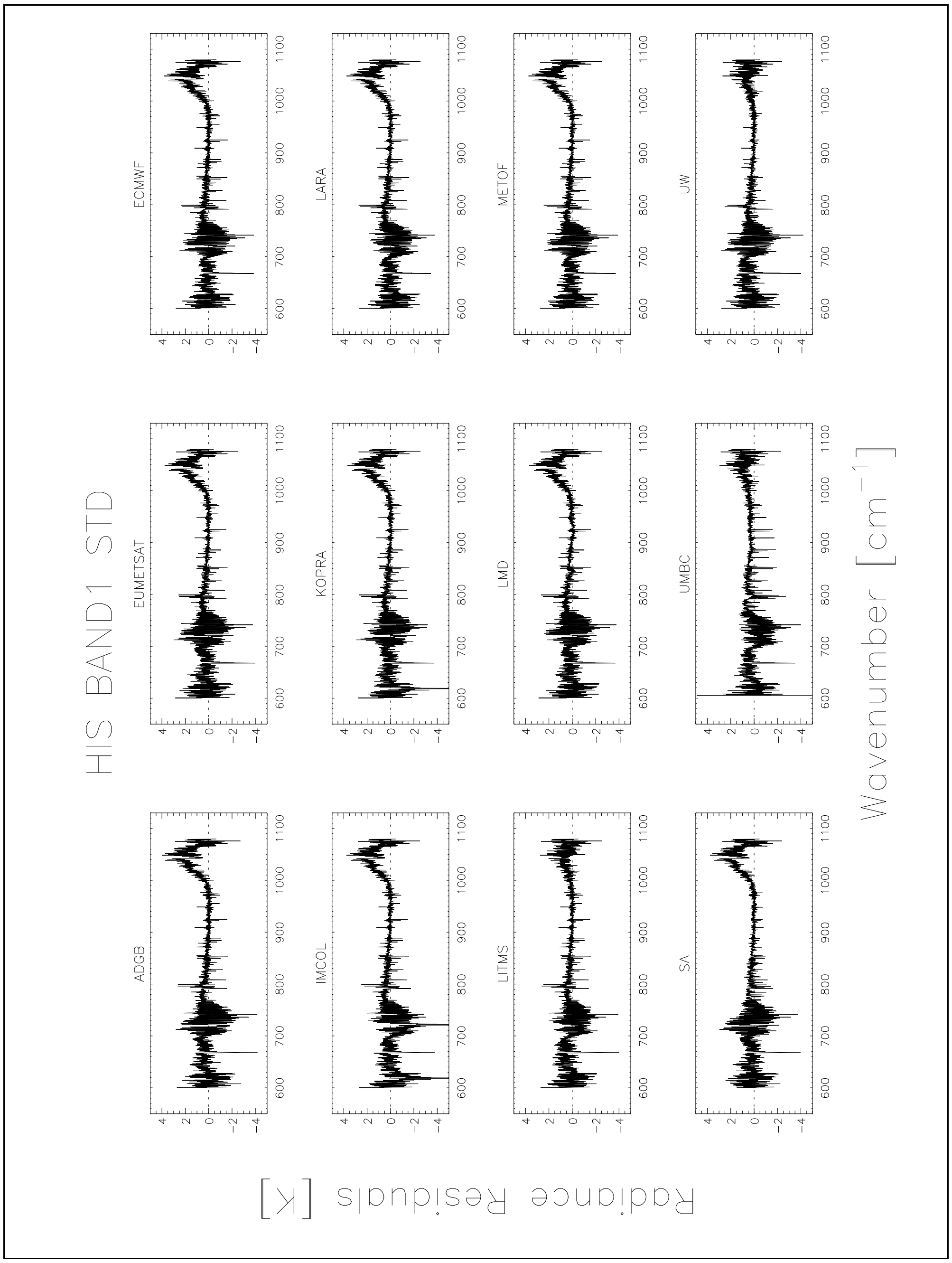

Figure 7.17: Radiance residuals between calculated and observed radiance in HIS band 1 for the particular submission indicated by the title above each panel. Note that the radiance residuals are converted into noise equivalent brightness temperature, using the equivalent brightness temperatures shown in Figure 7.15. Only the results in the optical filter range of HIS band 1 between 600 - 1080 cm^{-1} are shown.

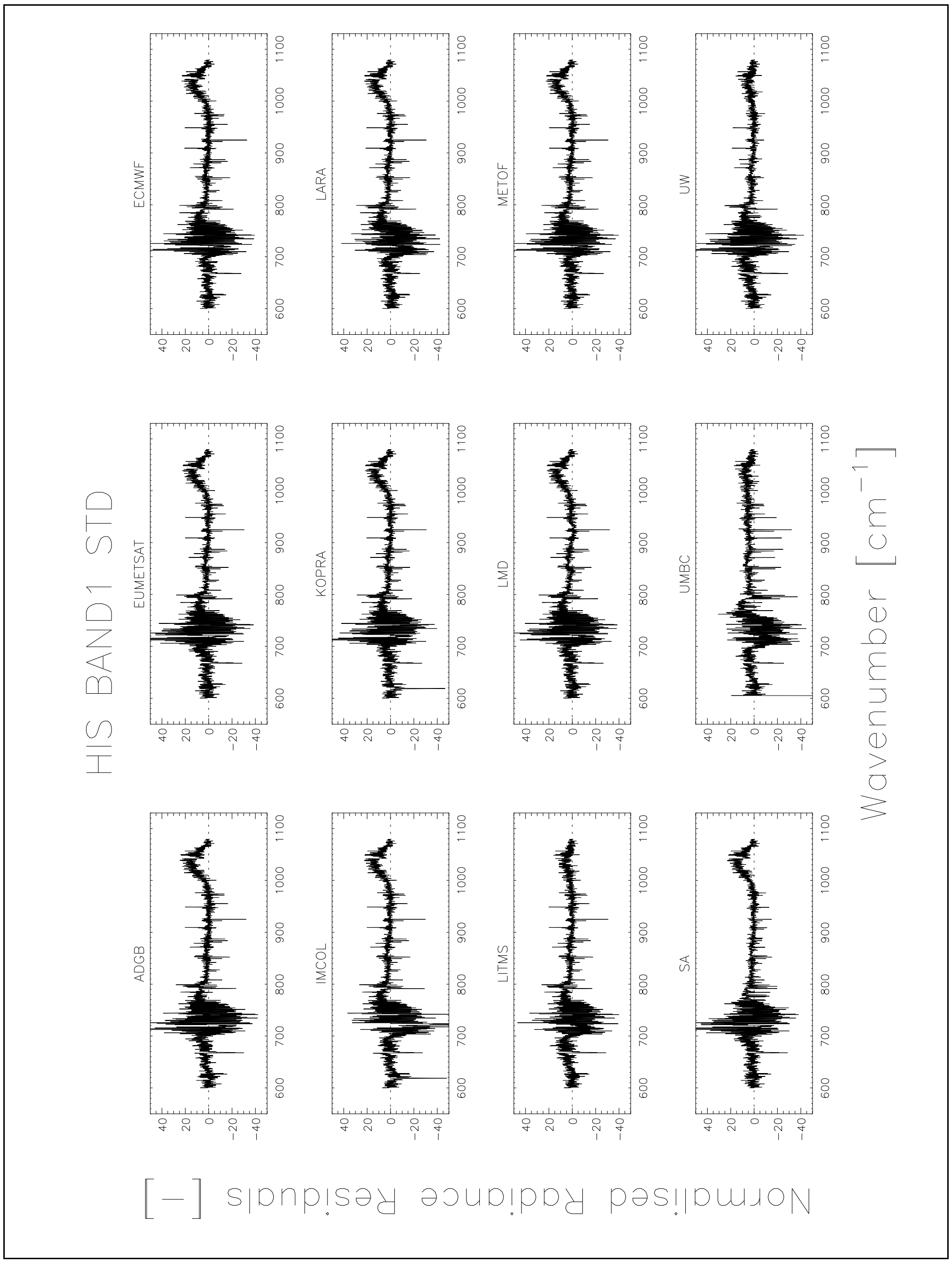

Figure 7.18: Radiance residuals between calculated and observed radiance in HIS band 1 for the particular submission indicated by the title above each panel. Note that the radiance residuals are normalised by the uncertainty in the observations. Only the results in the optical filter range of HIS band 1 between 600 - 1080 cm^{-1} are shown.

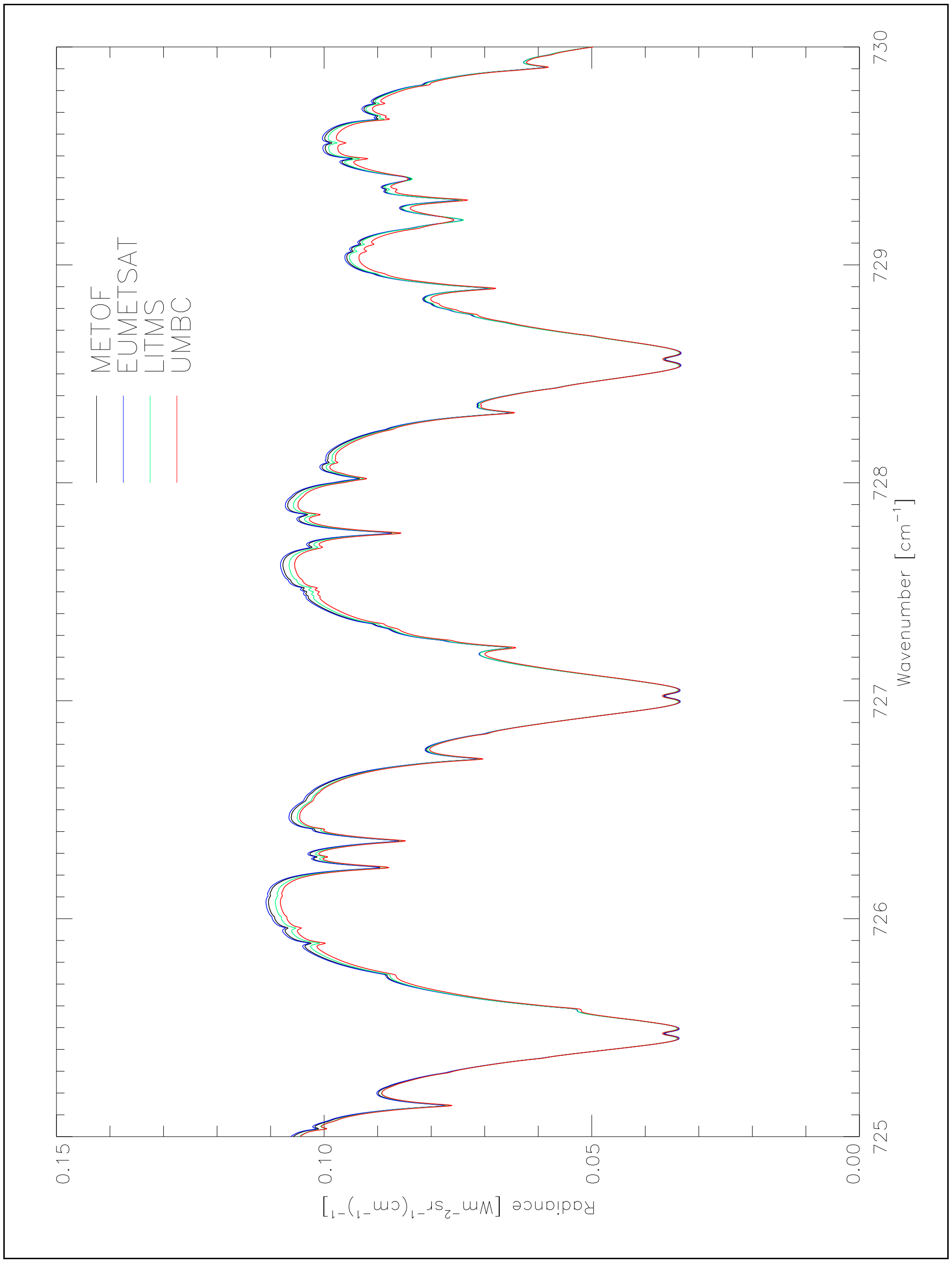

Figure 7.19: Upwelling Radiance in $mWm^{-2}sr^{-1}\left(cm^{-1}\right)^{-1}$ as a function of wavenumber at the observational level of 19.97 km, according to the METOF (black line), EUMETSAT (blue line), LITMS (green line) and UMBC (red line) submission in the spectral region between 725 – 730 cm^{-1}.

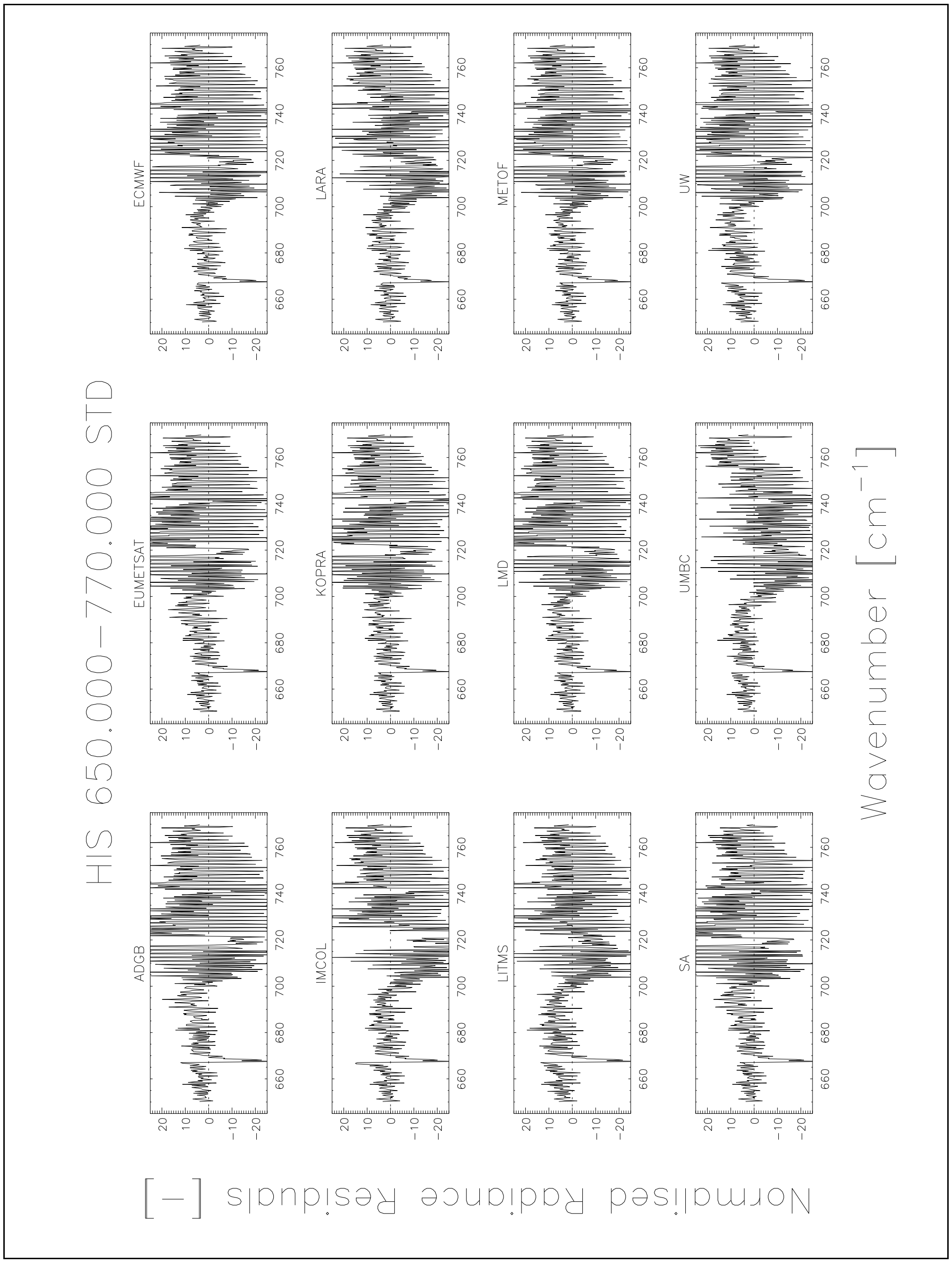

Figure 7.20: Radiance residuals between calculated and observed radiance in HIS band 1 for each of the submissions for the first spectral interval of Table 4.1. Note that the radiance residuals are normalised by the uncertainty in the observations.

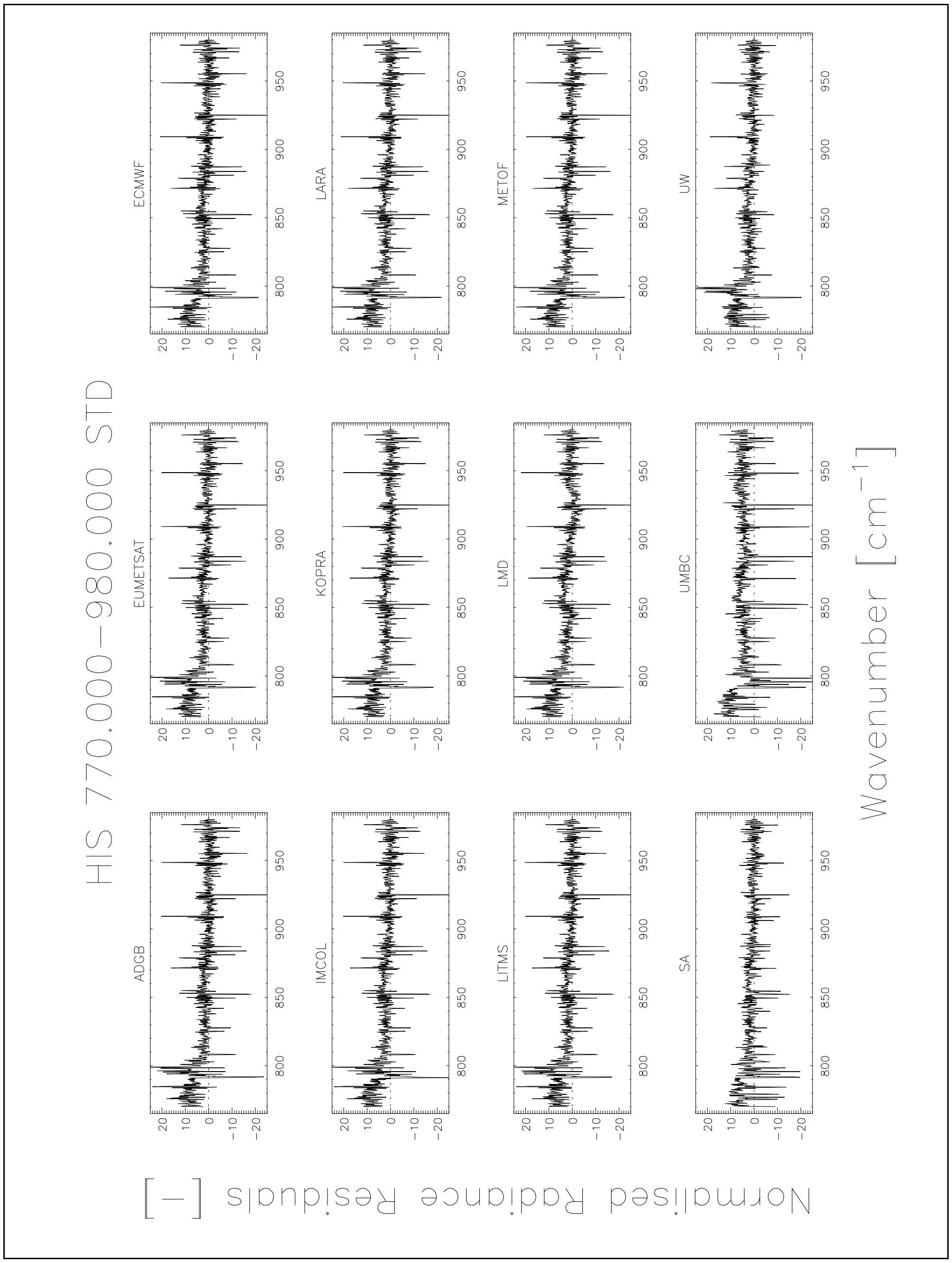

Figure 7.21: Radiance residuals between calculated and observed radiance in HIS band1 for each of the submissions for the second spectral interval of Table 4.1. Note that the radiance residuals are normalised by the uncertainty in the observations.

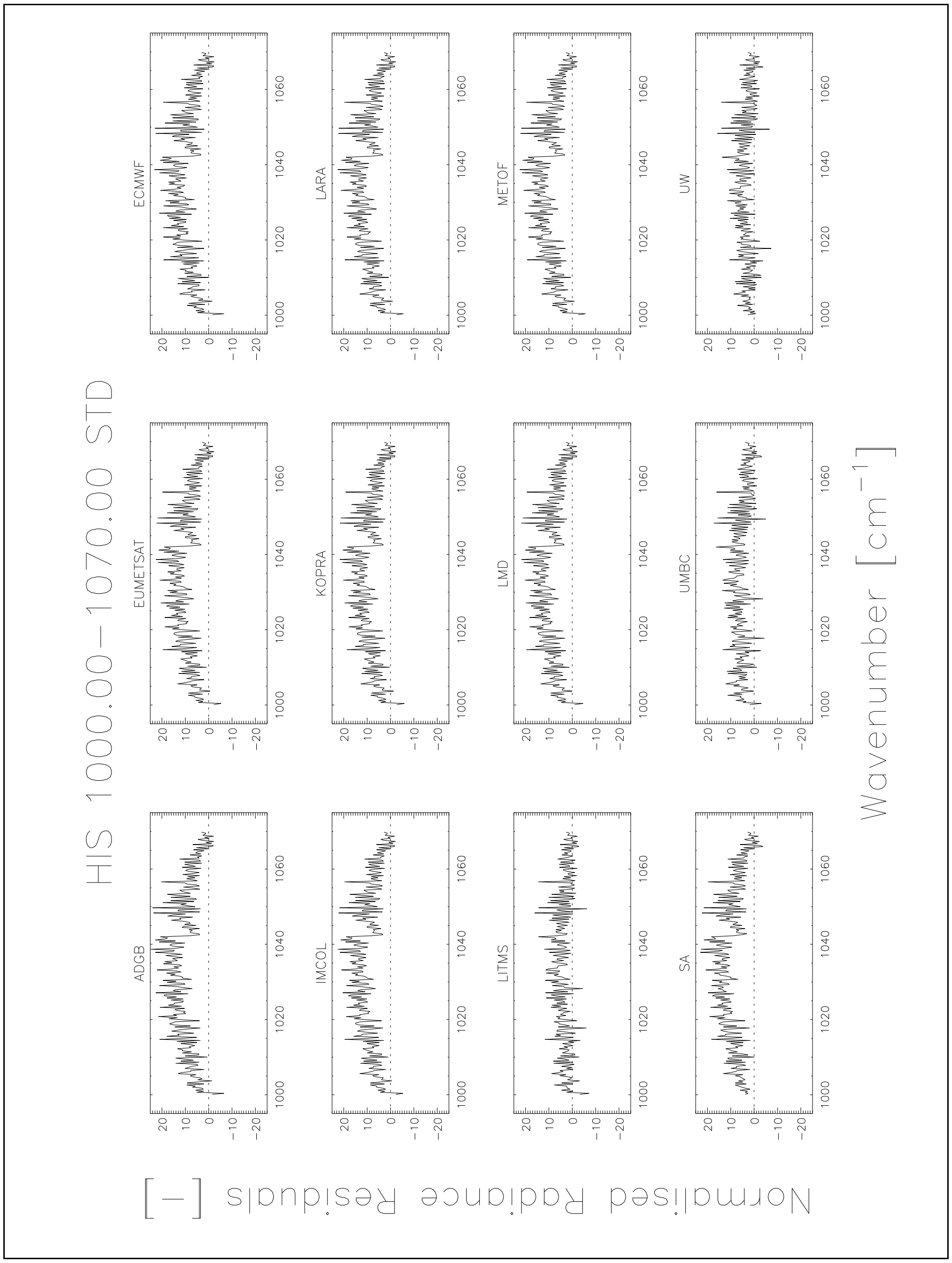

Figure 7.22: Radiance residuals between calculated and observed radiance in HIS band1 for each of the submissions for the third spectral interval of Table 4.1. Note that the radiance residuals are normalised by the uncertainty in the observations.

Figure 7.23: Same as 7.13 but now for HIS Band2.

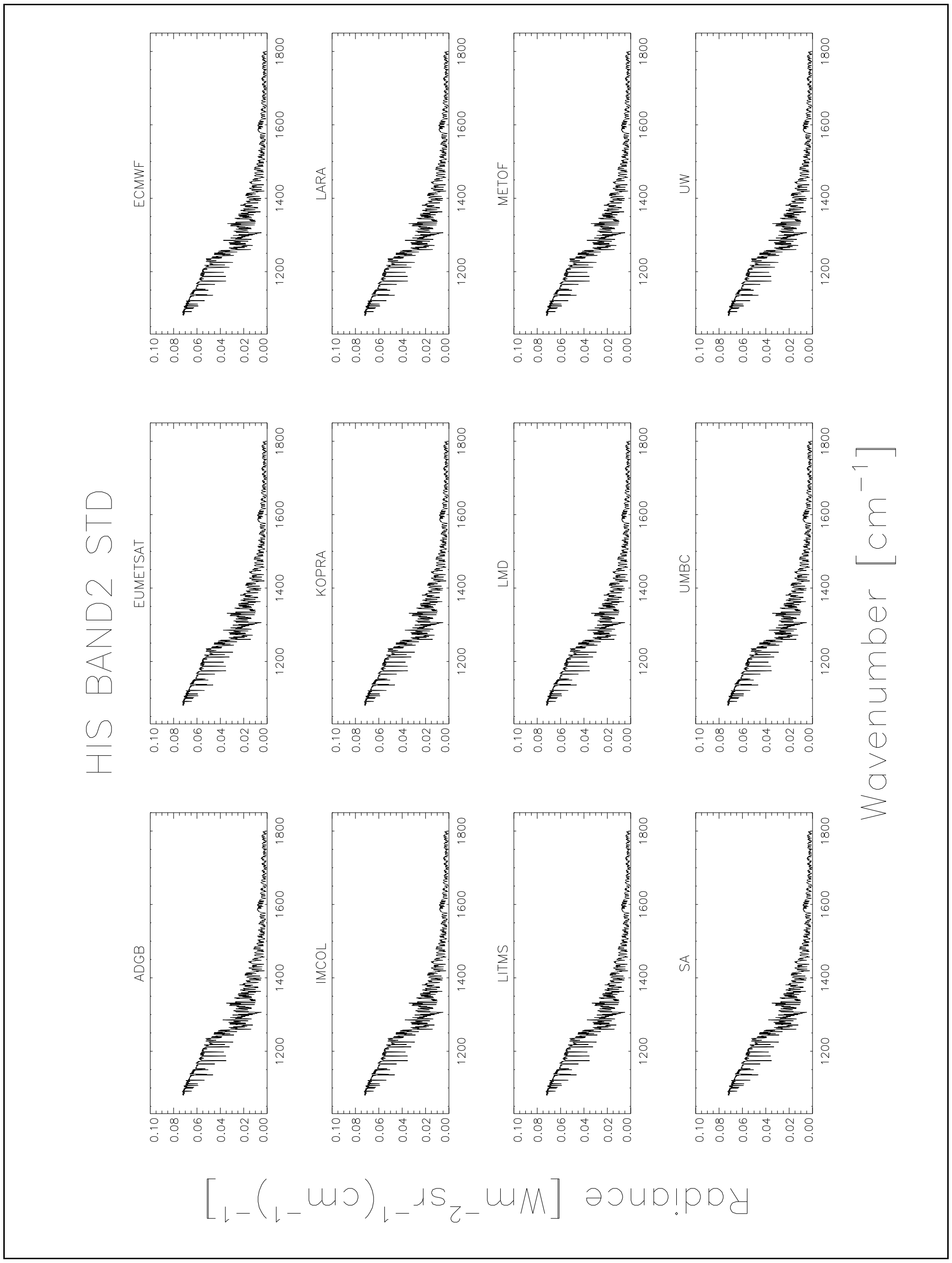

Figure 7.24: Radiance in HIS band 2 for the particular submission indicated by the title above each panel. Only the results in the optical filter range of HIS Band 2 between 1080 - 1800 cm^{-1} are shown.

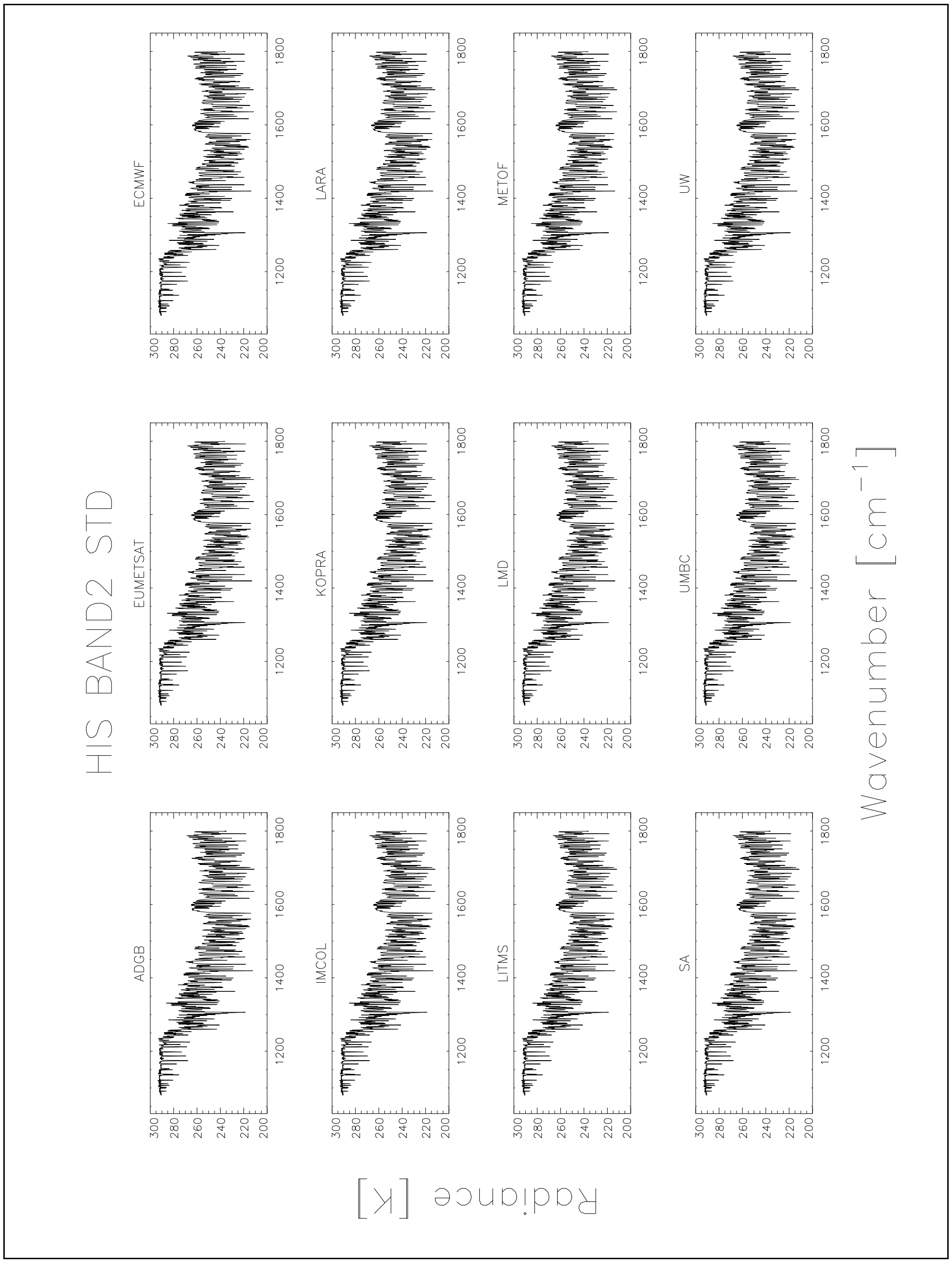

Figure 7.25: Radiance in HIS band 2 for the particular submission indicated by the title above each panel. Note that the radiances are converted into equivalent brightness temperatures using the inverse of the Planck-function. Only the results in the optical filter range of HIS Band 2 between 1080 - 1800 cm^{-1} are shown.

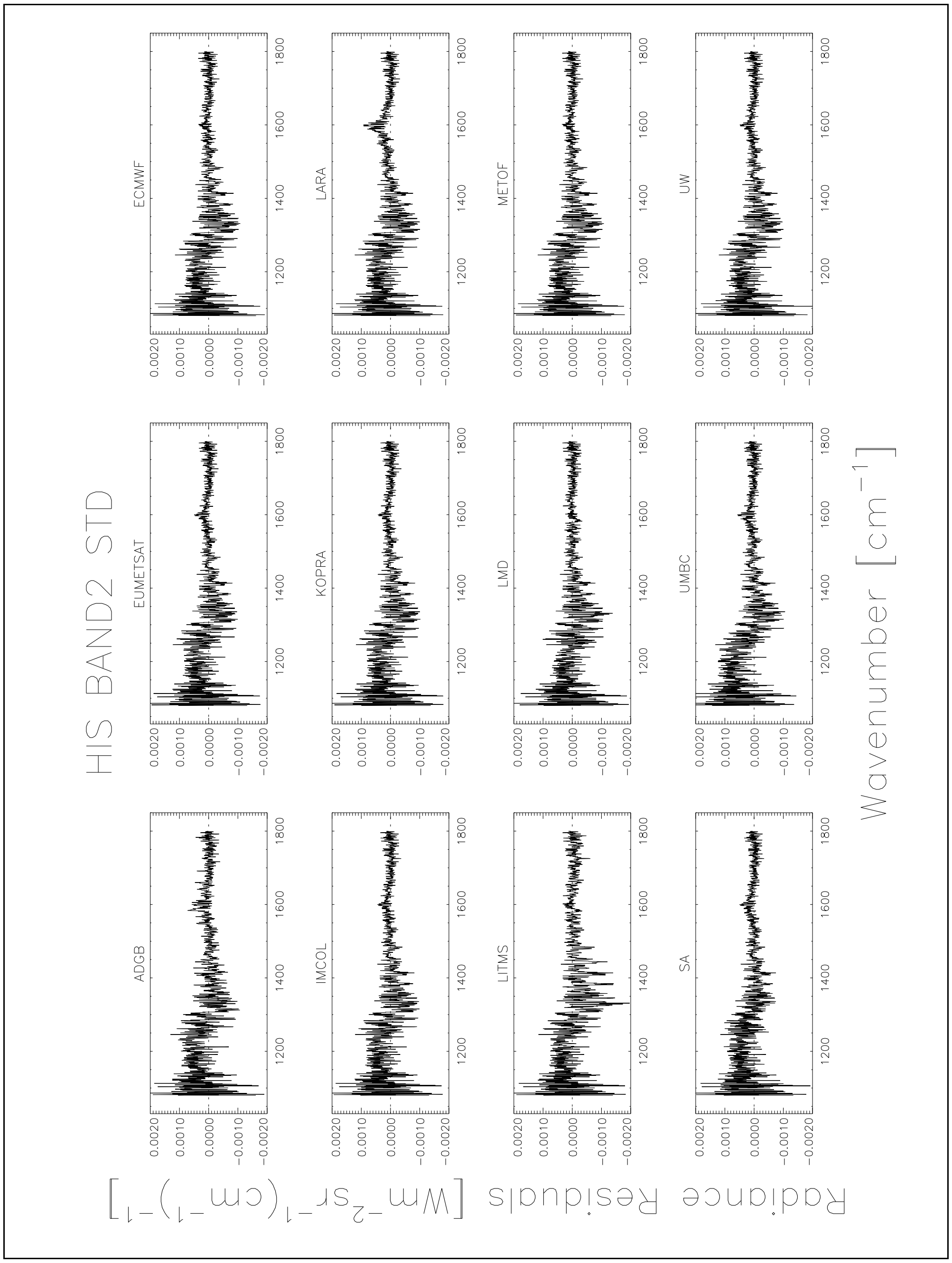

Figure 7.26: Radiance residuals between calculated and observed radiance in HIS band 2 for the particular submission indicated by the title above each panel. Only the results in the optical filter range of HIS Band 2 between 1080 - 1800 cm^{-1} are shown.

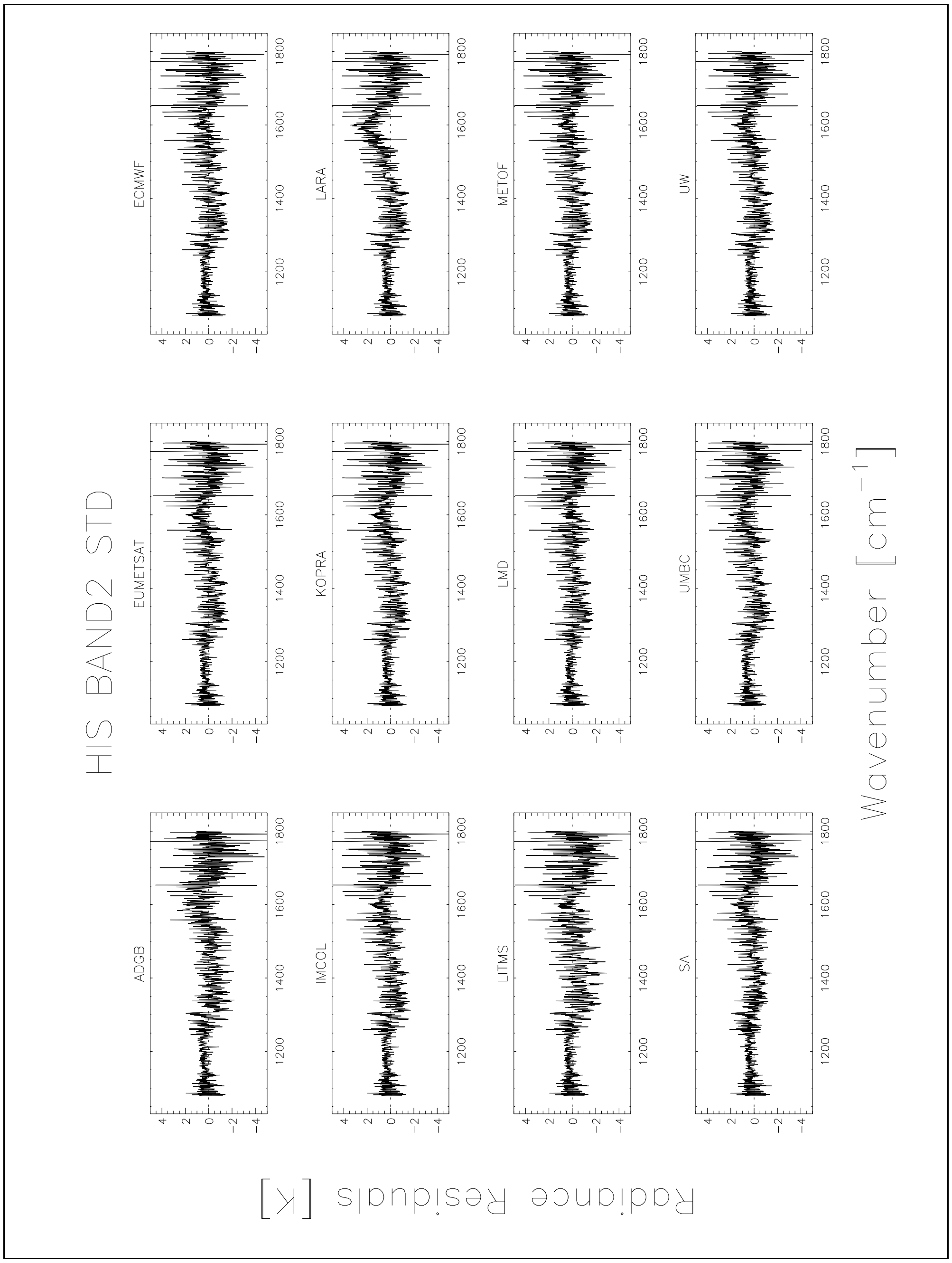

Figure 7.27: Radiance residuals between calculated and observed radiance in HIS band 2 for the particular submission indicated by the title above each panel. Note that the radiance residuals are converted into noise equivalent brightness temperature, using the equivalent brightness temperatures shown in Figure 7.25. Only the results in the optical filter range of HIS Band 2 between 1080 - 1800 cm^{-1} are shown.

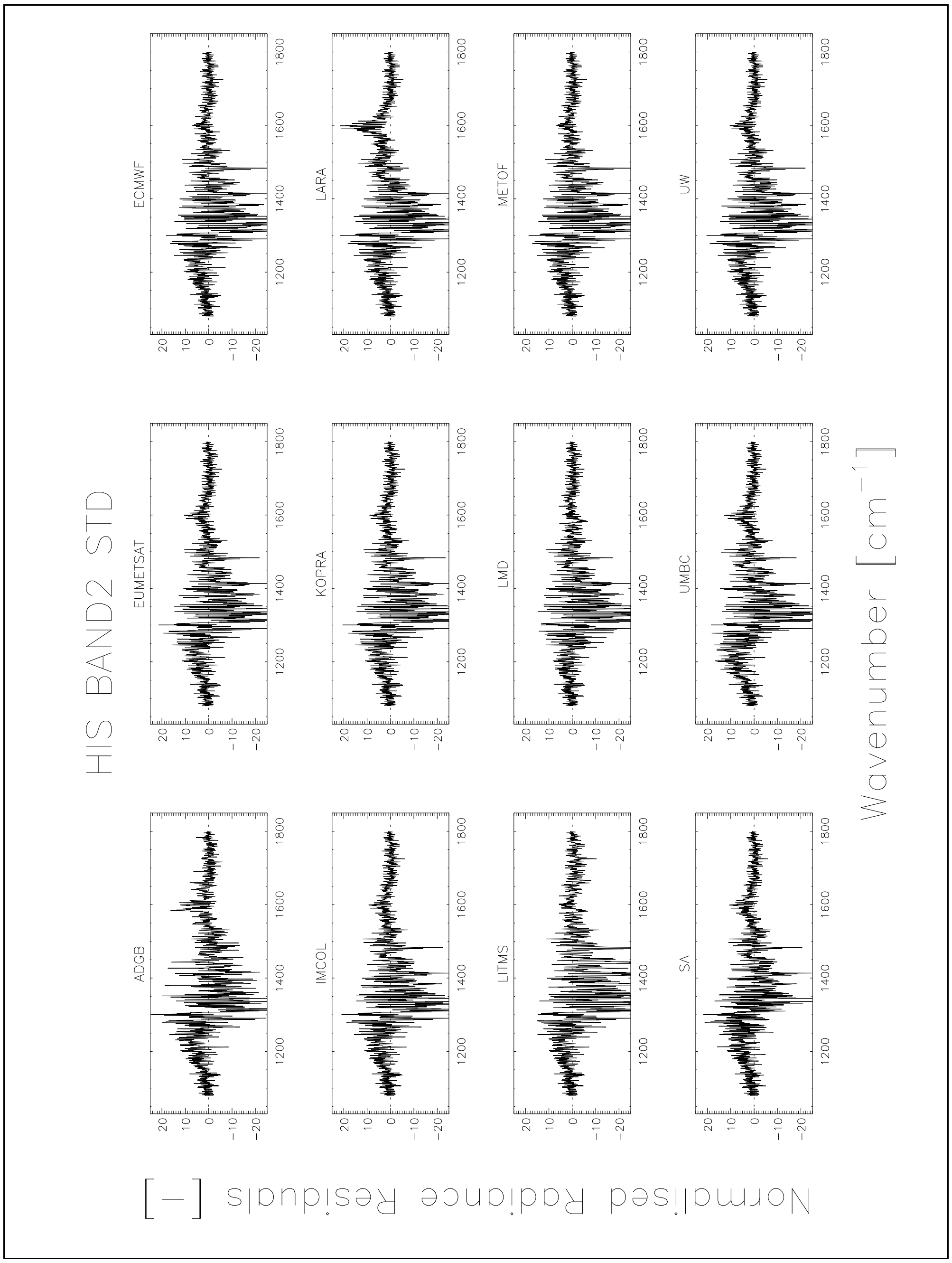

Figure 7.28: Radiance residuals between calculated and observed radiance in HIS band 2 for the particular submission indicated by the title above each panel. Note that the radiance residuals are normalised by the uncertainty in the observations. Only the results in the optical filter range of HIS band 2 between 1080 - 1800 cm^{-1} are shown.

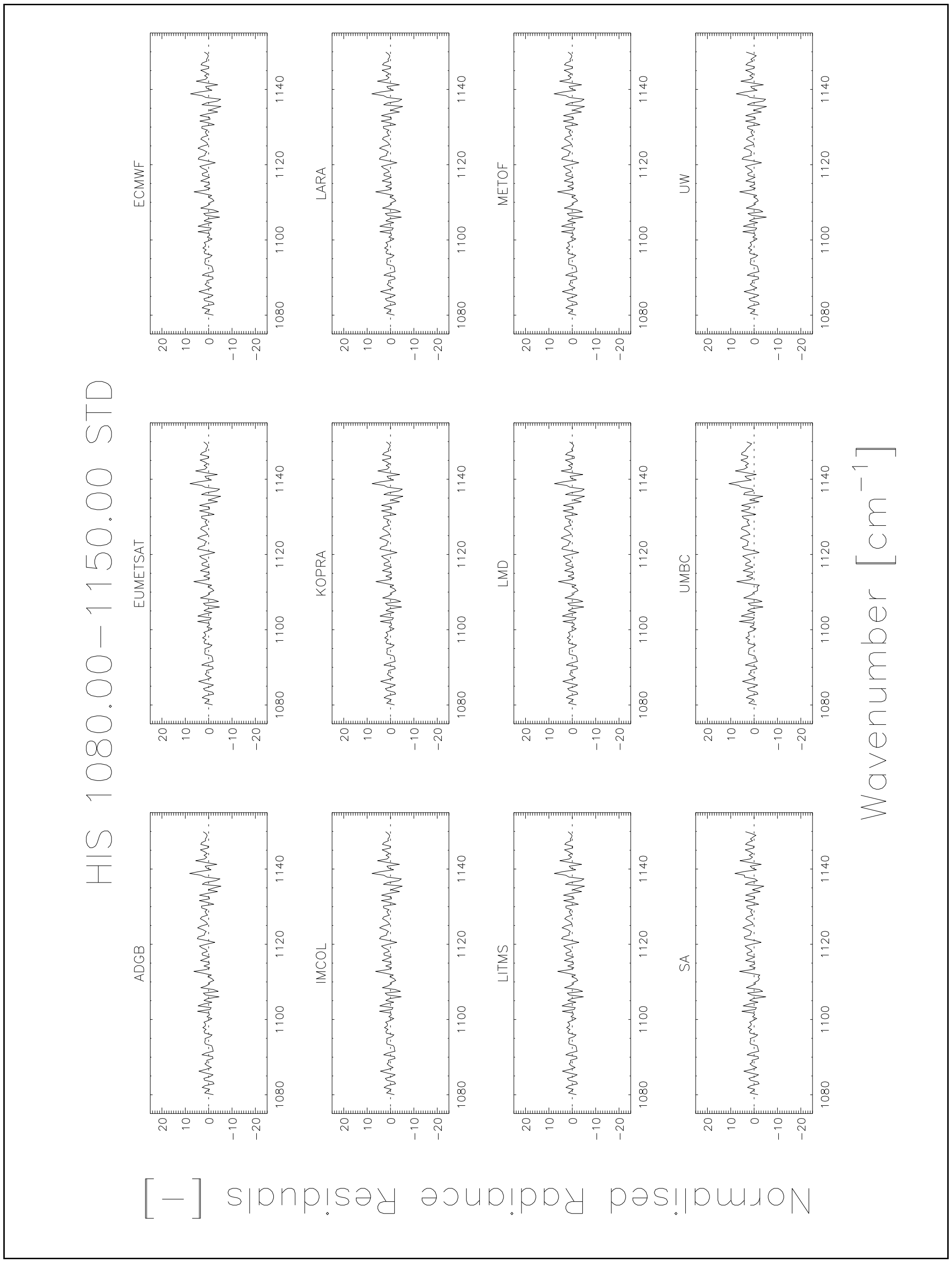

Figure 7.29: Radiance residuals between calculated and observed radiance in HIS band 2 for each of the submissions for the 4^{th} spectral interval of Table 4.1. Note that the radiance residuals are normalised by the uncertainty in the observations.

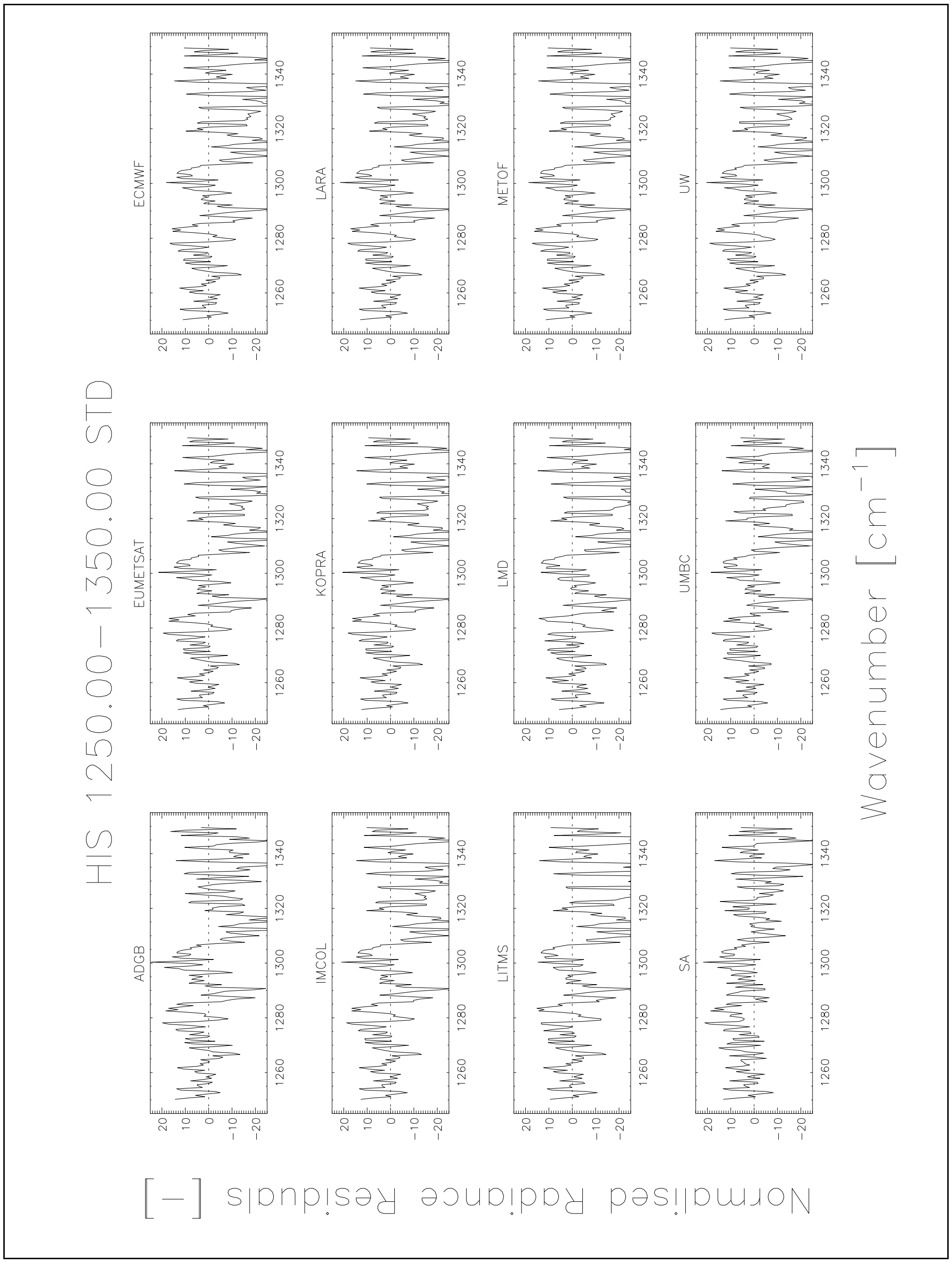

Figure 7.30: Radiance residuals between calculated and observed radiance in HIS band 2 for each of the submissions for the 5^{th} spectral interval of Table 4.1. Note that the radiance residuals are normalised by the uncertainty in the observations.

Figure 7.31: Same as 7.13 but now for HIS Band 3.

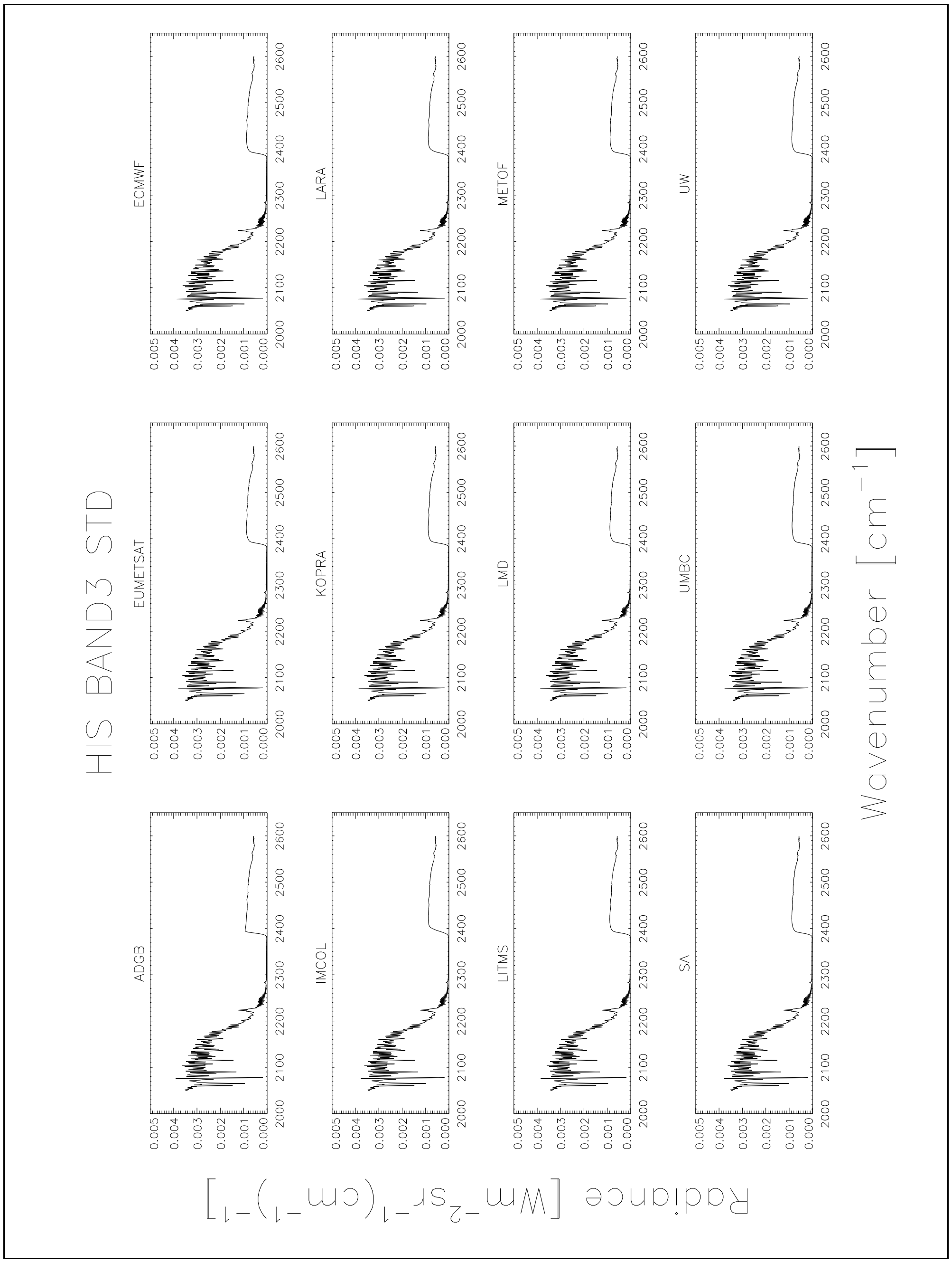

Figure 7.32: Radiance in HIS band 3 for the particular submission indicated by the title above each panel. Only the results in the optical filter range of HIS Band 3 between 2050 - 2600 cm^{-1} are shown.

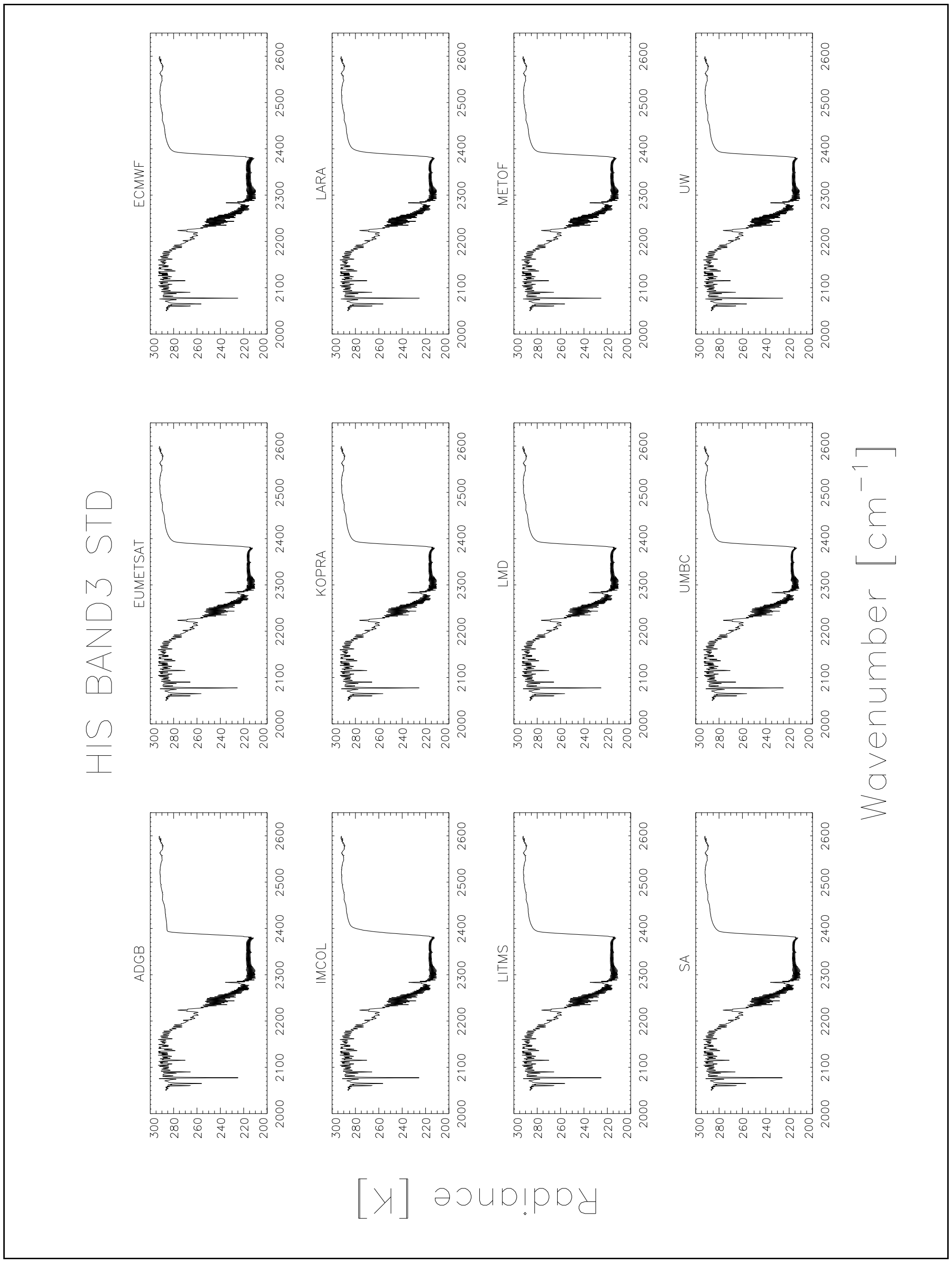

Figure 7.33: Radiance in HIS band 3 for the particular submission indicated by the title above each panel. Note that the radiances are converted into equivalent brightness temperatures using the inverse of the Planck-function. Only the results in the optical filter range of HIS Band 2 between 2050 - 2600 cm^{-1} are shown.

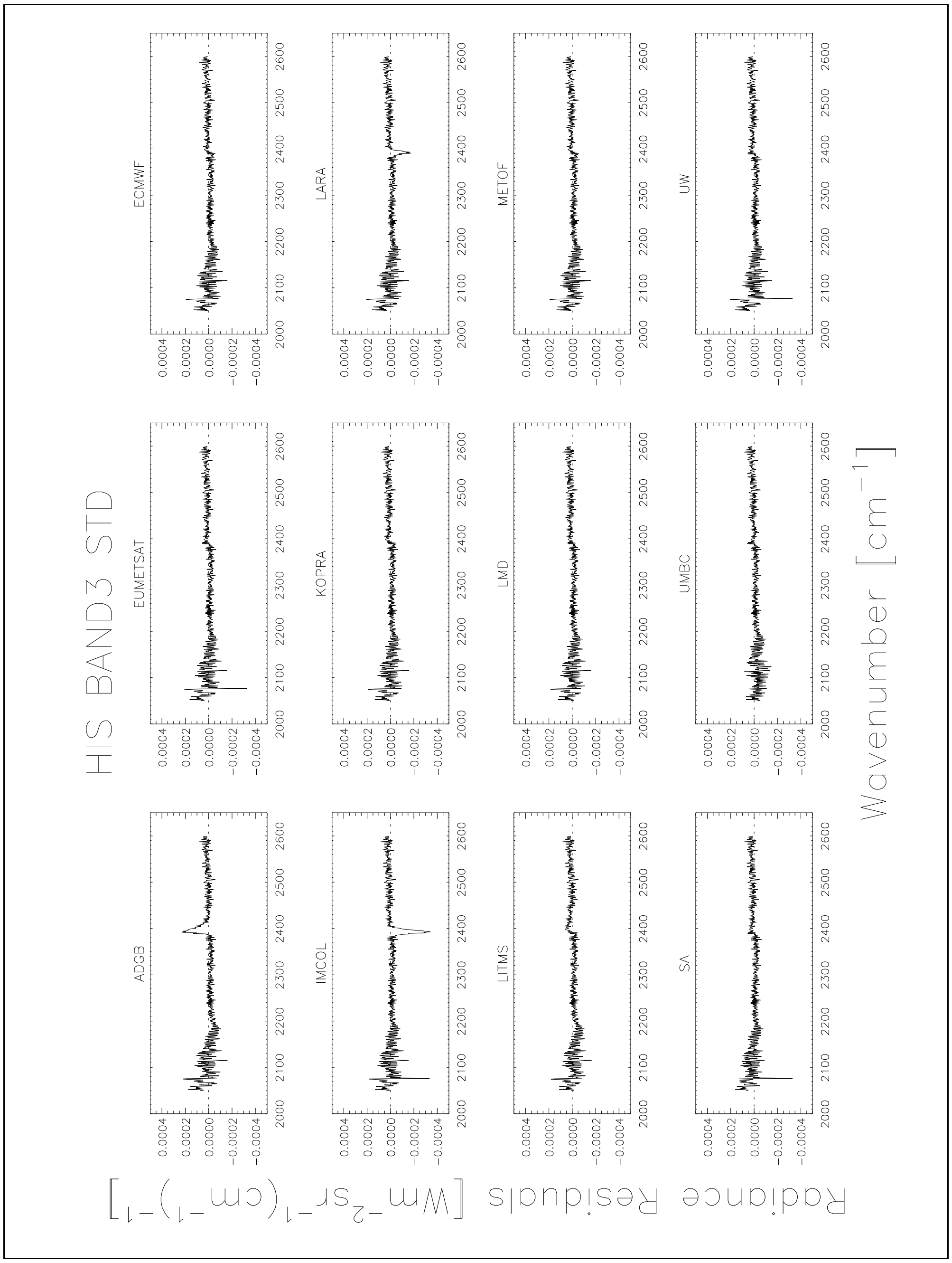

Figure 7.34: Radiance residuals between calculated and observed radiance in HIS band 3 for the particular submission indicated by the title above each panel. Only the results in the optical filter range of HIS Band 3 between 2050 - 2600 cm^{-1} are shown.

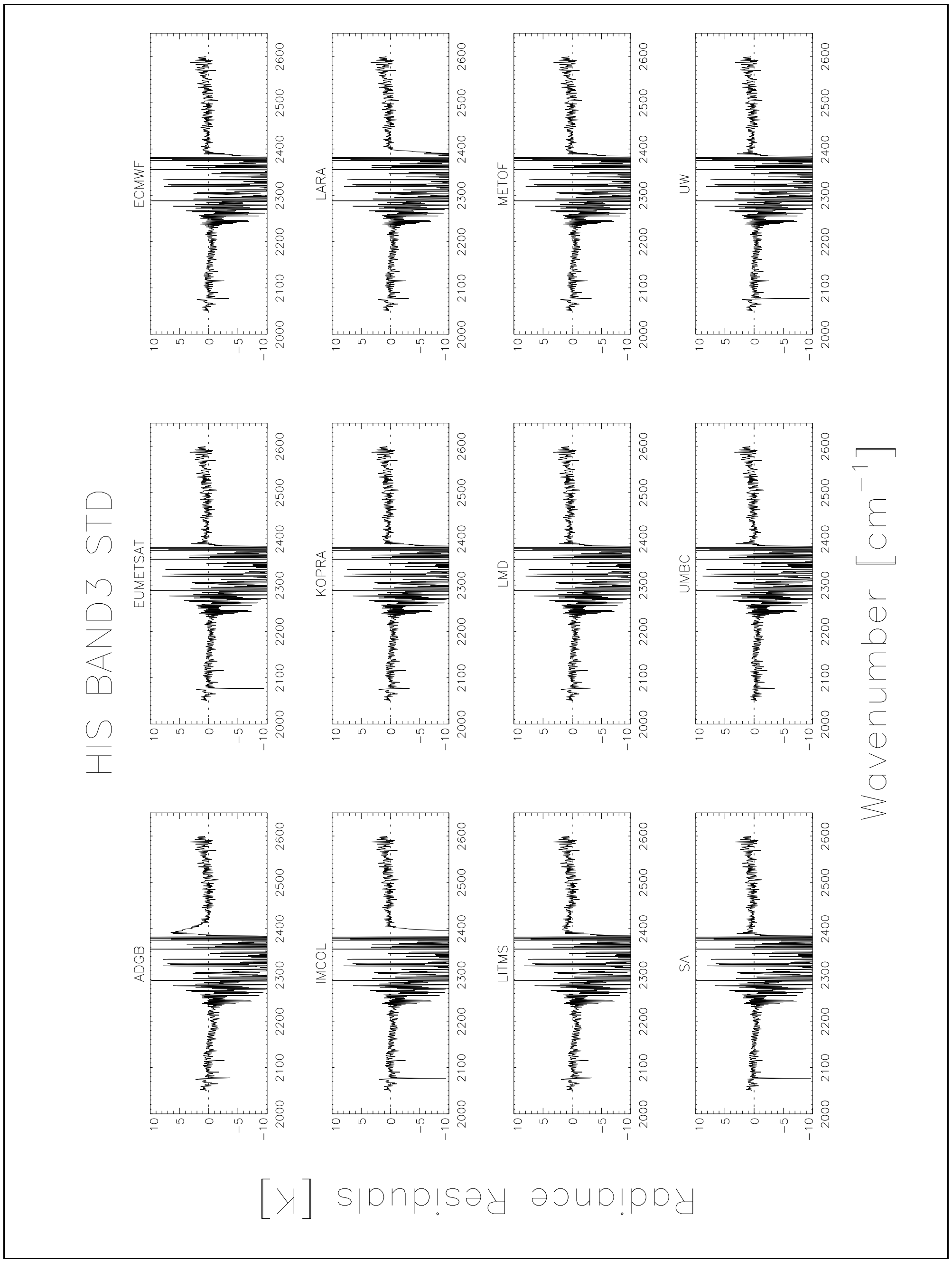

Figure 7.35: Radiance residuals between calculated and observed radiance in HIS band 3 for the particular submission indicated by the title above each panel. Note that the radiance residuals are converted into noise equivalent brightness temperature, using the equivalent brightness temperatures shown in Figure 7.33. Only the results in the optical filter range of HIS Band 3 between 2050 - 2600 cm^{-1} are shown.

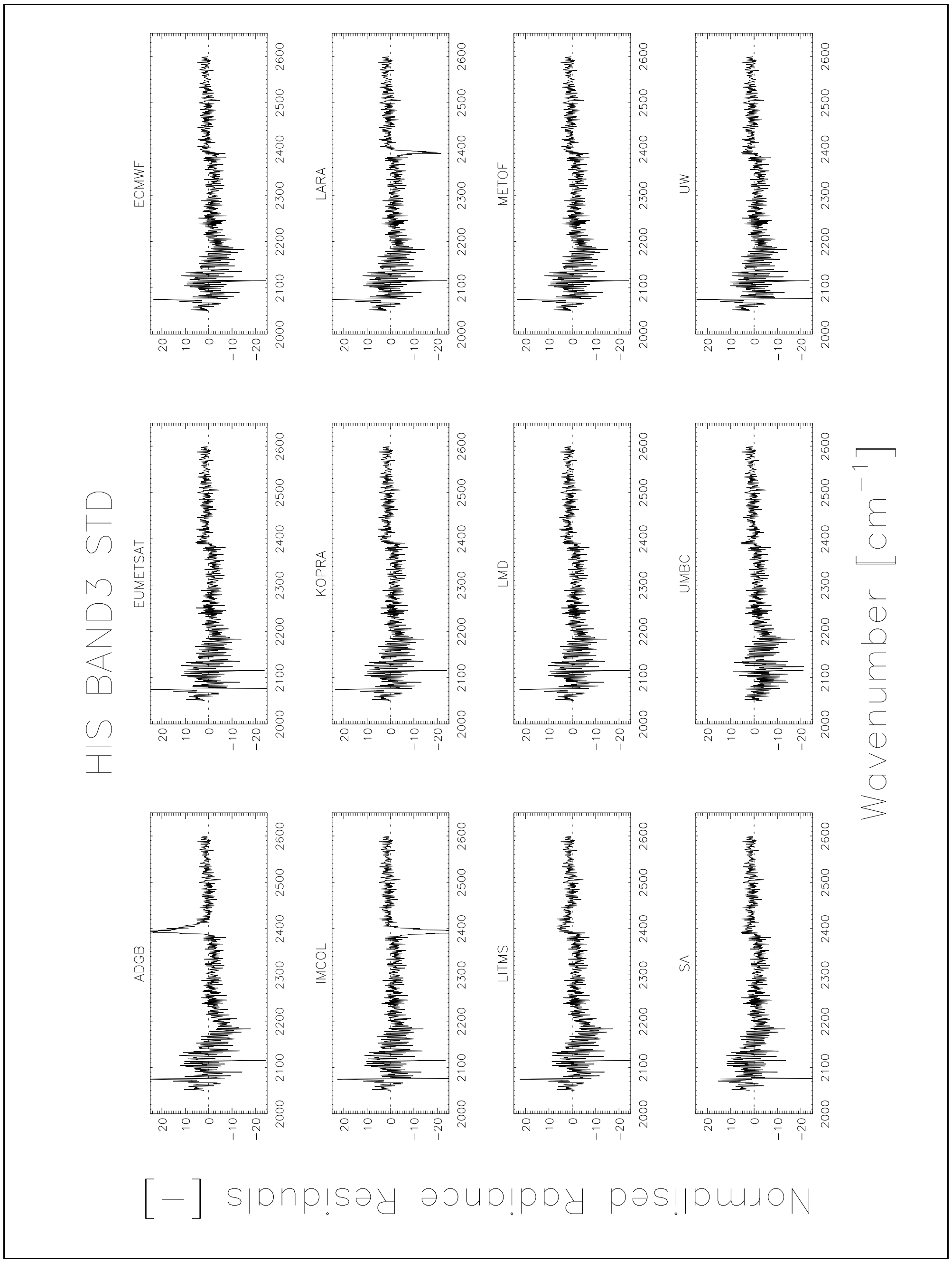

Figure 7.36: Radiance residuals between calculated and observed radiance in HIS band 3 for the particular submission indicated by the title above each panel. Note that the radiance residuals are normalised by the uncertainty in the observations. Only the results in the optical filter range of HIS band 3 between 2050 - 2600 cm^{-1} are shown.

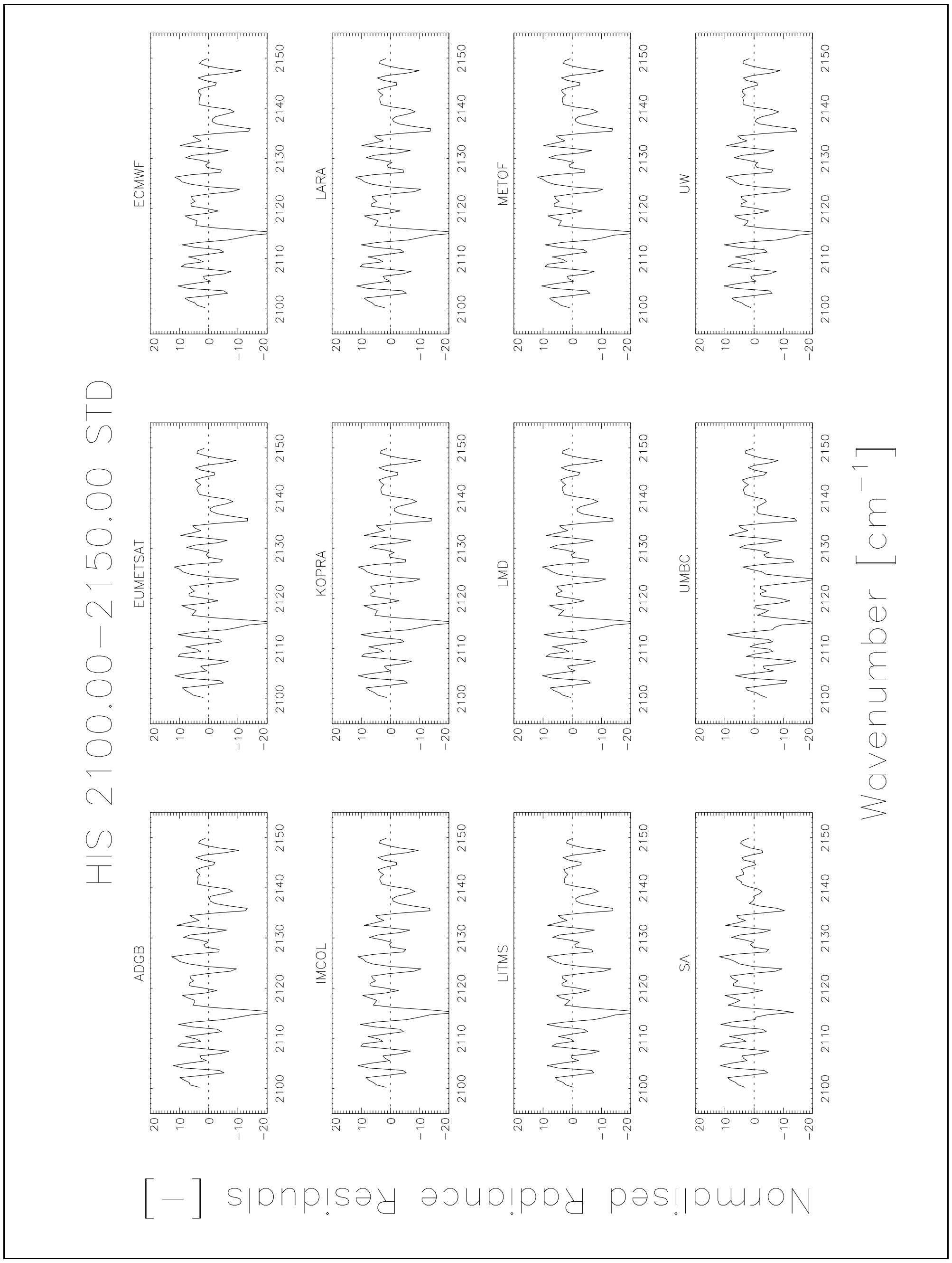

Figure 7.37: Radiance residuals between calculated and observed radiance in HIS band 3 for each of the submissions for the 6^{th} spectral interval of Table 4.1. Note that the radiance residuals are normalised by the uncertainty in the observations.

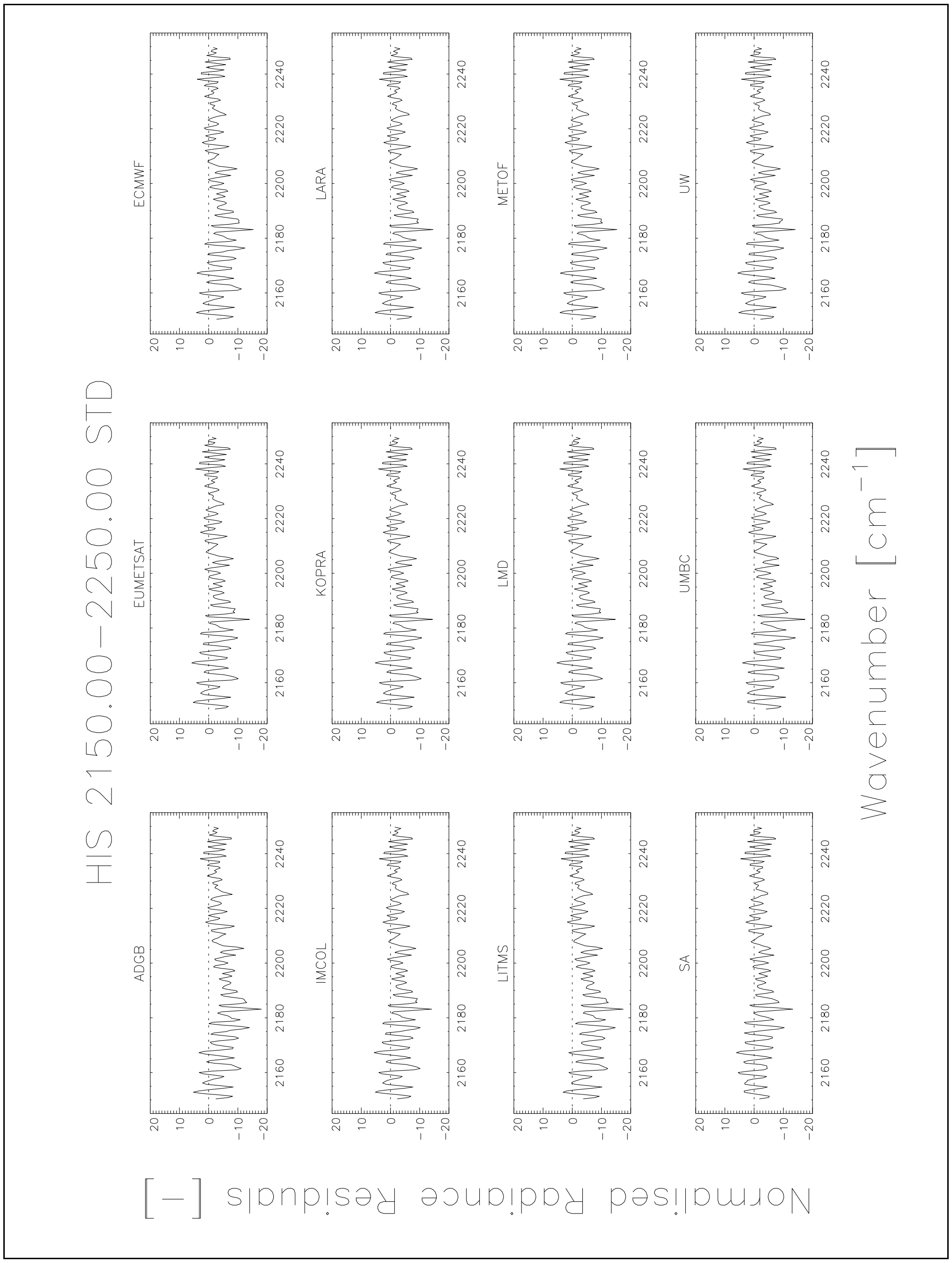

Figure 7.38: Radiance residuals between calculated and observed radiance in HIS band 3 for each of the submissions for the 7^{th} spectral interval of Table 4.1. Note that the radiance residuals are normalised by the uncertainty in the observations.

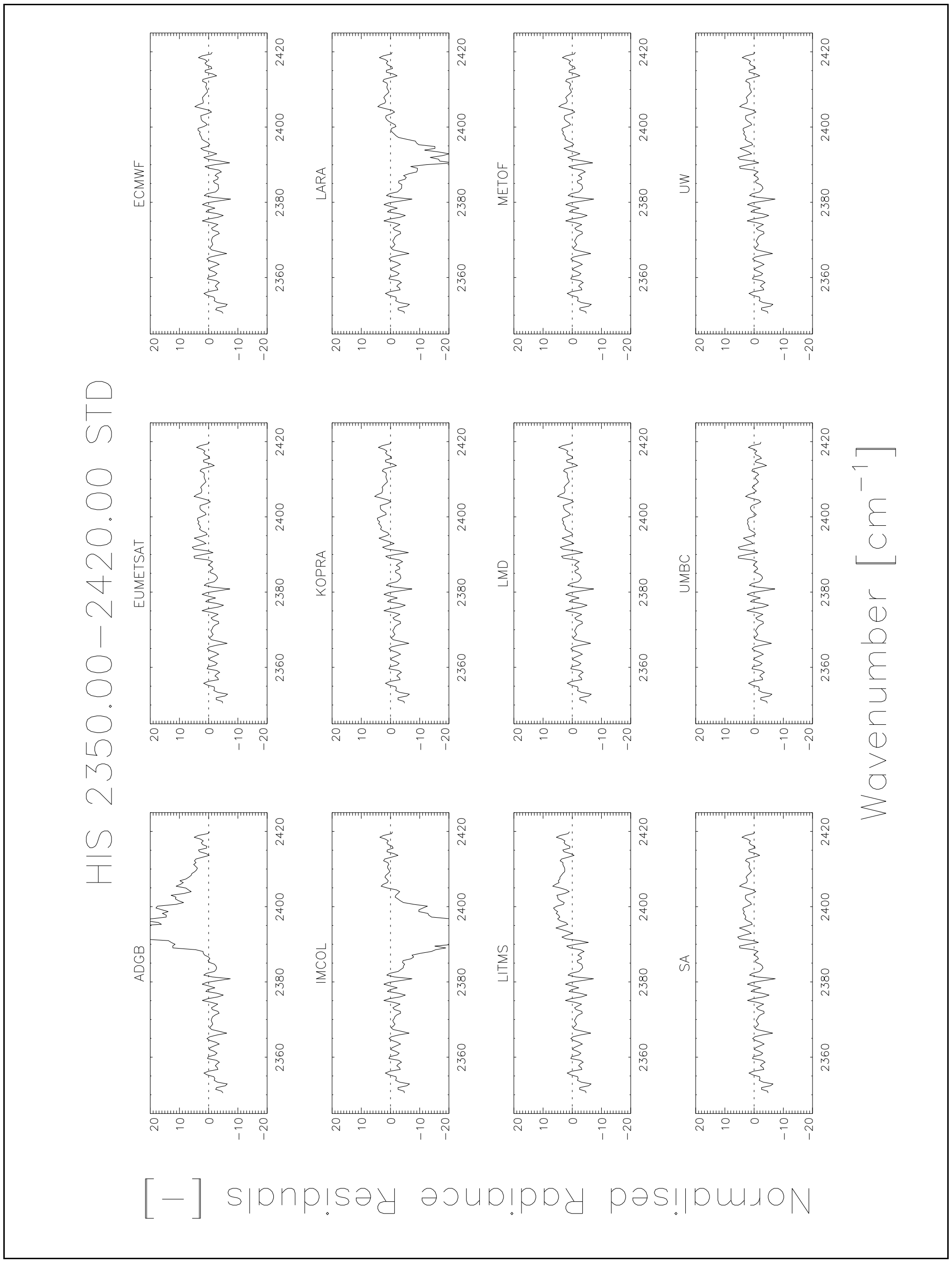

Figure 7.39: Radiance residuals between calculated and observed radiance in HIS band 3 for each of the submissions for the 8^{th} spectral interval of Table 4.1. Note that the radiance residuals are normalised by the uncertainty in the observations.

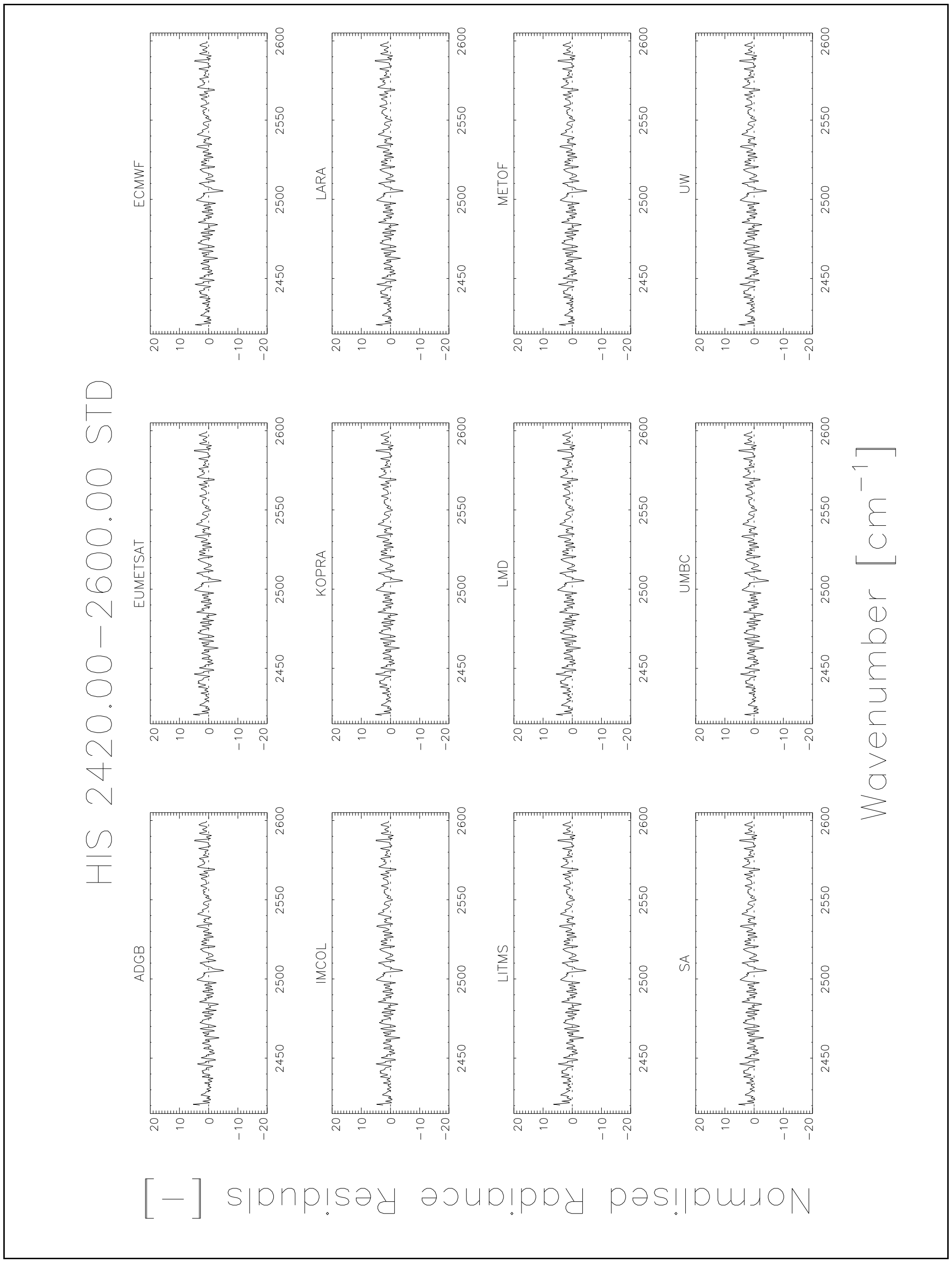

Figure 7.40: Radiance residuals between calculated and observed radiance in HIS band 3 for each of the submissions for the 9^{th} spectral interval of Table 4.1. Note that the radiance residuals are normalised by the uncertainty in the observations.

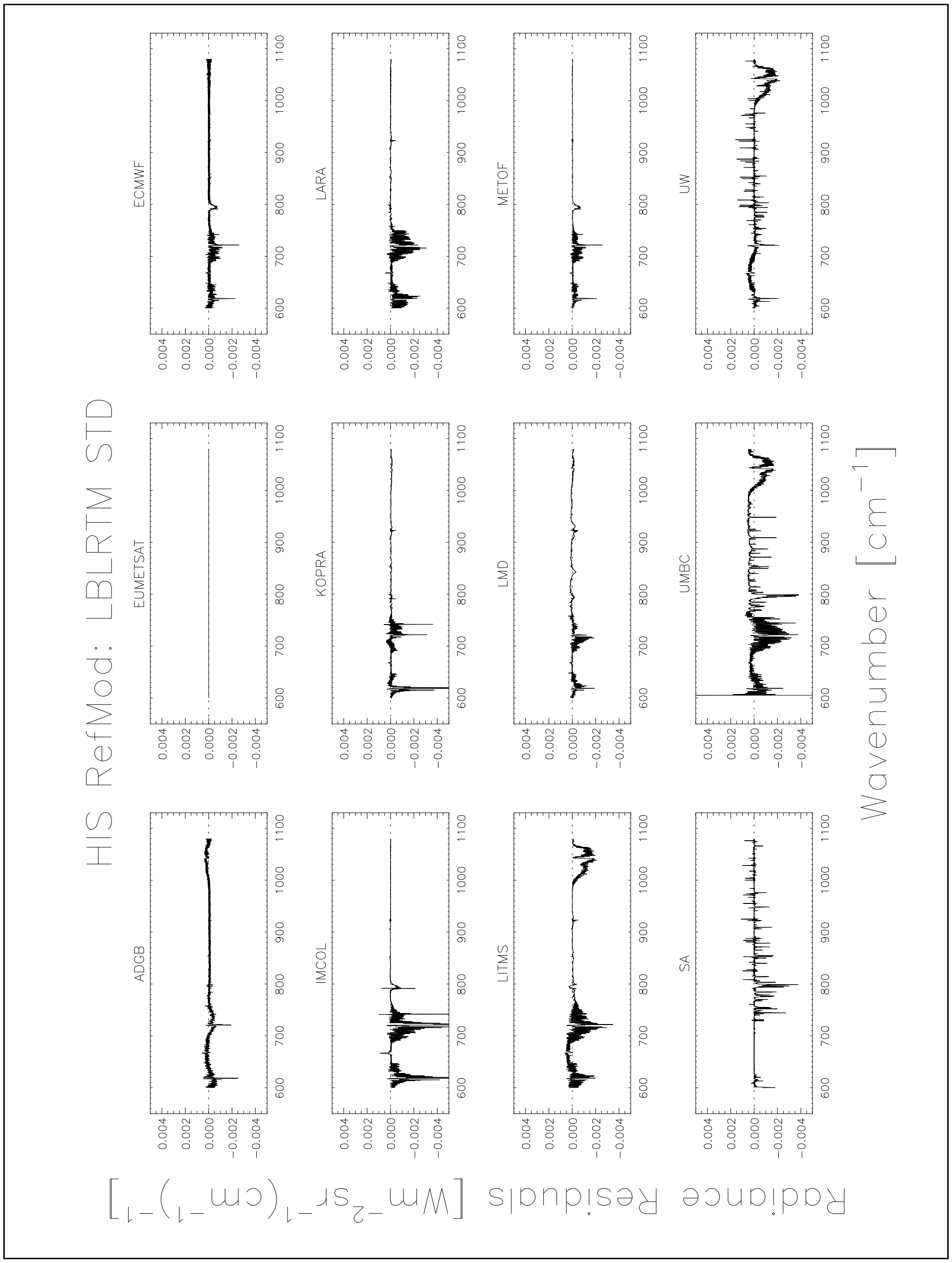

Figure 7.41: Radiance residuals between simulation by a particular submission as indicated by the title above each panel, and the LBLRTM model in HIS band 1. Only the results in the optical filter range of HIS Band 1 between 600 - 1080 cm^{-1} are shown.

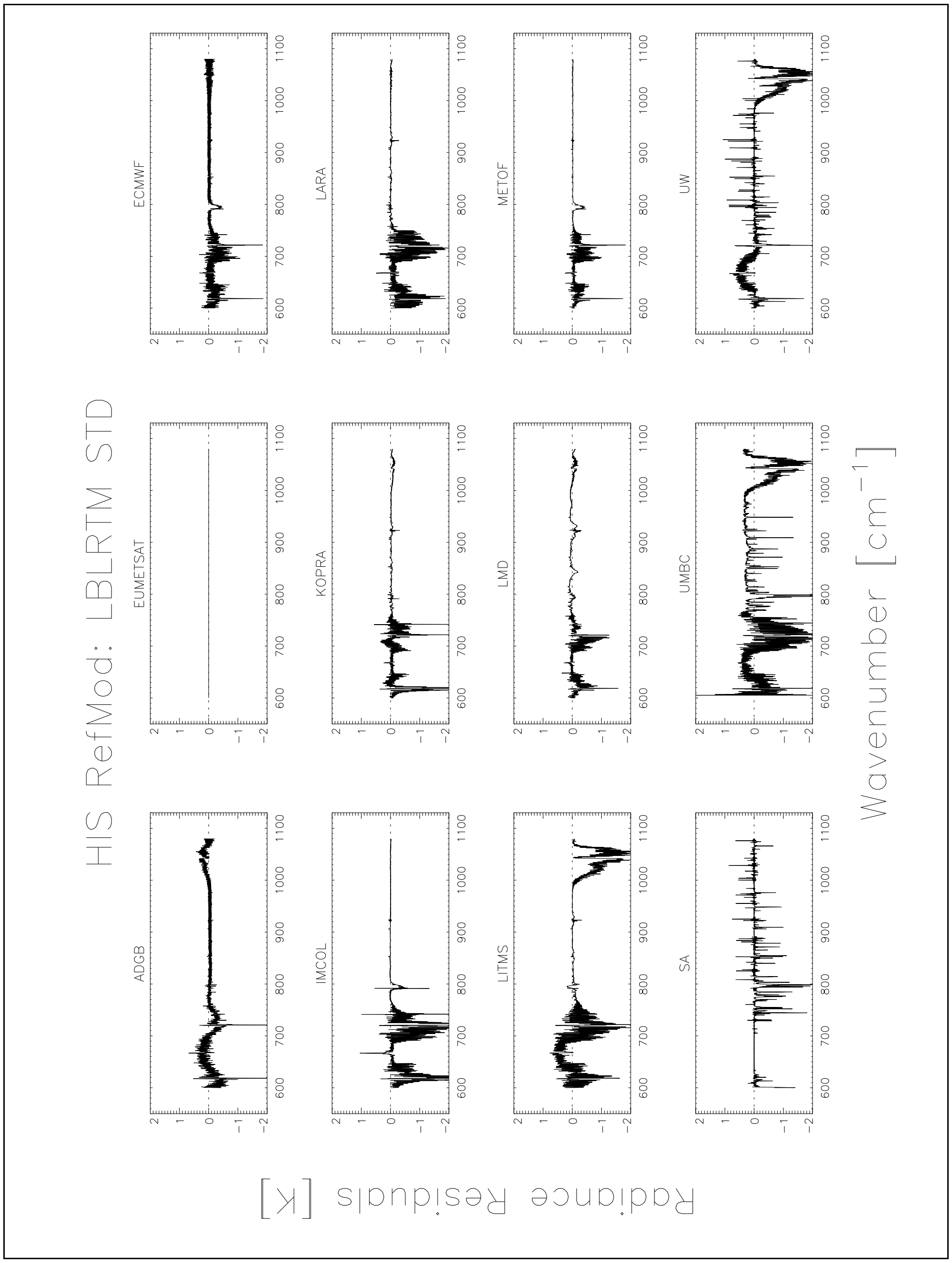

Figure 7.42: Radiance residuals between simulation by a particular submission as indicated by the title above each panel, and the LBLRTM model in HIS band 1. Only the results in the optical filter range of HIS Band 1 between 600 - 1080 cm^{-1} are shown.

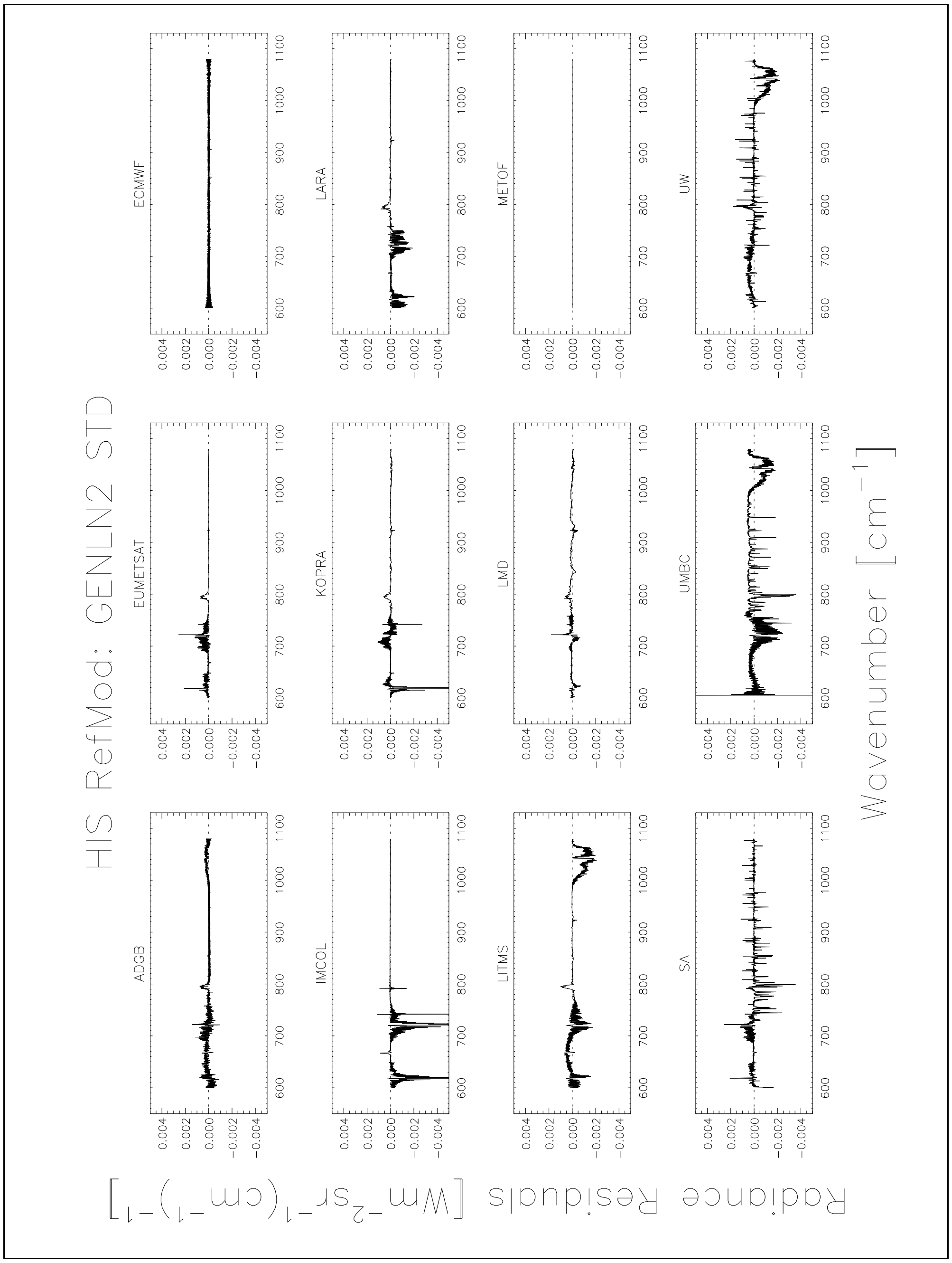

Figure 7.43: Radiance residuals between simulation by a particular submission as indicated by the title above each panel, and the GENLN2 model in HIS band 1. Only the results in the optical filter range of HIS Band 1 between 600 - 1080 cm^{-1} are shown.

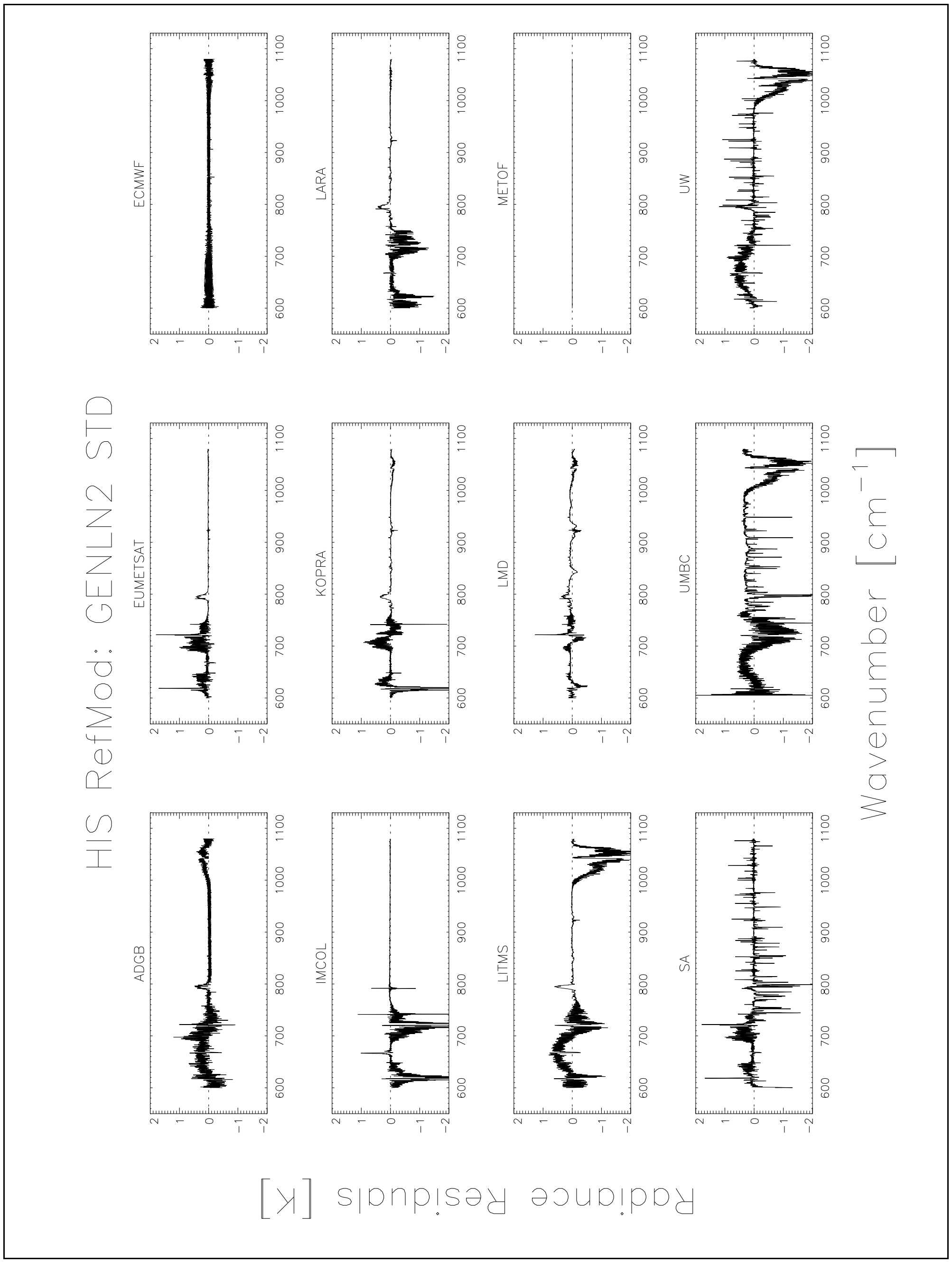

Figure 7.44: Radiance residuals between simulation by a particular submission as indicated by the title above each panel, and the GENLN2 model in HIS band 1. Only the results in the optical filter range of HIS Band 1 between 600 - 1080 cm^{-1} are shown.

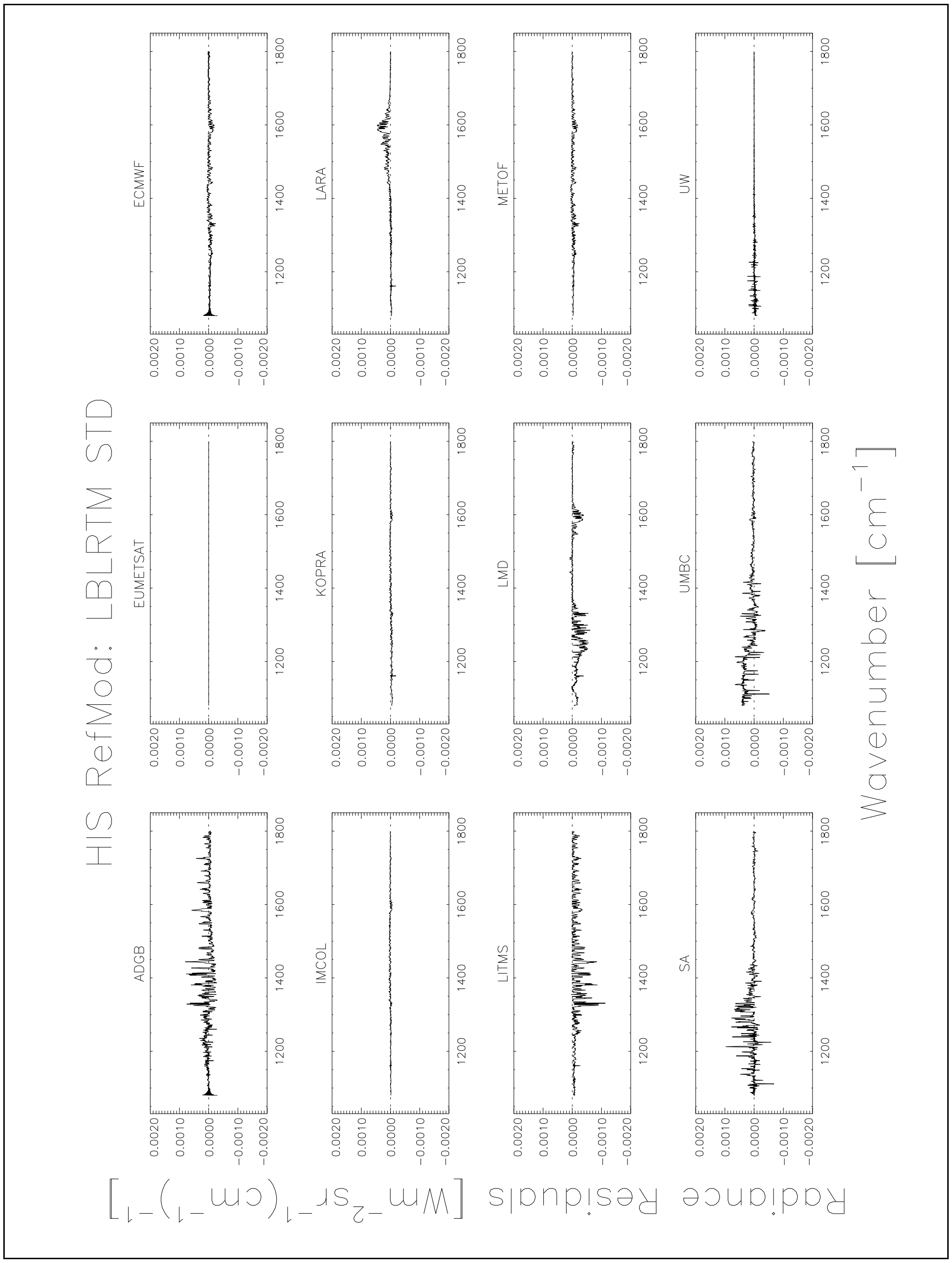

Figure 7.45: Radiance residuals between simulation by a particular submission as indicated by the title above each panel, and the LBLRTM model in HIS band 2. Only the results in the optical filter range of HIS band 2 between 1080 - 1800 cm^{-1} are shown.

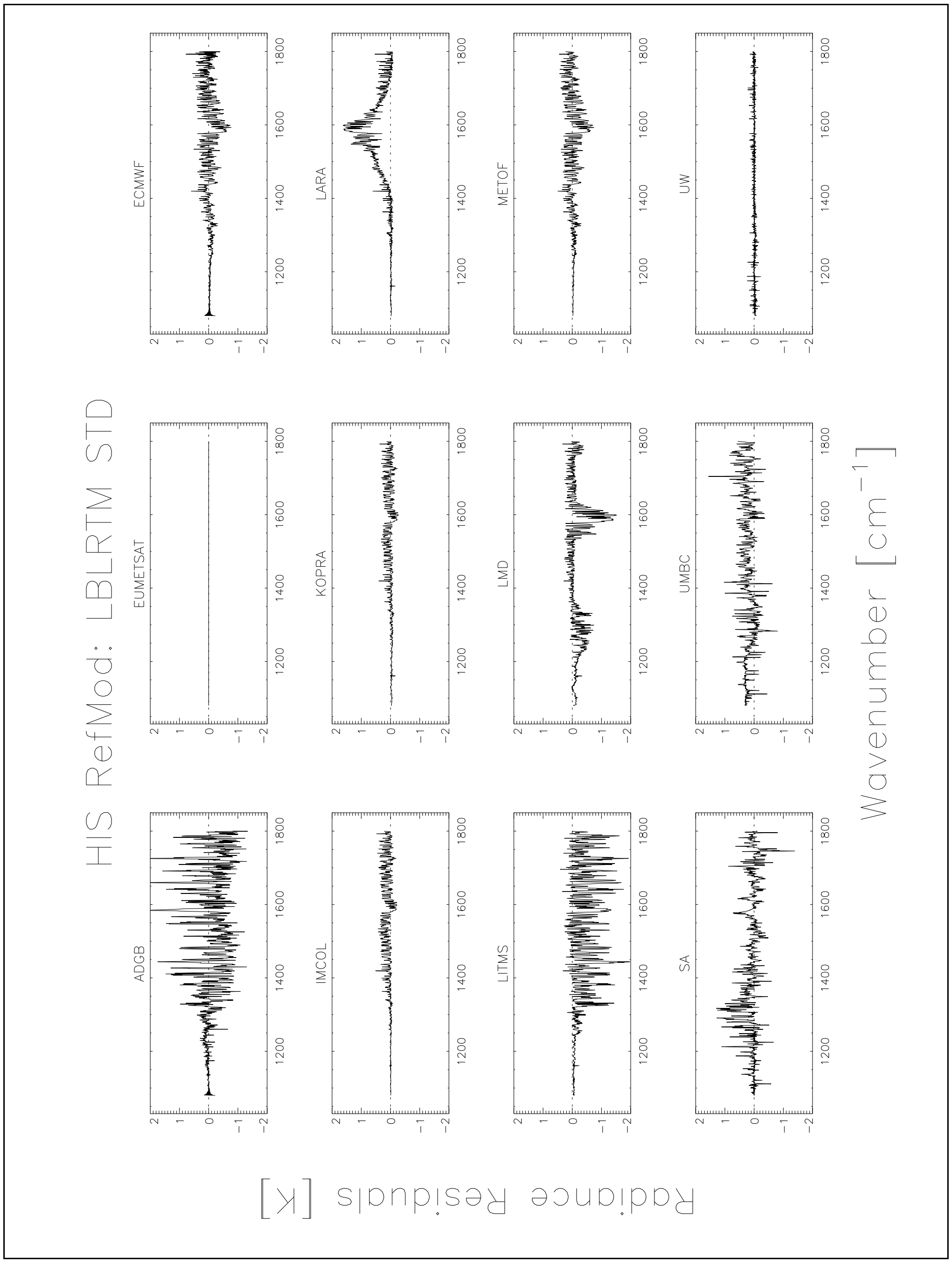

Figure 7.46: Radiance residuals between simulation by a particular submission as indicated by the title above each panel, and the LBLRTM model in HIS band 2. Only the results in the optical filter range of HIS band 2 between 1080 - 1800 cm^{-1} are shown.

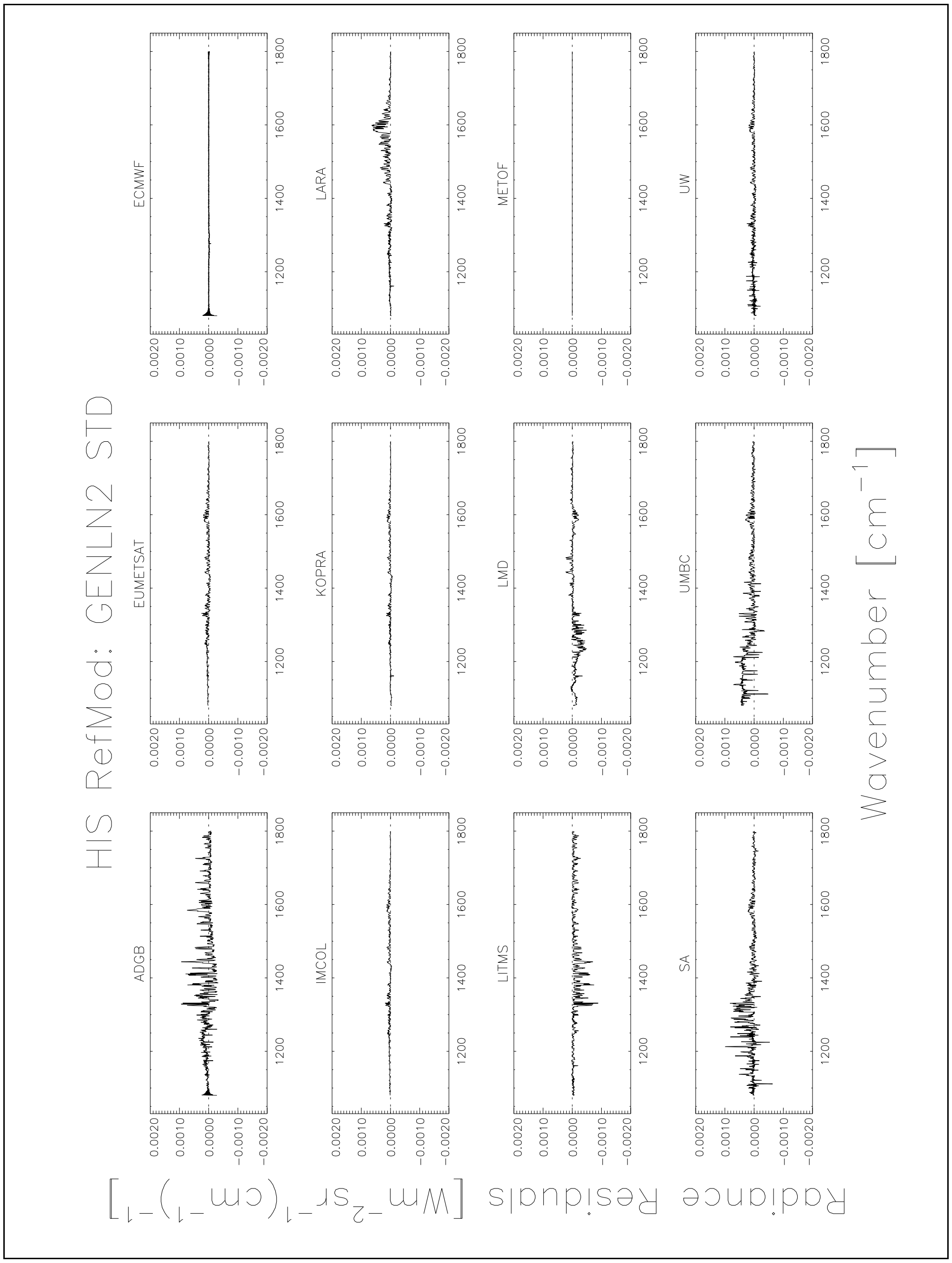

Figure 7.47: Radiance residuals between simulation by a particular submission as indicated by the title above each panel, and the GENLN2 model in HIS band 2. Only the results in the optical filter range of HIS band 2 between 1080 - 1800 cm^{-1} are shown.

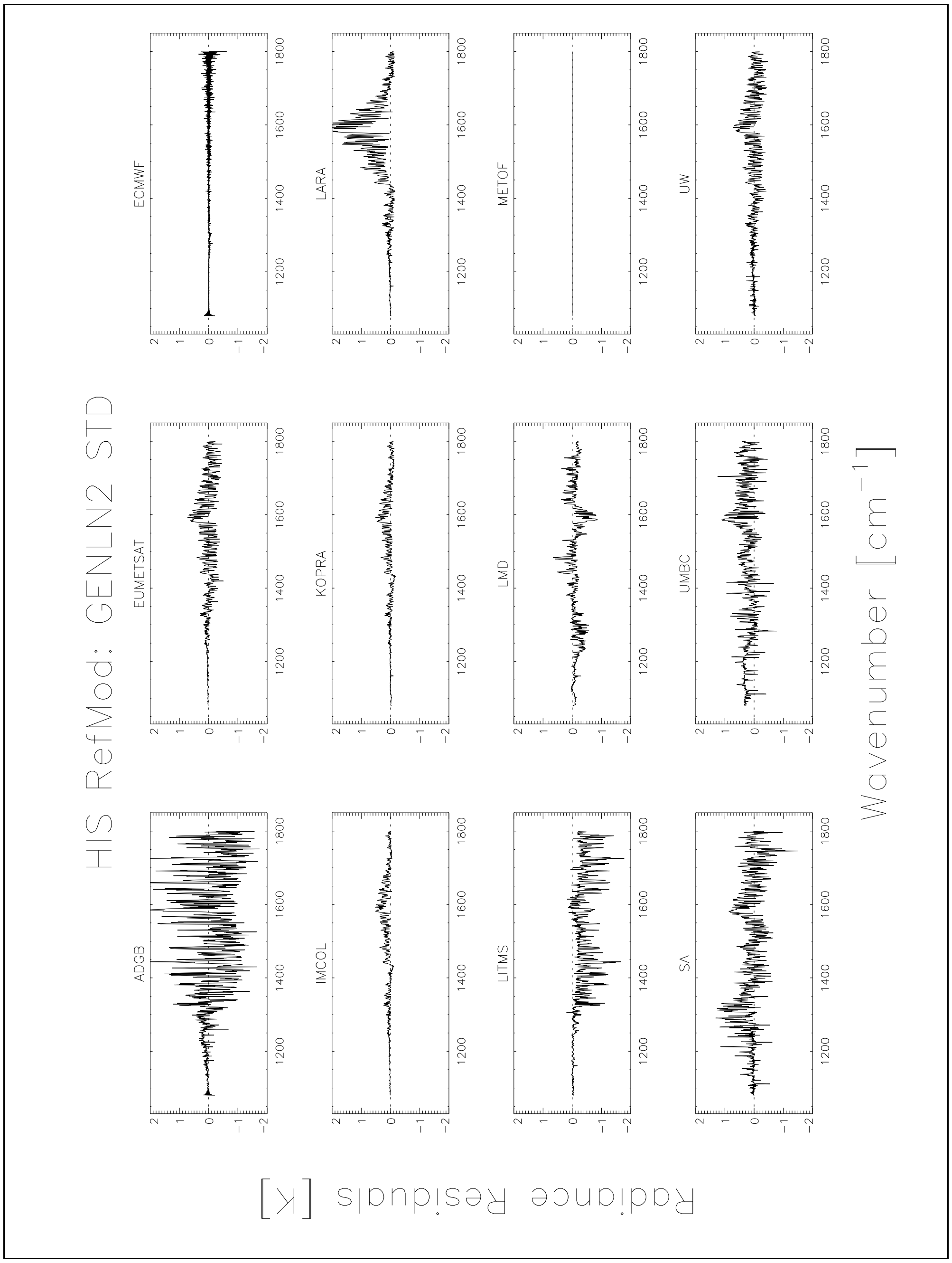

Figure 7.48: Radiance residuals between simulation by a particular submission as indicated by the title above each panel, and the GENLN2 model in HIS band 2. Only the results in the optical filter range of HIS band 2 between 1080 - 1800 cm^{-1} are shown.

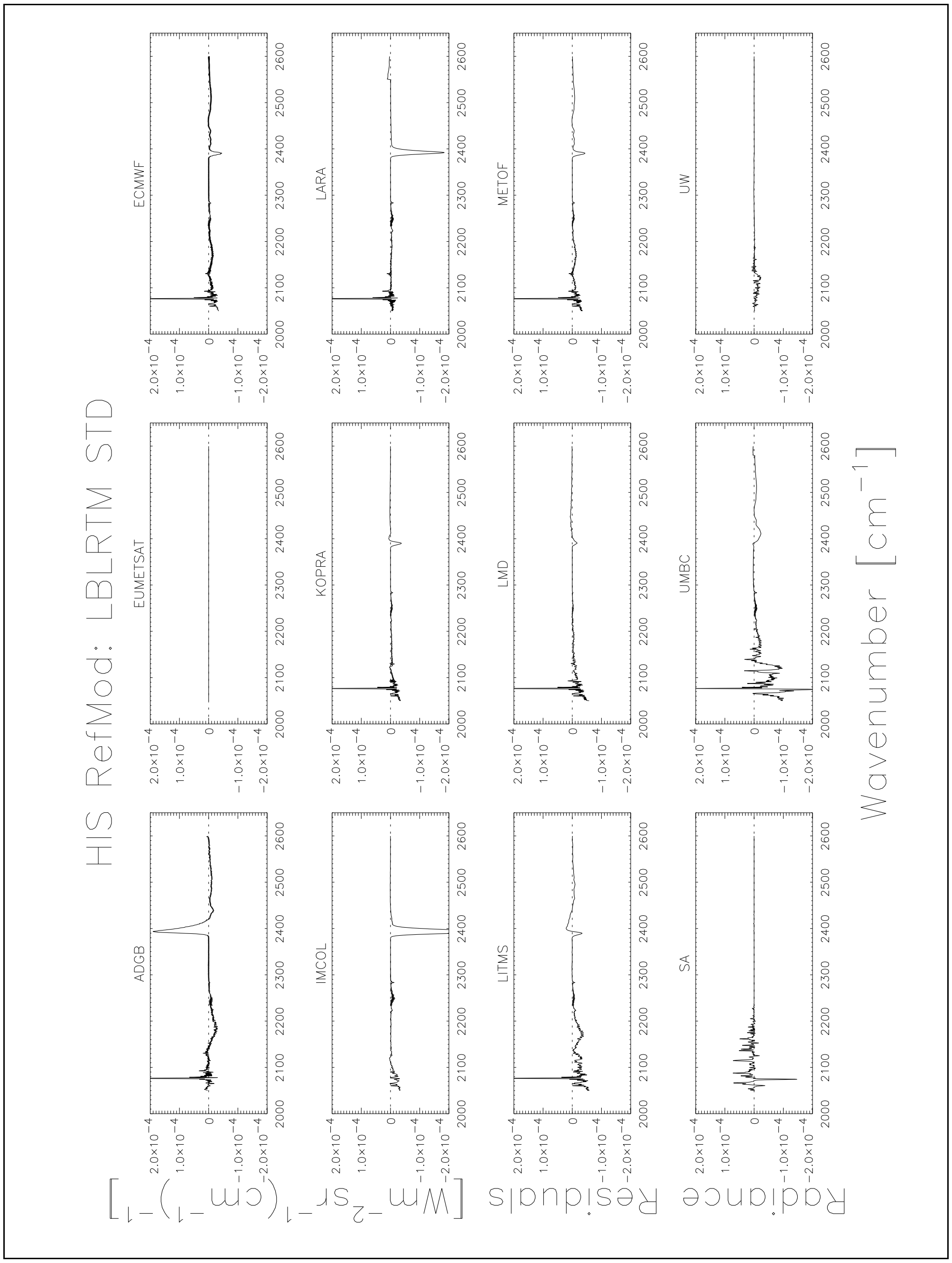

Figure 7.49: Radiance residuals between simulation by a particular submission as indicated by the title above each panel, and the LBLRTM model in HIS band 3. Only the results in the optical filter range of HIS band 3 between 2050 - 2600 cm^{-1} are shown.

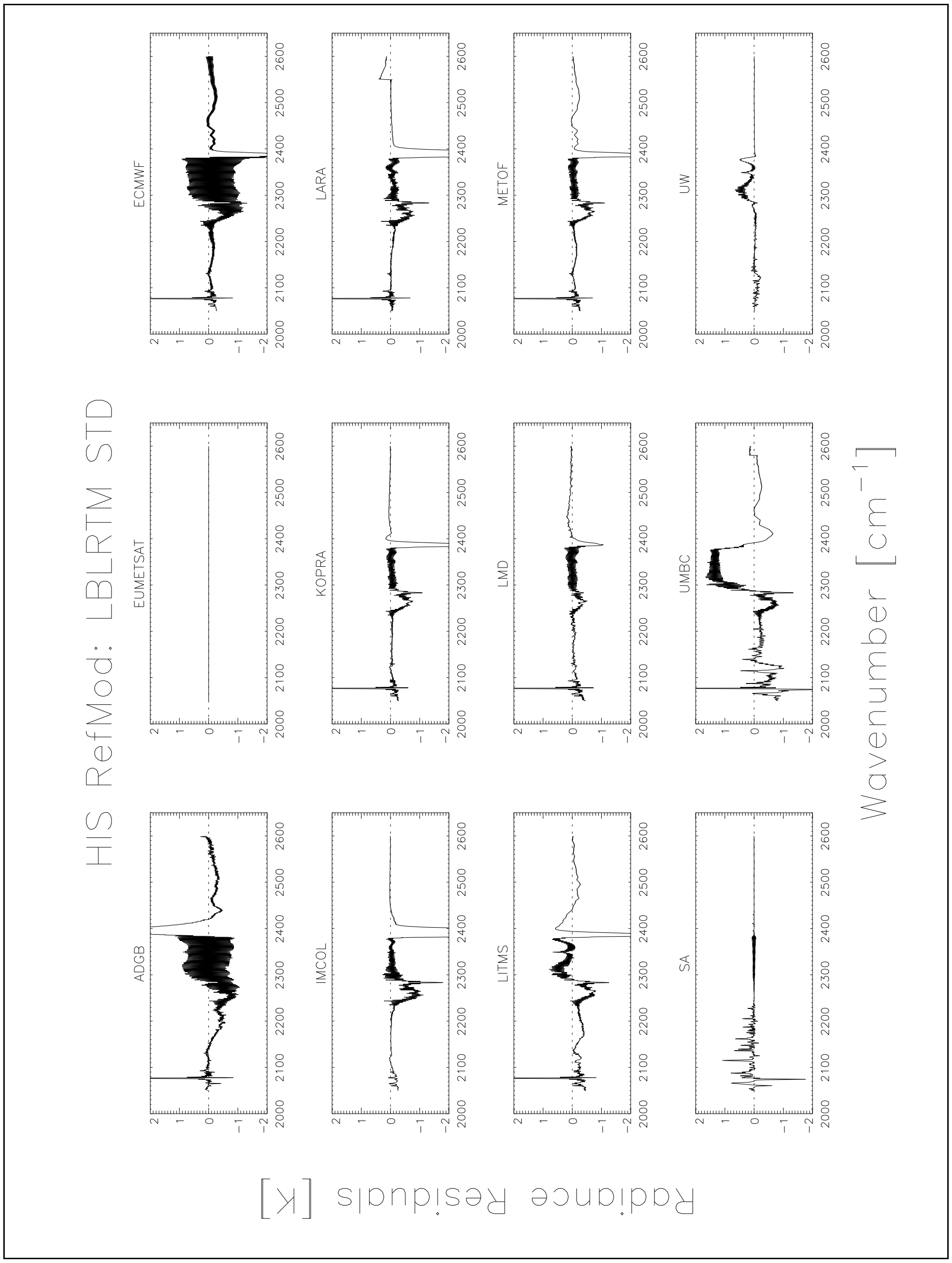

Figure 7.50: Radiance residuals between simulation by a particular submission as indicated by the title above each panel, and the LBLRTM model in HIS band 3. Only the results in the optical filter range of HIS band 3 between 2050 - 2600 cm^{-1} are shown.

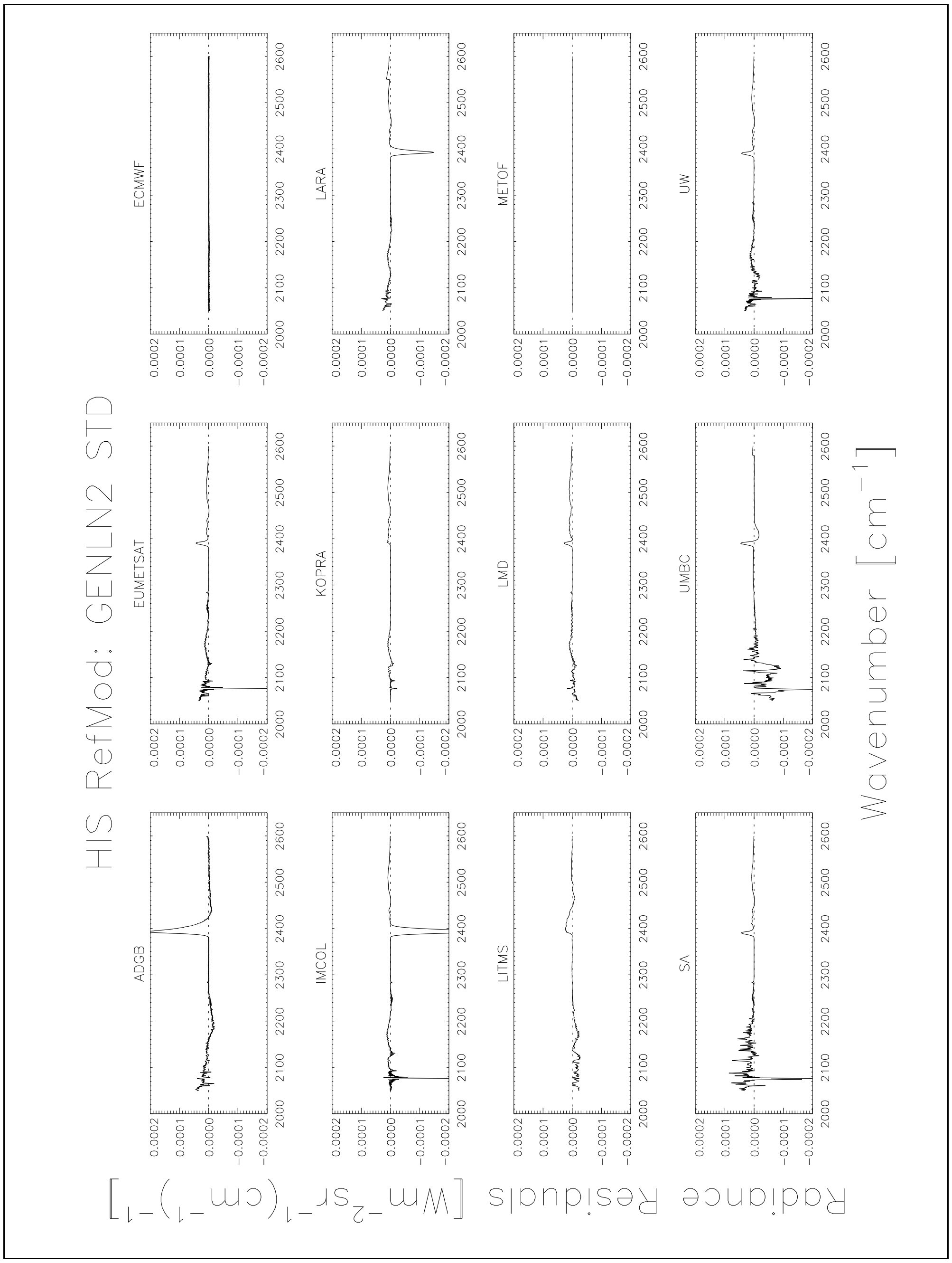

Figure 7.51: Radiance residuals between simulation by a particular submission as indicated by the title above each panel, and the GENLN2 model in HIS band 3. Only the results in the optical filter range of HIS band 3 between 2050 - 2600 cm^{-1} are shown.

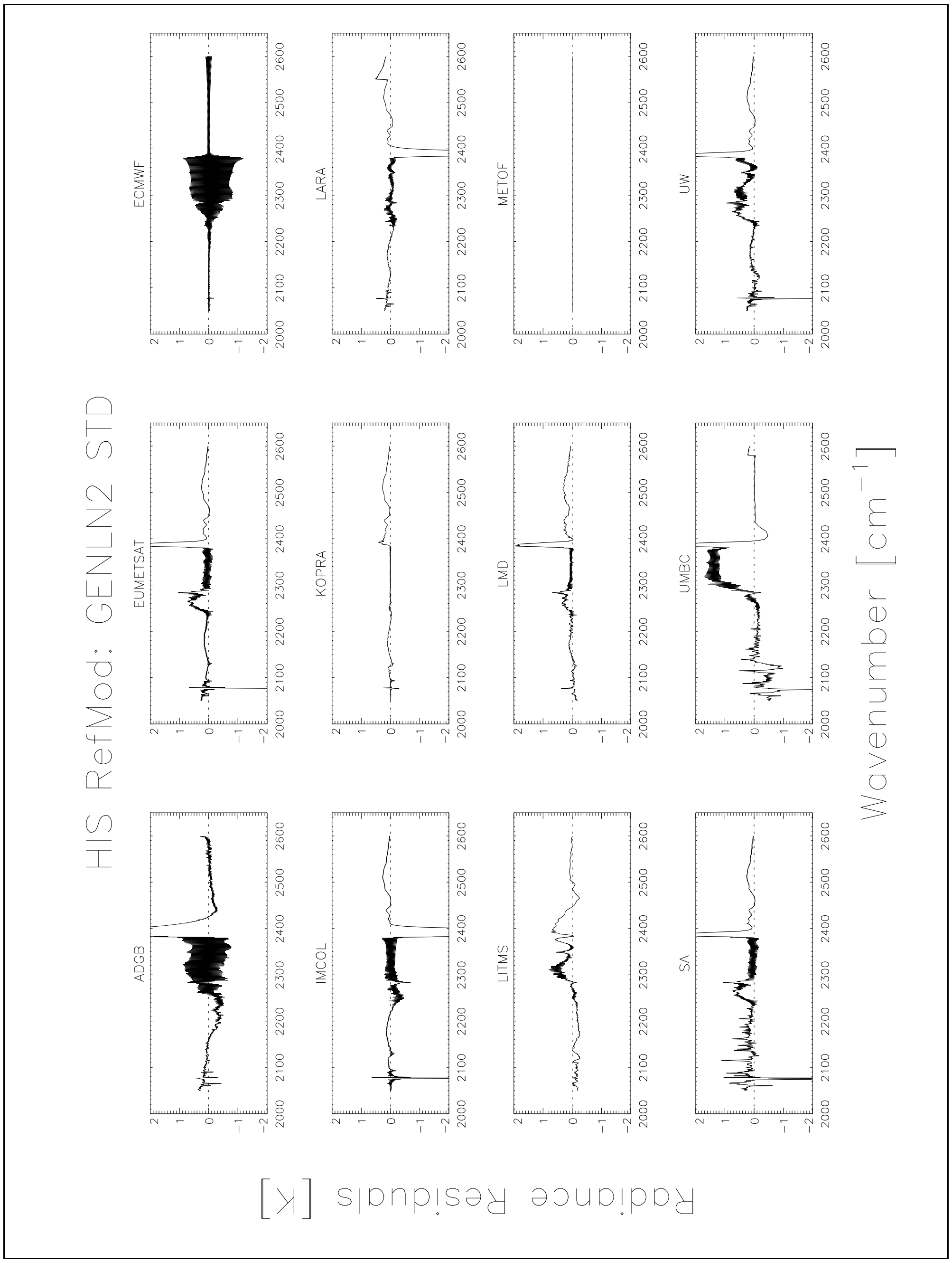

Figure 7.52: Radiance residuals between simulation by a particular submission as indicated by the title above each panel, and the GENLN2 model in HIS band 3. Only the results in the optical filter range of HIS band 3 between 2050 - 2600 cm^{-1} are shown.

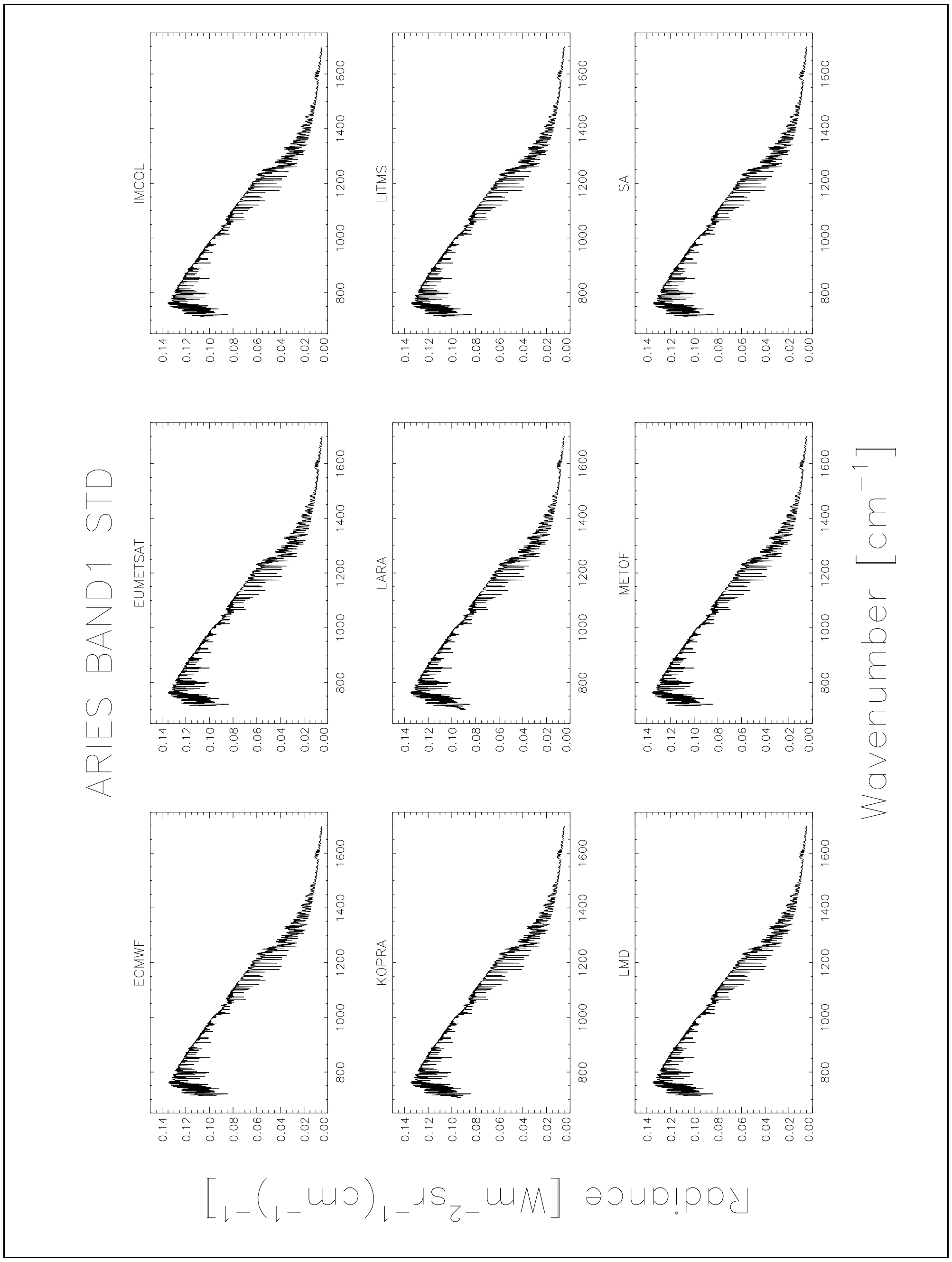

Figure 7.53: Radiance in ARIES band 1 for the particular submission indicated by the title above each panel.

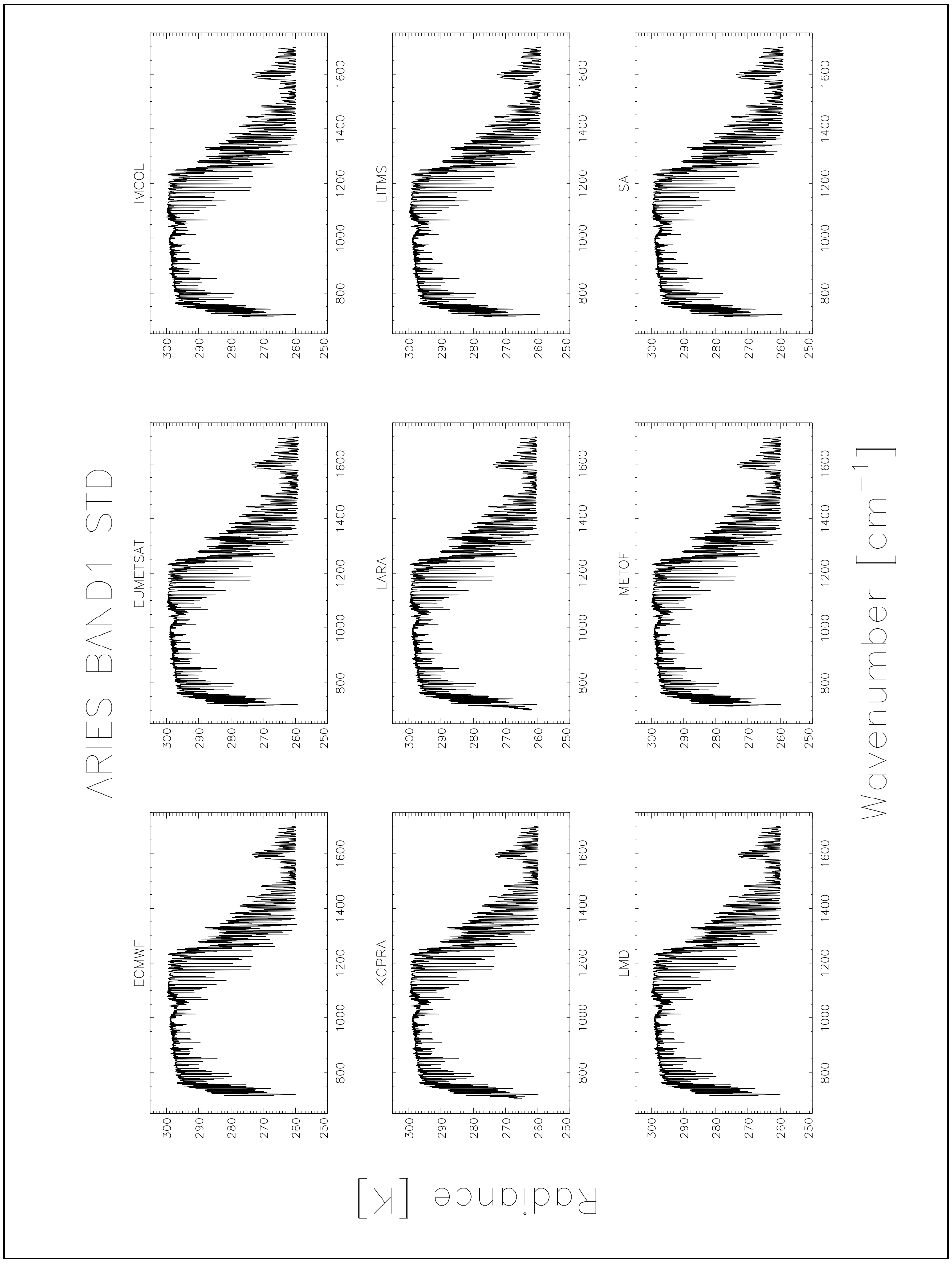

Figure 7.54: Radiance in ARIES band 1 for the particular submission indicated by the title above each panel. Note that the radiances are converted into equivalent brightness temperatures using the inverse of the Planck-function.

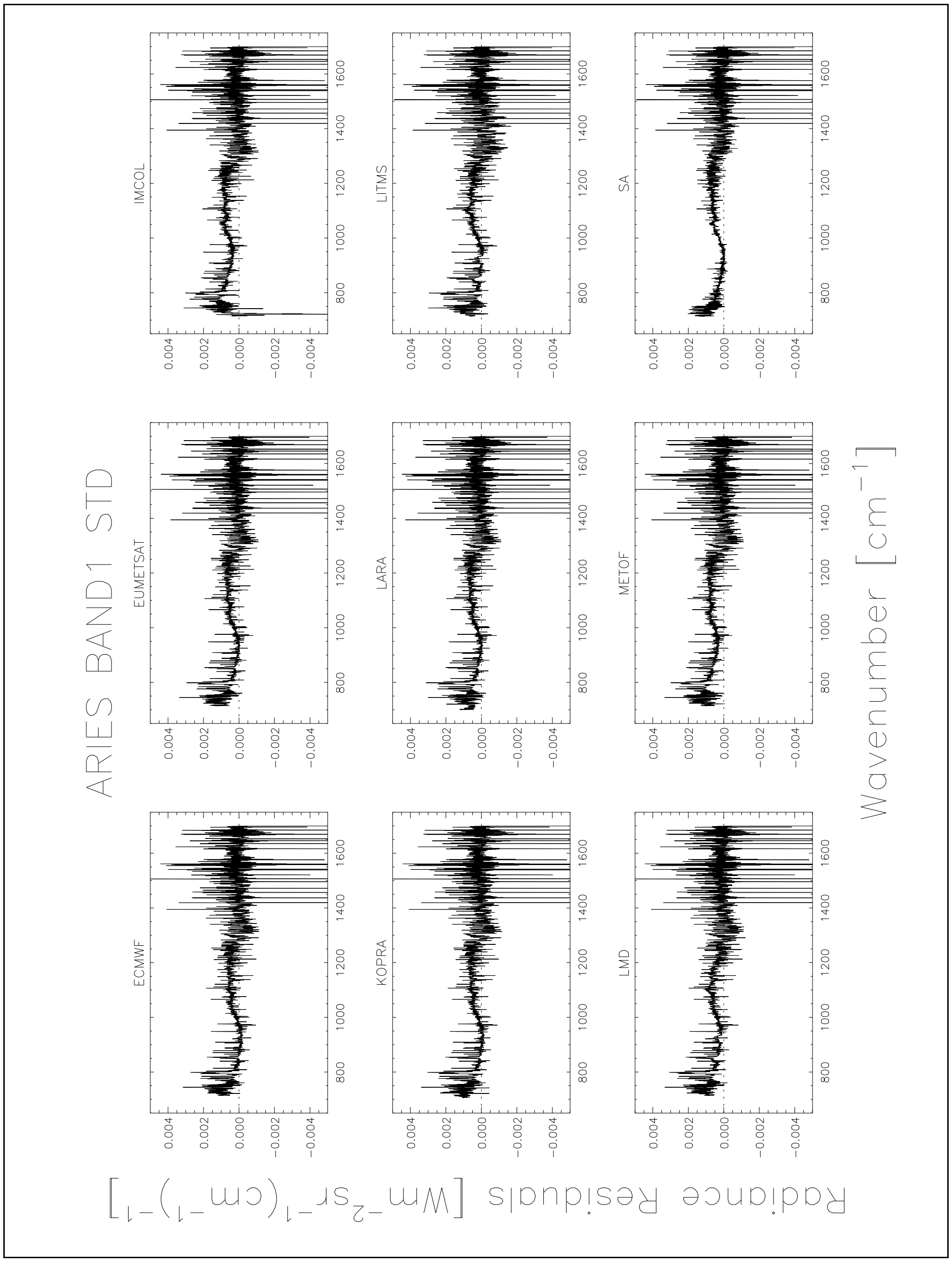

Figure 7.55: Radiance residuals between calculated and observed radiance in ARIES band 1 for the particular submission indicated by the title above each panel.

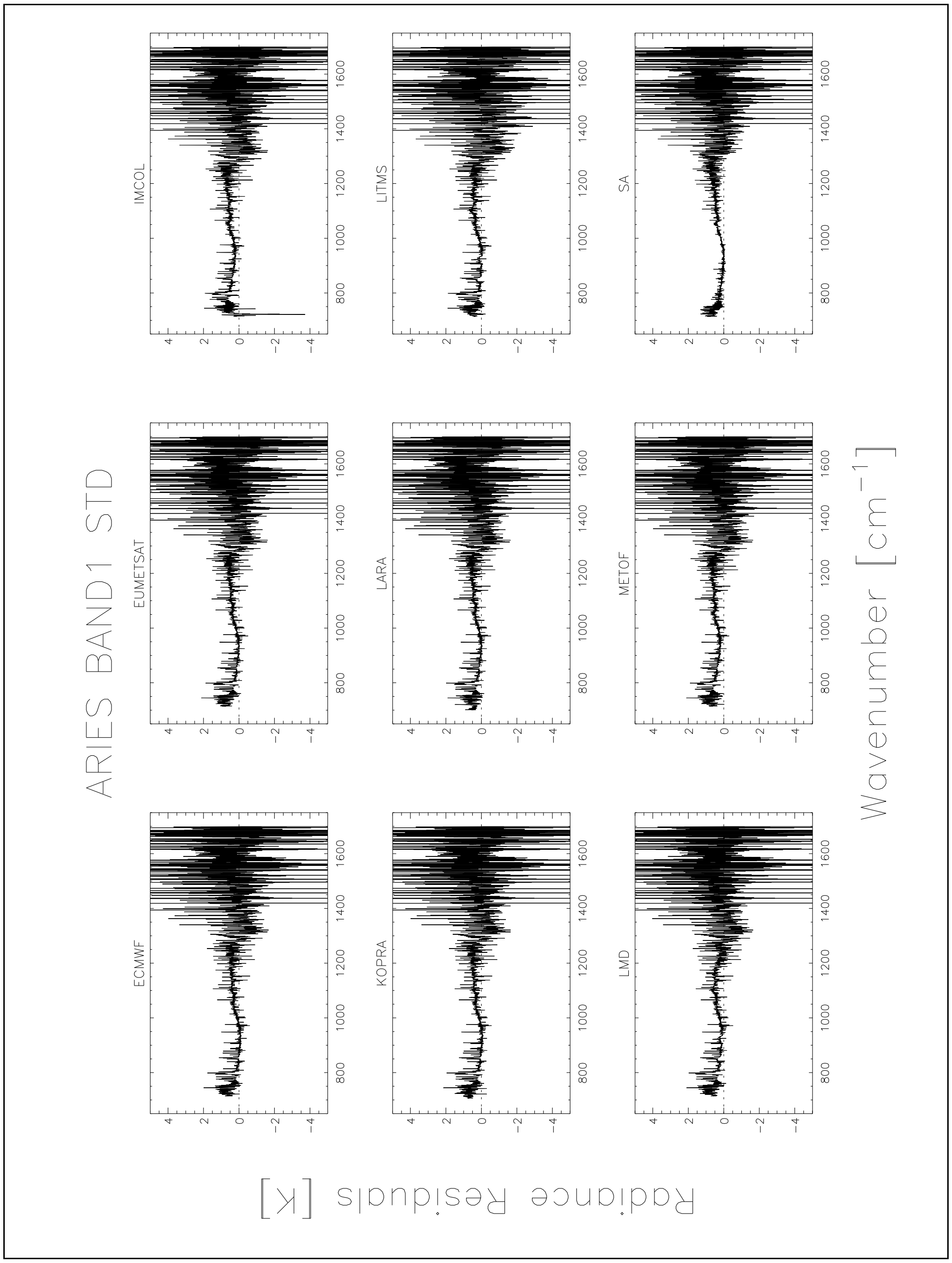

Figure 7.56: Radiance residuals between calculated and observed radiance in ARIES band 1 for the particular submission indicated by the title above each panel. Note that the radiance residuals are converted into noise equivalent brightness temperature, using the equivalent brightness temperatures shown in Figure 7.54.

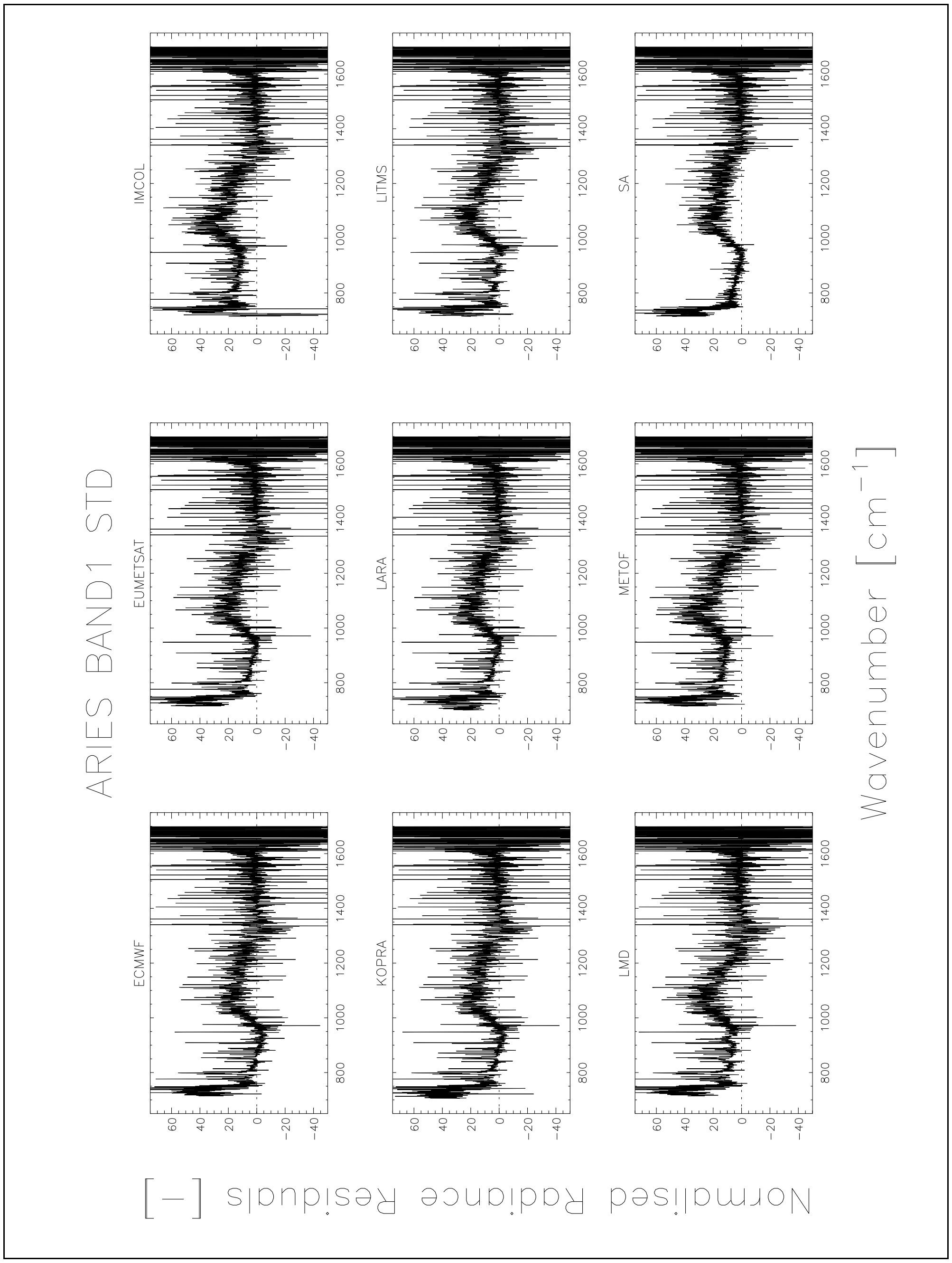

Figure 7.57: Radiance residuals between calculated and observed radiance in ARIES band 1 for the particular submission indicated by the title above each panel. Note that the radiance residuals are normalised by the uncertainty in the observations.

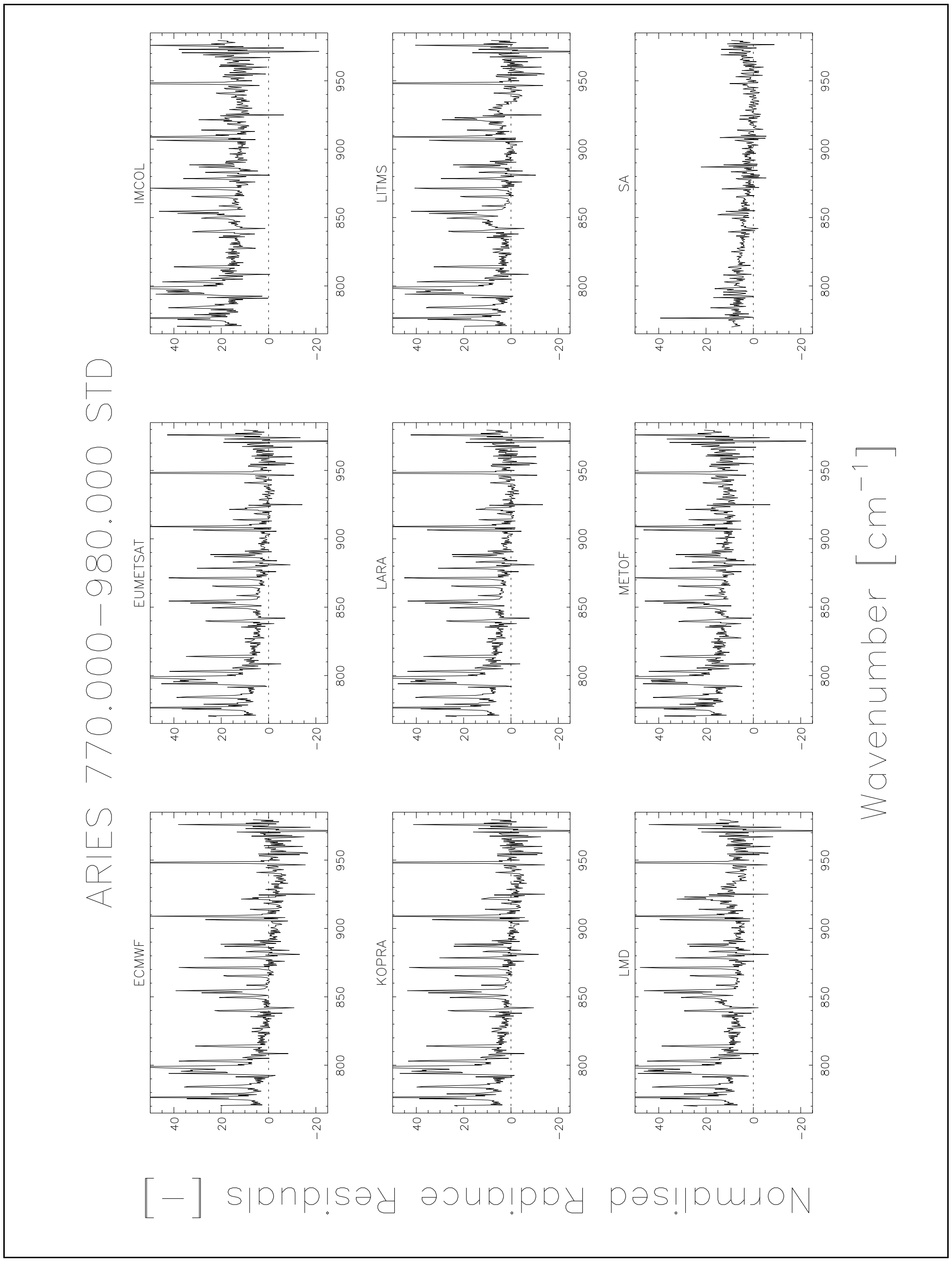

Figure 7.58: Normalised radiance residuals between calculated and observed radiance for the 2nd spectral interval of Table 4.1

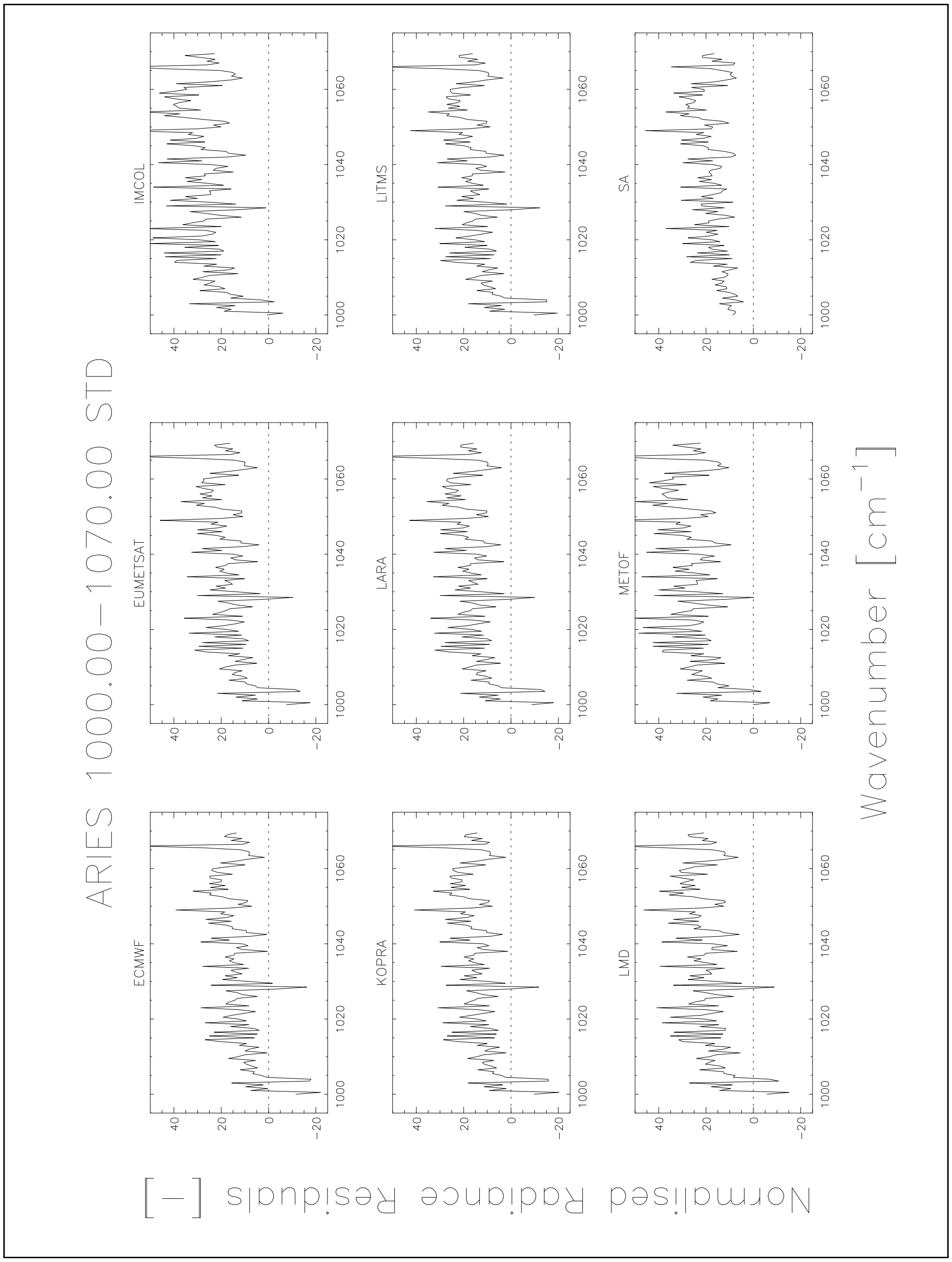

Figure 7.59: Normalised radiance residuals between calculated and observed radiance for the 3th spectral interval of Table 4.1

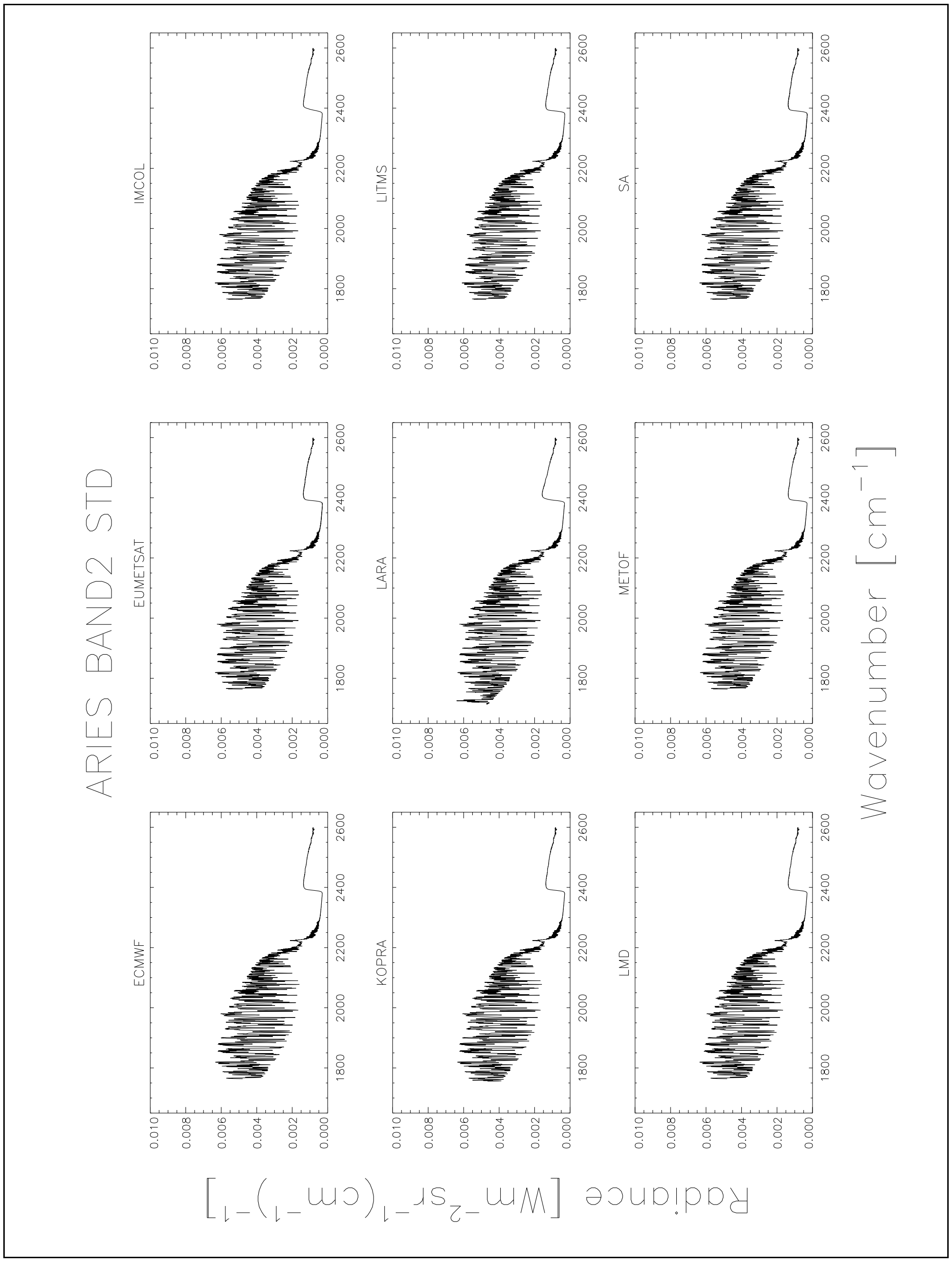

Figure 7.60: Radiance in ARIES band 1 for the particular submission indicated by the title above each panel.

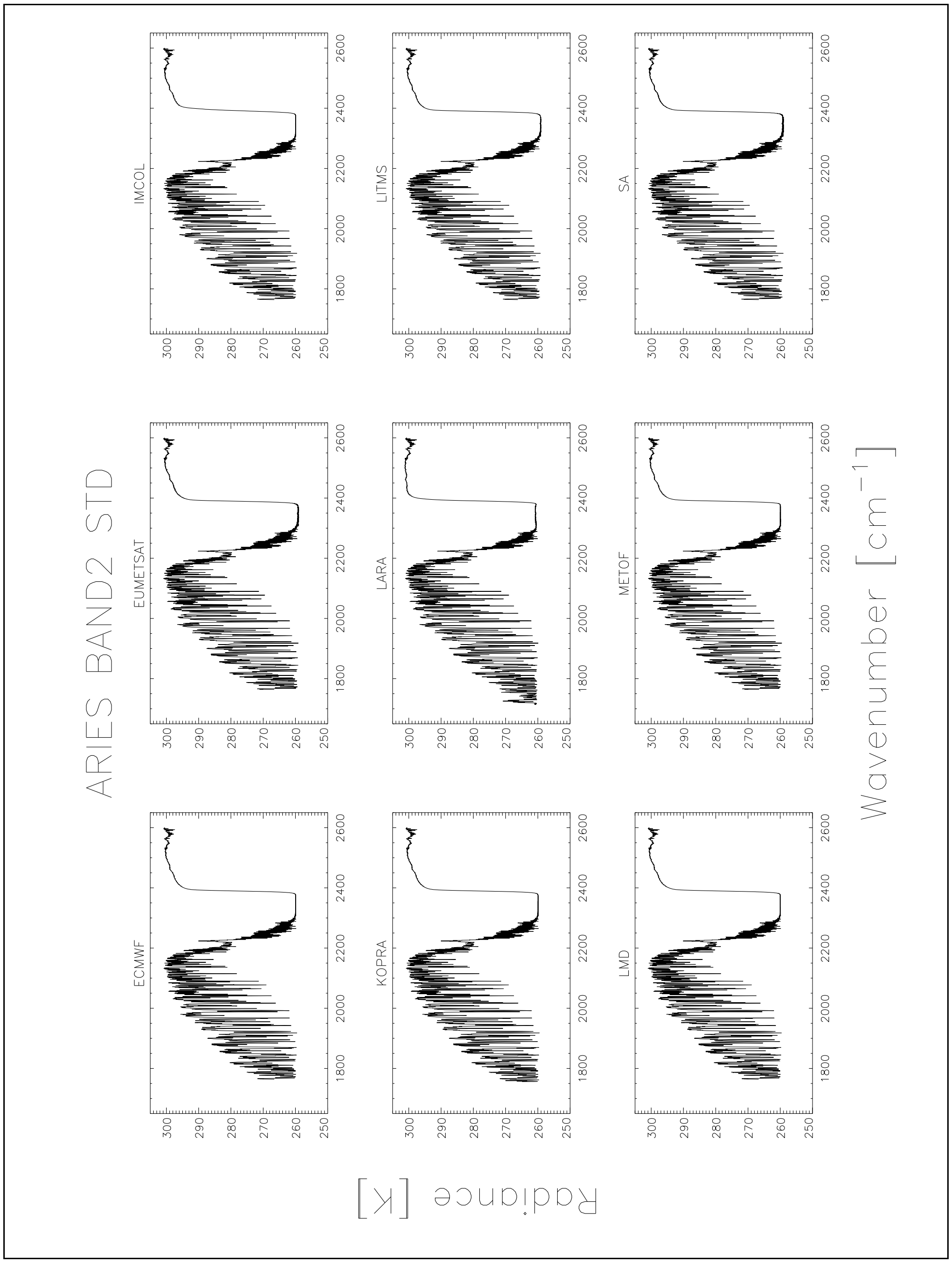

Figure 7.61: Radiance in ARIES band 1 for the particular submission indicated by the title above each panel. Note that the radiances are converted into equivalent brightness temperatures using the inverse of the Planck-function. .

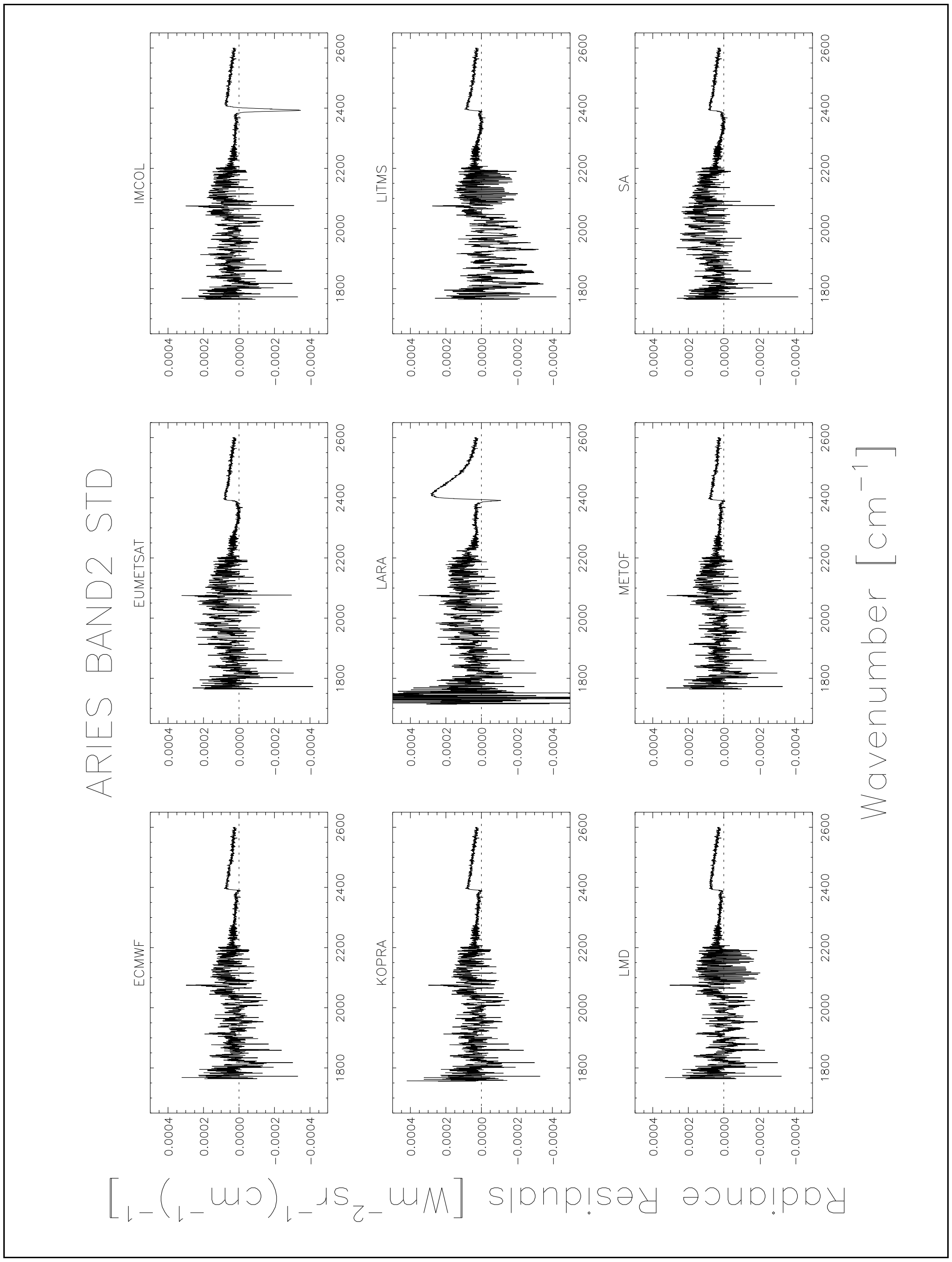

Figure 7.62: Radiance residuals between calculated and observed radiance in ARIES band 2 for the particular submission indicated by the title above each panel.

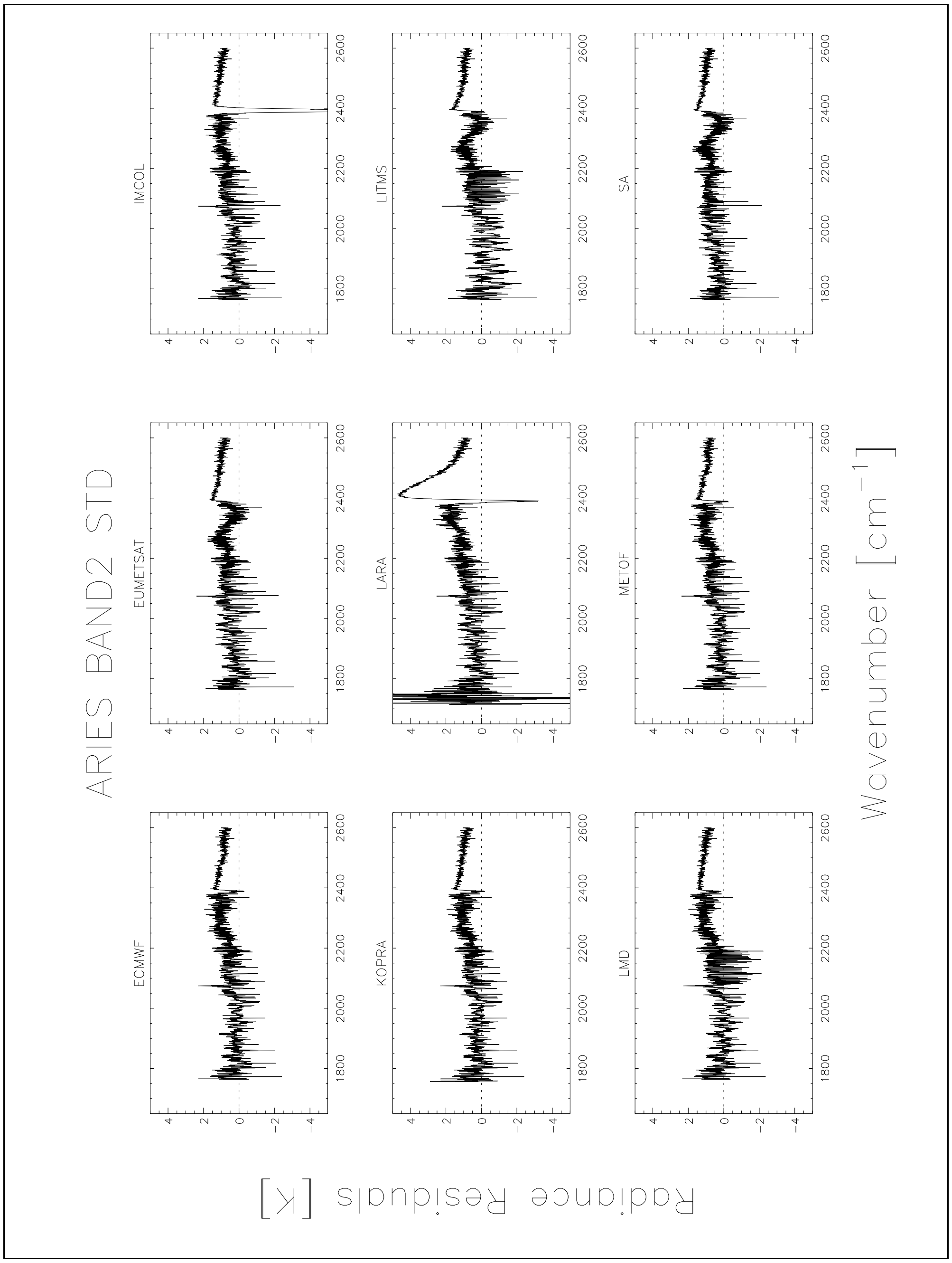

Figure 7.63: Radiance residuals between calculated and observed radiance in ARIES band 2 for the particular submission indicated by the title above each panel. Note that the radiance residuals are converted into noise equivalent brightness temperature, using the equivalent brightness temperatures shown in Figure 7.61.

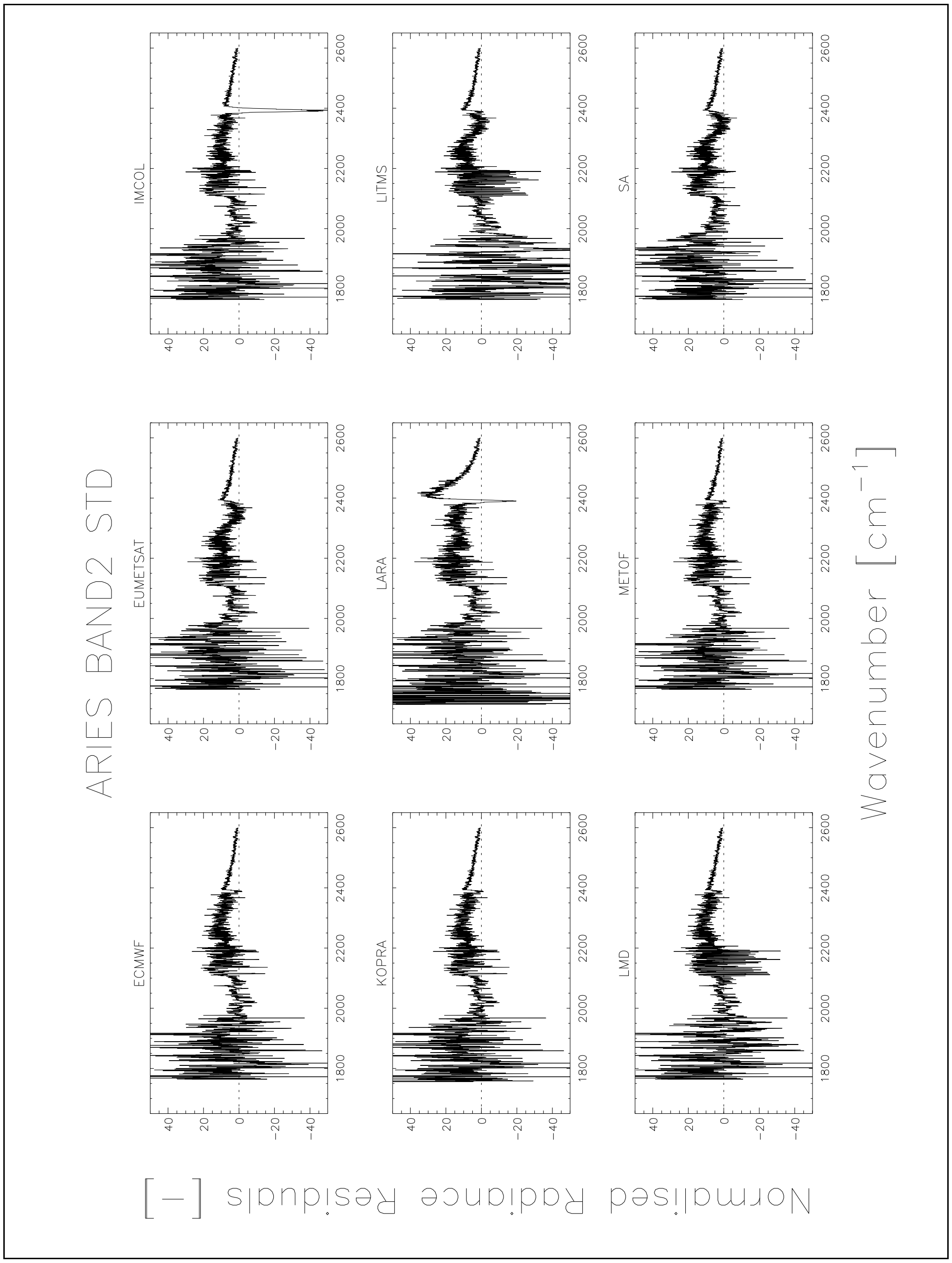

Figure 7.64: Radiance residuals between calculated and observed radiance in ARIES band 2 for the particular submission indicated by the title above each panel. Note that the radiance residuals are normalised by the uncertainty in the observations.

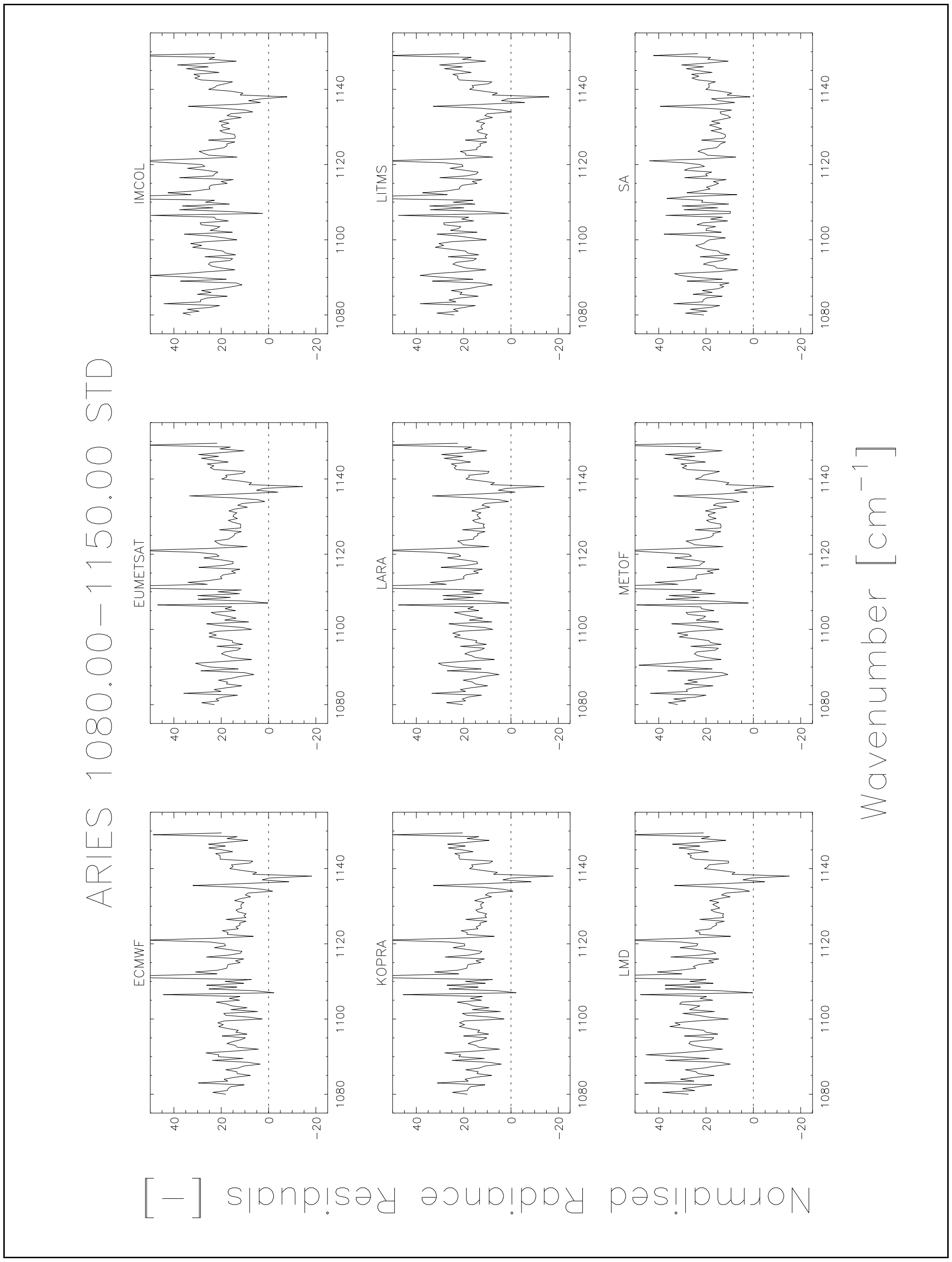

Figure 7.65: Normalised radiance residuals between calculated and observed radiance for the 4th spectral interval of Table 4.1

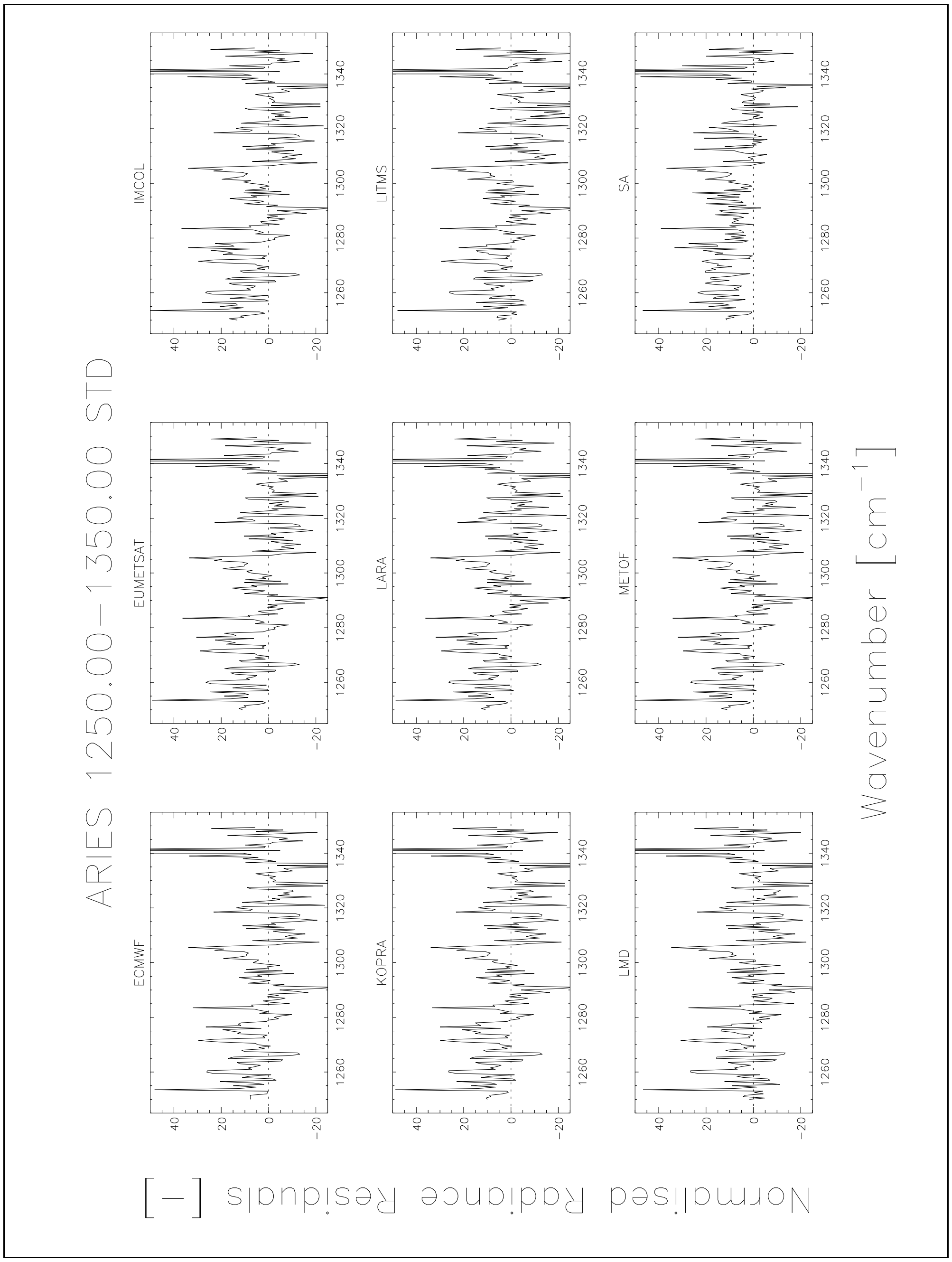

Figure 7.66: Normalised radiance residuals between calculated and observed radiance for the 5th spectral interval of Table 4.1

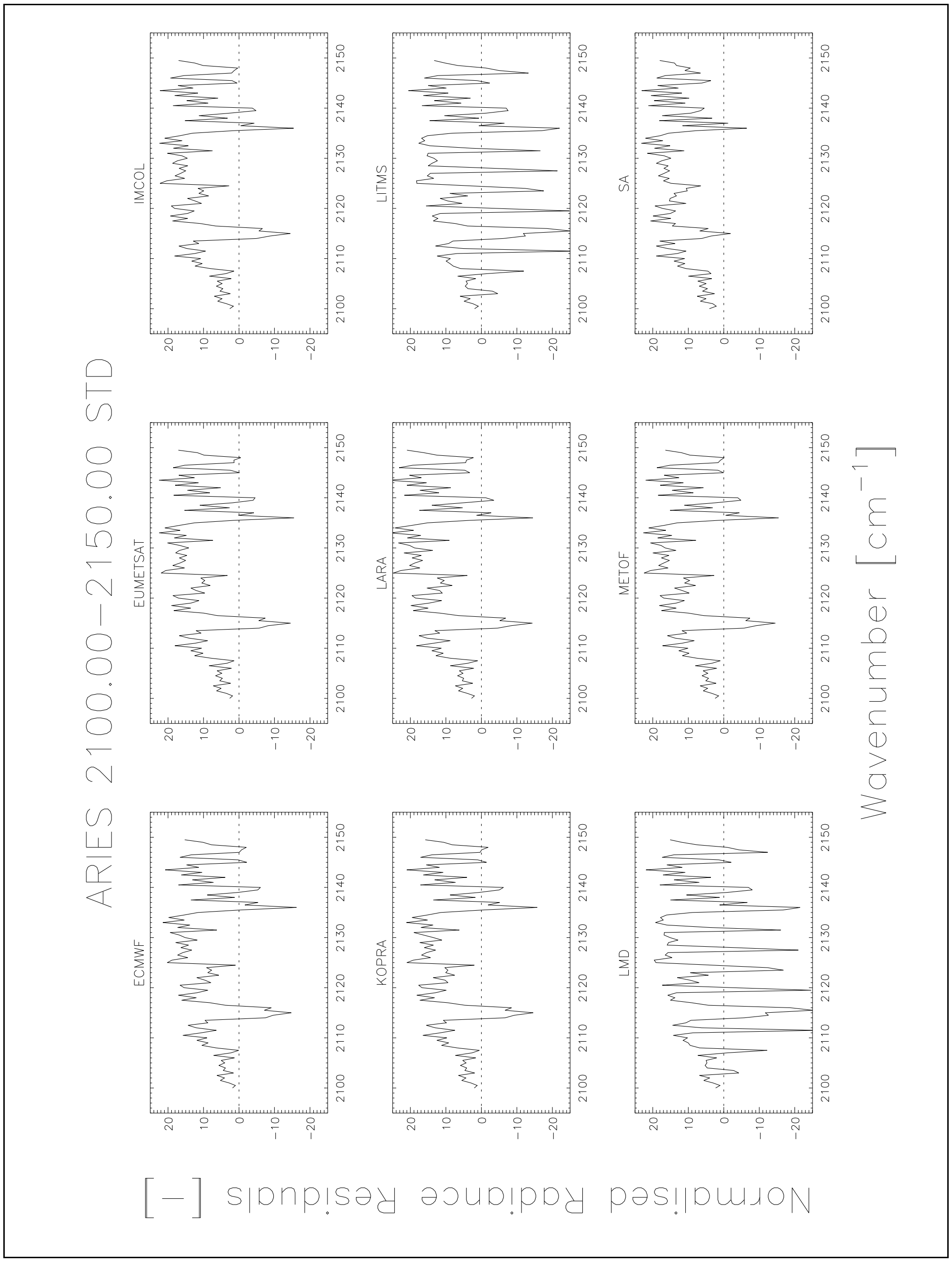

Figure 7.67: Normalised radiance residuals between calculated and observed radiance for the 6th spectral interval of Table 4.1

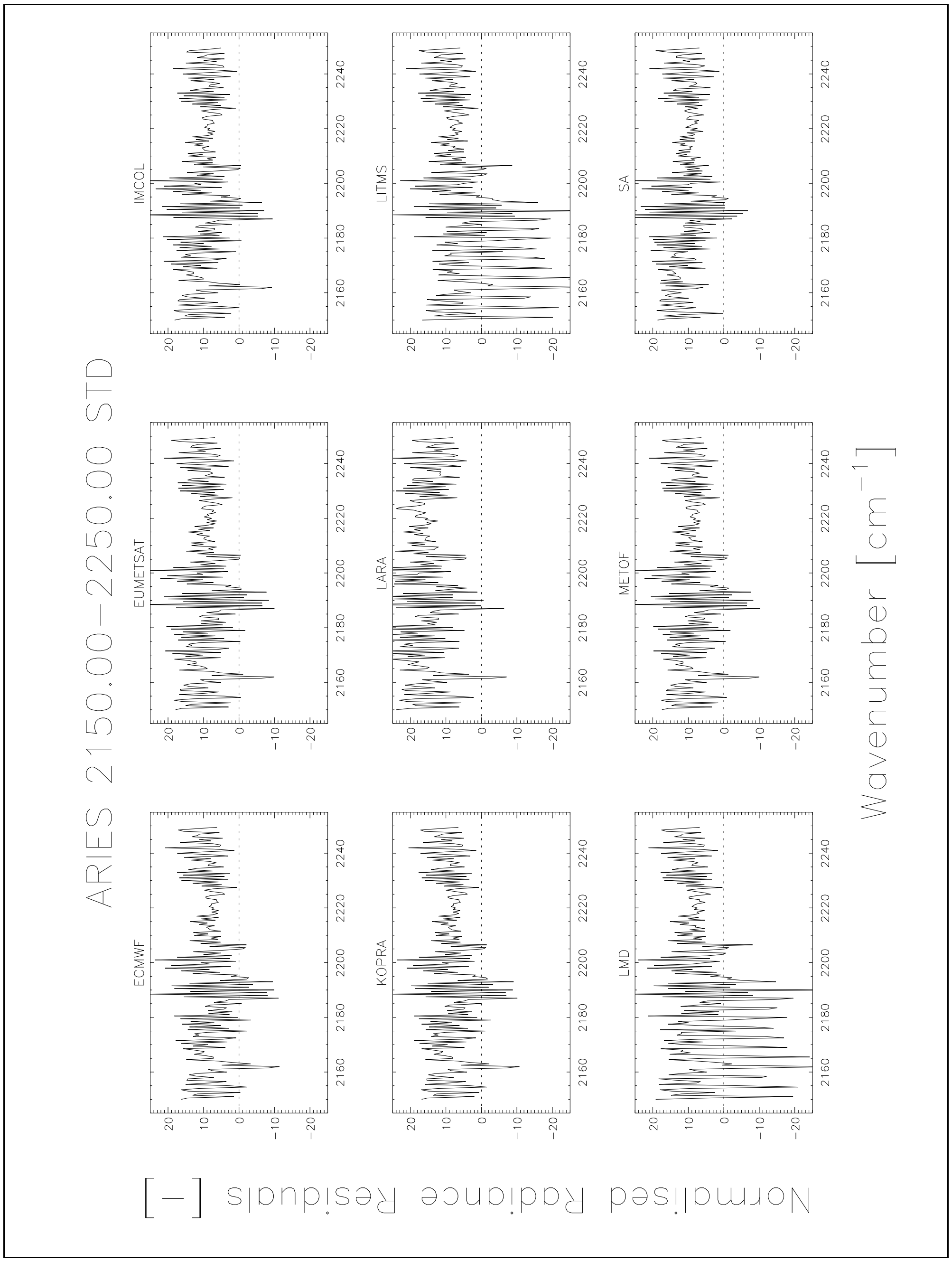

Figure 7.68: Normalised radiance residuals between calculated and observed radiance for the 7th spectral interval of Table 4.1

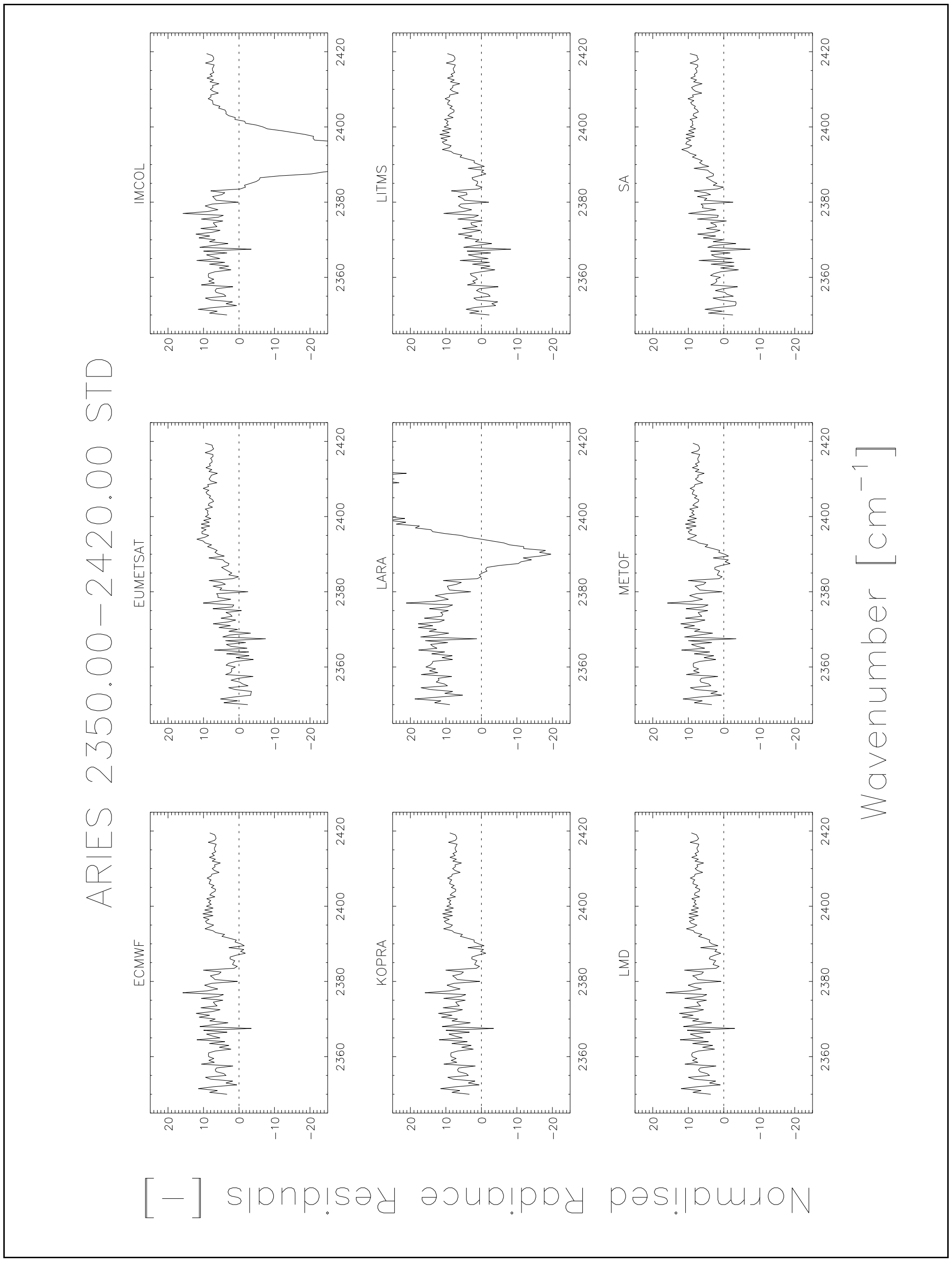

Figure 7.69: Normalised radiance residuals between calculated and observed radiance for the 8th spectral interval of Table 4.1

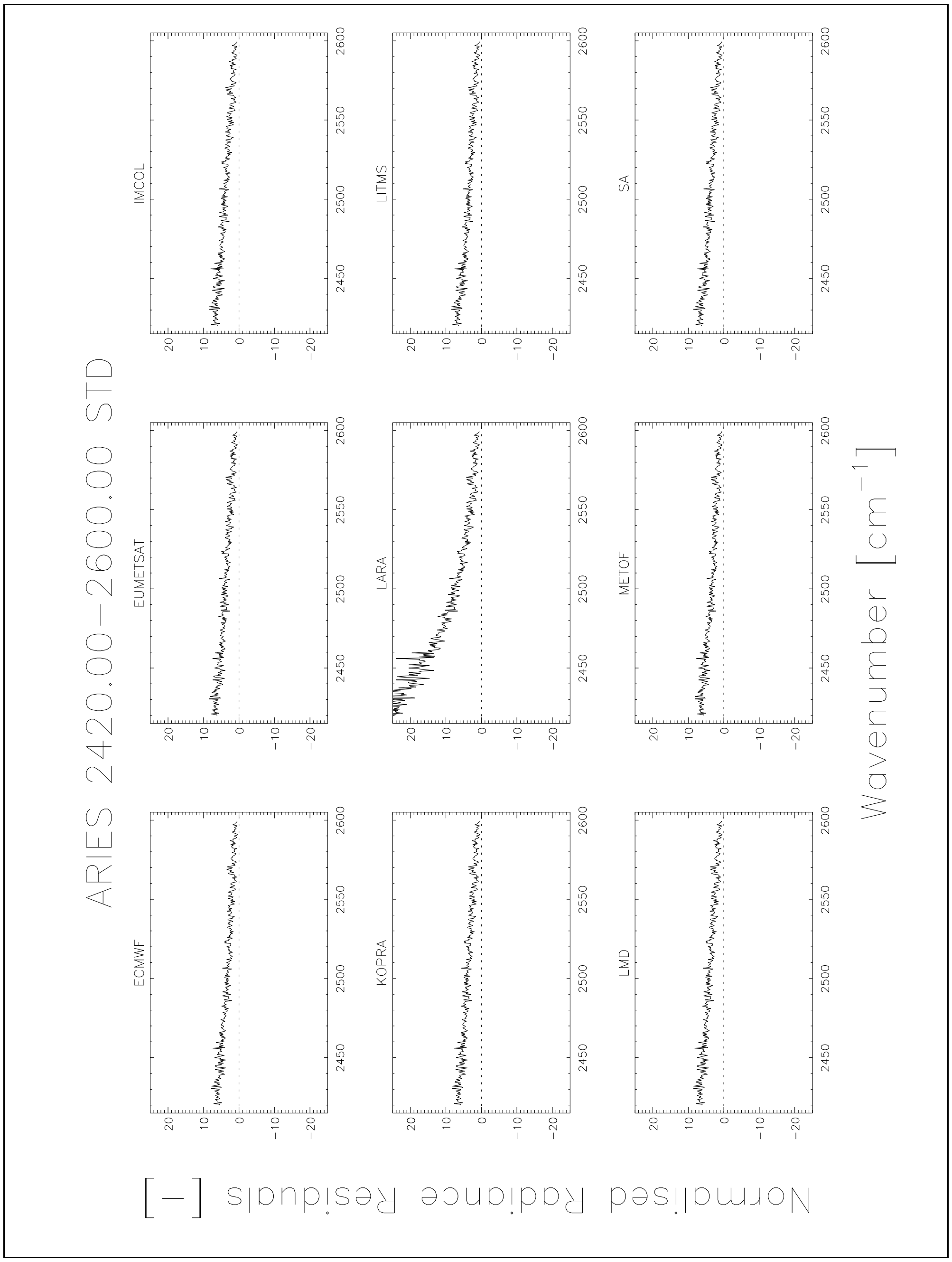

Figure 7.70: Normalised radiance residuals between calculated and observed radiance for the 9th spectral interval of Table 4.1

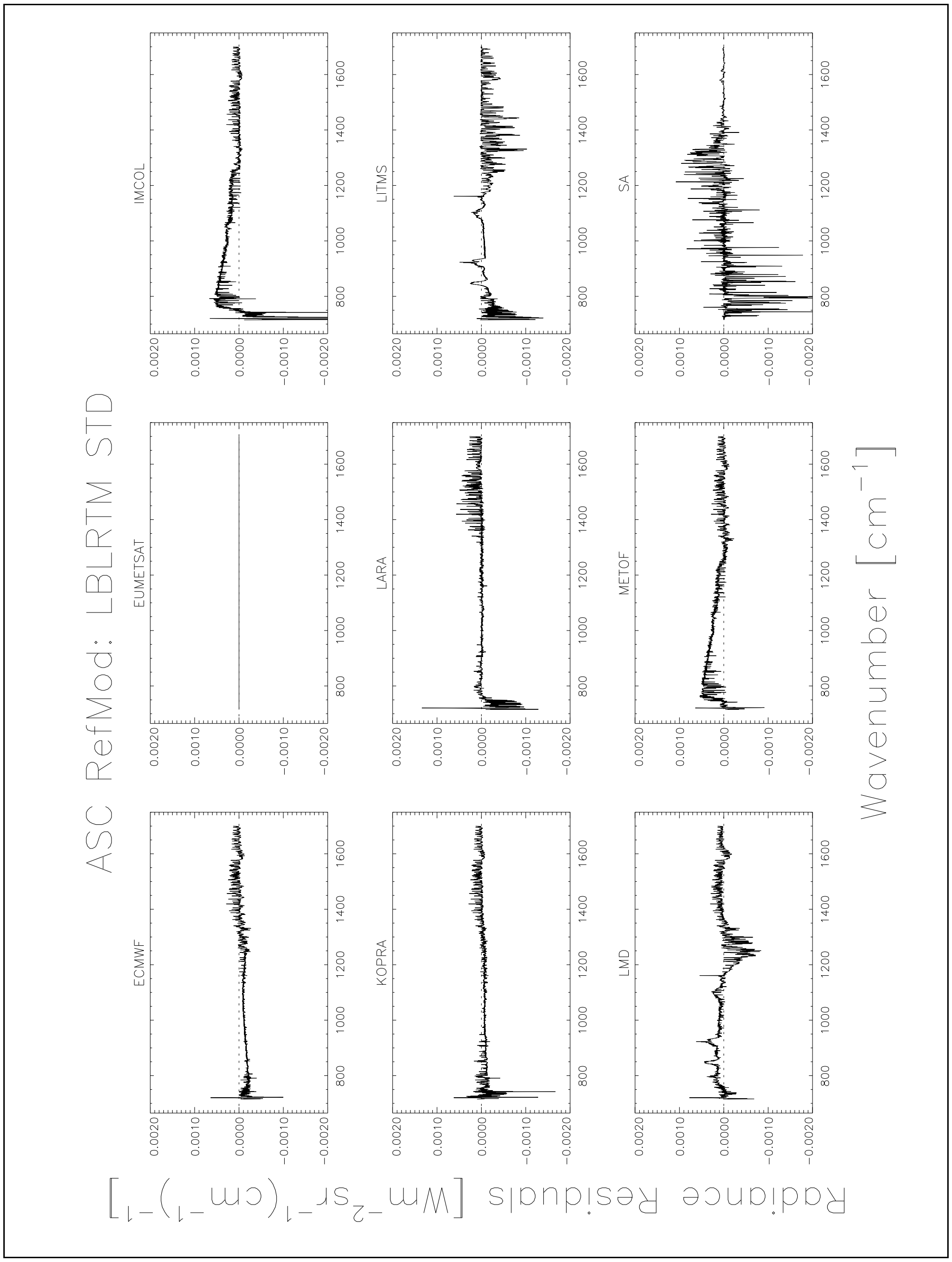

Figure 7.71: Radiance residuals between simulation by a particular submission as indicated by the title above each panel, and the LBLRTM model in ARIES band 1.

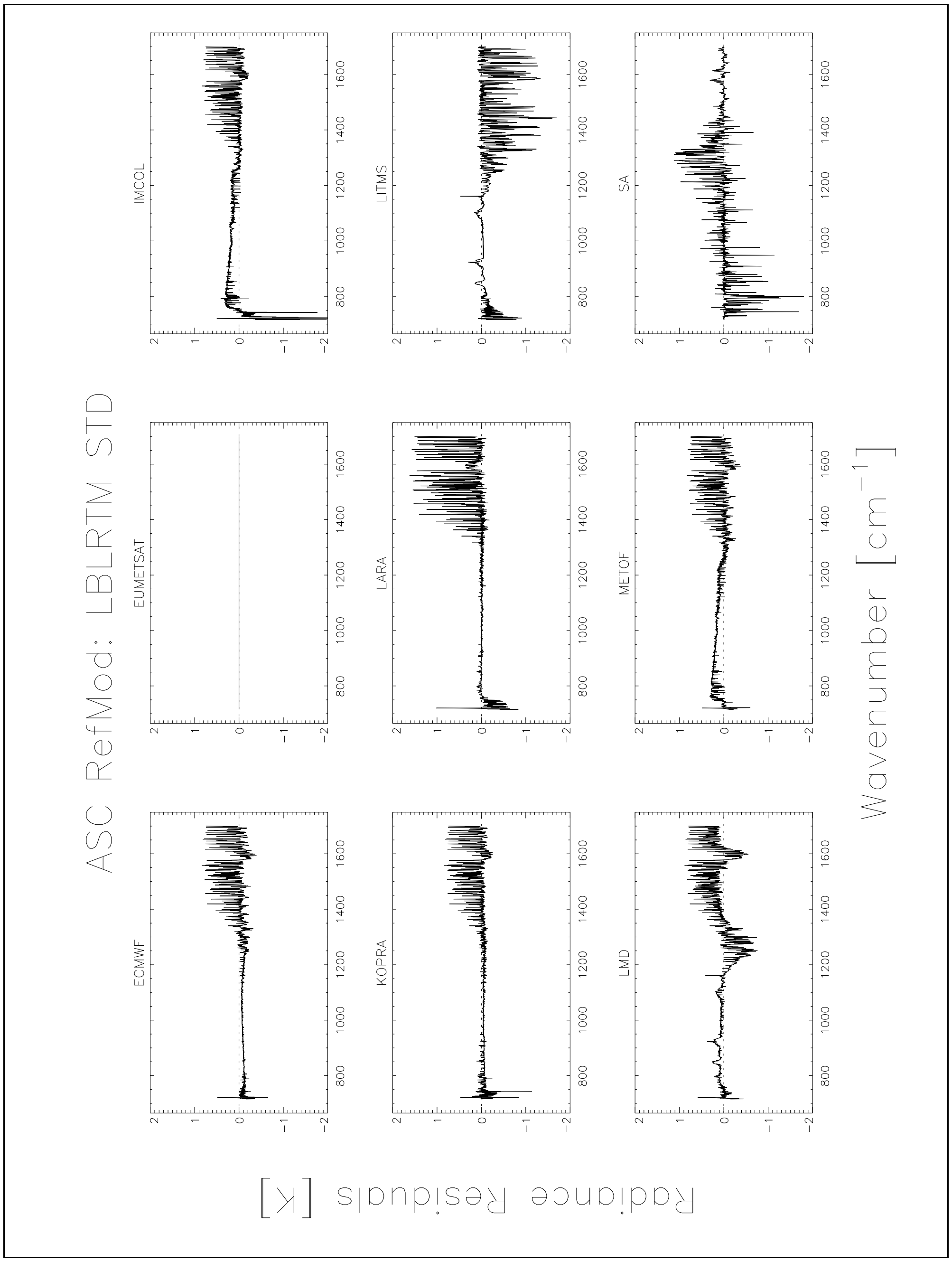

Figure 7.72: Radiance residuals between simulation by a particular submission as indicated by the title above each panel, and the LBLRTM model in ARIES band 1.

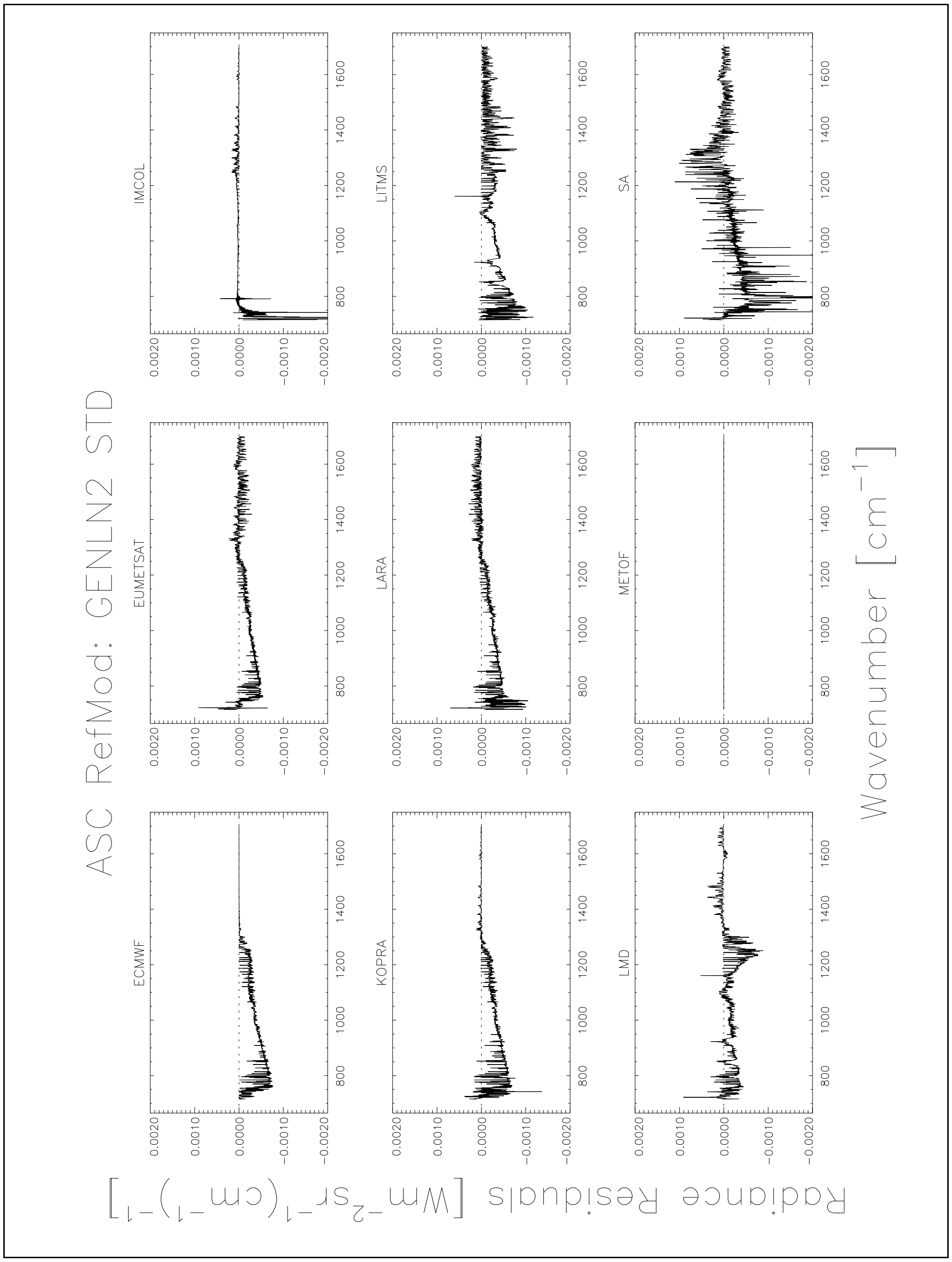

Figure 7.73: Radiance residuals between simulation by a particular submission as indicated by the title above each panel, and the GENLN2 model in ARIES band 1.

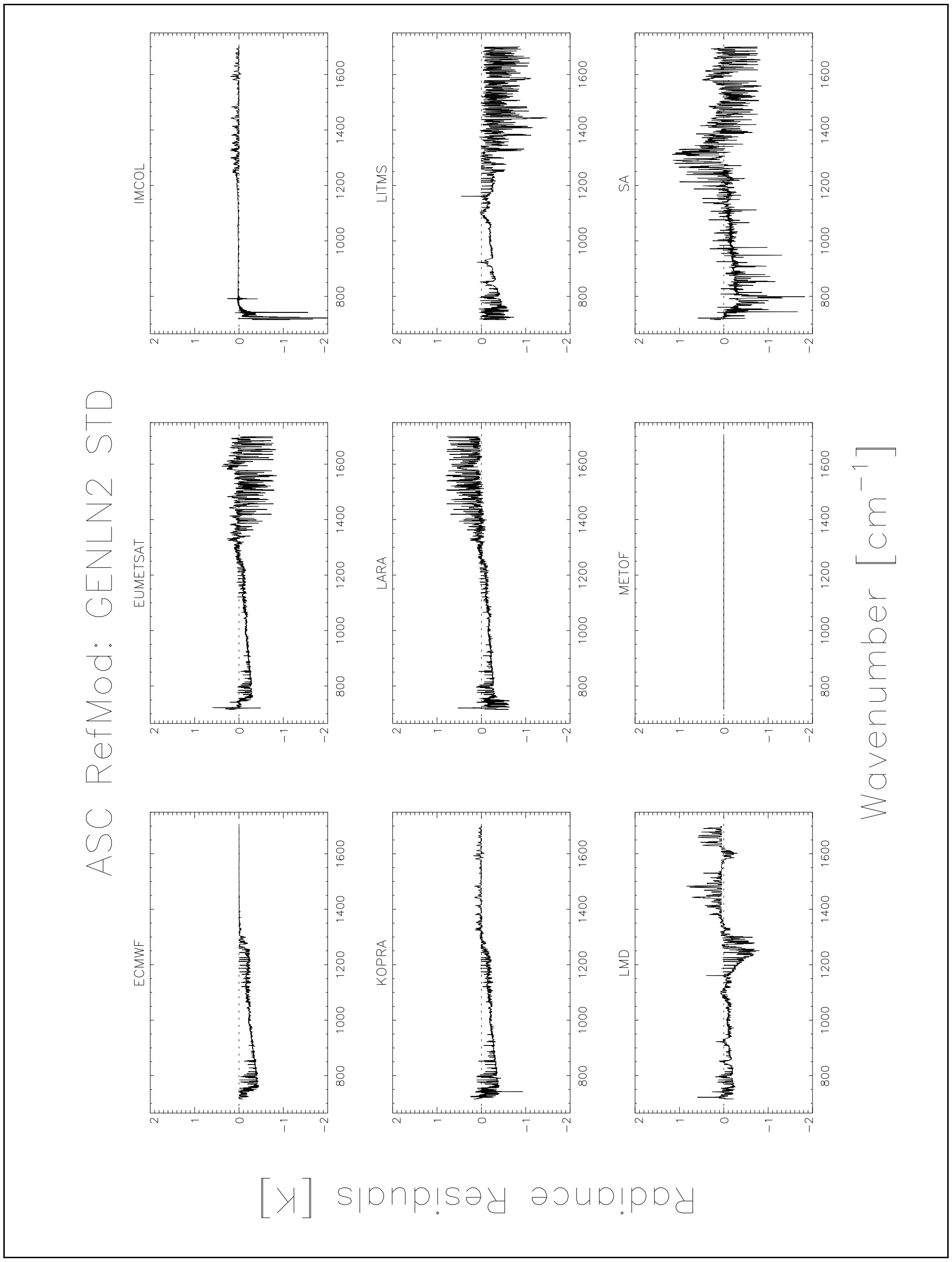

Figure 7.74: Radiance residuals between simulation by a particular submission as indicated by the title above each panel, and the GENLN2 model in ARIES band 1.

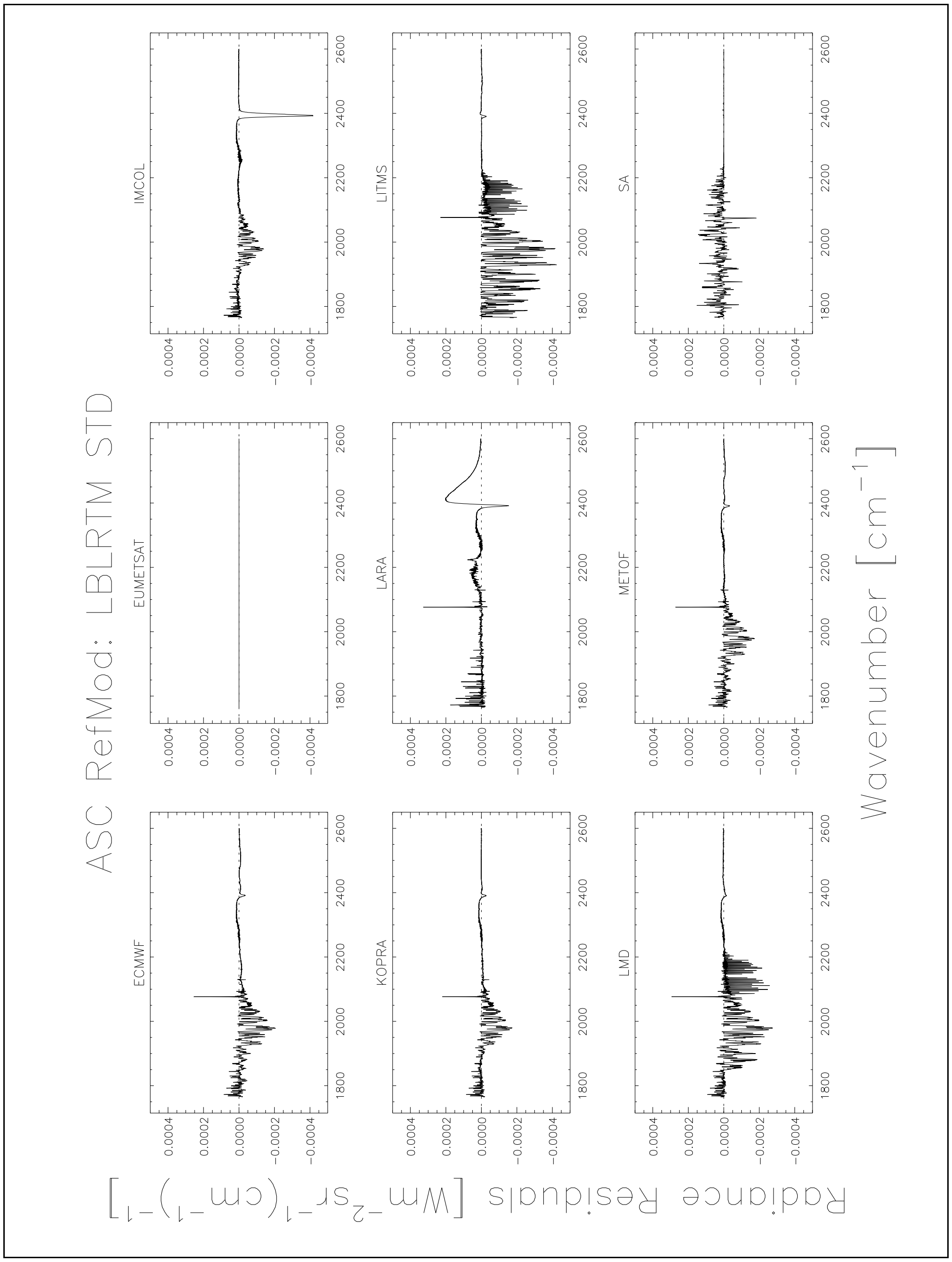

Figure 7.75: Radiance residuals between simulation by a particular submission as indicated by the title above each panel, and the LBLRTM model in ARIES band 2.

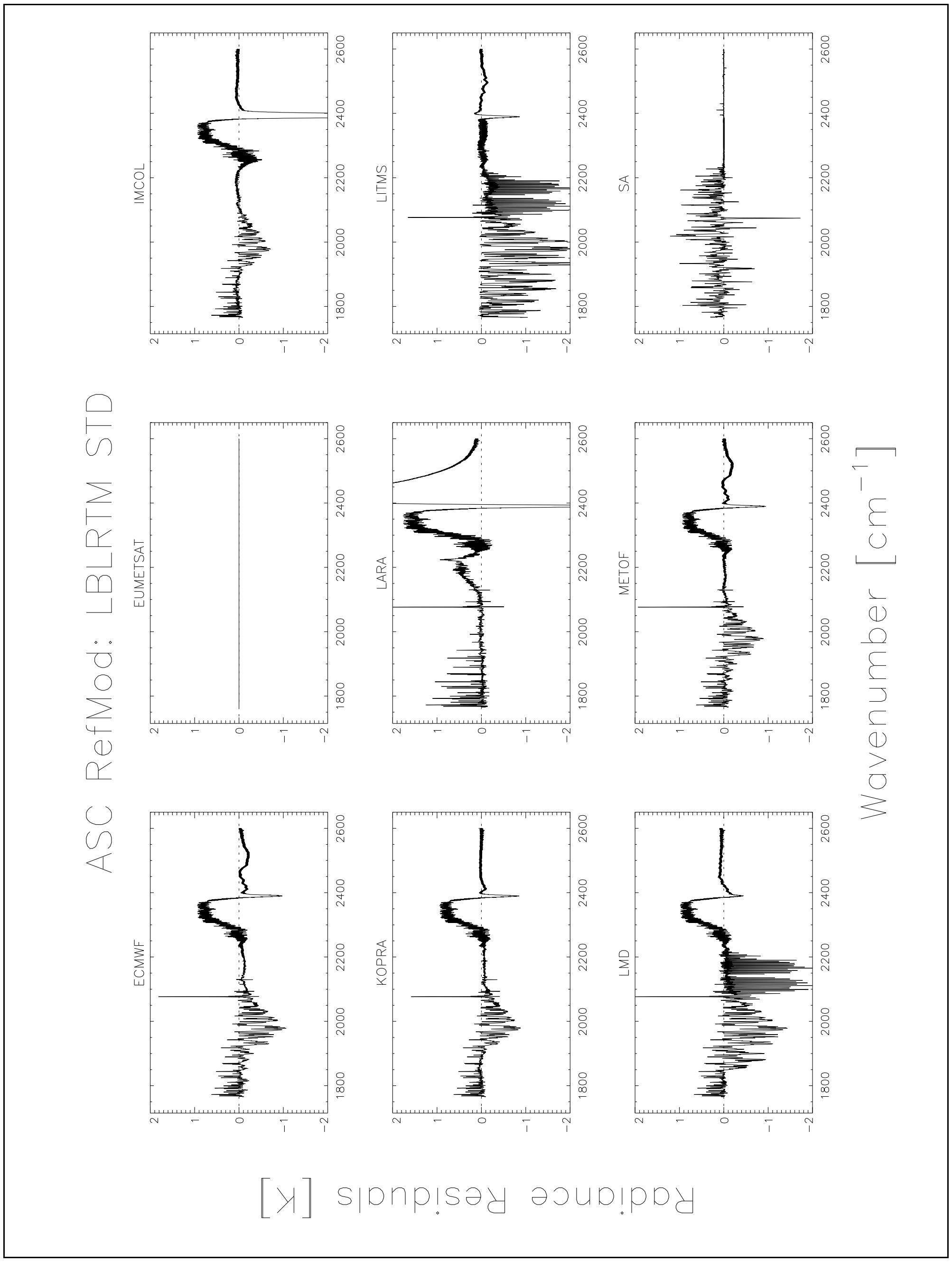

Figure 7.76: Radiance residuals between simulation by a particular submission as indicated by the title above each panel, and the LBLRTM model in ARIES band 2.

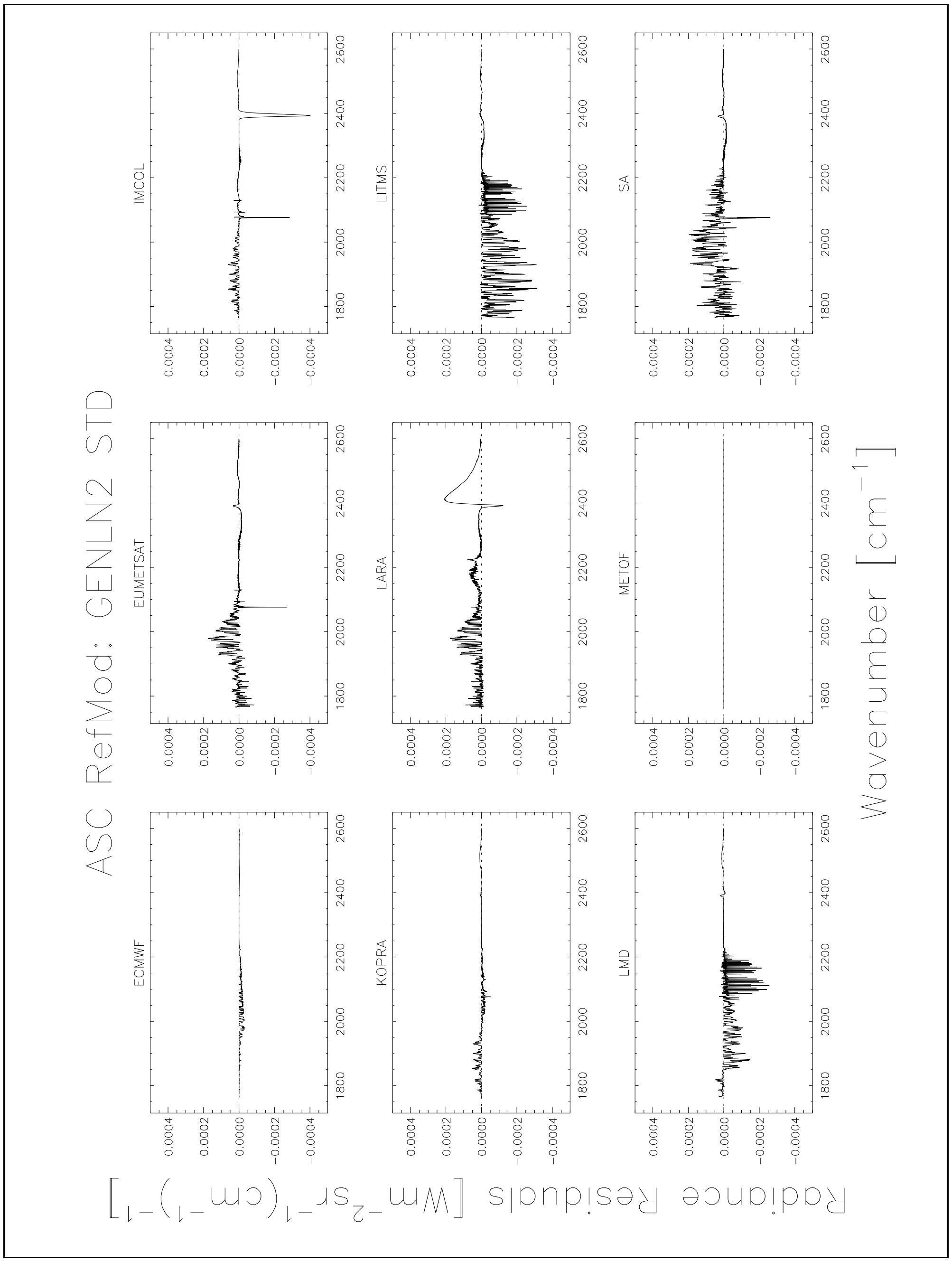

Figure 7.77: Radiance residuals between simulation by a particular submission as indicated by the title above each panel, and the GENLN2 model in ARIES band 2.

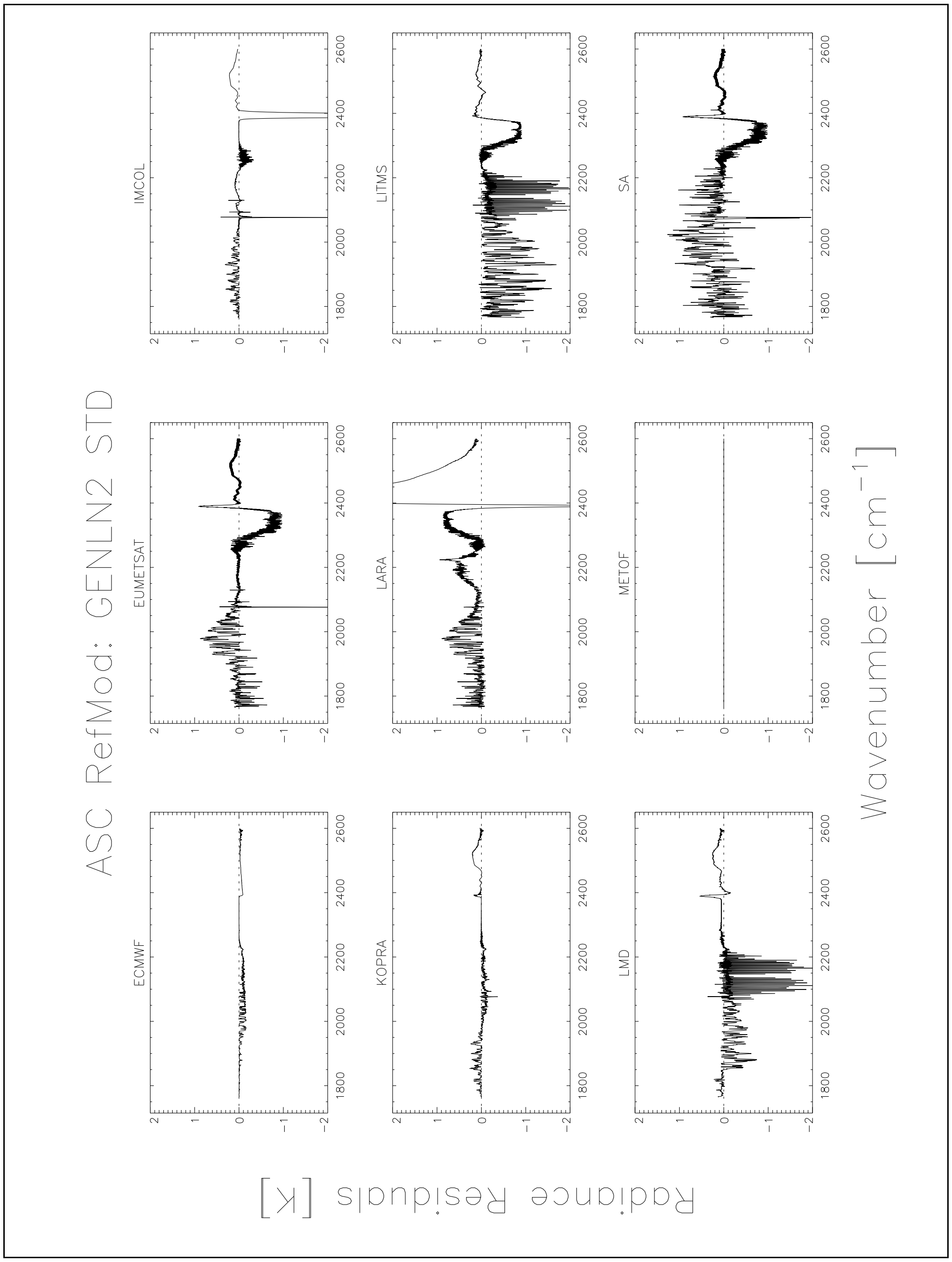

Figure 7.78: Radiance residuals between simulation by a particular submission as indicated by the title above each panel, and the GENLN2 model in ARIES band 2.

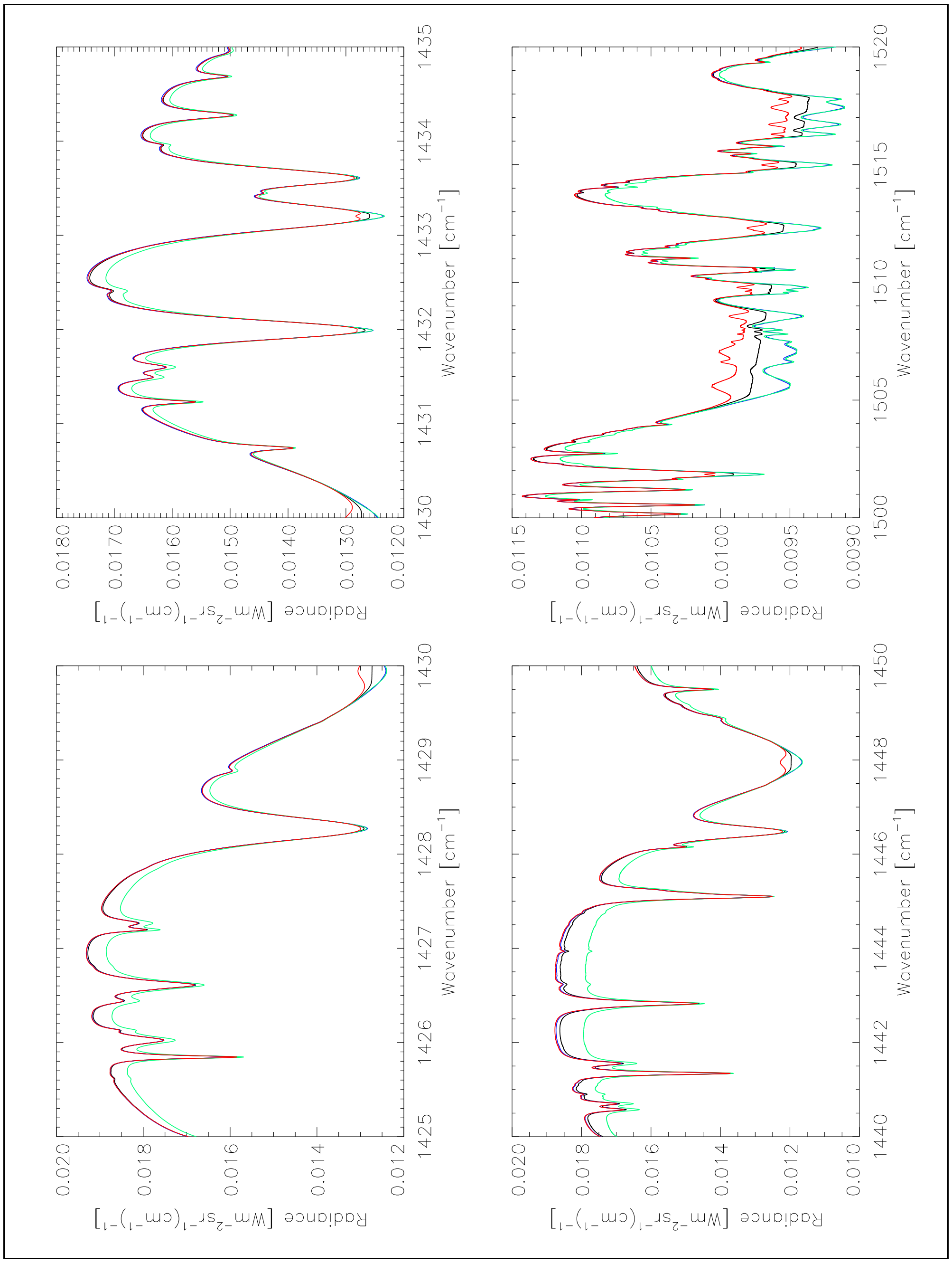

Figure 7.79: Upwelling radiance in $mWm^{-2}sr^{-1}\left(cm^{-1}\right)^{-1}$ as a function of wavenumber at the observational level of 7.924 km, according to the METOF (black line), EUMETSAT (blue line), LITMS (green line) and LARA (red line) submissions for different spectral domains in the ARIES band 1 region.

Figure 7.80: Upwelling radiance in $mWm^{-2}sr^{-1}\left(cm^{-1}\right)^{-1}$ as a function of wavenumber at the observational level of 7.924 km, according to the LBLRTM model as implemented at EUMETSAT (black line) and the GENLN2 model implemented at the Met Office (yellow line), for the ASCENSION Island test case.

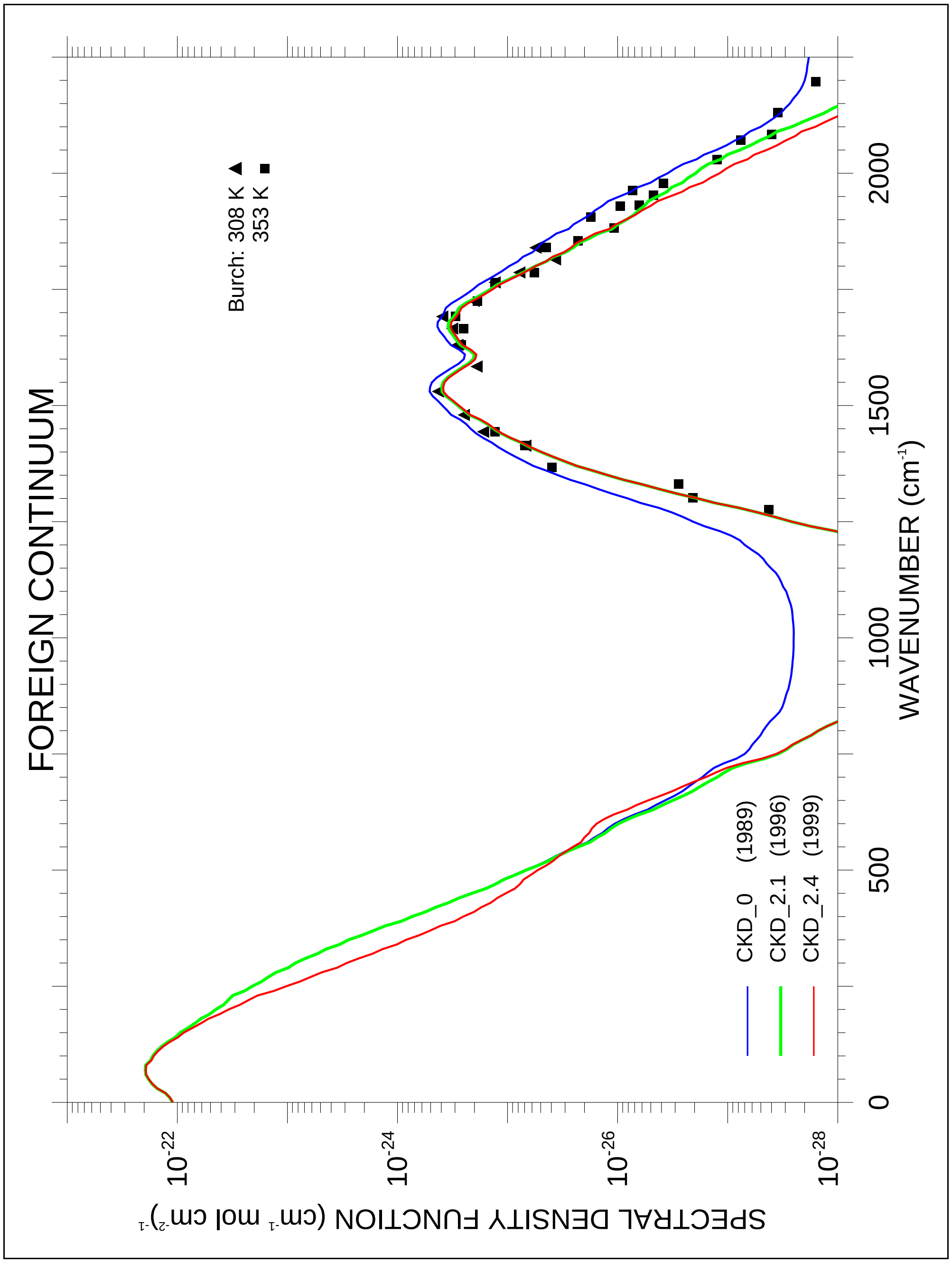

Figure 7.81: Variation of the foreign continuum with wavenumber for three different water vapour continuum models. (Courtesy of AER.)

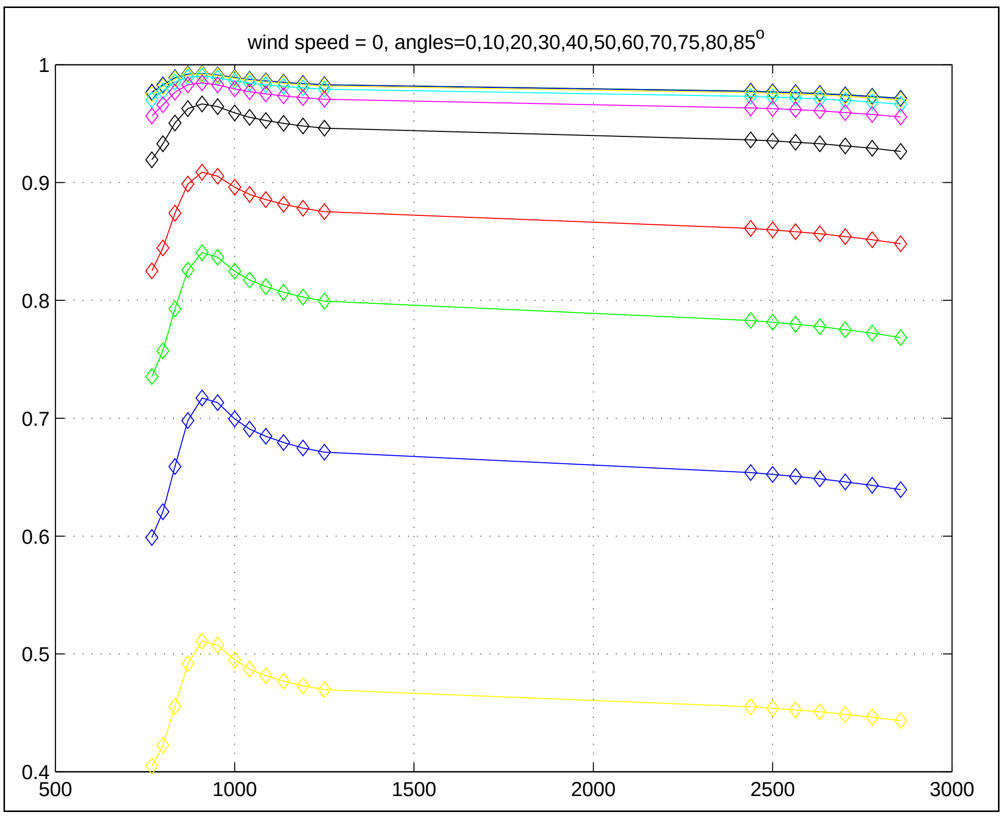

Figure 7.82: Sea surface emissivity as a function of wavenumber, and zenith angle at a wind speed of 0 m/s.

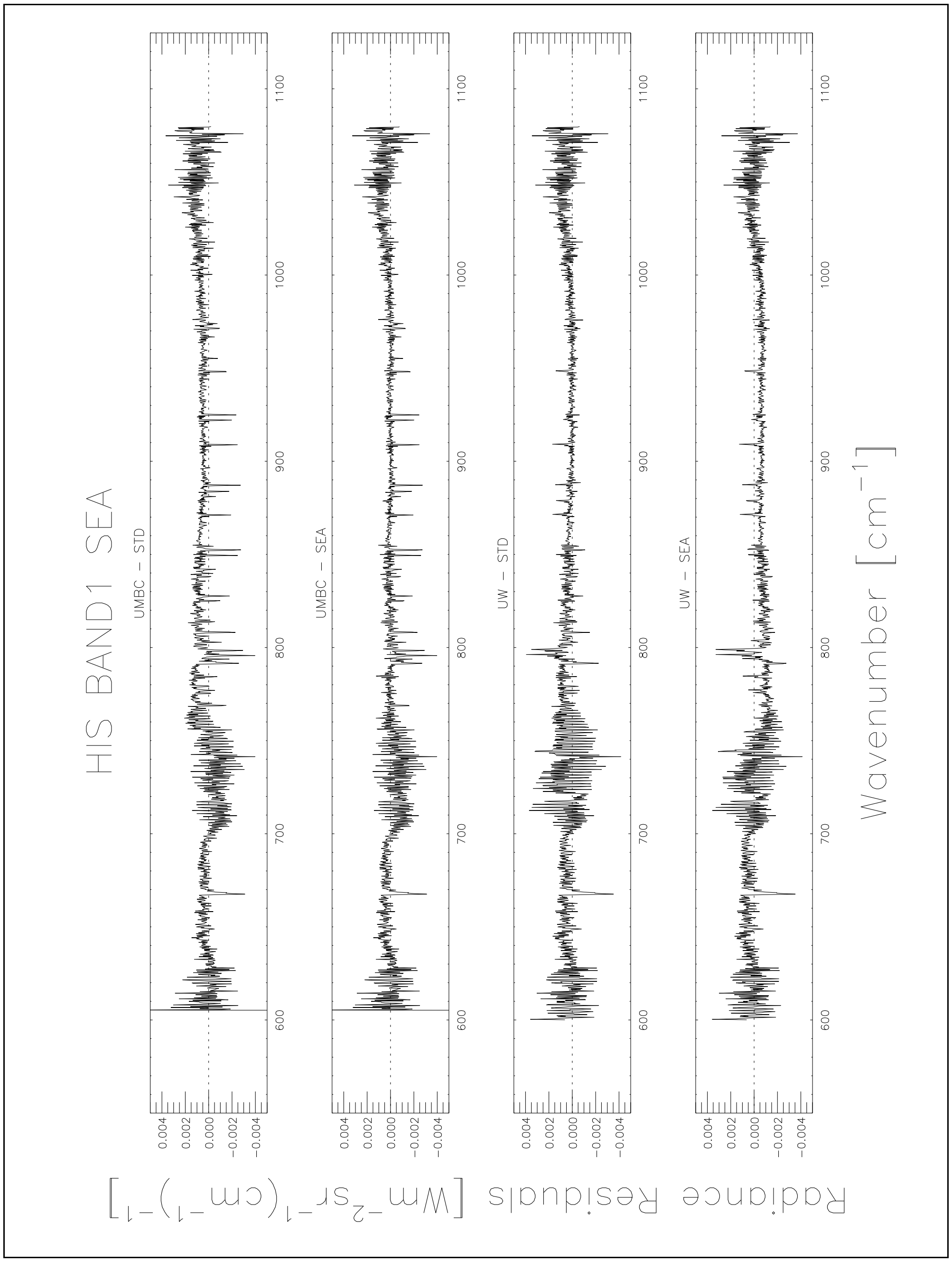

Figure 7.83: Radiance residuals between calculated and observed radiance in HIS band 1 for the particular submission indicated by the title above each panel. The Figure illustrates the effect on the upwelling radiances at observational level, when the fixed value of the surface emissivity adopted for the standard simulations, is replace with a wavelength dependent one according to the model of Masuda Watts et al. [1996], Masuda et al. [1988].

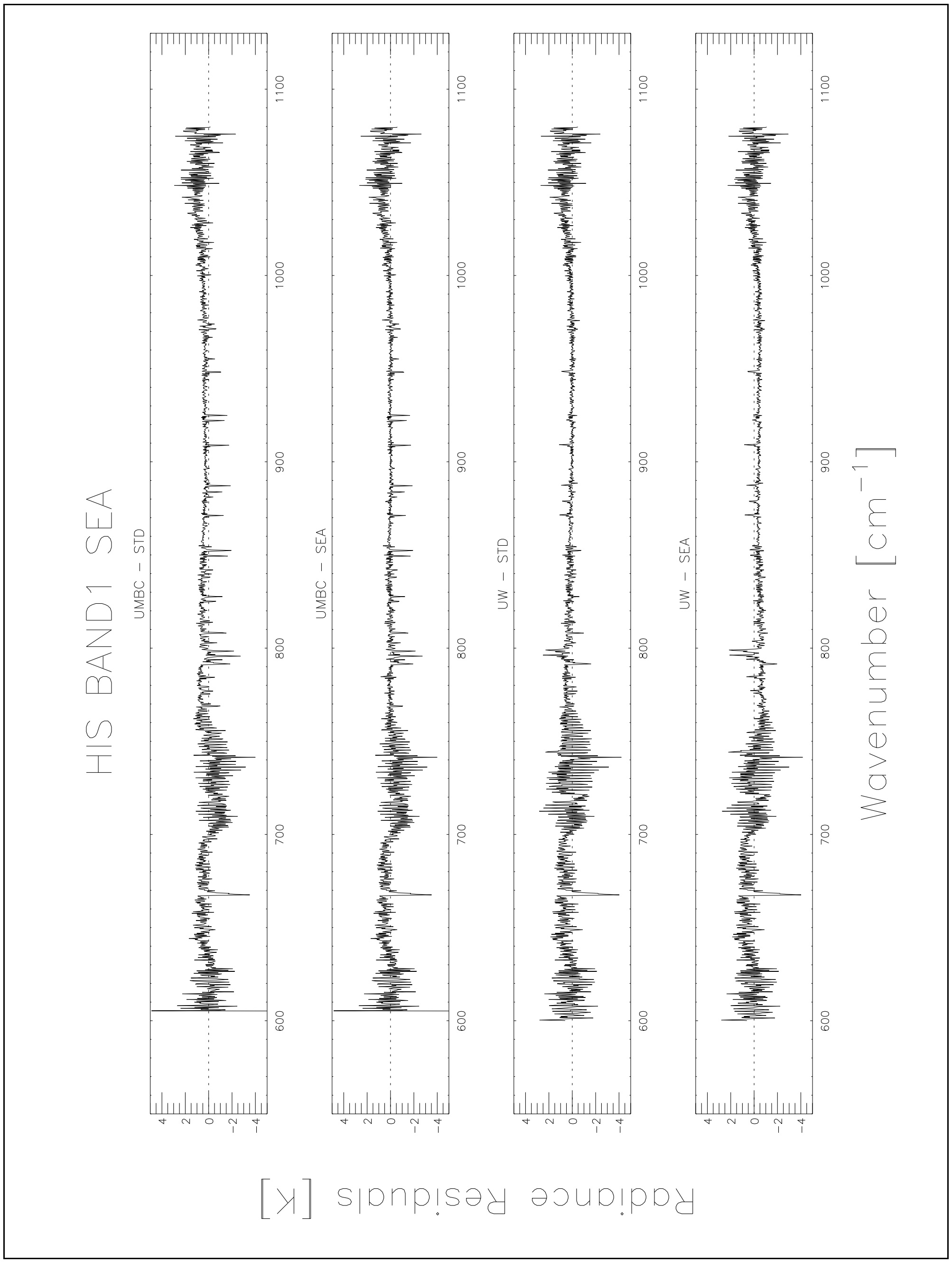

Figure 7.84: Radiance residuals between calculated and observed radiance in HIS band 1 for the particular submission indicated by the title above each panel. The Figure illustrates the effect on the upwelling radiances at observational level, when the fixed value of the surface emissivity adopted for the standard simulations, is replace with a wavelength dependent one according to the model of Masuda Watts et al. [1996], Masuda et al. [1988]. Note that the radiance residuals are converted into noise equivalent brightness temperature, using the equivalent brightness temperatures shown in Figure 7.15.

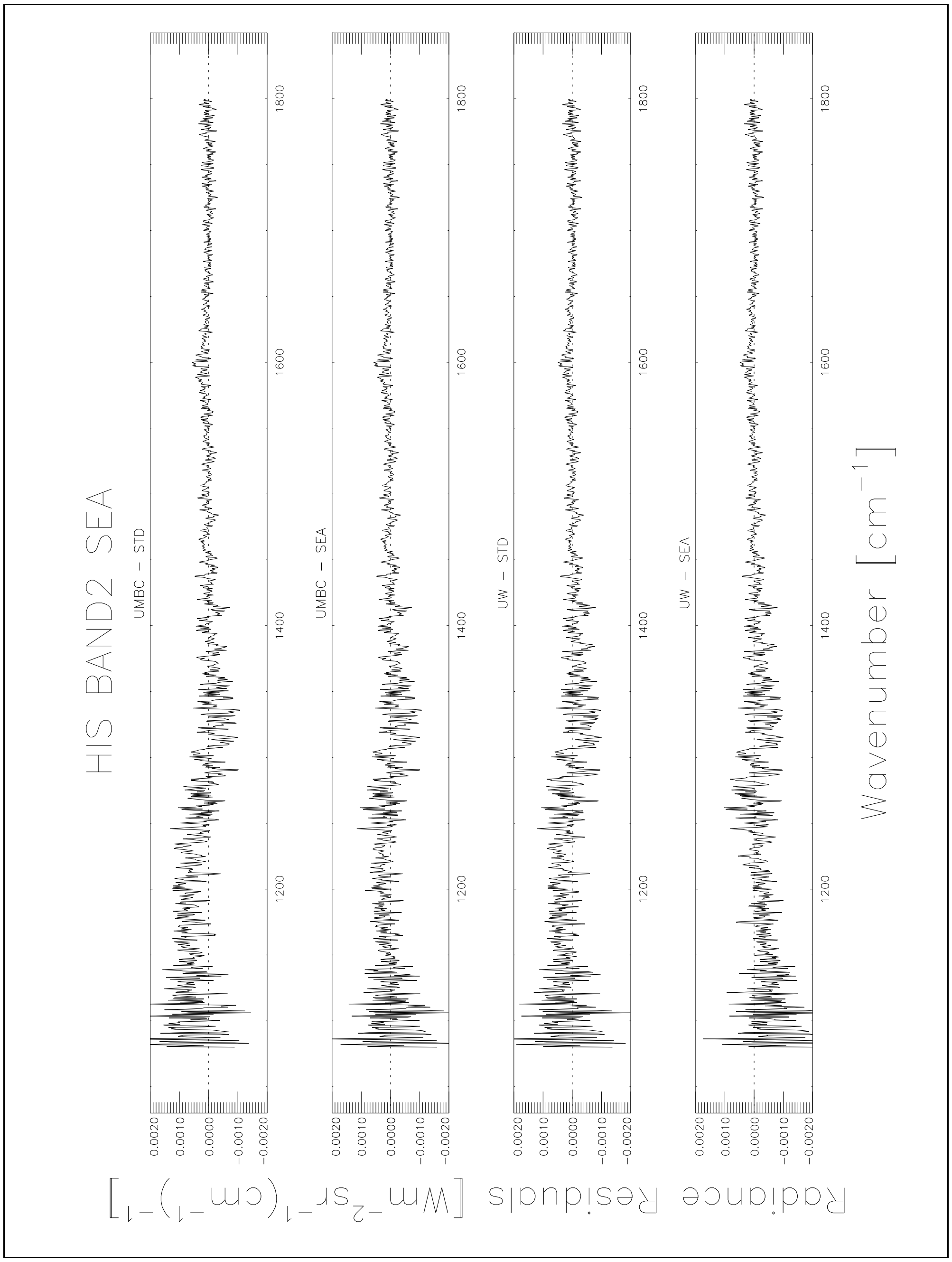

Figure 7.85: Radiance residuals between calculated and observed radiance in HIS band 2 for the particular submission indicated by the title above each panel.The Figure illustrates the effect on the upwelling radiances at observational level, when the fixed value of the surface emissivity adopted for the standard simulations, is replace with a wavelength dependent one according to the model of Masuda Watts et al. [1996], Masuda et al. [1988].

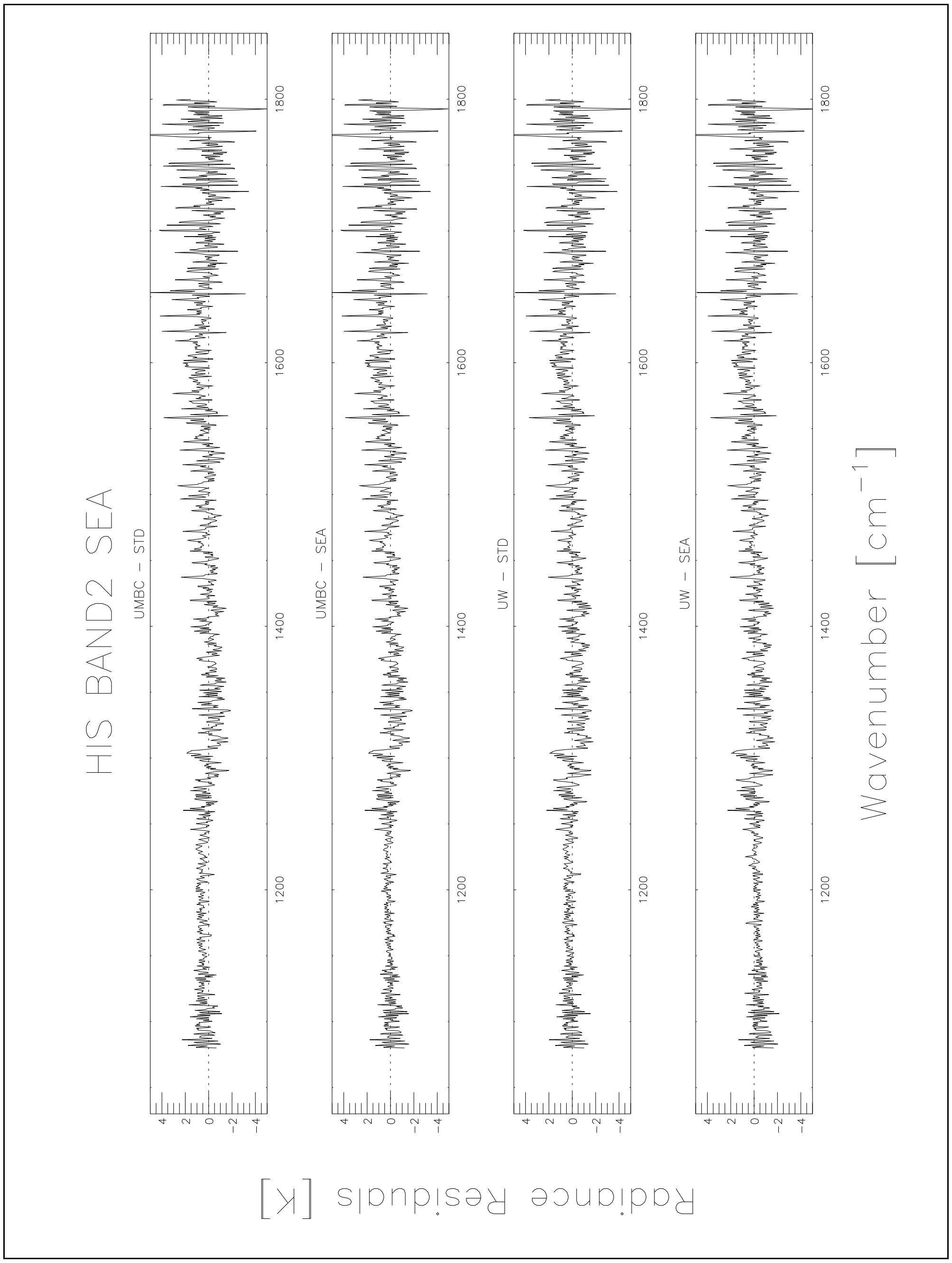

Figure 7.86: Radiance residuals between calculated and observed radiance in HIS band 2 for the particular submission indicated by the title above each panel. The Figure illustrates the effect on the upwelling radiances at observational level, when the fixed value of the surface emissivity adopted for the standard simulations, is replace with a wavelength dependent one according to the model of Masuda Watts et al. [1996], Masuda et al. [1988]. Note that the radiance residuals are converted into noise equivalent brightness temperature, using the equivalent brightness temperatures shown in Figure 7.25.

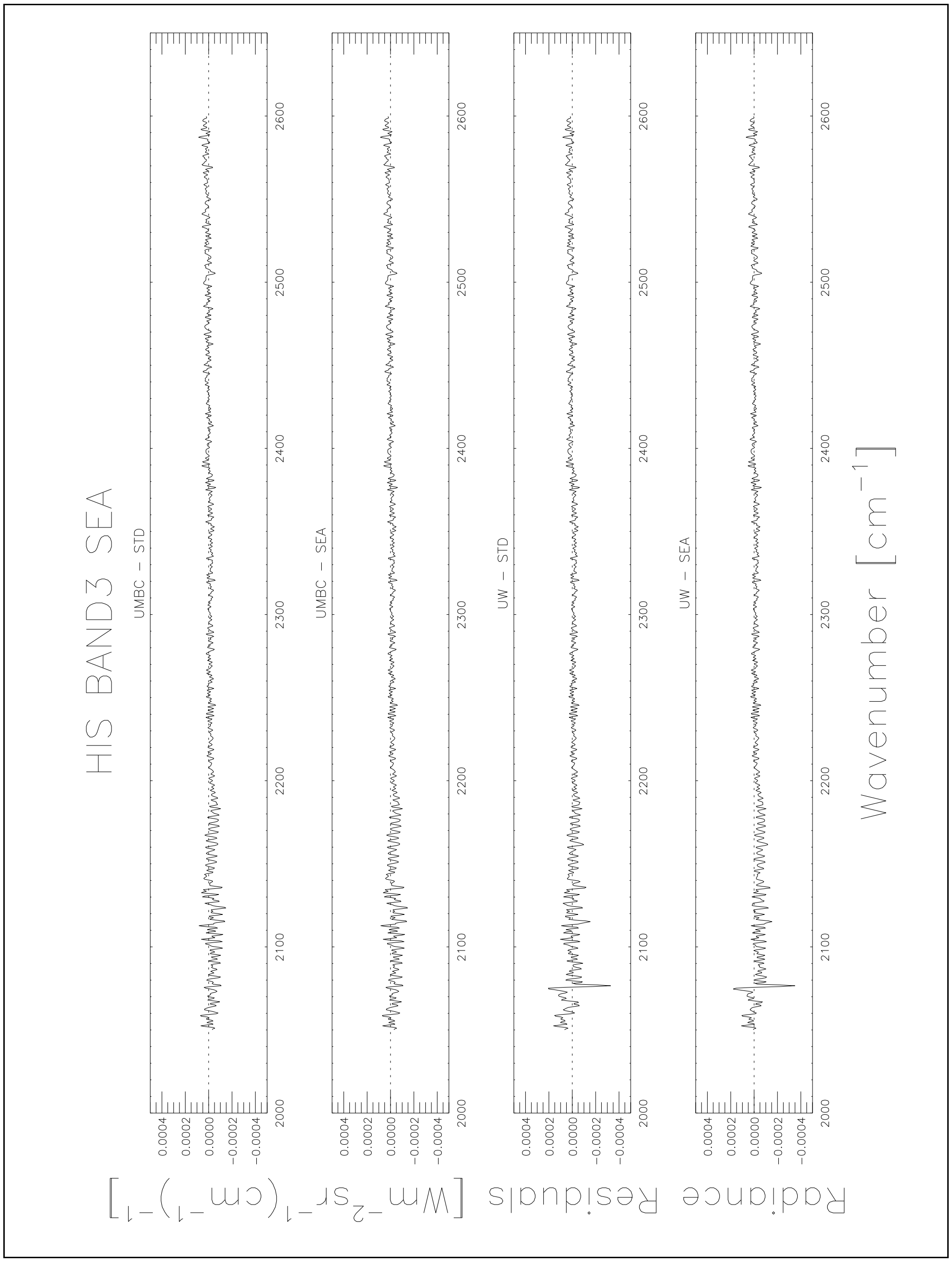

Figure 7.87: Radiance residuals between calculated and observed radiance in HIS band 2 for the particular submission indicated by the title above each panel. The Figure illustrates the effect on the upwelling radiances at observational level, when the fixed value of the surface emissivity adopted for the standard simulations, is replace with a wavelength dependent one according to the model of Masuda Watts et al. [1996], Masuda et al. [1988].

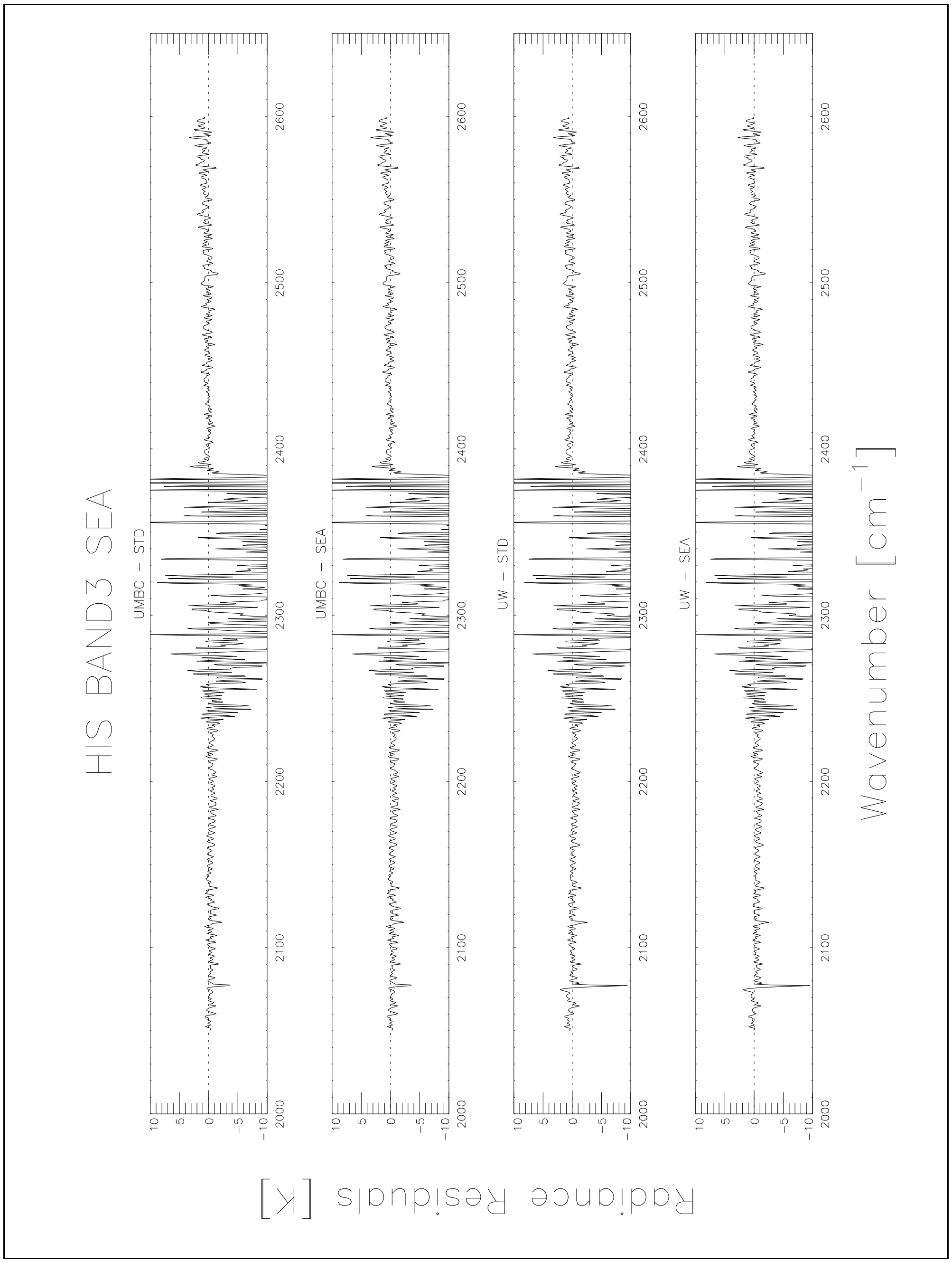

Figure 7.88: Radiance residuals between calculated and observed radiance in HIS band 2 for the particular submission indicated by the title above each panel. The Figure illustrates the effect on the upwelling radiances at observational level, when the fixed value of the surface emissivity adopted for the standard simulations, is replace with a wavelength dependent one according to the model of Masuda Watts et al. [1996], Masuda et al. [1988]. Note that the radiance residuals are converted into noise equivalent brightness temperature, using the equivalent brightness temperatures shown in Figure 7.25.

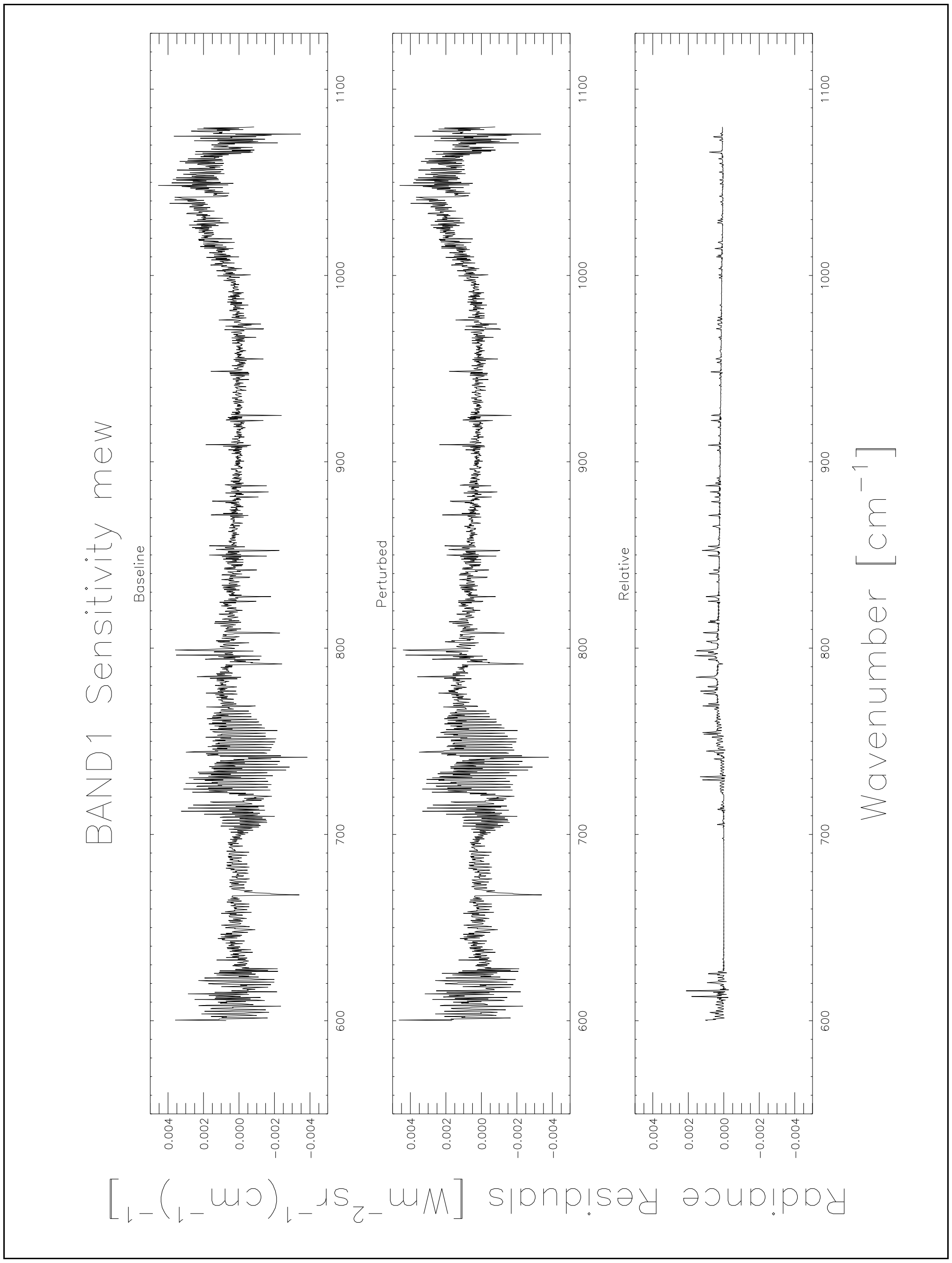

Figure 7.89: Effect on the upwelling radiation for the CAMEX experiment in HIS band 1 due to a modification of the humidity profile, by subtracting from the observed humidity profile the uncertainty. The top panel shows the radiance residual between the observation and the calculations with the original, unmodified humidity profile, the middle panel shows the radiance residual between the observations and the calculations with the perturbed humidity profile, and the lower panel shows the radiance residuals between the simulations with the perturbed and with the unperturbed humidity profile.

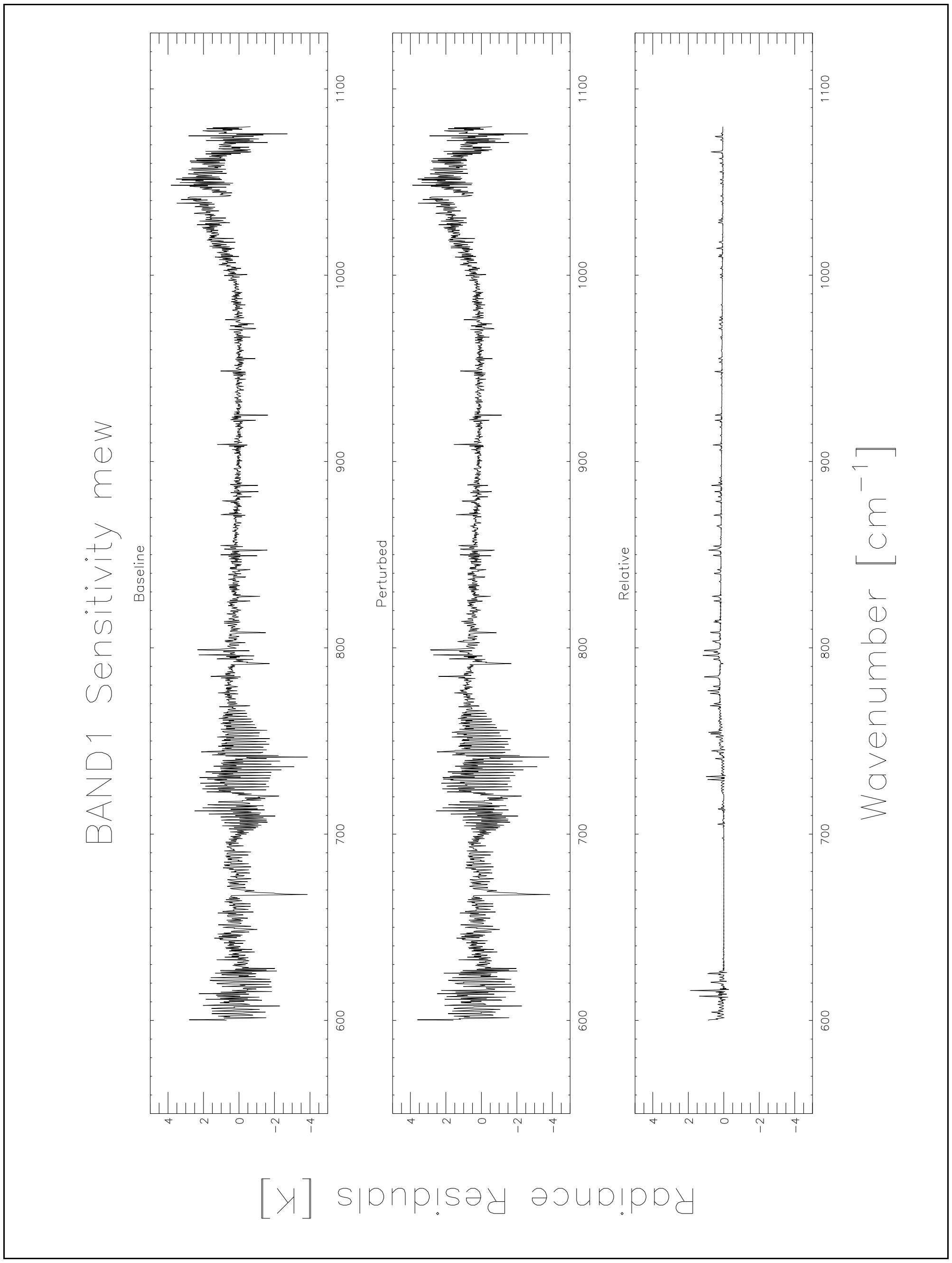

Figure 7.90: Effect on the upwelling radiation for the CAMEX experiment in HIS band 1 due to a modification of the humidity profile, by subtracting from the observed humidity profile the uncertainty. The panels are arranged as in Figure 7.89.

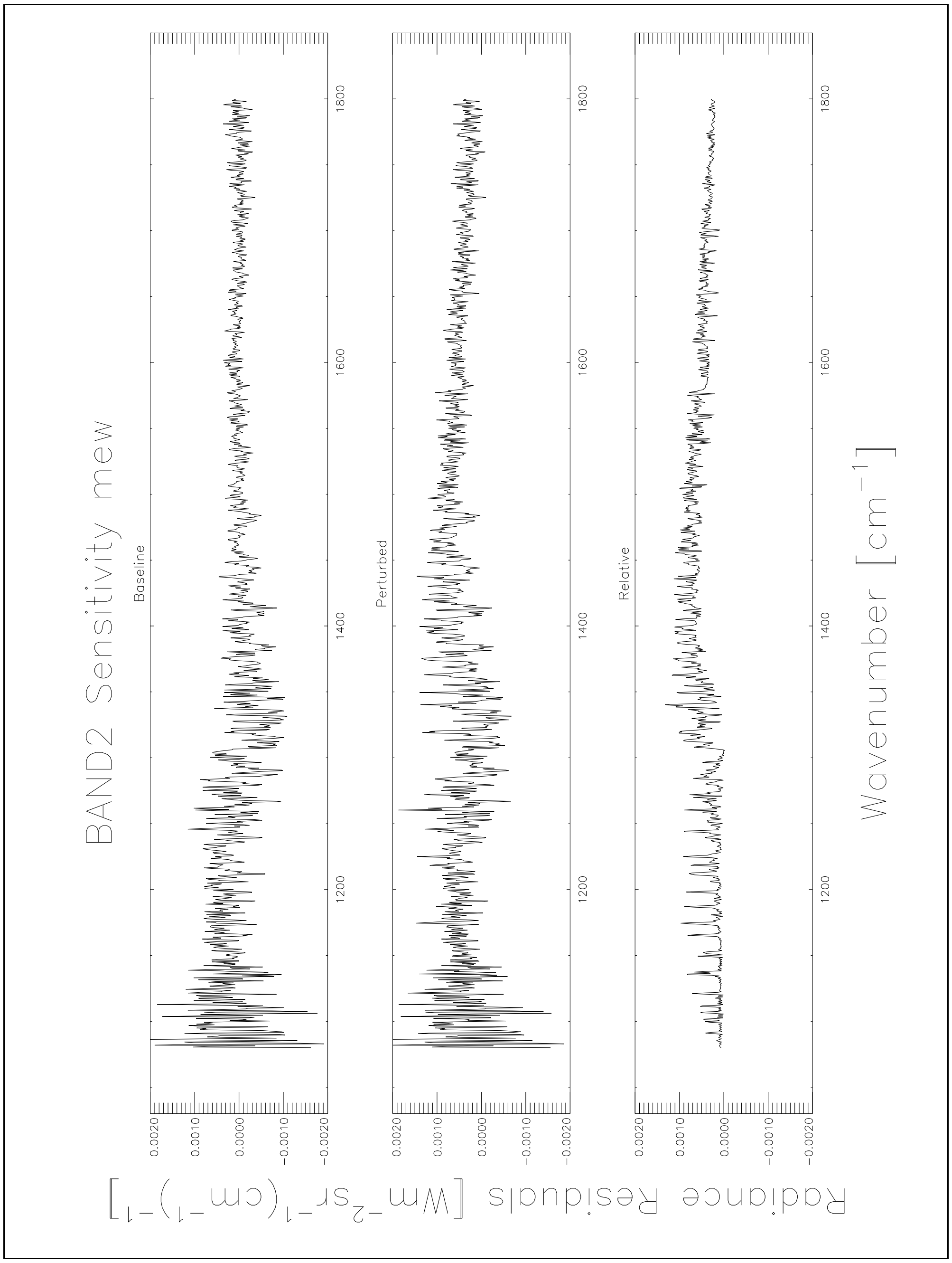

Figure 7.91: Effect on the upwelling radiation for the CAMEX experiment in HIS band 2 due to a modification of the humidity profile, by subtracting from the observed humidity profile the uncertainty. The panels are arranged as in Figure 7.89.

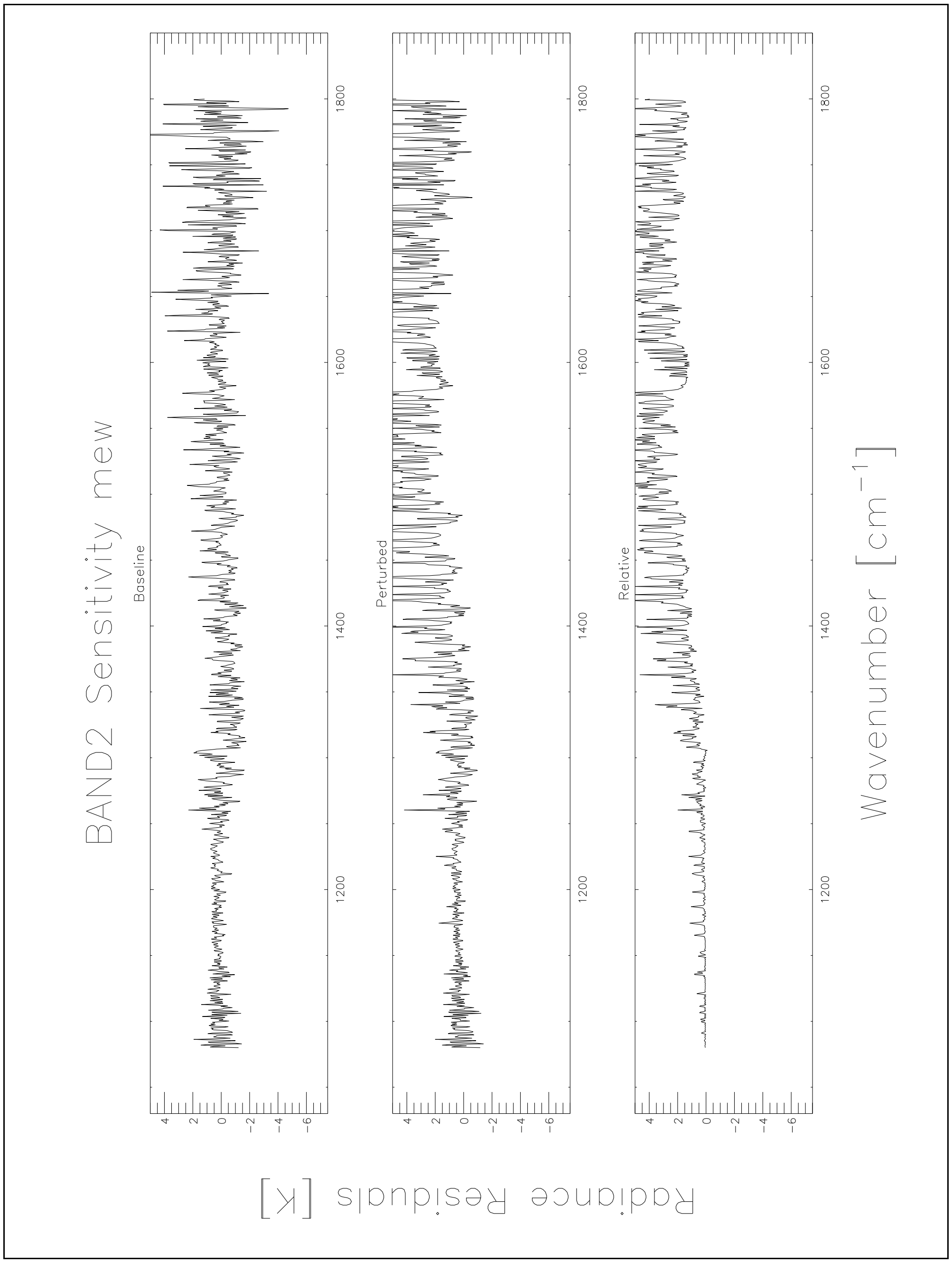

Figure 7.92: Effect on the upwelling radiation for the CAMEX experiment in HIS band 2 due to a modification of the humidity profile, by subtracting from the observed humidity profile the uncertainty. The panels are arranged as in Figure 7.89.

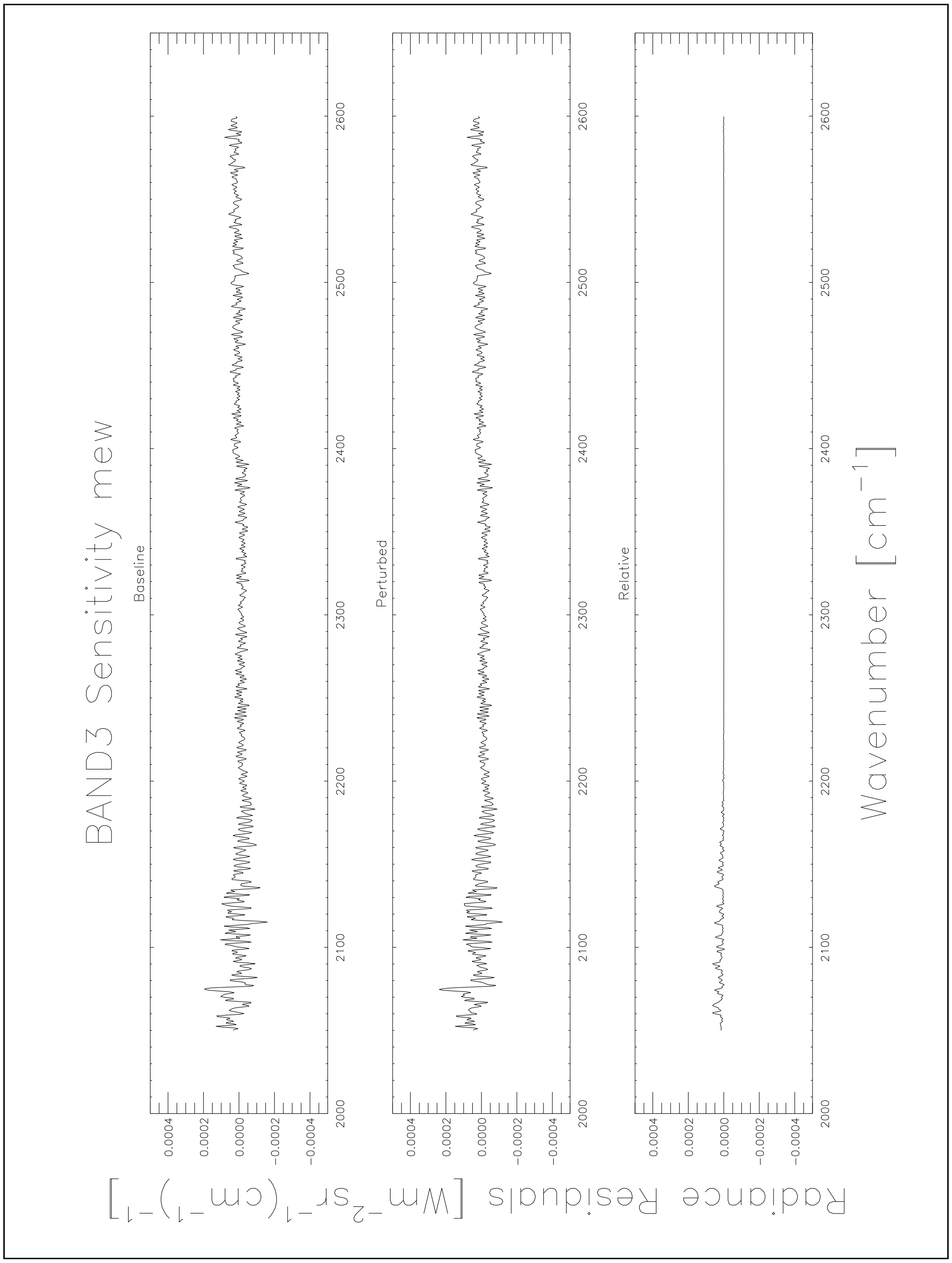

Figure 7.93: Effect on the upwelling radiation for the CAMEX experiment in HIS band 3 due to a modification of the humidity profile, by subtracting from the observed humidity profile the uncertainty. The panels are arranged as in Figure 7.89.

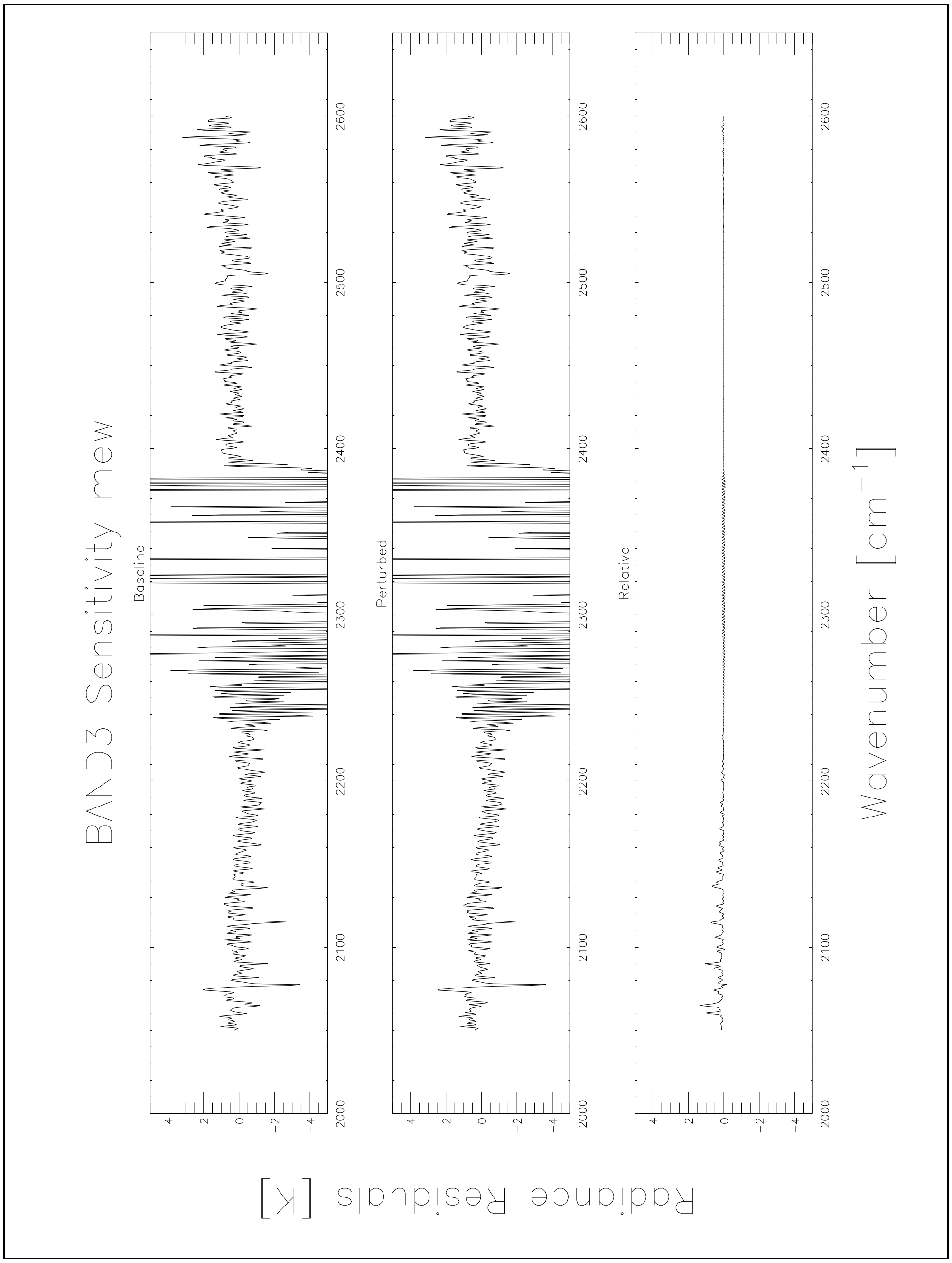

Figure 7.94: Effect on the upwelling radiation for the CAMEX experiment in HIS band 3 due to a modification of the humidity profile, by subtracting from the observed humidity profile the uncertainty. The panels are arranged as in Figure 7.89.

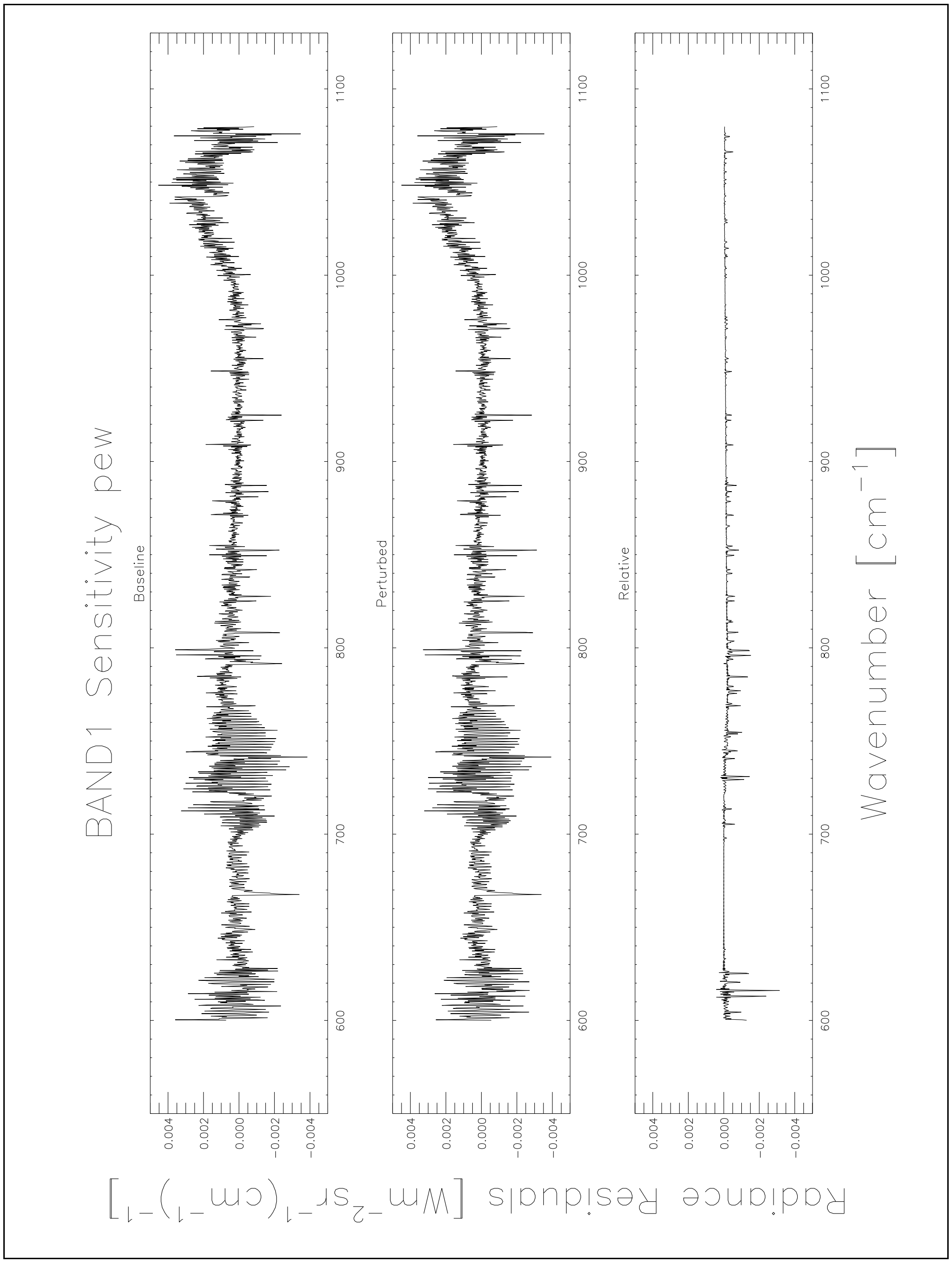

Figure 7.95: Effect on the upwelling radiation for the CAMEX experiment in HIS band 1 due to a modification of the humidity profile, by subtracting from the observed humidity profile the uncertainty. The panels are arranged as in Figure 7.89.

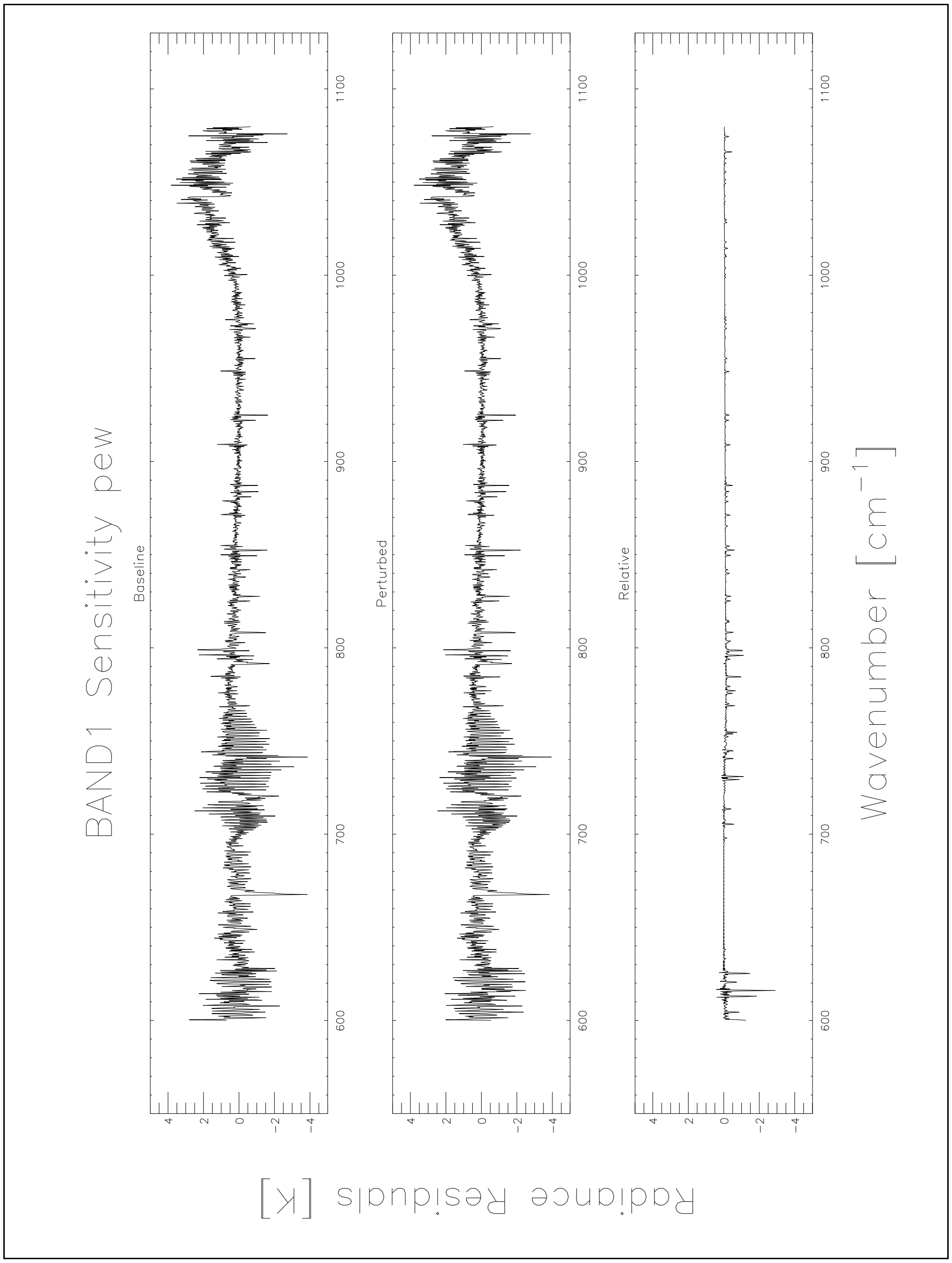

Figure 7.96: Effect on the upwelling radiation for the CAMEX experiment in HIS band 1 due to a modification of the humidity profile, by adding to the observed humidity profile the uncertainty. The panels are arranged as in Figure 7.89.

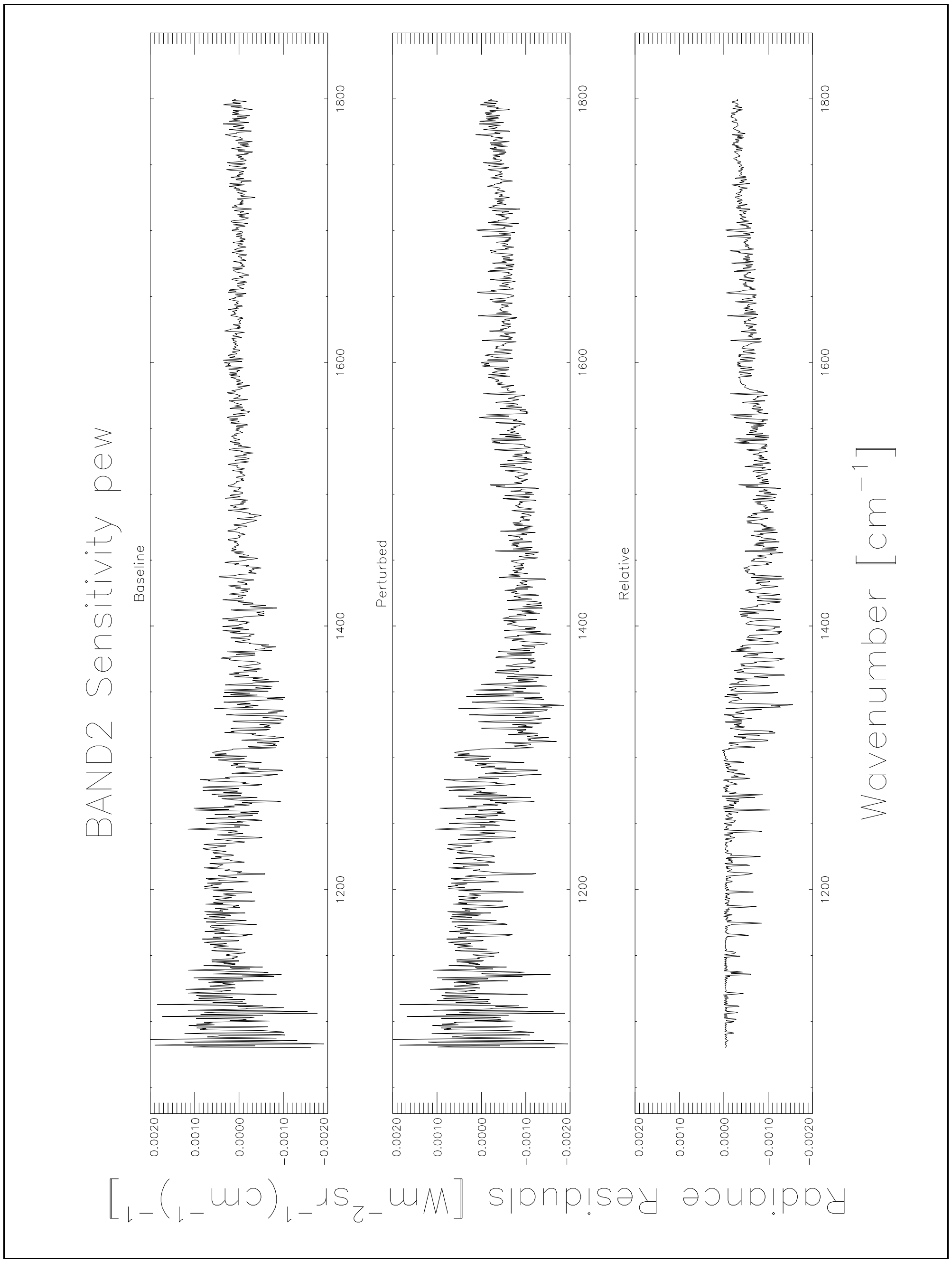

Figure 7.97: Effect on the upwelling radiation for the CAMEX experiment in HIS band 2 due to a modification of the humidity profile, by adding to the observed humidity profile the uncertainty. The panels are arranged as in Figure 7.89.

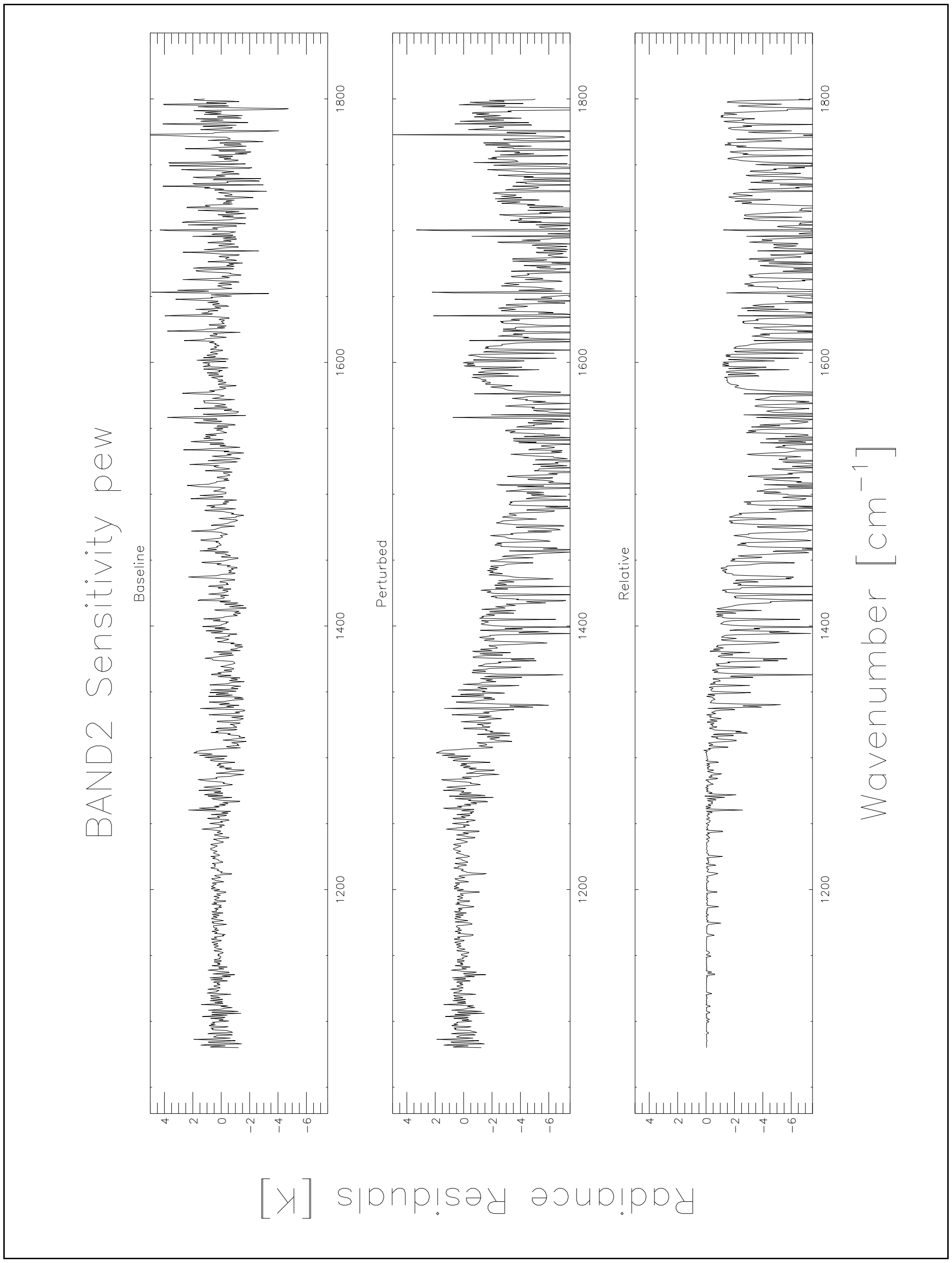

Figure 7.98: Effect on the upwelling radiation for the CAMEX experiment in HIS band 2 due to a modification of the humidity profile, by adding to the observed humidity profile the uncertainty. The panels are arranged as in Figure 7.89.

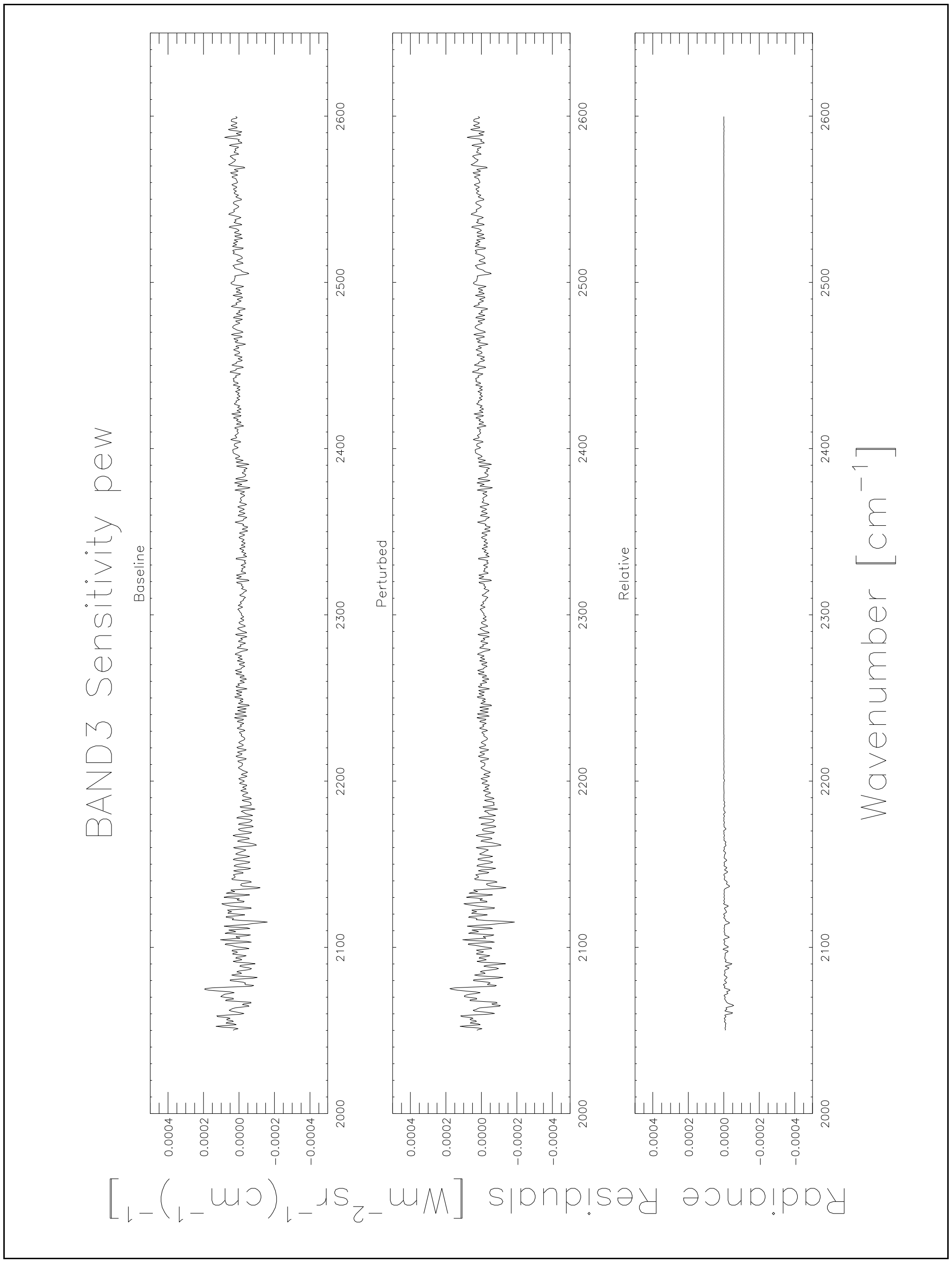

Figure 7.99: Effect on the upwelling radiation for the CAMEX experiment in HIS band 3 due to a modification of the humidity profile, by adding to the observed humidity profile the uncertainty. The panels are arranged as in Figure 7.89.

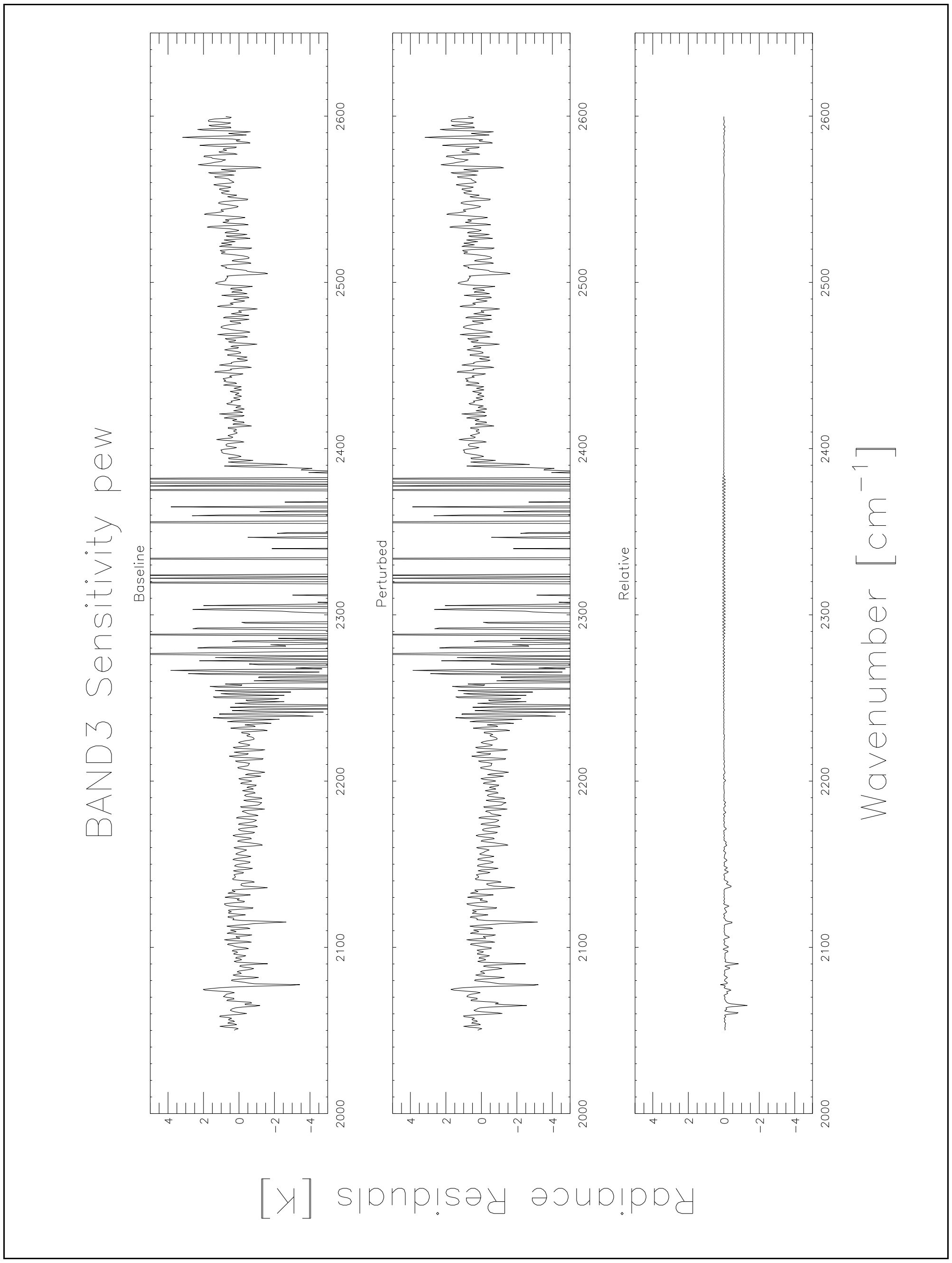

Figure 7.100: Effect on the upwelling radiation for the CAMEX experiment in HIS band 3 due to a modification of the humidity profile, by adding to the observed humidity profile the uncertainty. The panels are arranged as in Figure 7.89.

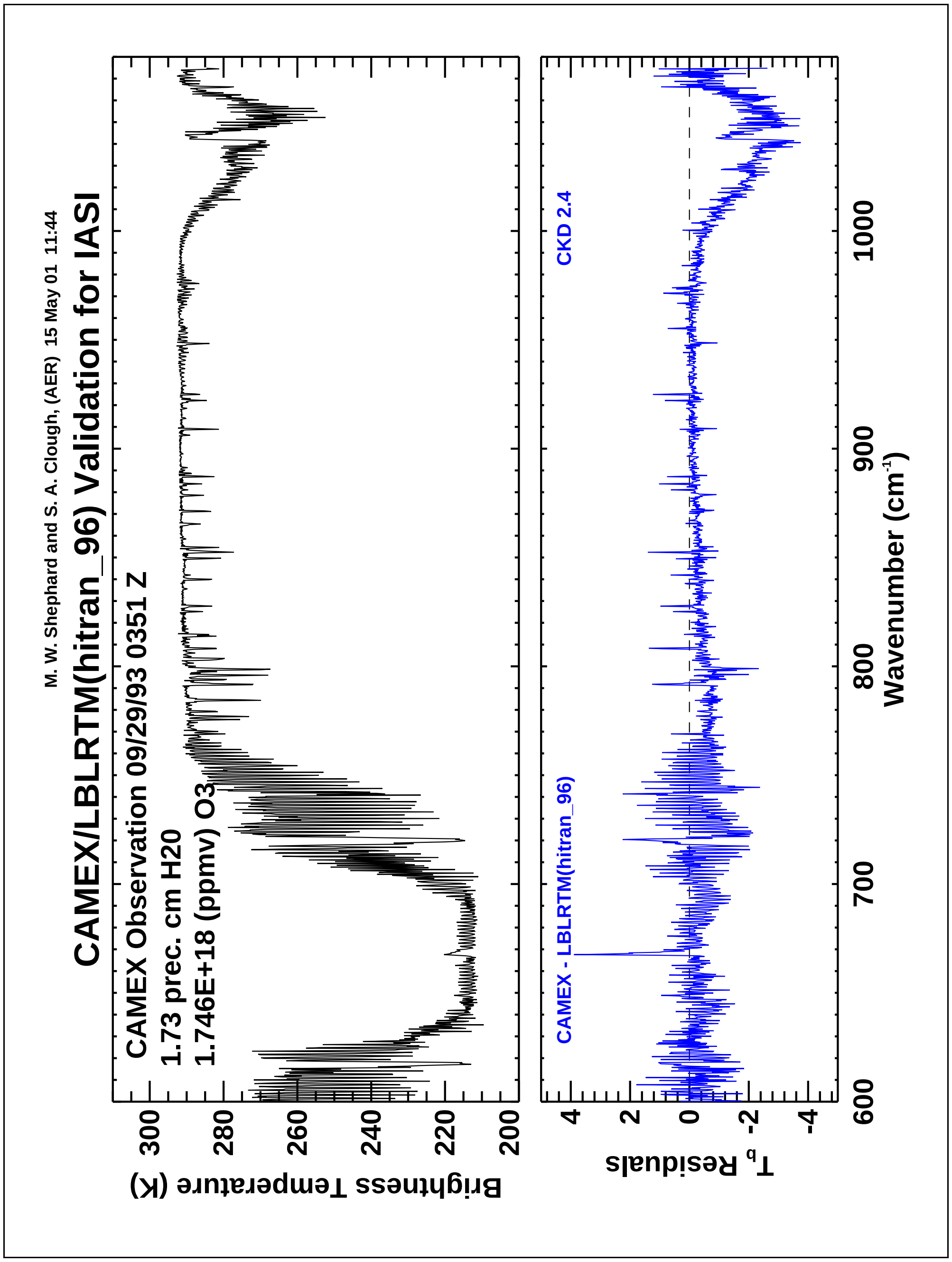

Figure 7.101: Initial reference case with original specified IASI intercomparison inputs.

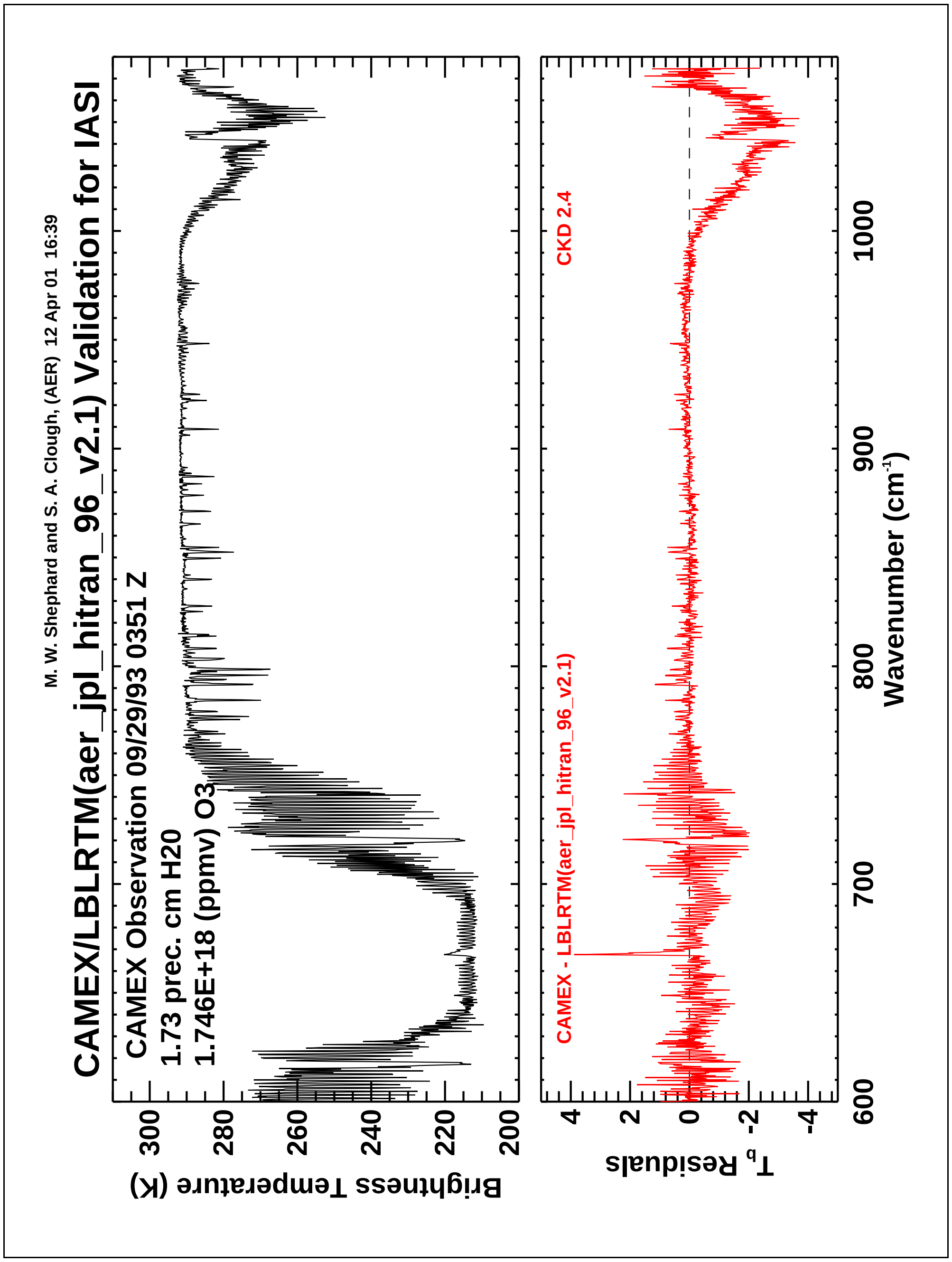

Figure 7.102: AER Reference Case for HIS CAMEX/LBLRTM Validation.

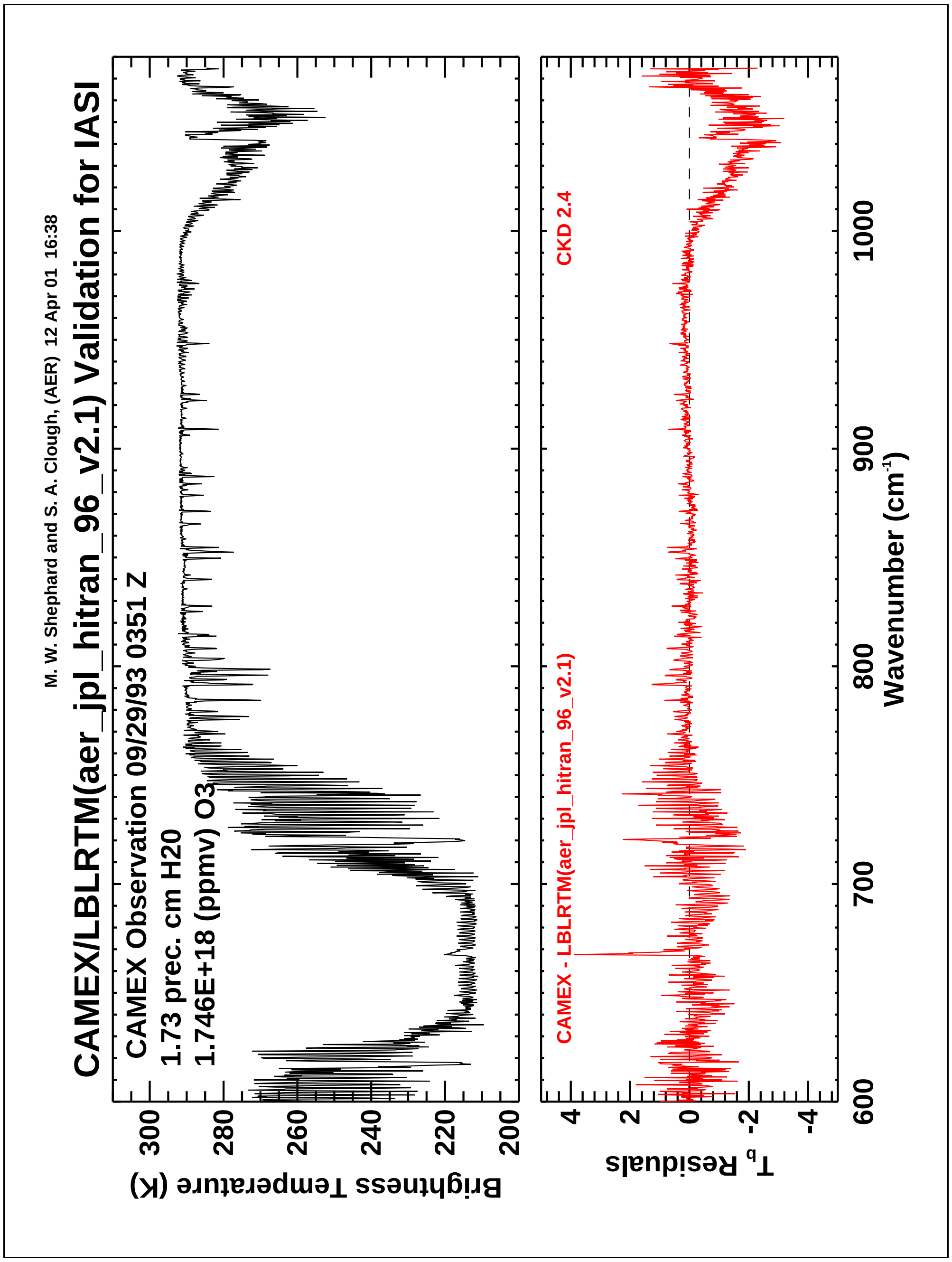

Figure 7.103: No Line Rejection Case for HIS CAMEX/LBLRTM Validation.

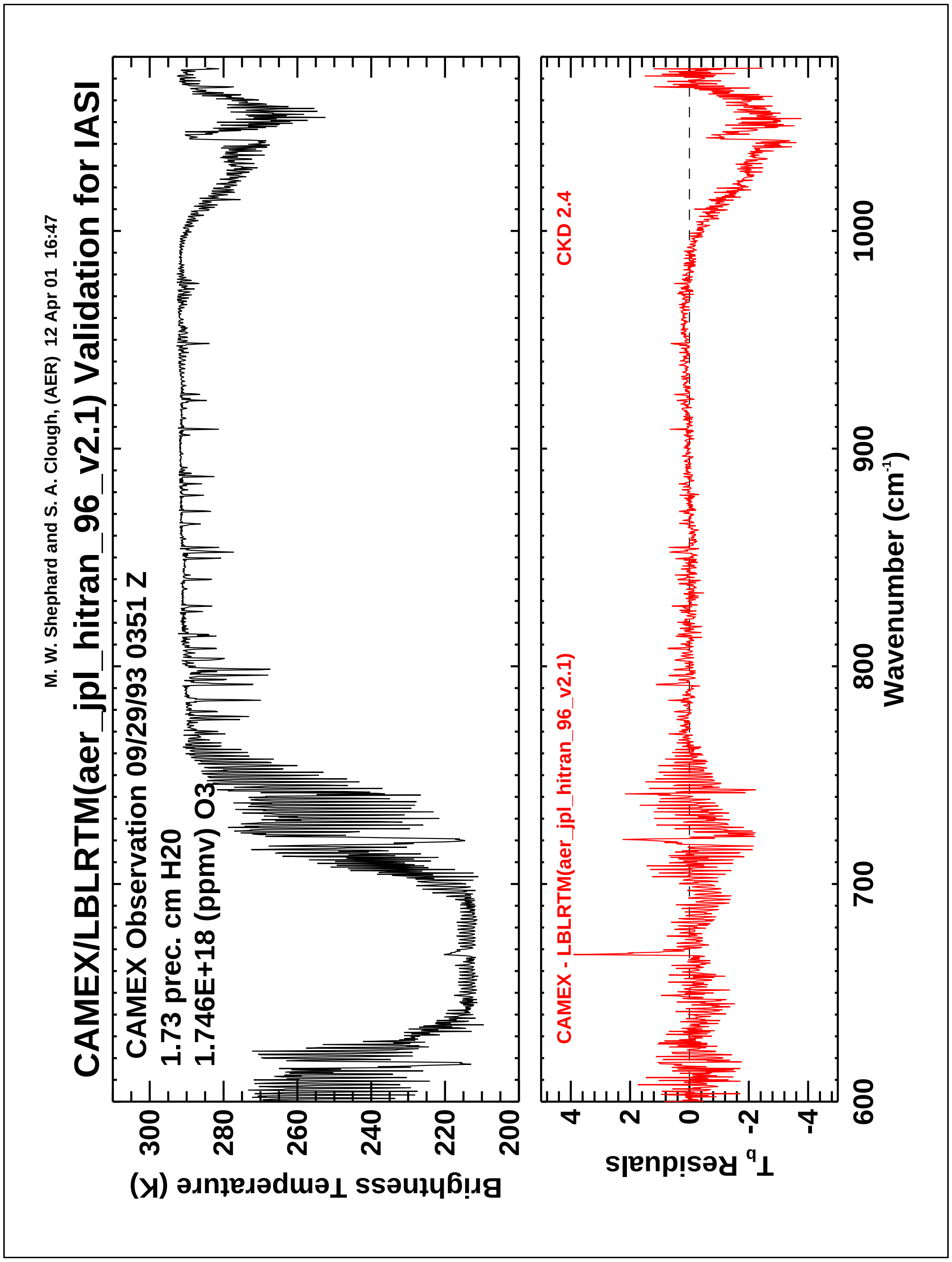

Figure 7.104: Finer Model Layering Case for HIS CAMEX/LBLRTM Validation.

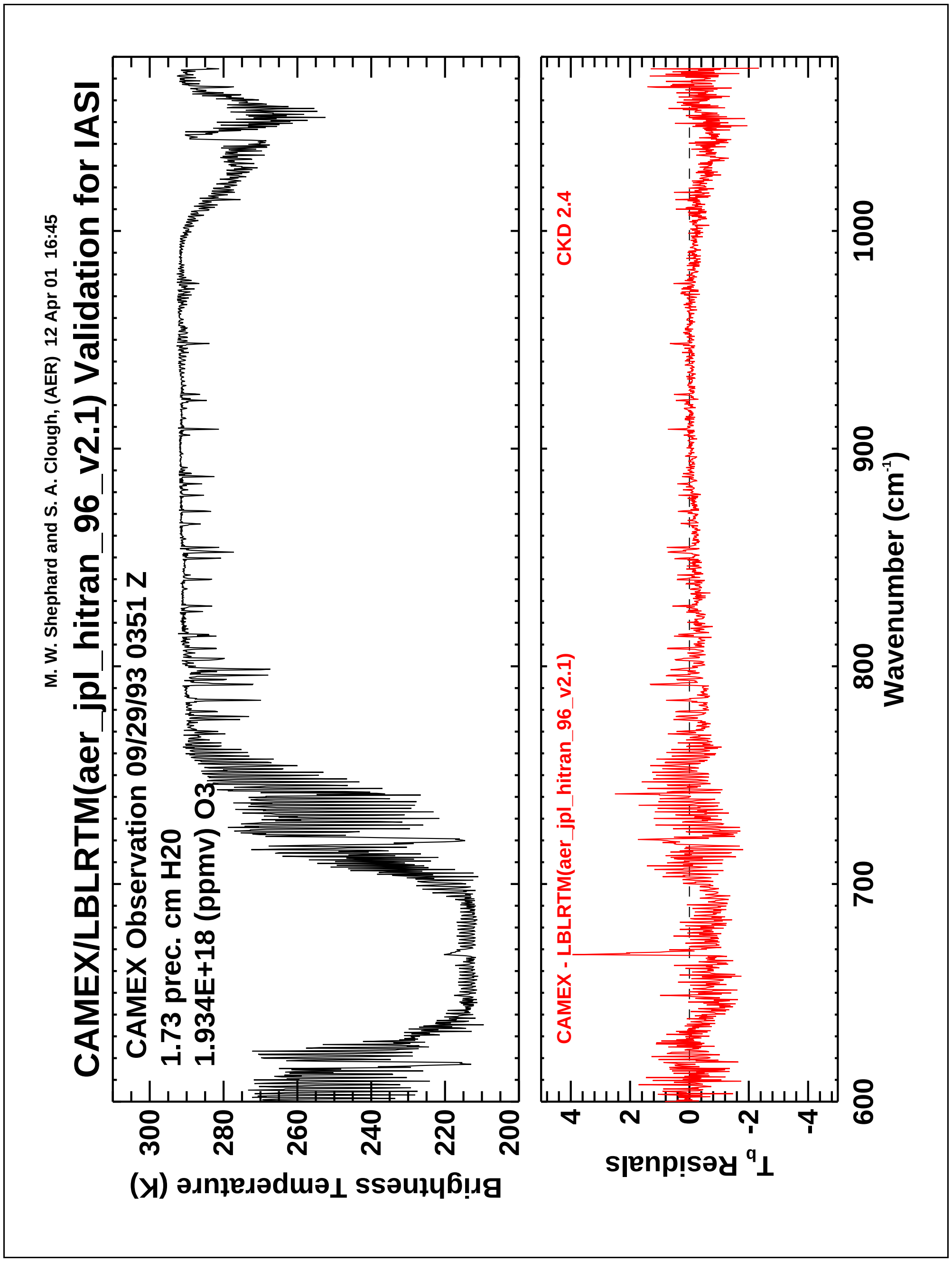

Figure 7.105: UW Case for HIS CAMEX/LBLRTM Validation.

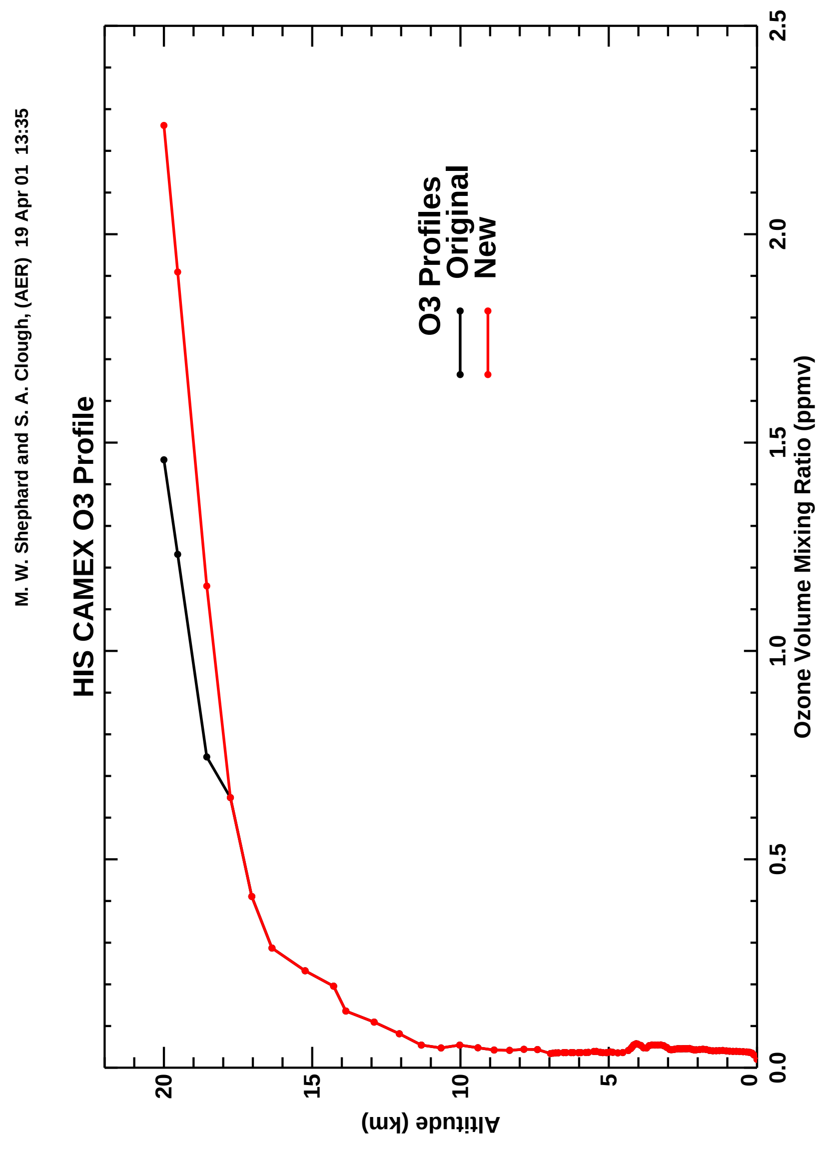

Figure 7.106: Comparison plot of AER scaled O_3 profile with reference profile.

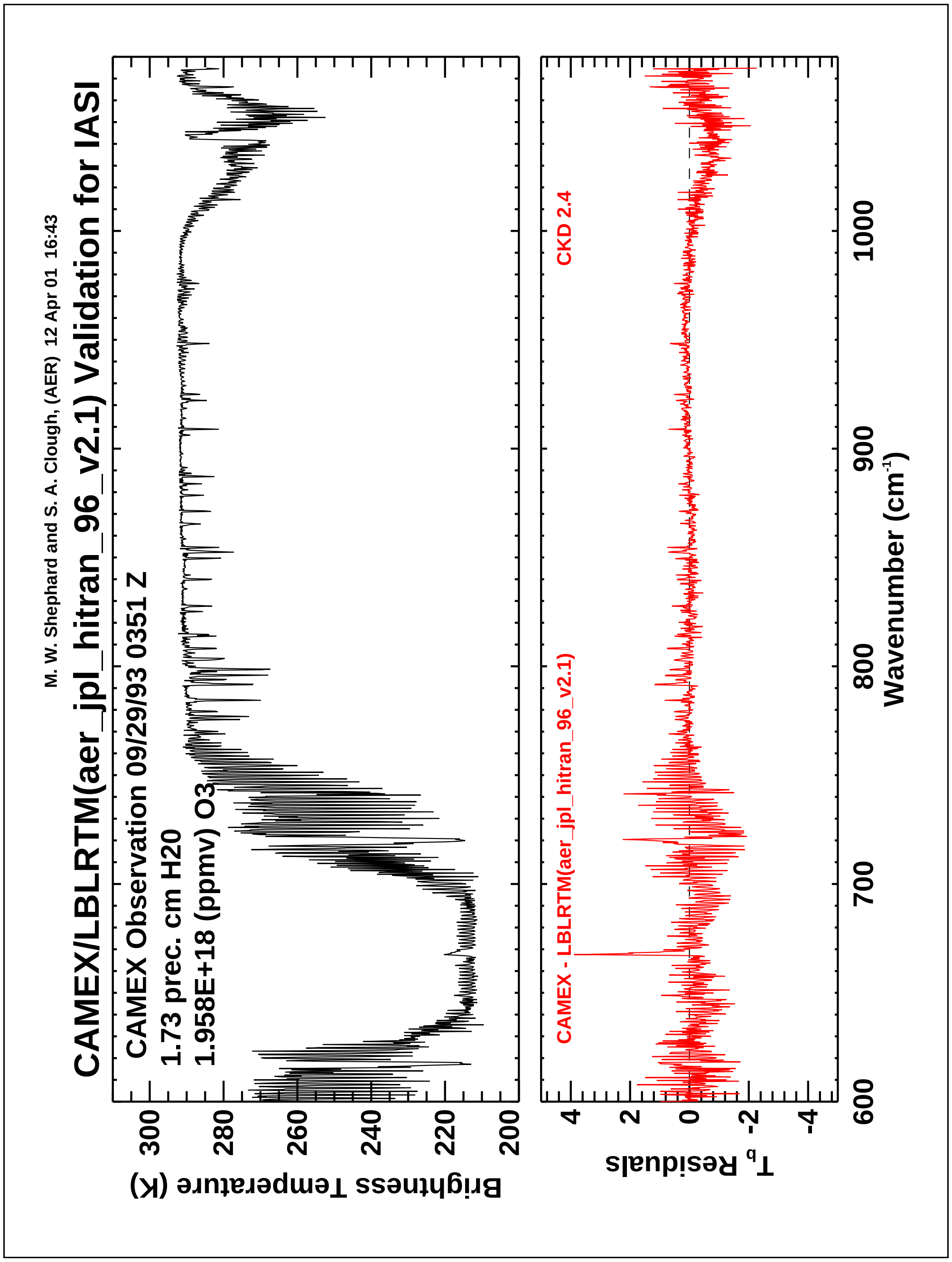

Figure 7.107: AER O_3 Scaled Case for HIS CAMEX/LBLRTM Validation.

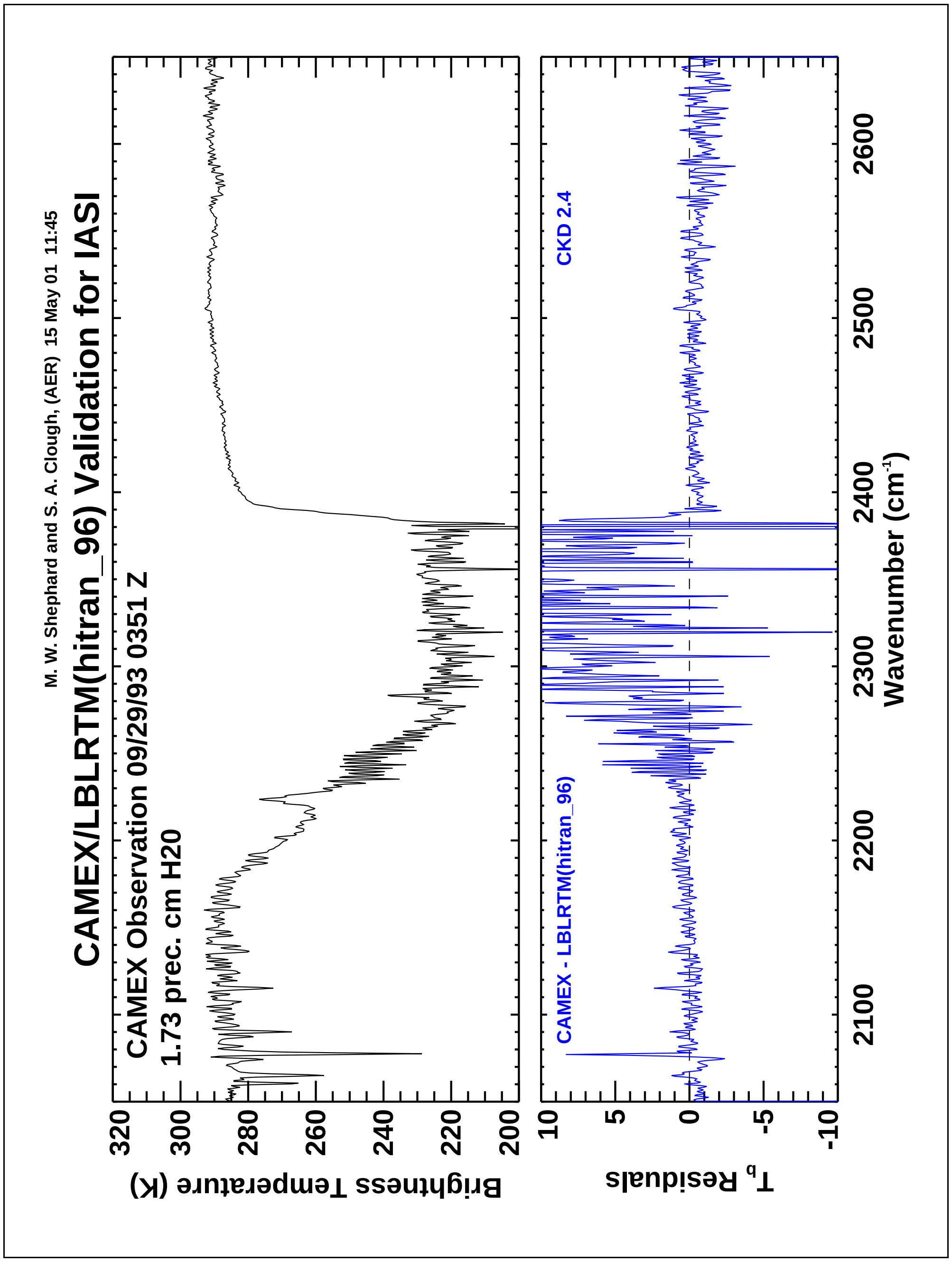

Figure 7.108: HIS CAMEX Band 3 LBLRTM Validation Without Line Coupling for Q-branches 1932, 2080, 2093, 2193 cm^{-1} using IASI reference conditions.

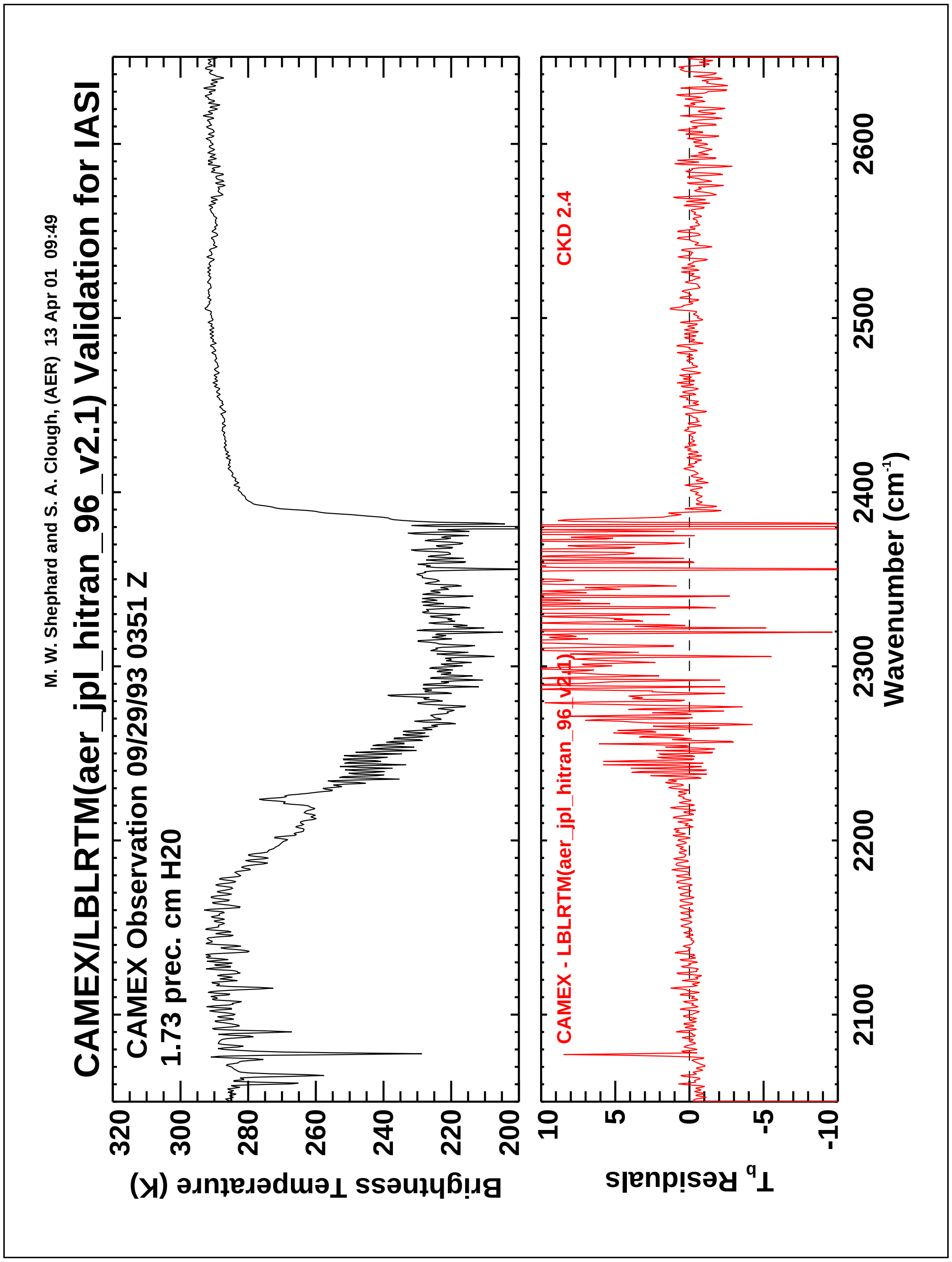

Figure 7.109: HIS CAMEX Band 3 LBLRTM Validation Without Line Coupling for Q-branches 1932, 2080, 2093, 2193 cm^{-1} using AER reference conditions.

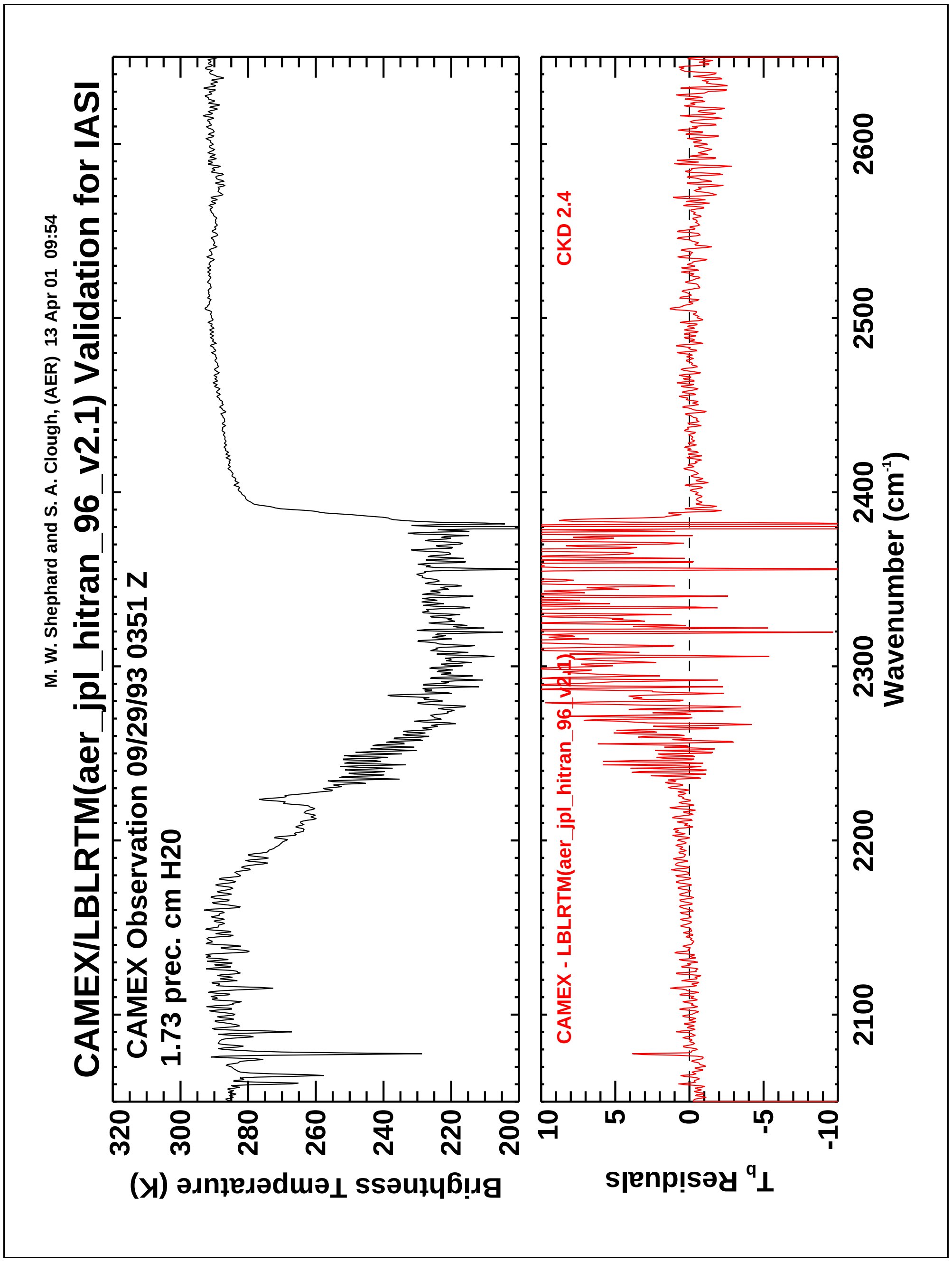

Figure 7.110: HIS CAMEX Band 3 LBLRTM Validation With Line Coupling for Q-branches 1932, 2080, 2093, 2193 cm^{-1} using AER reference conditions.

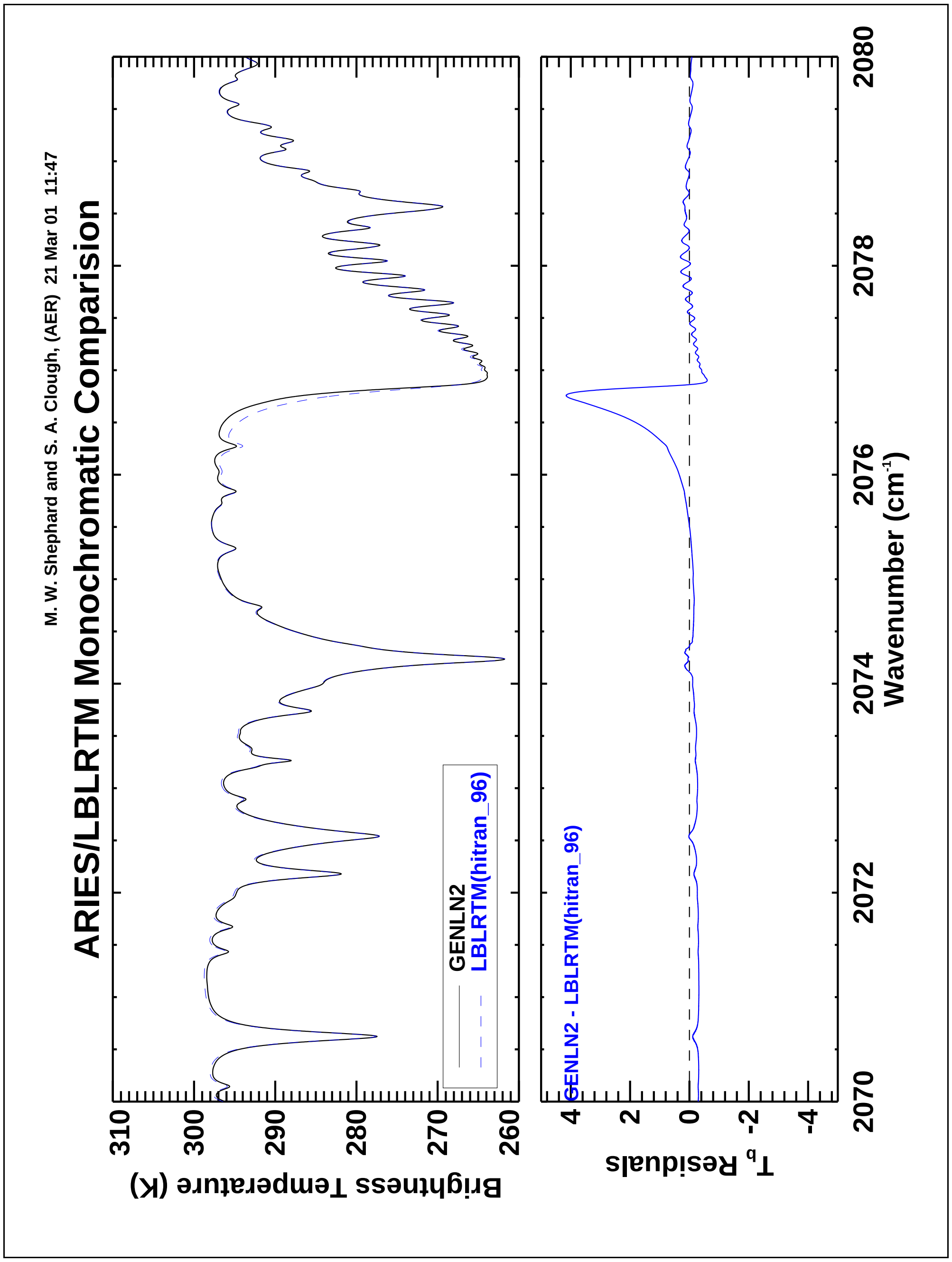

Figure 7.111: Comparison of GENLN2 with LBLRTM Without CO_2 2076 cm^{-1} Q-branch Line Coupling.

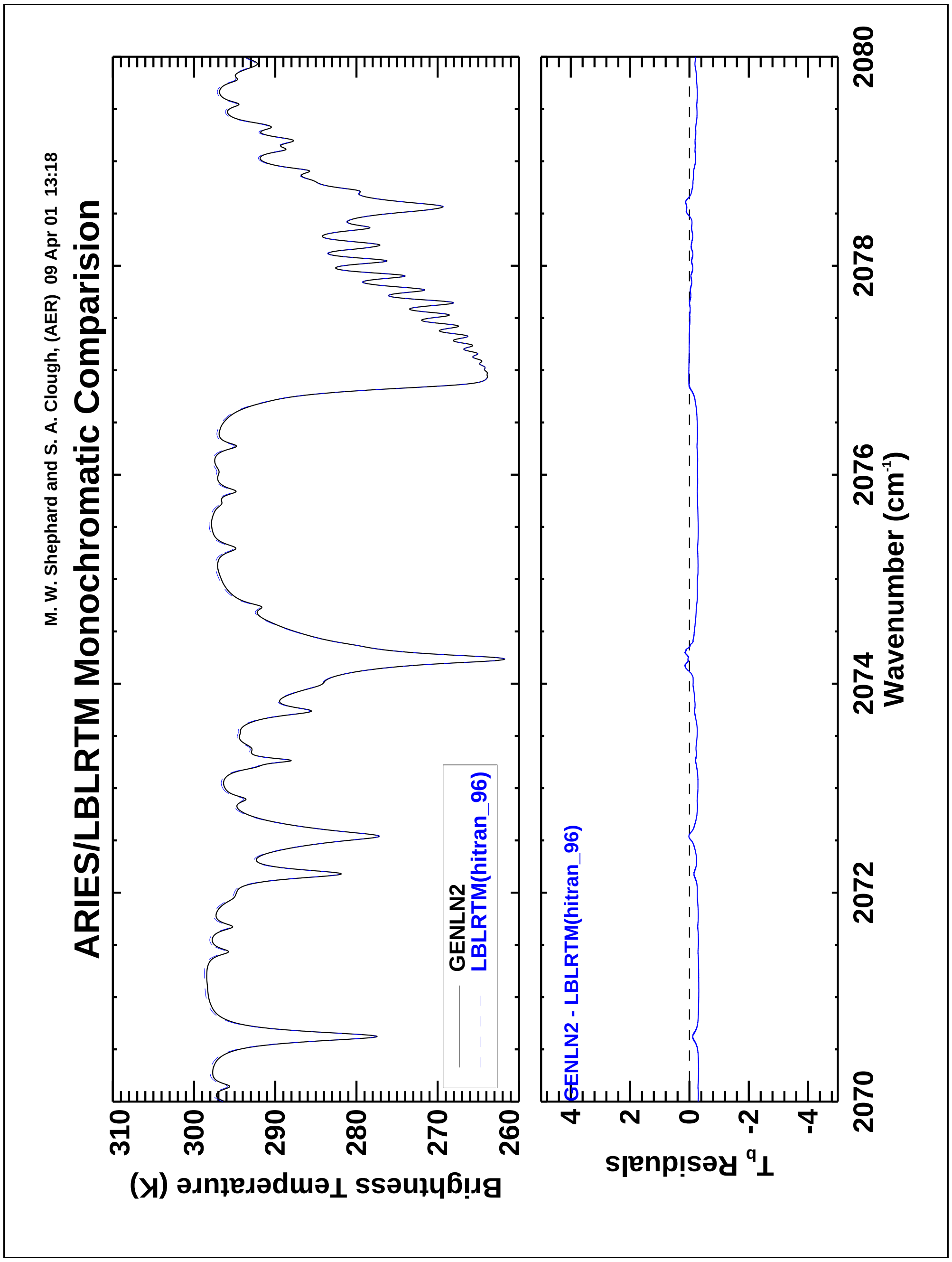

Figure 7.112: Comparison of GENLN2 with LBLRTM With CO_2 2076 cm^{-1} Q-branch Line Coupling.